ARO·9960.14-Ⓟ FC

REPORT DOCUMENTATION PAGE

READ INSTRUCTIONS
BEFORE COMPLETING FORM

1. REPORT NUMBER	2. GOVT ACCESSION NO.	3. RECIPIENT'S CATALOG NUMBER
9960.14-P		

4. TITLE (and Subtitle)	5. TYPE OF REPORT & PERIOD COVERED
COOPERATIVE PROPERTIES OF METAMAGNETIC MATERIALS.	Final Report. 1 Jun 72 - 30 Sep 76.
	6. PERFORMING ORG. REPORT NUMBER

7. AUTHOR(s)	8. CONTRACT OR GRANT NUMBER(s)
Werner P. Wolf	DA-ARO-D-31-124-72-G169

9. PERFORMING ORGANIZATION NAME AND ADDRESS	10. PROGRAM ELEMENT, PROJECT, TASK AREA & WORK UNIT NUMBERS
Yale University New Haven, Connecticut 06520	

11. CONTROLLING OFFICE NAME AND ADDRESS	12. REPORT DATE
U. S. Army Research Office Post Office Box 12211 Research Triangle Park, NC 27709	July 1976
	13. NUMBER OF PAGES
	212

14. MONITORING AGENCY NAME & ADDRESS(If different from Controlling Office)	15. SECURITY CLASS. (of this report)
	Unclassified
	15a. DECLASSIFICATION/DOWNGRADING SCHEDULE

16. DISTRIBUTION STATEMENT (of this Report)

Approved for public release; distribution unlimited.

D D C
RECEIVED
OCT 27 1976
D.

17. DISTRIBUTION STATEMENT (of the abstract entered in Block 20, if different from Report)

18. SUPPLEMENTARY NOTES

The findings in this report are not to be construed as an official Department of the Army position, unless so designated by other authorized documents.

19. KEY WORDS (Continue on reverse side if necessary and identify by block number)

Metamagnetic materials
Magnetic properties
Spin alignment
Magnetic field effects

Magnetization
Dysprosium compounds
Aluminum compounds
Garnets

Phase
Transformation

^{20.} ABSTRACT (Continue on reverse side if necessary and identify by block number)

Metamagnetic materials are ordered magnetic materials which in low field have zero moment, corresponding to antiferromagnetic spin alignment, but as the field is increased they undergo a more or less abrupt field induced phase transition to a state with a relatively large moment. The main body of the text consists of an extensive review of mose of the published work in this field. It includes discussion of some 75 different materials described in almost 300 papers and it reproduces over 200 figures of experimental results and extensive tables of important parameters.

DD _{1 JAN 73} **1473** FORM EDITION OF 1 NOV 65 IS OBSOLETE

Unclassified

COOPERATIVE PROPERTIES OF METAMAGNETIC MATERIALS

FINAL REPORT

WERNER P. WOLF

JULY 1976

SUPPORTED BY

U.S. ARMY RESEARCH OFFICE – DURHAM

UNDER GRANT NO.

DA AROD 31 124 72 G 169

APPROVED FOR PUBLIC RELEASE;
DISTRIBUTION UNLIMITED.

DEPARTMENT OF ENGINEERING

AND APPLIED SCIENCE

BECTON CENTER

YALE UNIVERSITY

NEW HAVEN, CT.   06520

Abstract

This report summarizes work done on metamagnetic materials. These are ordered magnetic materials which in low field have zero moment, corresponding to antiferromagnetic spin alignment, but as the field is increased they undergo a more or less abrupt field induced phase transition to a state with a relatively large moment. In some cases there are several successive transitions to various different magnetized states.

The main body of the text consists of a Technical Report which is an extensive review of most of the published work in this field. It includes discussion of some 75 different materials described in almost 300 papers and it reproduces over 200 figures of experimental results and extensive tables of important parameters. The report shows that metamagnetic materials have a wide variety of characteristic properties which are of interest both from a theoretical and from a practical point of view.

The report also includes a brief summary of the experimental and theoretical work which has been performed in this laboratory with AROD support. This work relates principally to a detailed study of the magnetic behavior of dysprosium aluminum garnet which is one of the most interesting of all the metamagnetic materials. For this material, some detailed comparisons between theory and experiment are possible, and a considerable amount of insight into the nature of the metamagnetic phase transition has been obtained.

Many further topics for research are indicated in this field and it is hoped that it will be possible to continue this work in the near future.

Introduction

This report summarizes the work performed by our group over the past four years. Initially, we had a great deal of trouble finding suitable staff and a number of students left after being found unsatisfactory. This delayed the start of the work, but we have finally achieved the goals which we had set.

The principal one of these was the preparation of an extensive review of all of the work which had previously been reported in the field of metamagnetism. It turned out that this was a major effort and it involved digesting almost 300 references which were found to be relevant (as well as discarding a large number that proved to be irrelevant). The final product of this work has been assembled as a technical report which has been incorporated as the final section of the present report.

It will be seen that the field of metamagnetism has indeed been an active one, and that a very wide variety of interesting properties have been studied. The most striking of all the properties is the very rapid change of magnetization with field at the first order field induced phase transitions, and the many changes in other properties which accompany the change in magnetization. So far, there do not appear to have been any practical applications of any of these effects, but it is certainly possible that such applications will be found. In any case, there can be no question that metamagnetism is one branch of solid state physics in which a large number of new phenomena remain to be discovered and explained.

One particular aspect to which we have paid attention in our own work
are the subtle effects which take place in the immediate vicinity of the
first order transition, and especially close to the point at which the first
order transition goes over into a second order transition. Such a point
is called a tricritical point and there has been a considerable amount of
theoretical interest in the related phenomena.

Our own work on tricritical point effects and related problems has been
discussed in some detail in sections III and IV of the attached Technical Report
1, and it seems redundant to repeat this material here. Moreover, our work
has been published in 14 technical papers and abstracts and reprint copies
are available for further details. We shall list below the titles and
references of these papers.

Experimental and Theoretical Results

We can summarize our contributions briefly under 5 main headings.

a) _Induced Staggered Field_. This was a new and completely unexpected
effect which was first noted explicitly in the neutron scattering experi-
ments of Blume et al. at Brookhaven National Lab. Our contribution consisted
in finding a microscopic explanation of this effect. The explanation involved
a completely new multiple spin correlation effect which had never been
considered before. The special interest of this effect is the fact that it
is not predicted even qualitatively by mean field theory. This is quite
unusual, since mean field theory generally predicts physical phenomena at
least approximately. This work was presented at two conferences. Refs. 5 and

8 and the principal result was incorporated into a Physical Review Letter publication (Ref. 6).

b) <u>Optical observation of domains in dysprosium aluminum garnet (DAG).</u> In the first instance we initiated a very active collaboration with Dr. J.F. Dillon at Bell Labs, Murray Hill, in which he and E. Yi Chen performed the actual experiments while we helped in the analysis. Various interesting results emerged from this work.

One was the first observation of antiferromagnetic and paramagnetic domains in the mixed phase region of a metamagnetic transition. Dr. Dillon managed to make a movie of some of the observation which has caused some interest. The movie (and also still photos) showed the nucleation and growth of various types of domains and it is clear that this is a very fruitful field for many further studies. Dr. Dillon is now extending this work without our direct participation and he continues to get many interesting results.

During the course of the early domain study experiments, an unusual hysteresis was noted in the magneto-optical rotation as a function of field. This was completely unexpected and it caused considerable surprise at the time. For example, it became the subject of an invited paper at the last International Magnetism Conference (held in Moscow in 1973) and no explanation was apparent at that time (Ref. 1) or at the following U.S. meeting (Ref. 2).

It subsequently turned out that the hysteresis was related to the induced staggered field mentioned above in connection with the Brookhaven

neutron experiments, and the same explanation resolved both puzzles.

The hysteresis is potentially interesting for possible applications since any new mechanism which provides a "memory feature" to an active material (in this case a material with both magnetic and optical characteristics) may turn out to be useful.

c) Light scattering by domains in DAG. In addition to direct visual observations of domains, one may also study domains by the scattering of monochromatic light. This is useful when the domains become very small, as they do near a critical or tricritical point. We have recently completed such a study on a "wing critical point" of DAG and we plan to present the results at the next International Magnetism Conference (Ref. 12). The method has allowed us to study the phase boundary in a new way and it promises to give results which are more accurate than those which can be obtained by the usual magnetic or magneto-optic measurements.

d) Relaxation methods for studying first order phase boundaries. A number of different experiments were tried to study the response of domains in the mixed phase region of a metamagnetic transition. In the end we found two new effects which made it possible to locate the first order phase boundary to considerably greater accuracy than had previously been possible. We applied the methods to study one of the tricritical points of DAG and found striking agreement with recent predictions of the theory. This work was published in a Physical Review Letter (Ref. 10) and it will be the subject of part of an invited talk by the principal investigator at the

next International Conference on Magnetism (Ref. 13).

e) <u>Equations of State (Scaling) near Tricritical Points</u>. One of the predictions of modern theories of phase transitions is a general method for finding universal equations of state with which to describe experimental results over a region of field, temperature and magnetization. Such equations of state are useful since they allow the reduction of a large amount of information into a single universal curve.

Initially, our work in this area was also collaborative and we had some fruitful interactions with Prof. H.E. Stanley at M.I.T. (see Ref. 3). When the results of our new relaxation method became available for analysis, we were able to test the theoretical predictions and we found excellent agreement. This work was presented at the 1975 Conference on Magnetism and Magnetic Materials and is described in Ref. 11.

Summary

The common thread which has characterized our work has been the development of new experimental and theoretical techniques with which to study field induced phase transitions in metamagnetic materials. We have applied these methods to situations where critical tests of general theoretical predictions could be made and we have found excellent agreement. Such agreement is not trivial in this field, since there are considerable difficulties in these kinds of experiments (see Ref. 13).

In parallel with this detailed work on special situations, we have also carried out a broad survey of the field as a whole. This survey has been

summarized in the Technical Report which is attached and we hope shortly to publish this in the open literature. The report shows that there are many kinds of interesting phenomena in the general area of metamagnetism which deserve further study, and we very much hope that we shall be able to continue to work in this field.

At this point in time there are no obvious practical applications which would be useful in current operational systems. However, it would seem clear that any field which has as many new and unusual phenomena as Metamagnetism must one day lead to applications which are both unique and useful.

Published Papers and Conference Abstracts

of Work Supported in Part by AROD Grant AROD 31 124 72 G 169

1. Optical Studies of Antiferromagnetic-Paramagnetic Phase Transitions in Dysprosium Aluminum Garnet (DAG). J.F. Dillon, Jr., E. Yi Chen and W.P. Wolf. Invited paper presented at International Conference on Magnetism, Moscow, September 1973.

2. Microscope Studies of the Mixed Phase Region of the Ising Antiferromagnet Dysprosium Aluminum Garnet (DAG). J.F. Dillon, Jr., E. Yi Chen and W.P. Wolf. Presented at the 19th Conference on Magnetism and Magnetic Materials, AIP Conf. Proc. 18, 334 (1974).

3. Magnetic Equation of State of Dysprosium Aluminum Garnet (DAG) Near a Tricritical Point. A.T. Skjeltorp, R. Alben and W.P. Wolf. Presented at the 19th Conference on Magnetism and Magnetic Materials, AIP Conf. Proc. 18, 770 (1974).

4. Practical Difficulties in the Determination of Magnetic Equations of State near Tricritical Points. W.P. Wolf, R. Alben and A.T. Skjeltorp. Invited paper presented at Conference on Critical Phenomena in Multicomponent Systems, April 1974 (unpublished).

5. DAG: An Example of an Unusual Kind of Ising Model. N. Giordano, W.P. Wolf, J.F. Dillon and E. Yi Chen. Presented at Conference on Critical Phenomena in Multicomponent Systems, April 1974 (unpublished).

6. Time-Reversed Antiferromagnet States in Dysprosium Aluminum Garnet. J.F. Dillon, Jr., E. Yi Chen, N. Giordano and W.P. Wolf. Phys. Rev. Lett. 33, 98 (1974).

7. Field Induced Magnetic Phase Transitions in DAG. W.P. Wolf. Invited paper presented at 20th Conference on Magnetism and Magnetic Materials, AIP Conf. Proc. 24, 255 (1975).

8. Multiple Spin Correlation Effects. N. Giordano and W.P. Wolf. Presented at 20th Conference on Magnetism and Magnetic Materials, AIP Conf. Proc. 24, 333 (1975).

9. Antiferromagnetic Domain Structures in Dysprosium Aluminum Garnet (DAG). J.F. Dillon, Jr., E. Yi Chen and W.P. Wolf. Bull. Am. Phys. Soc. 20, 501 (1975).

10. New Method for Investigating Magnetic Tricritical Points. N. Giordano and W.P. Wolf. Phys. Rev. Lett. 35, 799 (1975).

11. Tricritical Behavior of Dysprosium Aluminum Garnet. N. Giordano and W.P. Wolf. Presented at 21st Conference on Magnetism and Magnetic Materials, AIP Conf. Proc. 29, 459 (1976).

12. Light Scattering from Metamagnetic Domains in Dysprosium Aluminum Garnet. N. Giordano and W.P. Wolf. To be presented at the International Conference on Magnetism, Amsterdam, September 1976 (to be published).

13. Experimental Studies of Multicritical Points in Magnetic Systems. W.P. Wolf. Invited paper; to be presented at International Conference on Magnetism, Amsterdam, September 1976 (to be published).

14. Metamagnetism. E. Stryjewski and N. Giordano. Technical Report (to be published).

TECHNICAL REPORT 1

METAMAGNETISM

BY E. STRYJEWSKI AND N. GIORDANO

JULY 1976

DEPARTMENT OF ENGINEERING

AND APPLIED SCIENCE

YALE UNIVERSITY

NEW HAVEN, CT.   06520

Abstract

    This is a review of the physical properties of metamagnets. These

crystals are antiferromagnets which can undergo magnetic phase transitions

upon application of a magnetic field. The treatments of mean field

theory describing these materials are reviewed as are the treatments of

more modern theories. The experimental properties of many known meta-

magnets are described with emphasis on the variety of means by which the

metamagnetic transitions can be observed. For some materials there have

been studies of tricritical point behavior. A description of the

experimental results of these studies and a comparison of the results

with theory is also included.

III. MATERIALS (Continued)

    D. GARNETS

        1. Dysprosium Aluminum Garnet

        2. TbAlG, HoAlG

    E. MIXED CRYSTALS

        1. $Co(S_xSe_{1-x})_2$

        2. $UA_{1-x}B_x$; (A = P, As; B = S, Se)

IV. TRICRITICAL AND CRITICAL BEHAVIOR

    A. $FeCl_2$

    B. DAG

    C. $CsCoCl_3 \cdot 2D_2O$

    D. DISCUSSION

V. SUMMARY

APPENDIX I. MISCELLANEOUS METAMAGNETIC MATERIALS

APPENDIX II. TABLE OF BULK MAGNETIC PROPERTIES

    TABLES

    FIGURES

    REFERENCES

I. INTRODUCTION

Magnetic field induced phase transitions have been the subject of a large number of experimental studies. A wide variety of different kinds of phase transitions in many different materials have been investigated. In this report we survey the experimental work to date on field induced phase transitions in highly anisotropic magnetic systems. These systems are commonly referred to as metamagnets. Although the term "metamagnet" is often used in the literature,[1,2] it is appropriate at this point to discuss how we will use this term and hence define the scope of this report. Magnetic materials which exhibit field induced transitions can generally be divided into two classes; (1) those which are highly anisotropic, and (2) those which are isotropic or only weakly anisotropic. The phase transitions in anisotropic materials (class 1) are generally characterized by simple reversals in the local spin directions. This is in contrast with more isotropic materials (class 2) in which there is typically a rotation in the spin directions at the transitions. The body of this report will be concerned only with materials in class 1. We will however first discuss examples of both classes so as to make clear where we will draw the dividing line between them.

Well known examples of class (1) are $FeCl_2$[2] and $DyPO_4$[3], and the phase diagram of these two systems is shown schematically in fig. 1a. As the crystals are cooled in zero field they undergo a second order phase transition[4] at their respective Neel temperature (T_N). Below T_N they are ordered antiferromagnetically with a two sublattice structure in which the large anisotropy constrains the spins to point either parallel or anti-

parallel to the easy axis. Upon the application of a field at high temperatures (but below T_N) there is a second order phase transition from the antiferromagnetic to the paramagnetic phase. This behavior persists for a range of temperatures below T_N, and hence there is a line of second order transitions (or critical points) in low fields (see fig. 1). Upon the application of a field at low temperatures however, the behavior is strikingly different. There is still a phase transition from the antiferromagnetic phase directly to the paramagnetic phase, but now this transition is first order.[4] This behavior also persists over a range of temperatures (and also down to $T = 0$) and thus there is a line of first order transitions in high fields (shown dashed in fig. 1). The line of critical points at high temperatures and the line of first order transitions at low temperatures meet at a point which is known as a tricritical point.[5] The behavior near this point has been of great interest recently and will be discussed in more detail in the following sections. It is important to note that in both the antiferromagnetic and paramagnetic phases the spins are constrained by the anisotropy to lie along the easy axis.

Some other well known systems in class (1) are[6,7] $CoCl_2 \cdot 2H_2O$ and $FeCl_2 \cdot 2H_2O$. Schematic phase diagrams for these materials are shown in fig. 1b. Both order antiferromagnetically with a six sublattice structure in which the spins lie parallel or antiparallel to the easy axis. At high temperatures there is a line of critical points while at low temperatures the behavior is somewhat different. Upon the application of a field at low temperatures there is a first order transition from the antiferromagnetic to an intermediate phase which is believed to be ferrimagnetic with four

sublattices parallel and two antiparallel to the easy axis. At higher

fields there is another first order transition to the paramagnetic state.

As shown in fig. 1b the two phase boundaries boardering the ferri-

magnetic phase merge to a point at which the antiferromagnetic-paramagnetic

boundary begins. There is thus a triple point at which all three phases

are in coexistence. The temperature at which the phase transition changes

from first to second order is not yet known, although mean field theory

indicates that it could be either above or below the triple point temperature.[8]

We wish to emphasize that in the antiferromagnetic, ferrimagnetic and

paramagnetic phases the spins are constrained by the anisotropy to lie

along the easy axis.

Next we consider some systems which are typical of class (2):

MnF_2[9] and $GdAlO_3$.[10] Schematic phase diagrams for these two weakly aniso-

tropic materials are shown in fig. 1c. Both order antiferromagnetically

in zero field and display a line of critical points in low fields.

Upon the application of a field at low temperatures there is a first order

transition to the spin-flop phase in which the spins cant away from the

easy axis so as to partially satisfy both the (antiferromagnetic) spin-spin

interactions and the energy of interaction with the field. At higher fields

there is a second order transition to the paramagnetic phase, as the angle

the spins make with the easy axis goes continuously to zero. An important

point to note about these spin flop systems is that the weak anisotropy

allows the spins to rotate away from the easy axis.

From the above discussion we see that for the systems in class (1)

typified by $FeCl_2$, $DyPO_4$, $CoCl_2 \cdot 2H_2O$ and $FeCl_2 \cdot 2H_2O$ the phase transitions

involve only <u>reversals</u> of spin directions. The strong anisotropy prevents

the spins from rotating away from the easy axis at the phase transition. For the spin-flop systems (class (2)), however just the opposite is true. The transitions in these systems proceed via spin <u>rotations</u> and not simple reversals. We will use this basic difference to draw the line between class (1) and class (2). All those systems in which the dominant change in spin-direction at a transition is a simple reversal will be placed in class (1), and are referred to as metamagnetic in the following. Those materials for which the dominant change is a rotation will be placed in class (2); these systems are <u>not</u> discussed in this report. Note that our criterion allows for a small rotation of the spins away from the easy axis at a transition so long as it is accompanied by a reversal in direction. As in any classification scheme of this sort there are bound to be ambiguities. The materials which we feel are on the borderline between classes (1) and (2) have been included in this report.

The materials discussed above are all uniaxial with all spins having the same easy axis. This need not be the case--that is different spins may have easy axes which point in different crystallographic directions. This situation occurs in several systems including $Dy_3Al_5O_{12}$ and $TbAlO_3$.

The organization of this report is as follows. In Section II we give a brief review of the theoretical work on simple metamagnets. Section II also contains a discussion of the effects of the demagnetizing field on the experimentally observed properties including the magnetization and the specific heat. In Section III we discuss the general properties of the

metamagnetic systems which have been investigated. This includes the behavior of various bulk properties such as the magnetization, the Neel and tricritical temperatures, and the critical fields. Also included are certain material properties unrelated to the magnetic properties which are important considerations from the point of view of the experimentalist (e.g., chemical and mechanical characteristics). Section IV describes the detailed work which has been concerned with the behavior near both the tricritical point and the critical line. Section V contains a summary and an outlook for future work in this field. Appendix I briefly describes materials whose field induced behavior has not been studied in great detail. Appendix II summarizes in tabular form the bulk properties of the materials discussed in this review.

II. THEORY

In this section we will briefly review the theoretical work to date on metamagnetic systems. We will spend some time discussing the simplest mean field theory (MFT) both because of its simplicity and because more sophisticated theories verify many of the MFT results. After discussing the theoretical work, the effects of the demagnetizing field on the observable properties are also considered.

A. MEAN FIELD THEORY

One of the simplest models of a metamagnet is a system of $S = 1/2$ Ising spins in which there are interactions between first and second nearest neighbors. This model has been discussed using MFT by a number of workers and very recently Kincaid and Cohen[11] have exhaustively reviewed and extended these results. We refer the reader to their paper for extensive references to earlier theoretical work.

The Hamiltonian for the simple model introduced above is

$$\mathcal{H} = |J| \sum_{<nn>} S_{jz} S_{kz} + J' \sum_{<nnn>} S_{jz} S_{kz} - \mu H_i \sum S_{jz} . \qquad (2.1)$$

The first sum is over nearest neighbor pairs ($<nn>$), the second over next nearest neighbor pairs ($<nnn>$), $S_{iz} = \pm 1/2$, μ is the magnetic moment and H_i is the internal magnetic field. An important parameter in the MFT treatment of this model is $R \equiv Z'J'/Z|J|$, where Z and Z' are the number of first and second neighbors respectively. The type of behavior

exhibited by the model depends upon the value of R[11]. For $R < -3/5$
corresponding to a ferromagnetic second neighbor interaction (note that we
have restricted the nearest neighbor interaction to be antiferromagnetic)
the model behaves qualitatively like the materials $FeCl_2$ and $DyPO_4$
discussed in the introduction. At high temperatures the antiferromagnetic-
paramagnetic transition is second order, at low temperatures it is first
order and at the intermediate temperature where the changeover occurs is
the tricritical point.[5] The MFT predictions for the behavior of this
model are shown in fig. 2 where we show schematically the magnetization, M,
and the staggered magnetization, M_s, (the difference in the magnetizations
of the two sublattices) as a function of H_i at various temperatures.
For temperatures less than T_N but greater than the tricritical temperature,
T_t, M_s goes to zero continuously corresponding to a second order transition,[4]
while M displays a change in slope at the transition ($\chi \equiv (\partial M/\partial H_i)_T$ is finite
and discontinuous at the transition). For $T < T_t$ the transition is first
order as both M and M_s exhibit discontinuities. For $T = T_t$, M_s goes to
zero continuously while M displays a discontinuity in slope with an infinite
gradient when the tricritical point is approached from low fields. The
phase diagrams in the $H_i - T$ and $M - T$ planes are also shown in fig. 2.
In the $H_i - T$ plane the first and second order lines have equal slopes
(but unequal second derivatives) at the tricritical point. The $M - T$
diagram is double valued for $T < T_t$ since two phases with different values
of M are in coexistence there. MFT predicts that all three phase boundaries
in the $M - T$ plane approach the tricritical point linearly with the para-
magnetic line below T_t having the same slope as the second order line.

We have discussed the MFT results for $R < -3/5$ at some length since as will be seen, these results are qualitatively applicable to a large number of real systems. However, the behavior for other values of R is also of interest.

The $H_i - T$ phase diagram predicted by MFT[11,12] for $0 > R > -3/5$ is shown schematically in fig. 3. At high and low temperatures it is similar to that shown in fig. 2. However, the first order line does not end at the critical line, but instead extends into the antiferro-magnetic region of the phase diagram before ending. Thus, for a range of temperatures there is a first order transition between two different anti-ferromagnetic states. This behavior has been discussed by Kincaid and Cohen.[12] The point where the critical line meets the first order line is a critical endpoint while the point where the first order line ends has been termed a bicritical endpoint.[12] The motivation for these names is discussed in references 11 and 12. Although the type of phase diagram shown in fig. 3 has not yet been found in any real system, there is some evidence[12] that it may be applicable to $FeBr_2$ (see section III).

For $R = -3/5$ the $H_i - T$ phase diagram is identical to that given in fig. 2, while for $R \geq 0$ the phase transition is second order at all temperatures down to $T = 0$.[11]

Although this simple two sublattice model has been very successful in describing metamagnetic behavior, there are many materials for which it is inapplicable. These are materials which have more than two sublattices (such as $CoCl_2 \cdot 2H_2O$) and/or spin quantum numbers higher than $1/2$. The phase transitions in these and more complicated systems have in many cases been

successfully described by MFT treatments of models in which third and more
distant neighbor interactions have been included, etc. This theoretical
work will be discussed along with the experimental results for the appro-
priate materials.

B. MODERN THEORIES OF CRITICAL AND TRICRITICAL BEHAVIOR

In recent years there has been a great deal of interest in the behavior
of systems near critical points.[4] The so-called "modern" theories of phase
transitions[4] including series expansion[4] and renormalization group[13]
studies have shown that MFT is usually a reliable guide to qualitative
features such as the general topology of the phase diagram and the order
of the transition. These studies have also shown that MFT is often
incorrect as to more quantitative aspects of the behavior, such as the
characteristic exponents[4] which describe the way various quantities behave
upon approach to a critical point. Accordingly there has been a great
deal of work to determine which, if any, of the MFT predictions for the tricritical
behavior of metamagnets are reliable. The renormalization group theories of Riedel
and Wegner[14] and later Nelson and Fisher,[15] the reanalysis of MFT by
Bausch,[17] the series expansion work by Harbus and Stanley[18,19] and Saul,
Wortis and Stauffer,[20] and numerous other works[21] have shown that MFT is
correct as to the general topology of the metamagnetic phase diagrams. In
addition, this work has shown that many of the quantitative predictions of
MFT are also correct.

Just as in the case of ordinary critical phenomena[4] the quantitative behavior of a metamagnet can be described by various exponents. The definitions of a number of critical line and tricritical exponents are given in table 1 where we follow the notation of Griffiths[22] and Kincaid and Cohen.[11] Note that the exponents in table 1 pertain only to the MFT regime $R < - 3/5$ so that a tricritical point is present. See ref. 11 for a discussion of the exponents in the MFT regimes $0 > R \geq - 3/5$.

As an example of the exponents consider the behavior of M_s along various paths in the $H_i - T$ plane. For constant T with $T_t < T < T_N$ we have from table (2.1)

$$M_s \sim (H_c - H_i)^\beta \tag{2.2}$$

where β is a critical exponent and H_c is the critical internal field at that temperature. Note that the universality hypothesis[23] as well as the work discussed above[13-21] predict that all of the critical exponents are independent of position on the critical line. Thus, only one set of exponents are needed to describe the behavior along the entire critical line. Another theoretical prediction known as "smoothness"[24],[22] is that the exponents should be the same for all paths of approach to a critical point which are not parallel to the phase boundary. For example, if the critical line is approached at constant field then we expect

$$M_s \sim (T_c - T)^\beta \tag{2.3}$$

where this is the same exponent β as in Eq. (2.2). If, however, the critical line is approached along a path which is tangential to the phase

boundary then the exponent will in general be different.[24,22]

Although the exponents are independent of position on the critical line, they are predicted to change discontinuously at the tricritical point.[22] For example, for $T = T_t$ we have from table 1.

$$M_s \sim (H_t - H_i)^{\beta_t} \tag{2.4}$$

where the tricritical exponent β_t is not in general equal to the critical exponent β in Eq. (2.2). The concept of smoothness is expected to also apply at the tricritical point,[22] and thus if we measure M_s along a path of constant field we expect to observe the same exponent, β_t, as in Eq. (2.4) (we assume here that the phase boundary at the tricritical point is not parallel to either the H_i or T axis). If the tricritical point is approached along the first order phase boundary then the exponent will be different.[22]

Table 1 also lists the values of the exponents predicted by MFT and the modern theories. We see that there are a number of cases in which MFT is thought to be incorrect. Most notable among these are (1) $\chi_i \equiv (\partial M / \partial H_i)_T$ diverges as the critical line is approached from either side; (2) χ_i diverges as tricritical point is approached from the paramagnetic side; (3) the MFT values for all of the critical line exponents are incorrect; (4) although it is not shown in table 1, the modern theories[25,26] predict that in the $M - T$ phase diagram the paramagnetic line and the critical line have unequal slopes.

Renormalization group work[14,27] has also shown that at the tricritical point some of the power laws such as that given in Eq. (2.3) are modified by logarithmic correction factors. To date there is no direct experimental

evidence for their existence. It has been shown[28] however that if the log correction factors are not properly allowed for in the analysis of experimental data, they can give rise to an apparent exponent with a value lower than the true value. Thus, the presence of log correction factors may serve to complicate the interpretation of data near tricritical points.

Besides calculations of the various exponents, recent theoretical work has also emphasized a geometrical approach to phase transitions and phase diagrams. When Griffiths[5] introduced the term "tricritical point" he also made clear the importance of the symmetry breaking field which in this case is a staggered field, H_s. H_s is a field which alternates in sign on the two sublattices and is thermodynamically conjugate to M_s. Griffiths pointed out that the full $H_i - H_s - T$ phase diagram for a simple metamagnet with a tricritical point appears as shown in fig. 4. The shaded surfaces denote coexistence surfaces at which two phases coexist--that is, they are surfaces of first order transitions. There are three such surfaces and they separate the three possible combinations of the two antiferromagnetic and the paramagnetic phases. Bordering these first order surfaces are three lines of critical points which come together at the tricritical point. The full $H_i - H_s - T$ phase diagram shows very clearly the topological difference between the critical points and the tricritical point, and leads one to expect quite naturally that behavior (i.e., the exponents) in the two cases will not be the same.[5] While it is in general not possible to apply a real staggered field in the laboratory, it will be seen that in certain systems it may not be possible to avoid

applying such a field.

It is also interesting to consider the $H_i - H_s - T$ phase diagram when a bicritical end point is present, and this is shown in fig. 5 .[11] Now the two lines of critical points which extend out of the $H_s = 0$ plane do <u>not</u> meet at the edge of the coexistence surface in the $H_s = 0$ plane. The topology of the phase diagram in the vicinity of the bicritical end point is seen to be very different than near the tricritical point in fig. 4 . It is thus not surprising that the exponents at the bicritical endpoint are expected to be different from those at a tricritical point.[11,12]

Aside from predicting values of the various exponents, the modern theories also predict the form of the equation of state. More specifically the theory[22,29,30] predicts that near the tricritical point the free energy is a generalized homogeneous function of three scaling fields. The scaling fields are not simply H_i, H_s and T, but are certain combinations of these variables, and are determined by the geometry of the phase diagram. The theory prescribes that the scaling fields be chosen as follows. (1) One of them should be not parallel to the $H_s = 0$ plane at the tricritical point; (2) one should be in the $H_s = 0$ plane, but not parallel to the phase boundary at the tricritical point; (3) one should be parallel to the phase boundary in the $H_s = 0$ plane at the tricritical point. A convenient choice of scaling fields is H_s, t and g where

$$t = \frac{T - T_t}{T_t} \tag{2.5}$$

$$g = t - p \frac{H_i - H_t}{H_t} \tag{2.6}$$

with p the slope of the phase boundary at the tricritical point. A second choice for g which can be used[31] is

$$g' = \frac{H_i - H_c(t)}{H_c(t)} \tag{2.7}$$

where $H_c(t)$ is the value of H_i at the phase boundary. From the homogeneity of the free energy, the following scaling forms for M_s and M can be derived

$$M_s/|t|^{\beta_t} = \text{Function } (g/|t|^{1/\phi})$$

$$M_s/|g|^{\beta_t \phi} = \text{Function } (t/|g|\phi)$$

$$\frac{(M - M_t)}{M_t} / |t|^{\beta_u} = \text{Function } (g/|t|^{\beta_u \delta_u}) \tag{2.8}$$

$$\frac{(M - M_t)}{M_t} / |g|^{1/\delta_u} = \text{Function } (t/|g|^{1/\beta_u \delta_u})$$

where β_u, δ_u, β_t and ϕ are tricritical exponents (see table 2.1). For simplicity we have not included the dependence on H_s (since it is equal to zero in the laboratory) and we set it equal to zero in the following. Scaling theory does not predict either the values for the exponents or the form of the "Function". Equation (2.8) does indicate that if either M or M_s is plotted in the appropriate way (i.e., $(M - M_t)/|t|^{\beta_u}$ vs $g/|t|^{\beta_u \delta_u}$) then a family of curves M(t,g) or $M_s(t,g)$ will collapse onto a single curve. The "quality" of the data collapsing will depend upon the values of the exponents and hence data from the entire neighborhood of the tricritical point can be used to determine the exponents.

In addition to the form of the equation of state, scaling theory also predicts relations between different exponents. These are known as "scaling relations" and are discussed in detail in refs. 22, 29 and 30.

C. OTHER THEORETICAL WORK

In addition to the work concerned with the behavior at the phase transitions there has also been considerable theoretical work on various properties of the metamagnetic phases themselves. This work includes the theory of spin-cluster excitations in $CoCl_2 \cdot 2H_2O$ and similar materials by Tinkham and coworkers[32,33] and others, the theories of domain structure and nucleation by Mitsek[34,35] and theories of the hysteresis at the first order transitions by Tinkham[36] and Motokawa.[37] These theories will be discussed along with the relevant materials in section III.

D. DEMAGNETIZING EFFECTS

In our discussions to this point we have been concerned only with the internal magnetic field, H_i. However, in all finite samples the experimentally measured external field, H_o, is <u>not</u> equal to H_i. For an ellipsoidal sample with the field applied along one of the principal axes, the two are related by

$$H_i = H_o - NM \qquad (2.9)$$

where N is the demagnetizing factor and is a function only of the sample shape.[38] Thus sample shape is very important since it is clearly desirable to have H_i be homogeneous throughout the sample.

The presence of the demagnetizing field has several important consequences. From Eq. (2.9)

$$\delta(H_i) = \delta(H_o) - N \, \delta(M) \tag{2.10}$$

and thus at a first order transition where $\delta(H_i) = 0$

$$\delta(M) = \frac{1}{N} \, \delta(H_o) \tag{2.11}$$

i.e., M is linear in H_o with slope 1/N. Thus a first order transition is spread out over a range of applied field.[39] The reason for this can be simply understood by considering the behavior of H_i using Eq. (2.9). If at the first order transition M were to increase discontinuously, then from Eq. (2.9) H_i would correspondingly <u>decrease</u> to a value below that needed to induce the transition. Thus the transition cannot go all at once, but must take place gradually. This is accomplished by having the sample break up into coexisting domains of the two phases,[39] much as in a ferromagnet below its critical temperature. The resulting H_o-T phase diagram is shown in fig. (6); it is similar to the H_i - T phase diagram except that the first order line splits open to enclose the so called mixed phase region in which the domains are present. From Eq. (2.9) the susceptibility $\chi_o \equiv (\partial M/\partial H_o)_T$ is related to the susceptibility $\chi_i \equiv (\partial M/\partial H_i)_T$ by

$$\frac{1}{\chi_o} = \frac{1}{\chi_i} + N \tag{2.12}$$

Hence, the largest possible value for χ_o (which corresponds to $\chi_i \to \infty$) is 1/N which is just the value at a first order transition Eq. (2.11).

From Eqs. (2.9) and (2.12) we see that transforming the magnetic properties from functions of H_o to functions of H_i is relatively straightforward. The same is not true for the specific heat at constant applied field, C_{H_o}. It can be shown[40] using classical thermodynamics that C_{H_o} is related to the specific heat at constant internal field, C_{H_i}, by

$$C_{H_i} = C_{H_o} + \frac{T \left(\frac{\partial M}{\partial T}\right)^2_{H_i}}{\frac{1}{N} + \left(\frac{\partial M}{\partial H_i}\right)_T} \qquad (2.13)$$

Thus, to convert from C_{H_o} to C_{H_i} requires a rather detailed knowledge of $M(H_i,T)$. From table 2.1 we see that C_{H_i} diverges at the critical point with an exponent α. It is interesting to determine if this singularity is also present in C_{H_o}. According to the theoretical work of Fisner[41] C_{H_o} should not diverge, but rather have a cusp corresponding to a "renormalized" specific heat exponent α^* given by $\alpha^* = -\alpha/(1 - \alpha)$. Thus, it is possible to determine α^* and hence α along the critical line using only measurements of C_{H_o}. Note that this renormalization of the exponent should also occur at the tricritical point.

III. MATERIALS

A. CRYSTALS WITH TWO SUBLATTICES

1. $FeCl_2$

One of the most frequently studied metamagnets is $FeCl_2$. The properties
of this material played an important role in the development of the theory
of metamagnetism.[42-56] A review of its early history is given by Jacobs
and Lawrence.[57]

Figure 7 illustrates the structure and spin arrangement of $FeCl_2$. The
primitive nuclear cell is rhombohedral with space group D_{3d}^5. It is a layered
crystal of the $CdCl_2$ type in which the layers normal to the c-axis are
composed of Cl, Fe, Cl, Cl, Fe, Cl ... ions.[58-60] The crystal structure may
be generated from the rocksalt structure by removing alternate sheets of
metal ions along the [111] axis.[58]

The energy level structure of $FeCl_2$ is well understood. The free ion
^5D state is split by the predominantly cubic crystal field yielding an orbital
triplet ground state. This triplet then experiences smaller perturbations
from the spin-orbit coupling, a residual trigonal component of the crystal
field, and the exchange interactions. All of these are appreciably
weaker than the cubic crystal field so the ground state may be treated as an
effective $S = 1$, with a large uniaxial anisotropy.[58]

With this characterization of the energy level structure, the suscepti-
bility[48,61] magnetization[48,57] and Mossbauer data[59] can be explained.[62] A
neutron diffraction investigation by Birgeneau et al.[58] of the magnetic
excitations can also be understood with this model. Their results show that

the spin waves simulate those of a two dimensional ferromagnet with a large anisotropy. This is due to the fact that the exchange interactions are strongly ferromagnetic within a plane and weakly antiferromagnetic between planes. These properties of the exchange interactions give rise to the meta-magnetic nature of $FeCl_2$.

The metamagnetic transition of $FeCl_2$ was first observed by Starr et al.[53,54] who used polycrystalline material and dc magnetic fields. Jacobs and Lawerence,[57] using single crystals and pulsed magnetic fields, provided the first observation of the dependence of the order of the transition on temperature. With pulsed field measurements they were able to observe the hysteresis associated with a first order phase transition. They also observed that the transition changed from first to second order around T_t = 20.4 K, corresponding to 0.87 T_N, where T_N = 23.55 K. These results, shown in figs. 8 and 9, stimulated much of the later research.

A quantitative investigation of the hysteresis phenomena was performed by Chen, Dillon, and Guggenheim[63] who utilized the Faraday rotation of polarized incident light as it passed through the crystal. This rotation is strictly proportional to the magnetization in a single magnetic phase. In the mixed phase, this proportionality is valid if the light passing through the specimen encounters the two phases in an average proportion and if the rotation contrast is not too large. These conditions are experimentally accessible and fig. 10 shows Faraday rotation versus applied magnetic field field curves which are of the same shape as the magnetization isotherms of Jacobs and Lawerence.[57] This method of monitoring the magnetization was used

to measure the area of the hysteresis curves as a function of temperature.
Figure 11 shows an example of Faraday rotation in both increasing and de-
creasing applied fields, while fig. 12 shows how the area of the hysteresis
depends on temperature and sweep rate. The logarithmic dependence of the
hysteresis area on 1/T suggests that a thermally activated process is
involved. This may lie in the nucleation of the field induced phase or in
the motion of antiferromagnetic-paramagnetic domain walls.

By using a polarizing microscope, Dillon et al.[64,65] were actually able
to observe the growth of domains (see fig. 13) as the specimen passed into
the mixed phase from either the antiferromagnetic or paramagnetic regions.
At low temperatures (4.2 K) paramagnetic ribbons nucleated on antiferro-
magnetic domain walls as the specimen passed into the mixed phase from the
low field side. As the field increased, the ribbons convoluted and meandered
throughout the field of view. At higher temperatures, the paramagnetic
ribbons fragmented into bubbles as the field was increased. On approaching
the mixed phase from the high field side, there are no entities corresponding
to antiferromagnetic domain walls which serve as nuclei for the new phase.
At higher temperatures, extension and fragmentation of the antiferromagnetic
ribbons occur. This difference in the low and high field behavior of the
mixed phase is a factor in the hysteresis observed in the pulsed field results
of Jacobs and Lawerence.[57]

Optical methods have also been used in detailed studies of the magnetic phase
diagram. Griffin et al.[66,67] have observed that a magnetic circular dichroism
occurs at a wavelength of 600 nm when the crystal is in the mixed phase region.

Right and left circularly polarized light are scattered unequally by the domain structure in the mixed phase. The difference in the decrease in transmission for left and right handed polarizations is proportional to the magnetization in the mixed phase, while there is no measurable transparent magnetic circular dichroism in either the antiferromagnetic or para- magnetic phases. The magnetic phase diagram below the tricritical point was mapped by using this effect. Griffin et al. also found that the optical density of the 427 nm absorption line exhibited an abrupt change in shape when the sample passed from the antiferromagnetic to the paramagnetic phases. Similar work had been performed earlier by Robbins and Day.[68] The magnetic phase diagram was completed above T_t by using this latter effect and is shown in fig. 14.

Later measurements[69] used the magnetic circular dichroism of the absorption line at 1.45 μm. The dichroism was estimated to be linearly proportional to the magnetization to within 0.1%. The tricritical point behavior was extensively investigated with this technique and the results are discussed in section IV.

The metamagnetic properties have also been investigated by neutron diffraction. Trunov et al.[70,71] have shown that depolarization of neutrons occurs when the sample is in the mixed phase. Birgeneau et al.[72] have also studied the tricritical point properties of $FeCl_2$ using neutron diffraction. Their results are discussed further in section IV.

The effect of pressure on the magnetic properties of $FeCl_2$ has been studied experimentally by Vettier et al.[73,75] and Narath et al.,[76] while

theoretical discussions of this effect have been given by Tsallis[77] and
Nasser.[78,79] The experiments show that $FeCl_2$ has both a low and high
pressure phase of the $CdCl_2$ and CdI_2 types, respectively, which are shown
in fig. 15. Vettier and Yelon[75] have shown that the magnons in $FeCl_2$
simulate those of a two-dimensional ferromagnet with a large anisotropy at
all pressures, despite the larger coupling between planes in the high-pressure
phase. In each phase, the Neel temperature increases with pressure. The
tricritical point temperature decreases with pressure in the low pressure phase, while
the opposite behavior occurs in the high pressure phase.[73] These results
are shown in fig. 16. This increase of T_t, with pressure in the CdI_2 phase,
also occurs in $FeBr_2$ which has the same structure for all pressures.[73]
No attempts to correlate the changes of Neel and tricritical temperatures
with the changes in exchange and anisotropy parameters have yet been reported.

The metamagnetic transition was also observed by Motokawa and Date[80,81]
in their study of impurity spin resonance. The resonance absorption from 35-90
GHz, due to Fe^{3+} and Mn^{2+}, was measured as a function of field, both above
and below the critical fields. Their results enabled them to estimate the
exchange interaction with neighboring Fe^{2+} spins.

Crystals of $FeCl_2$ tend to be soft and easily cleaved perpendicular to
the c-axis. Despite this tendency, the study of $FeCl_2$ offers several advantages.
It is well described by a simple model and the wealth of experimental data
provide a basis for the study of more complicated behavior.

2. $FeBr_2$

$FeBr_2$ has an hexagonal crystal structure of the CdI_2 type with space group
$D_{3d}^3(P3m)$. The structure, shown in fig. 17, is very similar to that of $FeCl_2$,

in that sheets of ferrous ions are separated by two sheets of halide ions. Also, similar as in $FeCl_2$, the ground state energy levels can be described by an effective spin, $S = 1$, with a strong uniaxial anisotropy.[82,84]

$FeBr_2$ also exhibits field induced phase transitions which can be either first or second order as shown in figs. 18 and 19. However, the phase diagram of $FeBr_2$ differs from that of $FeCl_2$ in several interesting and significant respects. Figures 20 and 21 show phase diagrams of $FeBr_2$ obtained by magnetization measurements with[73,76,86] and without[82,85] an applied hydrostatic pressure. At the "tricritical" point the line of first order phase transitions meets that of the second order phase transitions with a markedly discontinuous slope, whereas in $FeCl_2$, the first and second order lines meet with a continuous slope.[82] Another special feature of the $FeBr_2$ phase boundary is that it has a maximum, which implies that the ordered phase could be entered from the paramagnetic phase by increasing the temperature at constant internal magnetic field.[82] The third marked difference with $FeCl_2$ is that the ratio $T_t/T_N = 0.33$ is too small to be consistent with the mean field theory of ferromagnetic intraplanar coupling, $|J|$, and antiferromagnetic interplanar coupling, J'.[87]

Several investigators have[87,12] suggested that this unusual phase diagram could be understood within the framework of mean field theory if the inequality $R \equiv Z|J|/Z'J' > -0.6$ were satisfied, where Z and Z' are the number of ferromagnetic and antiferromagnetic nearest neighbors respectively (see section II). In fact, a value of -0.28 has been proposed by Jacobs and Lawrence,[85] who

obtained that ratio from an analysis of their susceptibility and magnetization data. Kincaid and Cohen[12] point out that if that inequality were valid, then the "tricritical point" of $FeBr_2$ may in fact be a critical endpoint, and that there might exist in the antiferromagnetic region a bicritical endpoint. These predictions of mean field theory in the case where $R > 0.6$ are discussed in section II.

However, a recent neutron diffraction experiment by Yelon and Vettier[80] has determined that the ratio $R = -5$. This value was obtained from an analysis of the spin wave excitations, which were seen to be similar to those of $FeCl_2$, though slightly less two dimensional. Thus, the neutron diffraction results call into question the applicability of mean field theory as regards the understanding of the phase diagram of $FeBr_2$.

Fert et al.[87] have noted that theoretical work by Tsallis[77] suggests that magnetoelastic coupling could play an important role in magnetic behavior of $FeBr_2$. A thorough experimental analysis of the magnetoelastic coupling could yield a better understanding of this unusual phase diagram.

$FeBr_2$, despite the simplicity of its crystal and magnetic structure, has a very unusual and still not understood phase diagram. Interest in this material is growing despite the difficulty of getting good single crystals. Recent experimental work[89] shown in fig. 22 suggests that measurements of Faraday rotation should provide a sensitive means of examining the phase boundaries. Perhaps, as in $FeCl_2$, this type of measurement will be able to shed light on the domain dynamics in the mixed phase region and provide an overall view of the metamagnetic transitions.

3. $Ni(NO_3)_2 \cdot 2H_2O$

Nickel nitrate dihydrate forms monoclinic crystals belonging to the space group $P2_2/C$. The crystal structure is shown in fig. 23. The crystals are needle-like with the a-axis along the needle axis. This is convenient since the a-axis is the axis of prefered spin alignment and the needle-like form helps in the reduction of demagnetizing effects.[90,91]

Specific heat measurements[92] suggest that it is composed of antiferromagnetically coupled sheets of ferromagnetically aligned Ni^{++} spins. This conclusion is supported by susceptibility measurements[90] which yield a large susceptibility along the a-axis and a small, nearly isotropic value in the bc plane. The ground state properties of the Ni^{2+} ions are fairly well described by an effective spin Hamiltonian with S = 1 and uniaxial anisotropy. The interactions between the ions are taken to be isotropic and have so far been treated only using the mean field approximation.[91]

Magnetization isotherms have been measured with fields up to 16 kOe applied along the a-axis. Typical results (see fig. 24) show the characteristic change in the order of the metamagnetic transition as temperature increases past the tricritical point (T_t = 3.85°K). Using only magnetization measurements the H_i - T and M - T phase diagrams have been obtained. See figs. 25 and 26.[91] The large error bars in the latter diagram show that it is difficult to obtain the phase boundary near the tricritical point by magnetization measurements alone.

Schmidt and Friedberg[91] note that there are discrepencies between the calculated and experimental phase diagram of fig. 26, as for example, the

differences between the experimental and calculated upper and lower phase boundaries at low temperatures. They suggest that the discrepancies could be due to a small relative canting of the spins on the two inequivalent Ni^{2+} ions in the unit cell. If this is the case, $Ni(NO_3)_2 \cdot 2H_2O$ should be described by a model with four sublattices.

More experimental work to test the validity of the two sublattice models and to determine the phase boundary more accurately would clearly be of interest. The temperatures and fields needed for the study of $Ni(NO_3)_2 \cdot 2H_2O$ are easily accessible experimentally. However, it is a difficult crystal to work with because it tends to cleave spontaneously in the bc plane, allowing water to enter and causing the crystal to deteriorate.

4. $DyPO_4$

$DyPO_4$ is an excellent approximation to the three dimensional Ising model with $g_{||} = 19.5$ and $g_{\perp} = 0.2$. The lowest lying energy levels constitute an exchange and dipole split Kramers doublet whose separation from the nearest excited level is ~ 70 cm^{-1}, about 10 times the doublet splitting. Therefore, $DyPO_4$ is well described by a fictitious $S = 1/2$. In zero applied field the dipolar and exchange interactions for other than nearest neighbors partially cancel, hence in zero field $DyPO_4$ is well discribed by a model with nearest-neighbor-only interactions.[93] In an applied field the behavior is qualitatively that of a two-sublattice anti-ferromagnetic in which dipolar interactions are important.[93] The crystal and magnetic structures are shown in figs. 27 and 28.[94,93]

The Ising-like character of $DyPO_4$ is revealed in spectroscopic[95],[96] and magnetoelectric studies.[97] The magnetoelectric susceptibility, α, is the constant relating the induced electric polarization to the applied magnetic field or the induced magnetization to the applied electric field. Rado[97] has shown that in $DyPO_4$ the magnetoelectric susceptibility is proportional to the sublattice magnetization. This proportionality also holds in other systems as long as ground state properties are describable by an effective spin 1/2 formalism.[98] Measurements of α versus temperature show that the behavior of the sublattice magnetization of $DyPO_4$ is in excellent agreement with the predictions of the three-dimensional Ising model (see fig. 29).

The magnetoelectric effect has been used not only to probe the sublattice magnetization, but also to detect the occurence of metamagnetic transitions.[99] The discontinuous change in magnetic symmetry, caused by a sufficiently large magnetic field, produces an abrupt decrease in α. Fig. 30 shows the decrease, for the case of $DyPO_4$ when the magnetic symmetry changes from 4'/m'mm' to 4'/m m' m'. Figure 30 also illustrates that the relative sign of α is determined solely by the sign of that H which carried the most recent metamagnetic transition prior to the measurement of α.[99] This switching effect is potentially applicable to the storage and retrieval of information. The example of $DyPO_4$ (and also, as discussed in section III,B,1, $DyAlO_3$) suggests that for some crystals the magnetoelectric effect might be a sensitive means of investigating the magnetic phase boundaries.[98]

Several different types of measurements have been used to obtain the magnetic phase diagram of $DyPO_4$. Wright et al.[100] combined specific

heat and spectroscopic data to obtain their phase diagram shown in fig. 31. Koonce et al.[93] combined specific heat and susceptibility data to obtain their phase diagram (see fig. 32) and, in addition, from magnetization measurements (see fig. 33) located the tricritical point at 0.75 K. The phase diagram of Koonce et al. was found to be in agreement with the later results (see fig. 34) of Battison et al.[101] who used the proportionality between magnetization and Faraday rotation in their study. However, Battison et al.[101] by directly observing the domains in the mixed phase region, located the tricritical point at $T_t = 1.95$ K, in marked conflict with the earlier value of 0.75. The value $T_t \sim 2$ K later obtained by neutron diffraction (see figs. 35 and 36)[94] agrees well with that of Battison et al. No resolution of this conflict has been reported.

$DyPO_4$ crystals which have good optical quality can be grown. Unfortunately, they are brittle and cannot be fashioned into an ellipsoidal shape. Despite this, its close approximation to an Ising system will stimulate many more experiments.

5. $FeCO_3$

$FeCO_3$ has a rhombohedral structure. The magnetic moments point along the c-axis. They lie in (0001) ferromagnetic sheets, and the successive sheets are antiferromagnetically aligned. The six nearest (magnetic) neighbors to a given Fe^{2+} ion lie on the neighboring sheets, while the six next nearest neighbors lie in the same sheet[102, 103] (see fig. 37).

There is antiferromagnetic alignment between nearest neighbors and ferromagnetic alignment between next nearest neighbors, yielding a two

sublattice description of the magnetic structure. Neutron diffraction
sublattice magnetization measurements indicate that the ground state
properties of $FeCO_3$ are reasonably well described by a three dimensional,
$S = 1/2$ Ising model.[104,105] The Ising character has also been confirmed by
analysis of far-infrared absorption spectra[103] and Raman scattering data.[106]

The Neel temperature is rather high, $\sim 38°K$[107] implying strong exchange
interactions. The magnetic fields required to achieve the metamagnetic
transition are in the range of 150 kOe-180 kOe,[107,108] which are beyond the
range available to many laboratories. Another difficulty with this material is
that synthetic single crystals have not been available hence natural crystals
of siderite have been used in the experiments.

Magnetization measurements at $T = 4.2°K$ by Jacobs[107] yield a very
broad transition starting at 100 kOe and ending only at 200 kOe (see fig. 38).
Later unpublished measurements yielded a sharper transition, similar to the
results of Dudko et al.[108] whose magnetization and differential susceptibility
results are shown in fig. 39. The transition begins at 148 kOe and ends
at 176 kOe. Additional magnetization and differential susceptibility results
have been reported in refs. 109 and 110. Magnetocaloric effect studies yield
approximately the same transition fields,[111] as do Faraday effect studies[112]
(see fig. 40).

Spectroscopic[110] and magnetooptic studies[112,113] suggest that the
transition to ferromagnetic alignment is realized through a homogeneous
noncolinear magnetic structure, in which one of the sublattices remains fixed
along the C_3 axis and the other smoothly rotates with the increasing external
field.[110] However, Dudko et al.[108] suggest that the sublattice antiparallel

to the field breaks up into multiple sublattices, which then rotate into alignment with the field. Further evidence of the complicated behavior of $FeCO_3$ during the field induced transition was observed in a Raman scattering experiment[114] using pulsed magnetic fields, in which a field influenced exciton line shifted during the transition, despite the fact that the transition was presumed first order.

$FeCO_3$ is a difficult material to study because of the high magnetic fields required for the metamagnetic transition. However, its Ising-like character and the possible complexity of its intermediate state make it well worth further investigation.

6. DySb

The high temperature crystal structure of DySb is of the NaCl type. At $T_N = 9.52$ K there is a single first order magnetic phase transition to an antiferromagnetic state. This transition is accompanied by a large (0.7%) tetragonal and somewhat smaller (0.1%) monoclinic [111] distortion. The transition temperature is markedly strain dependent. These features suggest to several investigators[115,116] that strong biquadratic, as well as bilinear, exchange interactions influence the magnetic properties of DySb.

The ordered state consists of ferromagnetic (111) planes stacked anti-ferromagnetically along the [111] axis. The magnetic moment is aligned parallel to the [001] axis.[117] Magnetization studies by Brun et al.[117] reveal two transitions, first to a ferrimagnetic state at $H = H_{c1}$ and then to a para-magnetic state at $H = H_{c2}$. These transitions shown in fig. 41 can occur

for various directions of H. The magnetic phase diagrams are shown in figs. 42 and 43. Interestingly, when $H||[110]$ the boundary between the ferrimagnetic and paramagnetic states extends up to 15 K, that is, above the Neel temperature.[117]

Neutron diffraction measurements with $H||[110]$ have determined that the ferrimagnetic state has the HoP structure, which has a spin arrangement shown in fig. 44.[118] Further neutron diffraction work is needed to determine the ferrimagnetic structures when H is applied in other directions, and the role of biquadractic interactions in stabilizing these structures.[117]

Further magnetization measurements with $H||[110]$ have been performed by Streit et al.[119] These measurements, shown in fig. 45, are sufficiently detailed to reveal the existence of a tricritical point at T_t = 8.5 K and H_t = 14.7 kOe on the boundary between the antiferromagnetic and ferrimagnetic states. This is the first reported observation of a tricritical point between two ordered states. Figures 46 and 47 show the phase diagrams obtained from the measurements. As expected, a mixed ferrimagnetic and antiferromagnetic phase is apparent in the M versus T diagram. Note that the Neel temperature, T_N = 10.2 K, observed in these measurements is not in agreement with the previously observed value. This highlights the influence of strains and presumably also sample preparation and mounting on the Neel temperature.[119]

Clearly, much work is needed in order to understand the interesting and complex magnetic properties of DySb. The influence of strains and biquadratic exchange interactions make this a material worth further experimental and theoretical study. A theoretical study should be able to account for the

temperature and field dependence of the ferrimagnetic phase and the presence and location of the tricritical point. The experimental work involves study of elastic constants and the effect of strains. This is facilitated by the fact that the crystal itself is rather hard and can easily be cut to expose desired crystal planes. DySb should be the object of much future research.

7. TbPO$_4$

Flux grown crystals of TbPO$_4$ have a room temperature tetragonal zircon structure, as shown in fig. 48. At T_D = 3.5 K, a crystallographic phase transition occurs to a lower crystal symmetry, possibly monoclinic or ortho-rhombic. A crystal distortion can also be induced above T_D by application of a magnetic field perpendicular to the c-axis.[120] At T_N = 2.2 K, TbPO$_4$ orders antiferromagnetically with a two sublattice collinear structure whose antiferromagnetic axis is canted from the c-axis.[121,122] Ref. 123 notes that there is a conflict in the reported values for the canting angle, 40° and 26°. Far-infrared spectroscopy[123] indicates that the low lying levels of TbPO$_4$ consist of a doublet and two singlets. This is a more complicated low lying energy level structure than in previously discussed materials.

The metamagnetic behavior of TbPO$_4$ has not been extensively studied. Magnetization measurements shown in fig. 49 with H both parallel and perpendicular to the c-axis reveal very broad transitions.[120,124] High resolution optical spectra[121] show a discontinuity in the Zeeman pattern (see fig. 50) at a transition field of 5 kOe. Further work is needed to determine the exact nature of the transition.

Because of its low lying energy level scheme and its canted spin structure, $TbPO_4$ is an interesting system in which to study field induced phase transitions. However, further study of the basic interactions is needed.

B. CRYSTALS WITH FOUR SUBLATTICES

1. $TbAlO_3$ and $DyAlO_3$

The compounds $TbAlO_3$ and $DyAlO_3$ share the orthoaluminate structure. Each of the rare earth ions is surrounded by six nearest neighbors, four in the a-b plane and two along the c-axis. The Neel temperatures of $TbAlO_3$ and $DyAlO_3$ are 3.95 K and 3.52 K, respectively.[125]

Neutron diffraction studies show that the magnetic unit cell has $G_x A_y$ symmetry. Figures 51 and 52 show that the magnetic structures are composed of four sublattices. The spins lie only in the a-b plane. In $DyAlO_3$ four magnetic moments of 9.2 μ_B make angles of $\pm 33.5°$ and $\pm 146.5°$ with the b-axis. For $TbAlO_3$, the corresponding values are (9 ± 0.6) μ_B and $\pm 35°$ and $\pm 145°$. Consistent with the confinement of the spins to the a-b plane is the fact that χ_c is much smaller than χ_a or χ_b for both crystals.[126,127]

Crystal field interactions split the Dy^{3+} ground state $^6H_{15/2}$ into eight Kramers doublets. Similarly, the Tb^{3+} ground state $^7F_6$ is split into 13 singlets, with the two lowest singlets forming a near accidental doublet. For both $DyAlO_3$ and $TbAlO_3$ the ground state properties can be described at low temperatures as spin 1/2 Ising systems. The optical spectra of both materials for the absorption of light from the ground state doublets to excited states have triplet structures. These structures can arise if the dominant interaction between rare earth ions is with nearest neighbors

along the c-axis. In that case, the lowest energy level of a given ion can have one of three different values, depending on the direction of the magnetic moments of the ion and its neighbors. Figures 53 and 54 are pseudo-energy-level diagrams which show how all the ions in the crystal contribute to form a triplet structure in the optical spectra.[127,128]

At low temperatures the spectra are simpler because of depopulation of two of the triplet states. When taken in the presence of a magnetic field, these Zeeman patterns have given evidence of double metamagnetic transitions and selective reversal of sublattices.

To understand the Zeeman patterns, it is helpful to picture the Ising-like spins confined to the a-b plane as in fig. 55. Imagine two collinear antiferromagnets A and B comprising magnetic sublattices 1, 2 and 3, 4 respectively. The exchange and magnetic dipolar interactions within A or B are much stronger than the interactions between A and B. Thus, to a first approximation, the A and B sublattices behave independently and this makes it possible to reverse one of the A sublattices while leaving the B sublattices relatively undisturbed.[127]

The idealized Zeeman pattern of $TbAlO_3$ is given in fig. 55. For small magnetic fields parallel to μ, the absorption lines shift according to the first order Zeeman effect. The slopes are $\pm 9 \, \mu_B$ for ions 1 and 2, and $\pm 9 \, \mu_B \cos 70°$ for ions 3 and 4. If $H \geq H_{c1}$, the first transition field, the external field is then larger than the internal interactions acting on ion 2. This causes μ_2 to reverse sign and the interactions of all the other ions with ion 2 to change. When $H \geq H_{c2}$, the magnetic field is then greater than the internal interactions on ion 4, causing the second metamagnetic transition.

The experimental results are shown in fig. 56, $H_{c1} \sim 8.5$ kOe, and $H_{c2} \sim 21$ kOe. The deviation from the idealized case is due to weak interactions between neighbors (1 and 4, or 2 and 3) in the a-b plane and long range magnetic dipolar interactions.[127,129]

The situation in $DyAlO_3$ is entirely analagous. $H_1 \simeq 7.0$ kOe and $H_2 \simeq 7.3$ kOe and the Zeeman splitting as a function of field is given in fig. 57. Table 2 summarizes the magnetic properties obtained from the spectroscopic data of these rare earth aluminates.[130,128]

Magnetization measurements[131,126] on these crystals have yielded estimates of the internal fields and further understanding of the metamagnetic transitions. Figures 58 and 59 show that magnetization measurements also give evidence for double transitions and selective reversal of sublattices.

Consistent with the view of $DyAlO_3$ as a spin 1/2 system are the measurements of its magnetoelectric susceptibility as a function of temperature. As in the case of $DyPO_4$, which is well described by the three dimensional Ising model, the magnetoelectric susceptibility of $DyAlO_3$ is proportional to the sublattice magnetization. This condition provides a simple and elegant means of studying the critical behavior. Figure 60 shows that the magneto-electric data of $DyAlO_3$ and $DyPO_4$ are very similar. The critical exponents of both materials are in good agreement with the predictions of the three-dimensional Ising model.[98,132,133]

The effect of a metamagnetic transition on the spin alignment, and hence on the magnetoelectric effect in $DyAlO_3$ is summarized in fig. 61. These results were obtained by rotating the crystal until the component of a large applied magnetic field reached the transition field for a particular plane.

Figures 62 and 63 show how the magnetoelectric susceptibility, because of its strong dependence on magnetic symmetry, would then change abruptly.[133] This technique then provides a sensitive means of obtaining magnetic phase boundaries and, because of the dependence on symmetry, of studying the order of the metamagnetic transitions.

Similar, though less detailed, magnetoelectric effect studies have recently been performed on $TbAlO_3$.[134] As in $DyAlO_3$, the magnetoelectric susceptibility shown in figs. 64 and 65, is proportional to the sublattice magnetization and behaves in a way consistent with the predictions of the three dimensional Ising model. Figure 66 shows that the magnetoelectric susceptibility provides a sensitive means of determining the metamagnetic transition fields of $TbAlO_3$.

The basic magnetic interactions in $TbAlO_3$ and $DyAlO_3$ are well understood. This provides a basis for future research. For example, a detailed investigation of the magnetic phase boundaries has yet to be undertaken.

2. CeBi

In contrast to previous materials the basic magnetic and structural properties of CeBi are not well understood. The high temperature crystal structure is f.c.c. (NaCl type). At T_N (~ 25 K) there is a second order magnetic phase transition to an antiferromagnetic state with a (+ - + -) arrangement of ferromagnetic (001) layers. The spin direction is parallel to [001]. At 12.5 K a first order magnetic phase transition occurs to the

type IA strucutre, in which the spin direction remains unaltered, but the ferromagnetic sheets have a (+ + - -) alignment.[135,136] This type IA structure is not predicted by mean field theory and the mechanism which stablizes it is not understood.

In addition to the zero field magnetic transitions, structural transitions have been reported. Hulliger et al.[137] reports a tetragonal distortion of the cubic crystal lattice at T_N. The variation of lattice parameter with temperature is shown in fig. 67. However, Lander et al.[138] have performed similar X-ray measurements and report that no tetragonal distortion occurs at T_N nor at 12.5 K. They suggest that this discrepency might be due to unusual domain effects.

Anamalous domain effects have also been used to explain the unusual magnetization behavior. Tsuchida et al.[139] have observed two metamagnetic transitions. They postulated that the intermediate state has a (+ + + -) structure (see figs. 68 and 69). However, Bartholin et al.[140] have observed a much more complicated behavior with multiple transitions and intermediate states, as shown in figs. 70, 71 and 72. The neutron diffraction work of Lander et al.[138] shows the existence of only one intermediate state (with a + + + - arrangement). See fig. 73 for their phase diagram. This result is consistent with the theoretical work of Többe[141] who studied the magnetization process in an fcc lattice and found only two field induced transitions.

The basic interactions in CeBi are more complex than those in previously mentioned materials. More work is needed to understand the type IA structure and the effect of domains on the magnetization curves.

3. CeSb

There are also unresolved questions concerning the magnetic properties of CeSb. The antiferromagnetic transition at T_N (= 16 K) is to a non-commensurate sinusoidal structure. At T = 8.5 K there is a transition to a type IA(+ + - -) magnetic structure.[137]

As in CeBi, Hulliger et al.[137] have reported a tetragonal distortion at T_N. Figure 74 shows the variation of lattice parameters with temperature obtained by X-ray diffraction. In view of the disputed tetragonal distortion in CeBi, it would be interesting to see if the tetragonal distortion in CeSb can be confirmed.

The behavior of CeSb in a magnetic field has been studied by several investigators.[137,142-146] A peculiar aspect of the magnetization is, as in CeBi, the appearance of multiple steps (see figs. 75 and 76).

It is possible that these multiple steps are due to domain reorientation effects. Clearly a neutron diffraction study of CeSb in a magnetic field is needed to determine the number and nature of field induced magnetic structures.

4. $DyVO_4$ and $DyAsO_4$

$DyVO_4$ and $DyAsO_4$ are isomorphous with $DyPO_4$. Spectroscopic measurements show that their ground states are highly anisotropic, with the magnetic moments constrained to lie perpendicular to the tetragonal axis. The spectra taken in a field applied in the basal plane indicate that $DyAsO_4$ and $DyVO_4$ have almost identical magnetic properties.[147] Their magnetic structure is shown in fig. 77.

$DyVO_4$, which orders at 3.04 K,[148] also undergoes a Jahn-Teller transition at 14 K whereby the crystal symmetry changes from tetragonal ziron to the orthorhombic structure. The distortion direction is correlated with the direction of principal g value and can be influenced by the application of a magnetic field.[149]

Below T_N = 3.0 K, a magnetic field applied along the direction of spin alignment can induce a metamagnetic transition, as shown in fig. 78. The metamagnetic transition has also been observed in spectroscopic measurements, where the Zeeman splitting of the ground state doublet is linear with field for $H < H_{c1}$, approximately independent of field for $H_{c1} < H_{c2}$, and again linear with field for $H > H_{c2}$. These results are shown in figs. 79 and 80 which show the positions of H_{c1} and H_{c2}. The appearance of the extra lines when $H_{c1} < H < H_{c2}$ has been considered in detail by Kasten and Becker.[148]

$DyAsO_4$, which orders at 2.44 K, also undergoes a Jahn-Teller transition at 11.2 K.[150] The metamagnetic transition has been observed from spectroscopic studies, as shown in fig. 81. The behavior of the Zeeman lines is similar to that of $DyVO_4$.

These materials, though relatively complex, can be described by simple arguments. Good optical quality crystals can be grown. These factors make them ideal candidates for future research.

5. EuSe

EuSe is a magnetically ordered semiconductor with an fcc crystal structure. Nearest neighbor ferromagnetic and next nearest neighbor antiferromagnetic exchange interactions nearly cancel each other, leading to very complicated magnetic behavior.[151] Janssen[152] has theoretically

studied EuSe and shown that dipole-dipole and magnetoelastic interactions play a significant role in determining its magnetic properties.

The latest work[151] obtained from dilatometric and magnetization measurements[151] and analysis of neutron diffraction studies[153] shows that in zero field, EuSe becomes antiferromagnetic at 4.6 K, then ferrimagnetic at 2.8 K, then once again antiferromagnetic at 1.8 K (see fig. 82). The first AF phase consists of (111) planes with spins oriented according to (+ + - -). The spins in the ferrimagnetic phase are ordered (+ + -), while the second AF phase has the MnO type structure. Previous work[154] had neglected the low temperature AF phase.

Magnetization measurements[155-158] have revealed that two metamagnetic transitions are possible (see figs. 83-86). Each antiferromagnetic state can be forced into the ferrimagnetic state which can then be forced into the paramagnetic state. The variation of critical field with temperature for 2 < T < 5 is shown in fig. 87.[157] A complete magnetic phase diagram obtained by the dilatometric and magnetization measurements is shown in fig. 82. There have been some suggestions[154,158,159] that this phase diagram may be an oversimplication. For example, Komaru et al.[154] have performed NMR studies on EuSe which suggest that between the ferrimagnetic and ferromagnetic phases there exists an intermediate phase containing canted spins. Figure 88 contains their proposed phase diagram, which illustrates that the interactions in EuSe are extremely complex.

There have been several experiments which indicate that magnetoelastic energy plays a significant role in EuSe. The dilatometric measurements[151] show that each field induced transition is accompanied by large length changes, as shown in fig. 89. Magnetization measurements,[158] shown in

fig. 90, were made in the presence of a stress applied along the [111] direction, with the magnetic field applied in the (111) plane. According to Kwon and Everett[158] the linear variation of M between 2.2 and 2.4 kG, when T = 1.3 K and the applied pressure equals 150 kBar (see fig. 90) suggests yet another magnetic phase, not observed at zero stress.

Not only are the magnetic interactions in EuSe very complex, but its very properties have not been fully determined, so that much work on this material remains to be done. For example, neutron diffraction on EuSe with applied pressure and magnetic field would help to determine the exact nature and boundaries of the magnetic phases.

C. CRYSTALS WITH LINEAR CHAINS

1. $FeCl_2 \cdot 2H_2O$, $CoCl_2 \cdot 2H_2O$, $CoBr_2 \cdot 2H_2O$

The metamagnetic properties of the isomorphous compounds $FeCl_2 \cdot 2H_2O$, $CoCl_2 \cdot 2H_2O$ and $CoBr_2 \cdot 2H_2O$ have been extensively studied. The crystal structure is monoclinic with the C2/m space group (see figs. 91 and 92). The crystals consist of linear chains of $FeCl_2$, $CoCl_2$ or $CoBr_2$ parallel to the c-axis (see, for example, fig. 93), held together by relatively weak hydrogen bonds. In the cobalt compounds the spins are constrained to lie along the b-axis, while in $FeCl_2 \cdot 2H_2O$ the spins lie along the α-axis in the a-c plane.[160-162] The results of susceptibility measurements (shown in figs. 94 and 95) support this picutre of the spin orientation.[160 162]

The magnetization vs. field curves of each compound show two discontinuities, as shown in figs. 96, 97 and 98. There has been considerable discussion as to the nature of the intermediate state with canted,[163] four sublattice[164] and six sublattice structures having been proposed.[165,166] Neutron

diffraction investigations of $FeCl_2 \cdot 2H_2O$[7] and $CoCl_2 \cdot 2H_2O$[167] have confirmed Narath's six sublattice model and the same is probably true in $CoBr_2 \cdot 2H_2O$.[8] The advantage of the six sublattice model is that it can predict the 3:1 ratio of saturated to intermediate magnetization which is observed for all three substances (see figs. 99, 100).[168,163,162]

Narath's analysis[162] of his magnetization vs. field data for $FeCl_2 \cdot 2H_2O$ applies to all three compounds because of their similar magnetic structure. Figure 100 shows the directions of the exchange interactions. J_1 and J_2 are antiferromagnetic interactions, while J_3 is ferromagnetic. There is also a ferromagnetic interaction, J_o, between two spins on the linear chain. By comparing the energy at 0 K of the antiferromagnetic, ferrimagnetic, and paramagnetic configurations in the presence of an applied field, Narath[162] is able to obtain the transition fields in terms of the exchange constants. He also shows that if J_2 were ferromagnetic there would be only one discontinuity, so the experimental observation of two step behavior is due to an intrasublattice antiferromagnetic exchange.

Yamada and Kanamori[169,8] have performed a mean field treatment of the magnetization processes of these crystals. Using Narath's six sublattice intermediate state, they calculated the magnetic phases as a function of temperature and field. Figures 101 and 102 show their theoretical fit to the $CoCl_2 \cdot 2H_2O$ magnetization data of Kobayashi et al[163] and Narath.[168] The calculated magnetic phase diagrams for $CoCl_2 \cdot 2H_2O$ and $CoBr_2 \cdot 2H_2O$ are shown in figs. 103 and 104. The diagrams show the prediction of a triple point where the antiferromagnetic, intermediate and ferromagnetic phases coexist.

For $CoBr_2 \cdot 2H_2O$ a complicated magnetization process in which the system under-
goes three phase transitions is predicted in a narrow temperature range just
above the triple point temperature, yielding a calculated magnetization
isotherm shown in fig. 105. An experimental magnetization study of $CoBr_2 \cdot 2H_2O$
in that temperature range has not been reported.

Experimental determinations of the magnetic phase boundaries have been
performed with neutron diffraction, strain gauge, and susceptibility techniques.
The neutron diffraction work was carried out by Weitzel and Schneider on
$CoCl_2 \cdot 2H_2O$[6] and $FeCl_2 \cdot 2H_2O$.[7] Their phase diagrams (figs. 106 and 107) show
the existence of the triple points. Figures 108 and 109 show similar phase
diagrams obtained by Lowe et al.[170,171] who used strain gauges to detect the
change in lattice constant at each phase transition. The results from the
strain gauge experiments on $CoCl_2 \cdot 2H_2O$ do not agree well with the phase
boundary predicted from the mean field theory for $T > 10$ K. Better agreement
with the predicted phase boundary above 14 K was obtained by high frequency
ac susceptibility measurements, where the transition field shows up as a sharp
peak in the real part of the susceptibility. The phase diagram obtained by
this method is shown in fig. 110.[172] Points on the phase boundary of $CoCl_2 \cdot 2H_2O$,
shown in fig. 111, have also been obtained by noting the fields at which
peaks occur in measurements of $\partial M / \partial H$.[173]

From magnetization, susceptibility, and other studies the values of the
magnetic parameters have been determined. The values of the exchange
parameters depend a great deal on the form of the assumed spin Hamiltonian.
The lowest energy levels of $FeCl_2 \cdot 2H_2O$ have been described in terms of an
effective $S = 1/2$ with anisotropic exchange interactions by Narath,[162]
an effective $S = 2$ with isotropic exchange parameters and a single ion

anisotropy term by Hay and Torrance[174] and Johnson,[175] and an effective

$S = 1$ by Inomata and Oguchi.[176,177] The latter description is in disagree-

ment with the experiments of Hay and Torrance.[174] The effective $S = 1/2$

is actually more appropriate for $CoCl_2 \cdot 2H_2O$ and $CoBr_2 \cdot 2H_2O$ where the

longitudinal anisotropy is much larger than in $FeCl_2 \cdot 2H_2O$.

There have been a variety of resonance experiments on $CoCl_2 \cdot 2H_2O$ which

show the effect of the metamagnetic transition. Figure 112 shows how

nuclear magnetic resonance frequencies exhibit a discontinuity at the

transition fields.[178,179] This is due to the variation of effective field

on the up (+) and down (−) ferromagnetic chains as a function of applied

field, as shown in fig. 113.[180] Electron spin resonance spectra of Mn^{2+}

ions in $CoCl_2 \cdot 2H_2O$ show similar changes as the external magnetic field is

varied, as shown in fig. 114.[181] The variation of effective fields on the

chains also effects the resonance frequencies of spin waves.

Far infrared excitations of spin waves in $FeCl_2 \cdot 2H_2O$ has been investi-

gated by Hay and Torrance.[174] Figure 115 shows the far-infrared spectrum

as a function of magnetic field. The discontinuous changes in resonance

frequency at the metamagnetic transitions are evident. An interesting

feature of the spectra is the large (~ 6000 Oe) hysteresis at the antiferro-

magnetic to ferrimagnetic transition, and the absence of this hysteresis

at the ferrimagnetic to ferromagnetic transition. This hysteresis is

strongly temperature dependent and cannot be explained by demagnetization

effects. An increased understanding of the dynamics of the metamagnetic

transition has been obtained by Katsumata,[182] who has made magnetization

measurements using a slowly increasing field.

Figure 116 shows his M vs. H curves obtained with dH/dt = 60 Oe/sec. At 4.22 K sharp transitions to ferrimagnetic (with $M = M_s/3$) and ferromagnetic (with $M = M_s$) states are clearly seen. With decreasing temperature the antiferromagnetic state flips to an intermediate state whose magnetization is larger than $M_s/3$. This state then decays to the $M_s/3$ state. Below 3.00 K transitions from the antiferromagnetic state to a $M_s/2$ state, and thence to the ferromagnetic state are seen. The explanation for these effects involves the large single ion anisotropy which causes each spin to experience an activation energy for flipping. At the antiferromagnetic to ferrimagnetic ($M_s/3$) transition 2/3 of the down chains and 1/3 of the up chains must be reversed. Thus a very long time is required for that transition. Spin structures with $M = M_s/2$ can be constructed by a simple reversal of down chains in the antiferromagnetic state (see fig. 117 for illustration of the various spin structures). Hence, the time for the latter transition is shorter than the time for the former one. However, the $M_s/2$ state is not the lowest energy state so it must decay to the $M_s/3$ state. At low temperatures the $M_s/2$ state remains unchanged because of the long transition time compared to the field sweep rate.[182] These experiments show that the details of a metamagnetic transition can be strongly influenced by microscopic factors.

Unusual magnetization behavior has also been noted in $CoCl_2 \cdot 2H_2O$.[183,184] Date and Motokawa[183] have observed hysteresis at the antiferromagnetic to ferrimagnetic transition, H_{c1}, yet no hysteresis at the ferrimagnetic to ferromagnetic transition, H_{c2}. This is similar to the hysteretic behavior

in $FeCl_2 \cdot 2H_2O$. Detailed studies of the dynamics of the two metamagnetic transitions have been given by Tinkham[36] and Oguchi.[185] Their results agree with the observed behavior at H_{c1} and H_{c2}. However, additional magnetic transitions have been observed between H_{c1} and H_{c2} by Kuramitsu[186] and Motokawa.[37] These peaks, shown in fig. 118, at 36.8 kOe and 41.1 kOe, correspond to small changes in magnetization. The 36.8 kOe transition was observed by Kuramitsu[186] (see fig. 119) using a static magnetic field. By using a pulsed magnetic field, Motokawa[37] was not only able to observe the transitions between H_{c1} and H_{c2}, but also observed two small transitions below H_{c1}, as shown in fig. 118. Motokawa[37] studied in great detail the possible irregular spin sites which can arise when domains contact one another at H_{c1} and H_{c2}. From this study he was able to determine the critical fields needed to force the irregular spin clusters into the dominant antiferromagnetic or ferrimagnetic mode. His results not only show that two small magnetization jumps should occur between H_{c1} and H_{c2}, but also predict five small jumps below H_{c1}. These same jumps have been predicted in computer simulations by Ono.[187,188]

Excitations from the ground state spin structures are not only important for an understanding of the magnetization of $CoCl_2 \cdot 2H_2O$, but they also lead to interesting resonance effects. The nature of spin clusters in $CoCl_2 \cdot 2H_2O$ has been explained in great detail by Torrance and Tinkham,[189,32-33] and Date and Motokawa.[183,190]

An n-fold spin cluster or bound magnon is an excited state corresponding to the simultaneous reversal of n adjacent spins. The energy of this n magnon bound state can be less than the energy of n noninteracting magnons.

In a typical magnetic material such bound states will generally only exist near the zone boundary, and in this case they are difficult to observe.[33] The possibility of observing these bound states is increased when the spin S is small, the number of nearest neighbors is small, and the longitudinal anisotropy is large.[32,33] All of these conditions are met in $CoCl_2 \cdot 2H_2O$ and $CoBr_2 \cdot 2H_2O$.

Using microwave excitation, Date and Motokawa[183,190] have observed transitions between ordinary spin waves and these bound magnons and between bound magnons of different order. The transverse anisotropy within a chain, defined as $J_o^a = | J_o^{xx} - J_o^{yy} |/2$, admixes bound magnons of different order, making it possible to observe transitions from the ground state (where all the spins on a chain are aligned) to any n-fold spin cluster with far infrared radiation. This has been done by Torrance and Tinkham[189,32,33] and Nicoli and Tinkham.[191] The latter were able to excite as many as 17 spin reversals. Figures 120 and 121 show the theoretical and experimental spectra which demonstrate that the linear ferromagnetic chains experience different magnetic environments as a function of external field. The discontinuities in the spectra reflect the metamagnetic transition.

Figures 120 and 121 also show the existence of a phonon which is coupled to the magnons and becomes infrared active. In $CoBr_2 \cdot 2H_2O$ a magnon and phonon are so strongly coupled that they form a bound state.[192-194] In $FeCl_2 \cdot 2H_2O$ though it is isomorphous with the other two compounds, the magnon bound state spectrum does not appear because the anisotropy is uniaxial ($J_o^a \sim 0$) and it is not possible to excite the bound magnons.

The wealth of experimental data on these crystals from susceptibility, magnetization, microwave resonance, and far-infrared absorption experiments

have yielded a broad understanding of their complex magnetic behavior. With this rich background of information detailed measurements of, for example, tricritical point behavior can now be undertaken. All three of these crystals can be grown from temperature controlled aqueaous solutions. With $CoBr_2 \cdot 2H_2O$, care must be taken, as explained by Torrance and Hay,[192] to avoid shattering the crystal when it is brought to low temperatures. Aside from this proviso, these materials are prime candidates for future research.

2. $NiCl_2 \cdot 2H_2O$

The room temperature crystal structure of $NiCl_2 \cdot 2H_2O$ is monoclinic with space group I 2/m. Early neutron diffraction and X-ray analysis showed that at 230 ± 20 K a crystallographic phase transition occurs to either a Cc or a C 2/c structure.[195] The former (Cc) low temperature structure allows the presence of two inequivalent Ni^{2+} sites which provided a logical explanation for the unusual magnetization and specific heat behavior.[195,196] However, more recent neutron diffraction data tend to indicate C 2/c as the low temperature space group. In this structure the nickel ions only occupy a single eight fold position.[196] This result has stimulated experimental[196] and theoretical work[197] in an attempt to understand the unusual magnetic properties of $NiCl_2 \cdot 2H_2O$.

Magnetization measurements were first performed by Motokawa[198] who applied static magnetic fields up to 76 kOe and pulsed fields up to 120 kOe along the easy axis and observed three field induced transitions at T = 1.4 K, as shown in fig. 122. Figure 123 shows his proposed spin arrangements for each of the magnetic states. State I consists of antiferromagnetically

coupled ferromagnetic chains similar to $CoCl_2 \cdot 2H_2O$. State II is ferrimagnetic while a cone structure is proposed for the third state.[198]

The antiferromagnetic to ferrimagnetic transition reported by Motokawa occured at 18.6 kOe and 1.4 K. Later magnetization measurements by Bongaarts et al.[195] at 1.1 K revealed two transitions between 18 and 22 kOe, as shown in fig. 124. In an attempt to understand the origin of this double transition, Botterman et al.[196] performed magnetization and susceptibility measurements in which both the temperature and angle of the applied field were varied. Figure 125 shows that the critical fields H_{c1} and H_{c2}, between 18 and 22 kOe, do not depend on angle in the same way. H_{c2} obeys the relation $H_{c2} = H_{app}$ $\cos \theta_{cr2}$, where H_{app} is the applied magnetic field, whereas H_{c1} has a parabolic dependence on angle. Figure 126 shows that H_{c1} and H_{c2} have different dependencies on temperature. These differences suggest that different mechanisms underlie the two steps in the magnetization. Botterman et al.[196] suggest that the transition at H_{c1} is to a screw structure, which could result from a strong temperature dependence in the spin anisotropy. This anisotropy decreases and reduces to zero at 6.3 K.

The estimated low field phase boundaries in fig. 126 intersect the zero field axis at points where peaks in the specific heat have been observed.[199] This double peak structure, shown in fig. 127, is due to a reorientation of the Ni^{2+} spins, which results from a competition between the single ion anisotropy and exchange terms in the Hamiltonian.[197]

It would clearly be of interest to make a detailed study of the spin arrangement in the proposed screw state structure between H_{c1} and H_{c2}, and

to understand the temperature dependence of the anisotropy in that region. In fact, the complex interactions in $NiCl_2 \cdot 2H_2O$ would make a complete H_i - T phase diagram very interesting.

3. $CsCoCl_3 \cdot 2H_2O$

$CsCoCl_3 \cdot 2H_2O$ is a complex, Ising linear chain antiferromagnet. The room temperature crystallographic space group is Pcca, shown in fig. 128. Chains of Cl-Co-Cl atoms are separated in the $\vec{b}$ direction by layers of cesium atoms and in the $\vec{c}$ direction by layers of hydrogen atoms which cause easy cleavage parallel to the ab plane.[200] When exposed to the atmosphere at room temperature, the dihydrate converts to the blue anhydrate. To prevent this the samples were stored below -5°C in a sealed container.[201] In their studies of the magnetic properties, Herweijer et al.[200] found it difficult to avoid a small impurity concentration of $CoCl_2 \cdot 6H_2O$.

At T_N = 3.38 K the chains in each a-c plane couple ferromagnetically. The spins in each chain lie at an angle of 10° from the c-axis. Figure 129 shows how moments in alternate planes lie antiparallel.[201]

Magnetization measurements[201] (see fig. 130) show that at low temperatures a sufficiently large magnetic field, applied in the $\vec{a}$ direction, can overcome the antiferromagnetic coupling between spins in adjacent ac planes. The applied field reverses the spins in alternate planes, inducing a weak ferromagnetic moment parallel to $\vec{H}$. The temperature dependence of the critical field, obtained by nuclear magnetic resonance, antiferromagnetic resonance and magnetization measurements is shown in fig. 131.

From their antiferromagnetic resonance data, Herweijer et al.[200] conclude that spin-cluster excitations occur in $CsCoCl_3 \cdot 2H_2O$, further reinforcing the idea that it is an Ising-like system, and suggesting that it is an ideal candidate for further experimentation.

The detailed studies of the basic interactions in $CsCoCl_3 \cdot 2H_2O$ provide us with a thorough understanding of this complex system. This has led to extensive tricritical point studies of the isomorphous compound $CsCoCl_3 \cdot 2D_2O$, which are further discussed in section IV.

4. Eu_3O_4

Eu_3O_4 is isomorphous with calcium ferrite ($CaFe_2O_4$) with Eu^{2+} and Eu^{3+} ions occupying the sites of calcium and iron, respectively, in that structure.[202] Figure 132 shows a unit cell of Eu_3O_4 along with a model of the ordered spin structure (T_N = 5.0 K). The magnetic properties at low temperatures are determined almost exclusively by the strongly magnetic Eu^{2+} ions. The weakly magnetic Eu^{3+} ions provide a relatively inert magnetic background.[203] The Eu^{2+} ions form ferromagnetic linear chains which are antiferromagnetically coupled to neighboring chains.

When a magnetic field is applied along the c-axis a metamagnetic transition can occur in which alternate chains of spins are flipped into alignment with the field. Figure 133 shows typical magnetization isotherms and fig. 134 shows the variation of the critical field with temperature.[203]

From magnetization and susceptibility data it has been determined that the Eu^{2+} spins are strongly anisotropic with an anisotropy field, $H_A \simeq 7$ kOe. Magnetic dipolar interactions are sufficiently large to explain the observed

anisotropy, without having to invoke anisotropic exchange or coupling to trivalent europium.[203]

It is difficult to obtain good single crystals of Eu_3O_4. Polycrystalline material was used in these studies. When growing the crystals one must be careful to avoid EuO impurities, which is strongly ferromagnetic.

5. $Co(Pyr)_2Cl_2$, $Fe(Pyr)_2Cl_2$, $Fe(Pyr)_2(NCS)_2$ and $Ni(Pyr)_2Cl_2$

All of these materials have linear chain structures with ferromagnetic interactions along the chain and relatively weak antiferromagnetic inter-actions between chains.[204] These crystals are similar to $CoCl_2 \cdot 2H_2O$ with Pyr = pyridine taking the place of the H_2O. The main effect of dilution by the organic ligand is to lower the interchain interaction, and consequently T_N, as well as the metamagnetic transition fields.

Magnetization measurements[205,206] on polycrystalline samples of all of the above crystals have been reported. Figures 135-137 show the low transition fields, which are broadened due to the polycrystalline samples. In addition, the figures show that saturation is not reached ever for very high fields. This indicates that the spins experience a large anisotropy. The figures also show that the entire phase diagram of the Co pyridine compound can be studied at relatively low magnetic fields in the liquid He^4 temperature range.

Single crystal measurements on the Co pyridine compound have recently been reported.[204] The crystals used were small (< 1 mg) and tended to deteriorate on cycling between low and high temperatures, so that each batch of crystals could be used only once.[204]

The magnetization data in figs. 138 and 139 show that metamagnetic transitions occur along all three axes. At 1.25 K, metamagnetic transitions are observed along the a-axis at 700 G; along the b-axis at 800 G and 1.5 KG, and along the c-axis at ∿ 4 KG. Along the b-axis, the low field moment change is 1/2 the higher field moment change, suggesting a six-sublattice magnetic structure.

Because of the easily accessible magnetic field and temperature ranges there merit materials further study, however, single crystals are clearly desirable.

D. GARNETS

1. Dysprosium Aluminum Garnet

Dysprosium aluminum garnet (DAG, $Dy_3Al_5O_{12}$) has been studied extensively over the past several years. Measurements of the zero field properties by many different experimental techniques has led to a fairly complete microscopic picture of this material. Although we will not discuss the zero field work here (see refs. 207 and 208 for extensive references to earlier work) it is appropriate to briefly describe some of the results of these studies. Dy^{3+} is a Kramers ion and in DAG the lowest lying doublet is separated from the first excited states by 100 K; thus at liquid helium temperatures the ion can be represented by an effective spin $S' = 1/2$. The ground doublet is very anisotropic, with the magnetic moments constrained to lie along local z axes. The directions of these local z axes varies through the lattice--for one third of the spins it is along the X crystal

axis, etc., for the Y and Z axes (the X, Y and Z crystal axes are of course equivalent in this cubic crystal). In zero field the crystal orders at 2.5 K; in the ordered state there are spins pointing in the ±X, ±Y and ±Z directions and thus DAG is a six sublattice antiferromagnet.

The spin-spin interactions have been investigated in some detail.[209,210] It has been found that they are predominantly of the Ising form, $J_{ij}S_{iz}S_{jz}$, where z refers here to the local axes. Because of the anisotropy discussed above, the interaction with the field is to a good approximation given by $\mu H_z S_{iz}$, where μ is the magnetic moment and H_z is the component of H along the local z axis. Thus the microscopic Hamiltonian has the extremely simple Ising form. The analogy with the simplest Ising models would be complete were it not for the importance of long range dipolar interactions in DAG. The dipolar interactions are particularly important in DAG because of the high g value ($g_z \simeq 18$), and they contribute 75% of the total energy at 0 K.[209]

Despite the simple form of the microscopic interactions, the complexity of the garnet lattice together with the multisublattice ground state lead to a variety of novel properties. All of these features make DAG interesting both from an experimental and theoretical point of view. In this connection we should mention that a number of theoretical studies of metamagnets have been stimulated by the observed properties of DAG.

The first studies of field induced phase transitions in DAG were made by Wyatt et al.[212,213] Wyatt measured the magnetization as a function of both temperature and field, for 1 K < T < 4.2 K and fields along the {111}, {110}, and {001} crystallographic directions. It was found that for

$T \lesssim 1.6$ K and for all three field directions, M was discontinuous, indicating
a first order transition. For 2.5 K $> T > 1.6$ K, M displayed an inflection,
presumably indicating a second order transition.

Several years later, Wolf et al.[214],[207] reported more detailed measure-
ments of M for fields along {111}. Their results for $M(H_i, T)$ are shown in
fig. 140. As found by Wyatt, there was a first order transition for $T \leq$
1.6 K. However, the behavior above 1.6 K was unexpected. Wolf found that
$\chi_i \equiv (\partial M/\partial H_i)_T$ did not diverge in contrast to the expected divergence
at the second order transition. Striking evidence that χ_i does not diverge
is shown in fig. 141, where $(\partial M/\partial H_o)_T$ is plotted as a function of H_o at
fixed T. If χ_i diverges, then $(\partial M/\partial H_o)_T$ should reach the value $1/N$ (see
Eq. (2.12). At the lowest temperatures in fig. 141 the value $1/N$ is reached
for a range of H_o, as expected for a first order transition. For $T > 1.6$
however, the curves fall systematically below the $1/N$ limit, indicating
that χ_i does not diverge. The reason for this discrepancy was not then
understood, and will be discussed further below.

Landau et al.[207],[214],[215] have reported extensive specific heat and latent
heat measurements with fields along all three major directions. The measure-
ments yielded the specific heat at constant applied field, C_{H_o}, and the latent
heat, L, as a function of H_o and T. As discussed in section II, magnetiza-
tion data are required to convert C_{H_o} to the desired quantity, the specific
heat at constant internal field C_{H_i} as a function of H_i and T. For fields
along {111} it was possible to use the available M-H_i-T data,[207] and the
results for C_{H_i} and L are shown in figs. 142 and 143. For $T < 1.6$ K, C_{H_i}

exhibits a δ-function anamoly corresponding to the latent heat at the first order transition. For $T > 1.6$ K there are λ-type peaks at the apparent second order phase boundary, but the peaks were found to be finite[207] in contrast to the behavior in zero field where C_{H_i} was found to be divergent.[207] Since neither χ_i nor C_{H_i} exhibited the divergences expected at a second order phase boundary, Landau et al. termed the phase transition for $T > 1.6$ K "higher order."[207] The phase diagram in the $H_o - T$ plane for $H_o // \{111\}$ is shown in fig. 144a where both the magnetization and specific heat results are shown. Down to the lowest temperatures investigated, the phase transition proceeds directly from the antiferromagnetic to the paramagnetic phase.

Landau et al.[215] have also performed specific heat measurements with fields along $\{110\}$ and $\{001\}$. Magnetization data of sufficient detail to enable the conversion from C_{H_o} to C_{H_i} were not available, but it was possible to determine the phase diagrams in the $H_o - T$ plane, and these are shown in figs. 144b and c. For $T > 1.0$ K they are quite similar to the results for $H_o // \{111\}$. For $T < 1.0$ K, however, there are new phase transitions in high fields. The existence of these new low temperature phases is a direct consequence of the multisublattice structure, and can be understood as follows. For sufficiently high fields along say the $\{001\}$ direction, all of the spins in the $\pm Z$ sublattices will be 'locked' parallel to the field. The $\pm X$ and $\pm Y$ sublattices, however, will not be affected by the field, and at sufficiently low temperatures, the $\pm X$ and $\pm Y$ spins will order due to their mutual inter-actions. This argument implies that the new phase boundary should be vertical in the $H_o - T$ plane and we see that this is approximately correct.

The deviations are presumably due to components of the magnetic moment transverse to the local z axis and also to imperfect saturation of the spins parallel to the field. Similar arguments lead one to expect analogous behavior for fields along {110}, but since in this case fewer, more widely separated spins are involved, the transition temperature is somewhat lower.

The nature of these new high field ordered phases has been the object of several studies. The relative energies of the possible phases have been considered by Landau[215] and Bidaux et al.[216] For $H_1 // \{001\}$ the new phase appears to be one in which the spins transverse to H_o are aligned anti-ferromagnetically, but in a _different_ antiferromagnetic arrangement from that in zero field. For $H_o // \{110\}$ the new phase appears to be a ferromagnetic state, but there exists an antiferromagnetic state which calculations show to have nearly the same energy, and the experiments to date cannot rule out that this antiferromagnetic state is the stable phase. As one might imagine, the behavior for fields off the symmetry directions is also quite unusual, and has been studied theoretically and experimentally by Bidaux et al.[217]

A great deal of attention has also been focussed on the tricritical behavior of DAG. For reasons which will become clear shortly, we will discuss some of this work here rather than in section IV. Several analyses of the data of Wolf et al.[207] for $M(H_i, T)$ for $H_i // \{111\}$ yielded values for the exponents substantially different from the theoretical predictions for a tricritical point.[209,218] More detailed magnetization measurements for fields along {111} were subsequently made by Skjeltorp et al.[219] These measurements served to confirm most of the earlier results--χ_i was found to be finite at the "higher order" transition, and the tricritical exponents were again

significantly different from the values predicted by the theory. The new
work did seem to indicate, however, that the equation of state could not
be described by a simple scaling form (Eq. (2.8)).

Soon after Skjeltorp's work, Dillon and coworkers[220-222] reported
extensive magneto-optical studies of DAG for fields along {111}. They
found a totally unexpected hysteresis in the magnetization which is shown
in fig. 145. Dillon found that if the sample had previously been exposed to
a large positive field, M would follow the upper curve while if the sample
had previously been exposed to a large negative field, M would follow the
lower curve. This hysteresis was found to occur in regions of the phase
diagram well away from the first order antiferromagnetic-paramagnetic
transition, and was interpreted as due to an inequivalence of the two
antiferromagnetic states which are degenerate in zero field. Microscope
studies supported this interpretation, and it was possible to observe and
photograph the two antiferromagnetic states as well as phase transitions
between them.

At about the same time as Dillon's work, Blume et al.[223] measured the
staggered magnetization for fields along {111} in the vicinity of the "higher
order" transition, and the results at one temperature are shown in fig. 146.
M_s is continuous and nonzero over the entire range, in contrast to the expected
behavior at a second order transition (see fig. 21a). Thus, Blume et al.[223]
found that the "higher order" transition was actually no phase transition at
all! Blume et al. also proposed a qualitative explanation of this behavior
which explained both their results and the hysteresis observed by Dillon et al.[220]
They showed that for fields along {111} the symmetry of DAG allowed a coupling

between the applied field and the staggered magnetization. This effect is formally analogous to the coupling between the staggered field and M_s and hence when the applied field is nonzero, DAG behaves as if a nonzero staggered field were also present. This induced staggered field, "H_s", has the following effects. (1) From fig. 4 we see that if there is an induced staggered field which is proportional to H_i, then there will be no line of second order transitions in a field. This accounts for both the neutron results and also the nondivergence of χ_i and C_{H_i} at the "higher order" transition. (2) A nonzero "H_s" will lift the degeneracy of the two antiferromagnetic states. This accounts for the effects observed by Dillon et al.

A quantitative calculation of these effects was provided by Giordano et al.[224],[222] They considered in detail two microscopic mechanisms which could account for "H_s". They were able to make quantitative calculations of the hysteresis observed by Dillon et al. and found good agreement.

Alben et al.[226] have recently used symmetry arguments to determine the form of the induced staggered field for an arbitrary direction of the field. They have shown that "H_s" $\sim H_x H_y H_z$ where H_x is the component of H along the X crystal axis, etc. Thus for fields in a [110] plane, "H_s" should be zero and thus a tricritical point is expected for these field directions. Very recently, Giordano et al. have investigated the tricritical behavior with the field along {110}. This experiment is discussed in section IV.

In addition to studying the effect of the induced staggered field, Dillon[222],[225] has also examined the domain nucleation process at the first

order transition. The fact that the two antiferromagnetic states are distinguishable has made it possible to verify the theoretical prediction of Mitsek and Gaidanskii[34],[35] that the paramagnetic phase will nucleate at the domain walls between the two antiferromagnetic phases. A photo of this behavior is shown in fig. 147. This picture was taken using the same polarizing microscope used in their studies of $FeCl_2$ (see section III-A). The dark background is one antiferromagnetic phase, the gray regions are the other antiferromagnetic phase and the bright dots on the boundaries are the paramagnetic phase. The wealth of knowledge concerning its basic properties combined with the fact that large, high quality accurately shaped samples are readily available, make DAG a particularly attractive material for further research.

2. TbAlG, HoAlG

Terbium aluminum garnet has structural and magnetic properties which are very similar to those of the exhaustively studied DAG. At $T_N = 1.35$ K, TbAlG orders into a six sublattice antiferromagnetic structure with magnetic moments pointing along the $\pm x$, $\pm y$, $\pm z$ axes of the garnet cubic cell. Unlike DAG, whose ground state is a Kramers doublet, the ground state energy levels of TbAlG comprise two singlets with a separation of 2.5 K.[227] A theoretical study of the magnetic properties of antiferromagnetic two singlet systems[228] shows that metamagnet transitions and phase diagrams with tricritical points can occur.

Magnetization measurements[227] on TbAlG indeed show that metamagnetic transitions do occur when H is parallel to the [111], [110] and [001] directions (see figs. 148-150). An analysis of the magnetic properties

indicates that the interactions in TbAlG are predominantly dipolar, as is the case in DAG.

The phase boundary of TbAlG, shown in fig. 151, with $H||[111]$ has been mapped by locating the kinks or inflections in the magnetization isotherms, as shown in fig. 152. Gavignet-Tillard et al.[227] claim that the transitions passed from first to second order at T = 0.71 K. However, the peaks of the dM/dH isotherms for T > 0.71 do not reach the 1/N value (where N = the demagnetization factor), as is expected for a second order transition (see fig. 153). Hence, it is quite possible that the line of first order transitions for $H||[111]$ ends at a critical point, as occurs for the same field direction in the case of DAG.

Another material whose structural and magnetic properties are similar to those of DAG is HoAlG. At T_N = 0.86 K it orders into a six sublattice antiferromagnetic structure[229] similar to that of DAG and TbAlG. As is the case in TbAlG, the two lowest energy levels of HoAlG are singlets. Magnetization isotherms,[230] shown in fig. 154, show that metamagnetic transitions can occur when $H||[111]$ or $H||[001]$. Further work on the metamagnetic transitions of HoAlG has not been reported perhaps because of its low Neel temperature.

TbAlG and HoAlG are good examples of two singlets systems which exhibit metamagnetic properties. Much more work on these materials is possible: e.g., more detailed magnetization studies, and optical and neutron studies.

E. MIXED CRYSTALS

1. $Co(S_x Se_{1-x})_2$

The solid solution $Co(S_x Se_{1-x})_2$ can be antiferromagnetic, paramagnetic,

or ferromagnetic when $0 \leq x \leq 0.5$, $0.5 < x < 0.88$, or $0.88 \leq x \leq 1$,
respectively, as shown in fig. 155. X-ray analysis shows that the crystal
structure is pyrite for all x, and that the lattice parameters change
linearly with x.[231] It also shows that the arrangement of the S and Se
atoms is disordered. The antiferromagnetic behavior with increase of Se
concentration is not due to the lattice parameter change but rather to the
appearance of superexchange paths with the appearance of Se ions.[232]

The existence of the paramagnetic state for $0.5 < x < 0.88$ has been
confirmed by neutron diffraction for temperatures as low as 4.2 K. Adachi
et al.[233] suggest that the paramagnetic state results from the competition
of ferromagnetic and antiferromagnetic exchange interactions and the inability
of the Co ions' f.c.c. structure to stablize any helical spin ordering, when
exchange interactions up to second neighbor are taken into account.[233]
Adachi et al.[233] have called this paramagnetism "exchange compensated
paramagnetism."

This paramagnetic state exhibits unusual magnetization behavior. Measure-
ments have been performed on a pressed powdered sample of $Co(S_{0.86}Se_{0.14})_2$.
Figure 156 shows that at 4.2 K a sharp transition to a saturated magnetic
state occurs when the applied field is sufficiently large. The figure also
shows an unusual hysteresis behavior (see curve 3, in fig. 156) corresponding
to a "memory effect." Adachi et al.[233] report that this effect vanishes
after the sample has been brought to room temperature. No explanation for
this effect has been offered.

The field induced transition from the exchange compensated paramagnetic

state to a state of saturated magnetic moment has been observed below 78 K
with field strengths less than 75 kOe. The curves, shown in fig. 157, below
40 K exhibit hysteresis and none of the curves exhibit remanence at zero
field. By dividing the hysteresis loop into two equal area parts, Adachi
et al.[233] have located the transition fields on the magnetization isotherms,
as shown in fig. 158. Figure 159 shows the transition temperatures on curves
of magnetization versus temperature at constant magnetic field. The dependence
of transition field with temperature, shown in fig. 160, resembles the phase
diagram of a liquid gas system. This analogy has been noted by Adachi et al.[233]
who obtained the exponents governing the behavior of the reduced magnetization,
near the critical point (m^*, H^*_{tr}, T^*_{tr}), which they located by the vanishing
hysteresis. The experimental exponents are close to those obtained from class-
ical theories.

The experimental data on $Co(S_xSe_{1-x})_2$ have stimulated numerous theoretical
explanations. Hattori, Adachi, and Nakano[234,235] actually predicted before
the experimental evidence, that a field induced phase transition could occur
for a range of S concentration. Their statistical mechanical calculation
employed an f.c.c. lattice of $S = 1/2$ spins, which couple to nearest neighbors
with ferromagnetic interactions J_1 and couple to next nearest neighbors with
antiferromagnetic interactions J_2. By performing a high temperature series
expansion they showed how the magnetic properties varied with the ratio J_2/J_1.
Their results are in good agreement with the data on $Co(S_xSe_{1-x})_2$.

There are other model systems, employing statistical mechanical calculations,
which exhibit magnetic behavior qualitatively similar to the experimental data.[236-239]
A different type of explanation has been offered by Mott and Zinamon[240] who note
that $Co(S_xSe_{1-x})_2$ is metallic for all x. They suggest that the localized spins

on the Co ions interact with the conduction band, resulting in a degenerate gas of spin polarons. Field induced transitions would occur when the magnetic field energy exceeds the coupling energy between the conduction electron and the localized spin.

Clearly $Co(S_xSe_{1-x})_2$ is an interesting system with novel magnetic properties. The availability of single crystals would be an aid toward further understanding of its complicated properties.

2. $UA_{1-x}B_x$; (A = P, As; B = S, Se)

The uranium monopnictides, UA, and the uranium monchalcogenides, UB, can form solid solutions, $UA_{1-x}B_x$, which are all good conductors of electricity. These solutions also contain localized 5 f electrons on the uranium elements. It is the interaction of the localized moments with the conduction electrons which gives these crystals their interesting and complex magnetic properties.[241]

In common with the UA and UB compounds, all the solid solutions have the NaCl structure. For all concentrations, the A and B atoms are distributed randomly. However, variations in concentration over a given sample are sometimes large enough to cause more than one magnetic phase to coexist at some temperatures.[242]

The most studied UAB compound is $UP_{1-x}S_x$. UP orders antiferromagnetically at $T_N = 125$ K with the type I (+, -) structure. It exhibits a "moment jump" at 22 K which results from a partial delocalization of electrons with decreasing temperature.[243] US is a highly anisotropic ferromagnet with $T_c = 178$ K. The magnetic phase diagram of the solid solution depends very strongly on the concentration.[244] Figure 161 obtained from neutron diffraction,[242] shows the magnetic phases for $UP_{0.90}S_{0.10}$. In all of the phases, the spins are aligned

in (001) ferromagnetic sheets with the spin direction parallel to the [001] axis. In the type IA structure the sheets are stacked in the (+ + - -) sequence, while in the type I structure the sheets are stacked (+ -).[242] For other concentrations, an antiphase (5+, 4-) structure is possible as, for example, in $UP_{0.75}S_{0.25}$.[245,246] The magnetic phase diagram also obtained by neutron diffraction, is shown in fig. 162. Table 3 summarizes the magnetic properties of $UP_{1-x}S_x$ solutions, and fig. 163 shows how the phases depend on temperature and concentration.[242] The important feature of the type IA and antiphase magnetic structures is their long range character. Such structures can be accounted for by long-range (RKKY-type) magnetic interactions. This is the dominant interaction in the UP-US solid solutions and presumably in other UAB solid solutions.[241]

Magnetization isotherms[242,247] on powdered samples of $UP_{0.75}S_{0.25}$ and $UP_{0.90}S_{0.10}$ show that field induced phase transitions can occur, as shown in figs. 164 and 165. In the former sample the transitions occured from the antiphase structure, while in the $x = 0.10$ case the transition occured from the mixed type I, type IA region. Clearly measurements on homogeneous single crystals would yield more detailed information on the transition.

Complex magnetic behavior also occurs in the other UAB systems. Neutron diffraction on powder samples of $UAs_{1-x}Se_x$ reveal at least seven possible magnetic structures depending on the value of x.[248,249] These results are summarized in table 4 and fig. 166, which shows the stacking arrangement of the ferromagnetic layers for the multilayer structures. Metamagnetic behavior has been observed in a powder of $UAs_{0.75}Se_{0.25}$ by using pulsed magnetic fields up to 200 kOe, as shown in fig. 167.[250] High magnetic fields are also needed to

induce transitions in $UP_{0.80}Se_{0.20}$ and $UP_{0.90}Se_{0.10}$, as shown in fig. 168.[251] As determined by neutron diffraction the $UP_{1-x}Se_x$ system also has magnetic structures which depend on X. These are summarized in Table 5.[252] The type IA structures for this system also exhibit marked changes in magnetic moment at certain temperatures which are listed in Table 5.

The UAB systems exhibit unusual magnetic structures as the A and B concentrations are varied. This class of materials provides a test of our understanding of RKKY interactions. The metamagnetic behavior offers a means of probing these interactions. The development of single crystals would greatly aid the understanding of these systems.

IV. TRICRITICAL AND CRITICAL BEHAVIOR

In this section we discuss the experiments which have investigated the quantitative properties of metamagnets near the tricritical point and the critical line. We consider here only those systems for which the available data are sufficiently detailed and precise so as to allow critical comparisons with the predictions of the theory outlined in Section II. The materials for which this is the case are $FeCl_2$, DAG and $CsCoCl_3 \cdot 2D_2O$. That only a relative small number of systems have been investigated is an indication of the difficulty of these experiments.

In these studies, it is extremely important to locate the phase boundaries and the tricritical point as accurately as possible. The critical line is relatively easy to locate--thus is usually accomplished by looking for either the inflection in M, or for the point where M_s goes to zero. The first order line is much more difficult to locate--it is usually found from the "kinks" in M or M_s as a function of H_o. However, as the tricritical point is approached, the susceptibility diverges and hence the slopes of these curves just before the kinks approaches the slopes of the linear portions. Thus as the tricritical point is approached, the kinks become less and less distinct until at the tricritical point they have vanished.

In practice, the kinks are never infinitely sharp because of inhomogeneous demagnetizing fields, sample imperfections, etc. Combined with the divergent susceptibility, this "rounding" makes the first order phase boundaries and hence the tricritical point extremely difficult to locate. This is the major experimental problem encountered in these studies. It would appear that

measurements of M_s, presumably with neutron diffraction or magnetic resonance enable one to overcome the above problems at the upper or paramagnetic phase boundary below T_t, since at this boundary M_s simply goes to zero rather than displaying a "kink".

A. $FeCl_2$

The first detailed tricritical study was performed on $FeCl_2$ by Birgeneau et al.[72] These authors used neutron diffraction techniques to measure both the magnetization and the staggered magnetization. As noted in section II, $FeCl_2$ is a layered material which cannot be formed into an ellipsoidal shape. Birgeneau et al. were able to overcome this problem by using a thin platelet of $FeCl_2$ and masking its edges so as to use only the central portion over which the demagnetizing field was approximately uniform. The phase boundaries both above and below T_t were determined from the behavior of M_s.

The resulting M-T phase diagram is shown in fig. 169. We see that the paramagnetic line and the λ-line both approach the tricritical point linearly, as predicted by the theory (see section II), although the range of T over which the λ-line is linear is much smaller than for the paramagnetic line. In addition, these two phase boundaries have unequal slopes at the tricritical point, also as predicted. The antiferromagnetic phase boundary, however, appears to approach the tricritical point with an infinite gradient. When the data for the antiferromagnetic line shown in fig. 169 were fitted to a power law, the exponent β_- was found to be[72] 0.36 which is well below the predicted value of 1 (see section II and table 1).

Figure 170 shows the results of Birgeneau et al.[72] for the discontinuity in M_s across the first order phase boundary. The corresponding exponent was found to be $2\beta_1 = 0.38$ in sharp contrast with the theoretical prediction $2\beta_1 = 1$. Figure 171 shows the $H_i - T$ phase diagram reported in ref. 72. The phase boundary appears to be continuous through the tricritical point, but the data are not accurate enough to detect the theoretically predicted discontinuity in the second derivative.

Birgineau[253] has also reported additional measurements of M_s near the critical line and the tricritical point. These data shown in fig. 172 are for M_s as a function of H_o at constant T. From the work of Fisher[41] we expect these results to yield "renormalized" exponents. Fisher has shown that if $M_s \sim (H_c - H_i)^\beta$ where H_c is the critical <u>internal</u> field, then $M_s \sim (H_{co} - H_o)^{\beta^*}$ where H_{co} is the critical external field and β^* is a re-normalized exponent which is related to β by $\beta^* = \beta/(1 - \alpha)$ where α is the specific heat exponent. This exponent renormalization should also occur for measurements made at constant H_o and one also expects the same relation between β^* and β at the tricritical point.

As indicated in fig. 172, Birgeneau et al. found along the critical line $\beta^* = 0.35 \pm 0.04$ in good agreement with the theoretical prediction $\beta^* = 0.35 \pm 0.01$ corresponding to ($\beta = 0.312 \pm 0.005$, $\alpha = 0.10 \pm 0.02$).[4] At the tricritical point they found $\beta^* = 0.37 \pm 0.03$ in disagreement with the prediction $\beta^* = 1/2$ (corresponding to $\beta_t = 1/4$, $\alpha_t = 1/2$). Thus the results of the neutron scattering study of Birgeneau et al.[72,253,254] appear to be in disagreement with several predictions of the theory, and this

will be discussed after the other experimental results for $FeCl_2$ have been presented.

Griffin and Schnatterly[255,67] have reported a magneto-optical study of $FeCl_2$. These authors measured the magnetic circular dichroism (MCD); that is, the field induced difference in the absorption coefficients of the two senses of circularly polarized light. They have argued that the MCD is proportional to the magnetization, and thus they were able to use the MCD to determine the behavior of the magnetization in the vicinity of the tricritical point. As in the neutron diffraction experiments of Birgeneau et al., this optical method allowed the sample edges to be masked, ensuring a uniform demagnetizing field. Results for the MCD as a function of H_i and T are shown in fig. 173, and it can be seen that they are very similar to the magnetization curves found for DAG (fig. 140). The resulting MCD - T phase diagram near the tricritical point is shown in fig. 174. These data are plotted on the same scales as the corresponding neutron results shown in fig. 169. Although there is a small (2%) difference in the tricritical temperatures, the two phase diagrams are in good agreement with respect to the shapes of the paramagnetic line and the λ-line. However, there is a disagreement as to the shape of the antiferromagnetic line; while the neutron results for this line has pronounced curvature, the optical data over the same range of reduced temperature $((T_t - T)/T_t)$ are linear in temperature as predicted by the theory.

The H_i - T phase diagram reported by Griffin and Schnatterly is shown in fig. 175. As found in the neutron experiments, this phase boundary appears to be continuous through the tricritical point.

To summarize the available data for $FeCl_2$, both the neutron[72,254] and optical[255 67] results are in agreement with each other and the theory as to the H_i - T phase diagram and the shapes of the paramagnetic and λ-lines in the M - T phase diagram. The two experiments are in disagreement, however, as to the shape of the antiferromagnetic line. The neutron data along this same path give a value for β_1 well below the predicted value. Also, the neutron data for β^* indicate a value lower than the theoretical value. Some possible reasons for these discrepancies with theory are (1) the size of the appropriate asymptotic regions may be so small as to be unresolvable with the resolution of the experiment; (2) the log correction terms (see section II) may be influencing the behavior resulting in apparent exponents which are lower than the predicted values. In light of the disagreement between the neutron and optical results, however, it is clear that further experiments are needed to resolve this matter.

B. DAG

As discussed in section III, much of the previous work on DAG has been for fields applied along the {111} direction, for which there is no tricritical point. It is expected[226] however, that there will be a tricritical point for fields in a [110] plane. Giordano and Wolf[256,257] have recently reported a study of the tricritical point with the field along the {110} direction. Because of its excellent mechanical properties, it was possible to perform measurements on an accurately shaped spherical single crystal of DAG. To overcome the problems associated with finding the first order phase boundaries,

these authors utilized a technique which detected the presence of domains to locate the first order phase boundaries in the H_o - T phase diagram. This was accomplished by examining the low frequency (1 - 10 Hz) response of the magnetization to small step changes in the applied field. This response was found to exhibit several hysteresis type effects[256] when domains were present, and these were used to locate the extent of the mixed phase region.

Giordano and Wolf also measured the magnetization in the neighborhood of the tricritical point, using the locations of the phase boundaries determined from the hysteresis measurements. Results for the M - T phase diagram are shown in fig. 176; from it one can see that all three phase boundaries are linear as predicted by the theory. In addition, the slopes of the paramagnetic line and the λ-line are unequal, also as predicted. Figure 177 shows magnetization data for DAG along the tricritical isotherm. The quantity $(M - M_t)^2$ is plotted versus H_i so as to test the prediction $\delta_u = 2$ (see section II) and good agreement is found. The asymmetry in the slopes above and below H_t are quite striking, as is the asymmetry in the size of the asymptotic region below and above the tricritical point with the region being much smaller below the tricritical field than above. Figure 178 shows data for the susceptibility along the path $M = M_t$. The data are plotted as $1/\chi$ versus T so as to test the theoretical prediction $\gamma_u = 1$ and again good agreement is found.

Figure 179 shows the H_i - T phase diagram. The solid line is a fit of the data to the form

$$H_{i\pm} - H_t = A_\pm(T - T_t) + B_\pm(T - T_t)^2 \quad . \tag{4.1}$$

This is consistent with the theory, which predicts a continuous first derivative and a discontinuous second derivative at the tricritical point.

For reasons discussed by Riedel, Meyer and Behringer,[258] it is difficult to estimate the crossover exponent from experimental data. Giordano[259] has recently shown how this may be accomplished, and has found the value $\phi = 1.95 \pm 0.11$ for DAG in good agreement with the theory.

Giordano and Wolf[257] have also tested the scaling hypothesis for the magnetization. Figure 180 shows the DAG data plotted in the two scaling forms (see Eq. (2.8)) with the values of the exponents β_u and δ_u fixed at the predicted values 1 and 2, respectively. The data, which cover roughly one decade of reduced temperature are seen to fall onto common curves when plotted in either of the two scaling forms, in good agreement with scaling theory. It is of interest to consider over what regions of the phase diagram the data scales--fig. 181 shows the scaling regions for DAG in both the $M - T$ and the $H_i - T$ planes. Although the scaling region in the $M - T$ plane is roughly symmetrical in the antiferromagnetic and paramagnetic phases, the region is extremely asymmetrical in the $H_i - T$ plane, being much smaller in the antiferromagnetic phase. This is the same asymmetry evidenced in the tricritical isotherm data (fig. 177). There are no theoretical predictions of any kind concerning this feature, and it is interesting to note that a very similar asymmetry has been found in another tricritical system, $^3\text{He}-^4\text{He}$ mixtures.[258]

C. $\text{CsCoCl}_3 \cdot 2\text{D}_2\text{O}$

Very recently, Bongaarts[260,261] has reported neutron diffraction measurements of both M and M_s near the tricritical point in $\text{CsCoCl}_3 \cdot 2\text{D}_2\text{O}$. Unfortunately,

Bongaarts was not able to obtain an accurately shaped sample and the estimated spread in demagnetizing field was rather large (±25 Oe as compared with $H_t \simeq$ 2.8 kOe).

The results for the M – T phase diagram are shown in fig. 182. It was found that the phase boundaries below the tricritical point are not linear (as predicted by the theory), but rather are discribed by the exponents $\beta_\pm = 0.65 \pm 0.2$. Figure 183 shows data for the discontinuity in M_s across the first order line. From these data, Bongaarts[260] finds $\beta_1 = 0.30 \pm 0.15$ in contrast with the theoretical prediction $\beta_1 = 1/2$.

Bongaarts has also studied the behavior of M_s near the λ-line and the tricritical point along paths of constant temperature. Figure 184 shows results for two paths through the λ-line and also the tricritical isotherm. Well above the tricritical point he finds $\beta \simeq 0.29$ in agreement with the three dimensional Ising model prediction $\beta = 0.31$. Nearer the tricritical point (curve b in fig. 184) we find $\beta \simeq 0.28$ near the λ-line, but farther away the data are consistent with $\beta = 0.15$. Bongaarts interprets this as crossover from tricritical to critical behavior as the λ-line is approached. The relatively small range of reduced temperature over which the crossover occurs would appear to be at odds with the theory,[258] which predicts that this crossover should occur over approximately two decades of reduced temperature. Figure 184 shows data for the tricritical isotherm. The data are well described by the exponent $\beta_t = 0.13$ in disagreement with the theoretical prediction $\beta_t = 1/4$.

Finally, in fig. 185-186, we show scaling plots for both M and M_s. In his analysis, Bongaarts used the scaling fields (2.7), and this accounts for the slightly different appearance of fig. 185 as compared with the analogous plot for DAG. The data are seen to be in agreement with the scaling hypothesis, but it should be emphasized that the values for the exponents used in this test of scaling are the ones determined from fig. 182-184 and are not the theoretically predicted values.

D. DISCUSSION

In table 6 we list the various exponents which have been reported for $FeCl_2$, DAG and $CsCoCl_3$, with the theoretical predictions shown for comparison. As discussed above, the results for $FeCl_2$ are only in partial agreement with the theory, and further work is needed to resolve the disagreement between the neutron scattering results of Birgeneau et al.[72] and optical results of Griffin and Schnatterly.[255] All of the results for DAG are in good agreement with the theory. The results for $CsCoCl_3 \cdot 2D_2O$ appear to conflict with the theory, but the experimental uncertainties are fairly large, and it is also possible that the large spread in the demagnetizing field could be the source of the discrepancies.

V. SUMMARY

The previous sections have reviewed the basic features of the mean field treatments of metamagnetism, described in some detail real meta-magnetic systems, and compared the tricritical point behavior of a few of these systems with the predictions of modern theories of phase transitions. The metamagnetic transitions can occur in crystals in which there is a high degree of local anisotropy. This large anisotropy is present in a wide variety of materials so that these transitions are observable through their effect on the basic properties of many crystals.

Magnetization and neutron diffraction measurements have been performed on many of the materials listed in this review and given direct evidence for the occurrence of the field induced transitions. The rapid increase of magnetization associated with the onset of such a transition is the most frequently cited evidence for a field induced change in magnetic structure, while neutron diffraction is often the only way to determine the structure of the field induced state.

Metamagnetic transitions have also been observed by their effect on a wide variety of other phenomena, e.g., the discontinuities in the far infrared and NMR spectra of $CoCl_2 \cdot 2H_2O$ are due to the variation of internal field caused by the transition. Similarly the sudden change in the magnitude of the magnetoelectric susceptibilities of $DyPO_4$ and $DyAlO_3$ are due to the change in magnetic symmetry associated with the transition.

In some cases the effect of the transition on optical and thermal
properties has been used to map the phase boundaries of the material.
Examples of this type of experiment include specific heat measurements of
DAG and $DyPO_4$, Faraday rotation measurements on DAG, $DyPO_4$ and $FeCl_2$, and
the measurements of magnetic circular dichroism in $FeCl_2$. The basis for the
optical work revolves around the different responses to polarized light
exhibited by antiferromagnetic and paramagnetic domains. The hysteretic
effects associated with the presence of these domains has also been used to
locate the phase boundaries, as in the case of DAG.

Within the class of metamagnetic materials there is a diversity in
the topology of phase boundaries and in the type of field induced states.
Archetypical metamagnets such as $FeCl_2$ and DAG undergo a single field
induced transition from the antiferromagnetic state to the paramagnetic
state. Other materials, such as $CoCl_2 \cdot 2H_2O$ and $DyAlO_3$ have an intermediate
field induced state which is ferrimagnetic. In the case of EuSe the field
induced transition can proceed from one of two antiferromagnetic states,
while in the case of the $Co(S_xSe_{1-x})_2$ systems the transition appears to
proceed from the paramagnetic state. The latter material is just one of
several which still require work in order to understand the basic magnetic
interactions.

For some of the materials in the review (e.g., $NiCl_2 \cdot 2H_2O$, EuSe and CeSb)
neutron diffraction would be very helpful in determining the phase boundaries
and the nature of the field induced state(s). For other materials there

has been sufficient work so that the basic interactions are well understood. Recent work on these materials ($FeCl_2$, DAG and $CsCoCl_3 \cdot 2H_2O$) has concentrated on the tricritical point behavior. Other crystals, notably $FeBr_2$, are candidates for future tricritical point studies.

In addition to their interest as a distinctly different class of phenomena, metamagnetic transitions provide an opportunity to test current theories of phase transitions. The critical fields and the size of the magnetization jumps have often been of use in determining the exchange constants describing the magnetic structure. For these reasons the study of metamagnetic transitions will no doubt thrive and continue to open ever wider areas of research.

Further research could well lead to the use of metamagnetic phenomena in practical devices. The essential feature of such applications would involve the relatively large change in magnetization achievable by very small driving fields. This property of metamagnetics might find important applications in digital memory elements. Using materials such as $CoCl_2 \cdot 2H_2O$ which undergo two magnetization jumps it might be possible to produce multistable devices. Another conceivable application concerns the coupling of optical properties with the field induced transitions. This coupling suggests the use of some metamagnetic crystals as optical modulators and deflectors. However, before metamagnetism finds widespread practical application, the development of new metamagnetic materials with significantly higher transition temperatures and lower critical fields is clearly necessary.

ACKNOWLEDGMENTS

We would like to thank Professor W. P. Wolf for his advice
and encouragement throughout the writing of this report.

APPENDIX I

MISCELLANEOUS METAMAGNETIC MATERIALS

The previous sections have reviewed in some detail the magnetic properties of some common metamagnetic materials. As mentioned in section I the scope of this report does not include materials such as MnP, in which the dominant response to an applied magnetic field is a rotation of the spins away from the direction of local anisotropy. The present section considers less commonly studied materials which come within the scope defined in section 1. In cases where there is an ambiguity as to the nature of the field induced transition, the material has been included for the sake of completeness.

1. Nd Monochalcogenides

Magnetization isotherms, fig. 187, show that NdS, NdSe and NdTe undergo field induced transitions upon application of high magnetic fields.[262]

2. ErCrO$_3$

Magnetization and neutron diffraction studies on a single crystal of ErCrO$_3$ reveal metamagnetic properties which can be described by a two sublattice model for the magnetic spins[263] (see fig. 188).

3. Mn(CH$_3$COO)$_2 \cdot$4H$_2$O

Mn(CH$_3$COO)$_2 \cdot$4H$_2$O is a monoclinic crystal which orders at 3.18 K. The Mn ions are located in planes separated by layers of H$_2$O molecules.[264] The structure is shown in fig. 189.

Magnetization measurements[265] on single crystal samples show that with H $||$ a-axis a metamagnetic transition occurs at $\sim$ 6 Oe (see fig. 190).

NMR on ellipsoidally shaped crystals also reveal, as shown in fig. 191, that the metamagnetic transition occurs at 6 Oe. The NMR results suggest that two dimensional ordering in the Mn planes persists above the Neel temperature until $\sim$ 30 K.[264] This is a very unusual feature and clearly deserves further study.

4. CeAl

CeAl which orders at $\sim$ 10 K undergoes a metamagnetic transition (fig. 192) at $\sim$ 8 kOe at 4.2 K as observed by magnetization measurements on powdered samples.[266]

5. ErAu, HoAu, DyAu

Magnetization measurements on ErAu, HoAu and DyAu shown in figs. 193 and 194, suggest the occurence of metamagnetic transitions. In all three cases[267,268] the measurements were performed on powder samples at 4.2 K.

6. $[C_6H_{22}N_4]$ $CuCl_6$

At 8.9 K $[C_6H_{22}N_4]$ $CuCl_6$ orders into antiferromagnetically coupled ferromagnetic layers. Magnetization measurements (fig. 195) on polycrystalline samples show that low field metamagnetic transitions occur.[269] At 4.2 K the transition field is only 50 Oe. From magnetization, susceptibility and EPR measurements estimates of the exchange parameters have been obtained. From these parameters a tricritical point temperature of 8.86 K has been estimated.[269]

7. $(NpO_2)_2$ $C_2O_4 \cdot 4H_2O$

Neptunium oxalate orders antiferromagnetically at T_N = 11.6 K. Metamagnetic behavior is discernible from magnetization measurements on powder
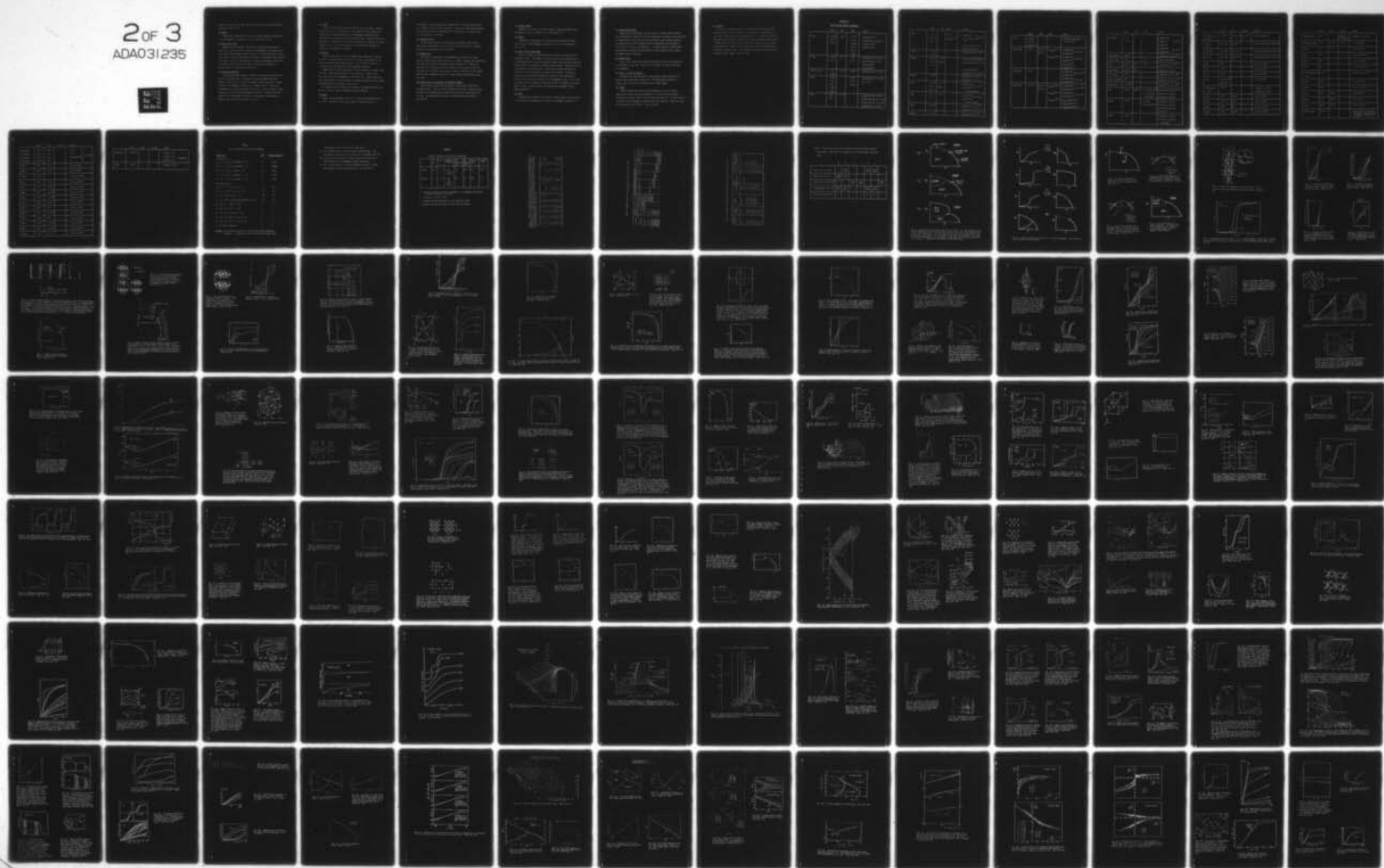
samples, as shown in fig. 196. Figure 197 shows that the isotherms display hysteresis below 9 K.[270]

8. $HoMnO_3$

Magnetization measurements, fig. 198, on powder samples of $HoMnO_3$ show that a metamagnetic transition occurs at $\sim$ 6 kOe and 4.2 K.[271]

9. $HoCu_2$, $DyCu_2$ $TbCu_2$

Magnetization measurements (fig. 199) on polycrystalline samples of $HoCu_2$, $DyCu_2$ and $TbCu_2$ at 4.2 K indicate that metamagnetic transitions occur with critical fields ranging from 10-30 kOe.[272] Neutron diffraction on $TbCu_2$ shows that in zero field the magnetic structure of orthorhombic $TbCu_2$ consists of Tb moments in the a-c plane forming a collinear configuration with 2/3 of the moments along the +a direction and 1/3 along the -a direction. In adjacent planes the moments are reversed.[273]

10. $CoCl_3[(CH_3)_3NH] \cdot 2H_2O$

$CoCl_3[(CH_3)_3NH] \cdot 2H_2O$ consists of planes of $CoCl_2 \cdot 2H_2O$ interleaved with planes of $(CH_3)_3NH$ groups. An analysis of NMR data suggests that this material orders at T_N = 4.1 K with the magnetic space group Pnm'a'. Figure 200 shows the arrangement of spins in the ordered state.[274] Three spin arrangements C_1, C_2 and C_3 are shown in fig. 201. C_1 and C_3 coexist in equal volumes in the zero field antiferromagnetic state.[274] NMR data (fig. 202) suggests that a metamagnetic transition to the magnetic configuration C_2 (magnetic space group Pn'm'a) occurs at 64 Oe.[275]

11. ErVO$_4$

ErVO$_4$ is structurally isomorphous with the Ising like DyPO$_4$. However, unlike DyPO$_4$, there is considerable mixing between the ErVO$_4$ ground state doublet with the higher energy levels. Metamagnetic behavior has been inferred from an analysis of thermal resistivity data. Figure 203 shows the appearance of large peaks in the thermal resistivity as a function of applied magnetic field. It has been suggested[276] that these peaks indicate the occurrence of metamagnetic transitions.

12. DyCoO$_3$

DyCoO$_3$ orders at T_N = 3.6 with a magnetic space group $G_x A_y$, shown in fig. 204. The ground state of the Dy^{3+} ion is $^6H_{15/2}$, which split by the crystal field into eight Kramers doublets. Only the lowest doublet is occupied at low temperatures and it has Ising-like character.

Magnetoelectric effect measurements[277] were performed on a powder sample of DyCoO$_3$. Measurements performed in the presence of a static field (fig. 205) suggest that metamagnetic transitions occur. These transitions, shown schematically in fig. 204 change the magnetic symmetry, thereby causing the magnetoelectric coefficient to equal zero.

If single crystals of DyCoO$_3$ were available, the magnetoelectric effect might be a sensitive means of mapping the phase boundaries.

13. Mn$_3$B$_4$

Mn$_3$B$_4$ is an orthorhombic crystal which orders antiferromagnetically at T_N = 392 K. Between 226 K and T_N the magnetic structure consists of

ferromagnetic layers aligned antiferromagnetically. Below 226 K the crystal has a canted or conical screw structure.[278] Below 226 K field induced behavior is observed, which may be metamagnetic[279] (see fig. 206). The exact nature of the transition is not known.

14. Gd_3(Fe, Co, Ni)

Field induced behavior has been observed in materials made from Gd_3 with various compositions of Fe, Co and Ni, as shown in fig. 207. The exact nature of the transitions is not certain.[280]

15. $RbCoCl_3 \cdot 2H_2O$

Differential susceptibility measurements were performed on a single crystal of $RbCoCl_3 \cdot 2H_2O$, which orders at T_N = 2.98 K. Peaks in the susceptibility have been identified with metamagnetic phase transitions.[281] Figure 208 shows that three transitions can occur when H $\parallel$ c-axis, where as fig. 209 shows that one transition occurs when H $\parallel$ b-axis. Flokstra et al.[281] suggest that the spin arrangement consists of strongly coupled canted chains along the c-axis.

16. NiX_2L_2 with X = cl, Br and L = Pyrazole, Pyridine

These materials order with ferromagnetic linear chains coupled anti-ferromagnetically. They all exhibit metamagnetic behavior. $NiCl_2(py)_2$ shows two steps in the magnetization isotherms while the other three exhibit only one step. The magnetization isotherms of powder $NiBr_2(pz)_2$ are shown in fig. 210.[282]

17. ErNiAl, TmNiAl

Magnetization isotherms on powder samples of ErNiAl and TmNiAl reveal metamagnetic behavior as shown in fig. 211 and 212.[283,284]

18. TbFeO_3

Magnetization measurements on a spherical single crystal of $TbFeO_3$ reveal a first order metamagnetic transition at $T = 1.15$ K, as shown in fig. 213.[285]

19. DyAu_2, TbAu_2, DyAg_2, TbAg_2

Except for $TbAg_2$, all the above materials exhibit two zero field low temperature states. The magnetic structures at the lowest temperatures has antiferromagnetically coupled ferromagnetic layers, while the high temperature ordered state has a transverse sinusoidal spin structure. $TbAg_2$ has only the low temperature layered structure. Field induced transitions have been observed in all four materials, as shown in figs. 214-216. In $DyAu_2$ the transition is first from the layered (β) structure to the sinusoidal (α) structure, then from the α structure to the paramagnetic state. In the other three materials the transition is directly from the β structure to the paramagnetic state. Figure 217 shows the magnetic phase diagrams of $TbAu_2$, $TbAg_2$ and $DyAu_2$.[286]

20. Gd_3In

A magnetization isotherms (fig. 218) of a powder sample of Gd_3In display two step behavior, suggesting the occurrence of metamagnetic behavior.[287]

21. TbOOH, DyOOH, ErOOH

Magnetization measurements on powder samples of TbOOH, DyOOH and ErOOH reveal metamagnetic behavior for all three compounds, as shown in figs. 219-221.[288] The magnetoelectric effect has also been observed in pressed powder samples of all three materials.[289] The magnetoelectric measurements were performed in zero field, as a function of temperature. If single crystals of TbOOH, DyOOH and ErOOH were available, the magnetoelectric effect might be used to detect the magnetic phase boundaries.

22. $TmZn_2$, $DyZn_2$

$TmZn_2$, $DyZn_2$ undergo field induced transitions as shown in the magnetization isotherms of fig. 222. Debray et al.[290] suggest that these transitions are metamagnetic.

23. R_5Ge_3 R = Er, Tb, Dy, Ho

According to Buschow and Fast[291] Er_5Ge_3, Tb_5Ge_3, Dy_5Ge_3 and Ho_5Ge_3 all exhibit field induced phase transitions. The magnetization isotherm of Er_5Ge_3, shown in fig. 223, was obtained with a powder sample.

24. ErGaG

Erbium Gallium Garnet orders antiferromagnetically at T_N = 0.789 K. Magnetization studies have been performed at T = 0.08 K with the external field applied along the [001], [011] and [111] directions.[292] For each direction of applied field metamagnetic transitions have been observed. Figure 224 shows such a transition with H∥[111]. After ref. 292.

25. TbAsO$_4$

At T_N = 27 K, TbAsO$_4$ undergoes a Jahn-Teller crystallographic phase transition which lowers the symmetry from tetragonal to orthorhombic. At T_N = 1.48 K, TbAsO$_4$ orders antiferromagnetically in a collinear sublattice structure with an Ising-like ground state. The metamagnetic phase transition of TbAsO$_4$, which is similar to that of DyVO$_4$ and DyAsO$_4$, has been studied spectroscopically. Figure 225 shows the variation of the Zeeman energy as a function of applied field. The metamagnetic transitions are shown for two different crystal shapes. After ref. 293.

APPENDIX II

TABLE OF BULK MAGNETIC PROPERTIES

	$T_N(K)$	$\theta(K)$	$T_t(K)$	$H_c(kG)$
$FeCl_2$	23.55^{60} 22.9^{73} 23.7^{66}	48^{53}	21.15^{72} 20.3^{73} 20.79^{69} 21.5^{66} 20.4^{57} 21.8^{65}	$H_t(app)=10.2^{72}$ $H_c(int)=10.45$ at 4.2 K^{73} $H_t(int)=7.55^{73}$ $H_t(int)=7.58^{65}$
$FeBr_2$	14.2^{82} 14.1^{73}	6^{83}	4.7^{82} 4.6^{73}	$H_c(app)=31.5$ at 4.2 K^{85} $H_c(int)=28.8$ at 4.2 K^{73} $H_t(int)=28.5^{73}$ $H_t(int)=28.2^{82}$
$Ni(NO_3)_2 \cdot 2H_2O$	4.2^{90} 4.105^{92}	2.5^{90}	3.85^{91}	$H_c(int)=3.4$ at $T \simeq 0$ K^{91}
$DyPO_4$	3.39^{93} 3.39^{94} 3.5^{99} 3.38^{100} 3.39^{97}		0.75^{93} 2.0^{94} 1.95^{101}	$H_c(int)=5.45$ at $T \simeq 0$ K^{93} $H_t = 4.3^{94}$
$FeCO_3$	38^{107} 38^{104}	-14^{108}		$H_c(app)=150$ at 4.2 K^{107} $H_c(app)=148-176$ at 4.2 K^{108} $H_c(app)=150-180$ at 4.2 K^{110} $H_c(app)=160$ at 4.2 K^{114}

	$T_N(K)$	$\theta(K)$	$T_t(K)$	$H_c(kG)$
DySb	9.5^{117} 10.2^{119} 9.5		8.5^{119} $T_{triple}=9.7^{119}$	$H_t(int)=14.7$ $H_{triple}(int)=12.4$ } $H\|\|<110>^{11}$ $H_{c1}=21.6$ } $T=4.2$ K^{117} $H_{c2}=40.6$ } $H\|\|<100>$
TbPO$_4$	2.17^{121} 2.17^{122}			$H_c(app)=4.8$ at 1.5 K^{121}
DyAlO$_3$	3.52^{125} 3.4^{128} 3.5^{126}	-5^{126} (powder)		$H_{c1}(app)=6.5$ } $H\|\|[110]$ $H_{c2}(app)=24$ at $T=1.2$ K^{126} $H_{c1}(app)=7.0$ } $H\|\|\mu$ $H_{c2}(app)=7.3$ } $T=3.4$ K^{128}
TbAlO$_3$	3.95^{125}			$H_c(app)=8$ at 1.5 K^{131} $H_c(app)=8$ at 1.4 K^{133}
CeBi	25.2^{135} 26^{136} 25^{139}	12^{139} powder		$H_{c1}(app)=10$ } $T=1.3$ K^{139} $H_{c2}(app)=45$ } powder samples
CeSb	16^{137} 16.2	8^{143}		$H_{c1}(app)=20$ } $T=1.9$ K^{143} $H_{c2}(app)=38$ } powder samples
DyVO$_4$	3.04^{149}			$H(app)=2.2$ at 1.4 K^{148} $H_c(int)=2.1$ K at 0.5 K^{149}
DyAsO$_4$	2.5^{147}			$H_c(app)=2$ at 1.5 K^{147}

	$T_N(K)$	$\theta(K)$	$T_t(K)$	$H_c(kG)$
EuSe	$T_{N1}=4.6$ $T_c=2.8$ $T_{N2}=1.8$[151]			H_c(int) all less than 2.5 K[151,158]
$FeCl_2 \cdot 2H_2O$	23[162]	$\theta_{11}=12$[162] $\theta_1=5$[162]	$T_{triple}=11.7$[7] $T_{triple}=11.5$[170]	$\left.\begin{array}{l}H_{c1}(app)=39\\H_{c2}(app)=46\end{array}\right\}$ T=4.0 K[162] $\left.\begin{array}{l}H_{c1}(app)=35\\H_{c2}(app)=45\end{array}\right\}$ T=2.0 K[174] $H_{triple}=42.0$[7] $H_{triple}=41.0$[170]
$CoBr_2 \cdot 2H_2O$	9.5[168]			$\left.\begin{array}{l}H_{c1}(app)=13.7\\H_{c2}(app)=29.8\end{array}\right\}$ T=1.5 K[168] $\left.\begin{array}{l}H_{c1}(app)=13.7\\H_{c2}(app)=29.3\end{array}\right\}$ T=2 K[192]
$CoCl_2 \cdot 2H_2O$	17.5[168]	$\theta_{11}=1$[160] $\theta_1=1$ [160]	$T_{triple}=8.8$[171] $T_{triple}=8.9$[6] $T_{triple}=8.9$[173]	$\left.\begin{array}{l}H_{c1}(app)=31.6\\H_{c2}(app)=46.0\end{array}\right\}$ T=1.5 K[168] $\left.\begin{array}{l}H_{c1}(app)=31.0\\H_{c2}(app)=44.9\end{array}\right\}$ T=1.6 K[33] $H_{triple}(app)=38.5$[171] $H_{triple}(app)=37.5$[6] $H_{triple}(app)=39.3$[173]

	$T_N(K)$	$\theta(K)$	$T_t(K)$	$H_c(kG)$
$NiCl_2 \cdot 2H_2O$	$6^{[198]}$ $7.2^{[199]}$			$H_{c1}(app)=18.6$ $H_{c2}(app)=51$ $\quad$ T=1.4 K[198] $H_{c2}(app)=82$ $H_{c1}(app)=18.5$ $\quad$ T=1.1 K[195] $H_{c1}(app)=20.9$
$CsCoCl_3 \cdot 2H_2O$	$3.38^{[200]}$			$H_c(app)=2.9$ at T=1.1 K[200]
$CsCoCl_3 \cdot 2H_2O$	$3.2^{[261]}$		$2^{[261]}$	$H_c(int)-2.85$ atT=0 K
Eu_3O_4	$5.0^{[203]}$	$5^{[203]}$	$2^{[203]}$	$H_c(app)=2.4$ at 2.2 K[203]
$Co(pyr)_2Cl_2$	$3.17^{[205]}$	$5^{[205]}$		$H_c(app)=0.7$ at T=3 K
$Fe(pyr)_2Cl_2$	$7^{[206]}$			$H_c(app)=0.7$ at T=4.2 K[206]
$Fe(pyr)_2 \cdot (NCS)_2$	$6^{[206]}$			$H_c(app)=1.1$ at T=4.2 K[206]
$Ni(pyr)_2Cl_2$	$\sim 6.75^{[292]}$			$H_c(app)=2.7$ at T=4.2 K[206]
DAG	$2.5^{[209]}$	$0.10^{[209]}$	$1.6,\ H\|\|\{111\}^{[214]}$ $1.8,\ H\|\|\{110\}$ $1.7,\ H\|\|\{001\}$	$H_c(int)=3.8,\ H\|\|\{111\}^{[214]}$ $H_c(int)=4.7,\ H\|\|\{110\}$ $H_c(int)=5.2,\ H\|\|\{001\}$
TbAlG	$1.35^{[227]}$		$T_{cr}=0.71$ with $H\|\|\{111\}^{[227]}$	$H_c(int)=2.2,\ H\|\|\{111\}$ $H_c(int)=2.3,\ H\|\|\{110\}$ $H_c(int)=2.6,\ H\|\|\{001\}$ T=0.36 K[227]
HoAlG	$0.86^{[230]}$			$H_c(int)=2.3,\ H\|\|\{111\}$ $H_c(int)=2.7,\ H\|\|\{001\}$ T=0.36 K[230]

	$T_N(K)$	$\theta(K)$	$T_{tri}(K)$	$H_c(kG)$
$Co(S_xSe_{1-x})_2$ X=0.86	78 with[231]	110 with[231]	$T_{cr}=34$[231]	39, with T=34 K[231]
$UP_{1-x}S_x$ X=0.1	see Table 3.	see Table 3.		15, with T=85K and X=0.10 K[242]
$UAs_{1-x}Se_x$	see Table 4.	see Table 4.		100, with T=80 K and X=0.25 K[256]
$UP_{1-x}S_x$	see Table 5.	see Table 5.		60, with T=4.2 K and X=0.20 K[251]
NdS	8[262]			75, at 4.2 K[262]
NdSe	14[262]			85, at 4.2 K[262]
NdTc	13[262]			90, at 4.2 K[262]
$ErCo_3$	$T_{N1}=133.1$[263] $T_{N2}=16.8$			2, at 4.2 K[263]
$Mn(CH_3COO)_2 \cdot 4H_2O$	3.18[264]			6 gauss at 1.1 K[264] 5 gauss at 1.41 K[265]
CeAl	10[266]	-19[266]		8, at 4.2 K[266]
ErAu	16.5[267]	5[267]		9, at 4.2 K[267]
HoAu	10[267]	0[267]		12, at 4.2 K[267]
DyAu	14[268]	-8.5[268]		22, at 4.2 K[268]

	$T_N(K)$	$\theta(K)$	$T_{tri}(K)$	$H_c(kG)$
$[C_6H_{22}N_4]CuCl_6$	$8.95[269]$		$8.86[269]$ (calculated)	50 gauss at 4.2 K[269]
$(NpO_2)_2C_2O_4\cdot4H_2O$	$11.6[270]$	$12.5[270]$	$\sim 9[270]$	~ 1, at 8 K[270]
$HoMnO_4$	$9[271]$	$-23[271]$		6, at 4.2 K[271]
$HoCu_2$	$9[272]$			~ 10, at 4.2 K[272]
$DyCu_2$	$24[272]$			~ 15, at 4.2 K[272]
$TbCu_2$	$54[272]$			~ 22, at 4.2 K[272]
$CoCl_3[(CH_3)_3NH]\cdot 2H_2O$	$4.13[275]$			64 gauss at 2 K[275]
$ErVO_4$	$0.4[276]$			2.7 at ~ 0 K[276]
$DyCoO_3$	$3.57[277]$			7, at ~ 3.56 K[277]
Mn_3B_4	$392[279]$	$543[279]$		300 at 83 K[279]
Gd_3Co	$127[280]$	$159[280]$		3 at 4.2 K[280]
Gd_3N_i	$100[280]$	$60[280]$		25 at 4.2 K[280]
$RbCoCl_3\cdot2H_2O$	$2.975[281]$			Three critical fields with $H\|\|$ c-axis. $H_c \leq 4$ kG. One transition in b-direction ≤ 15 kG.[281]

	T_N(K)	θ(K)	T_{tri}(K)	H_c(kG)
$NiCl_2(pz)_2$	6.05^{282}	18^{282}		0.45
$NiBr_2(pz)_2$	3.35^{282}	7^{282}		1.25
$NiCl_2(py)_2$	6.75^{282}	13^{282}		3.50 and 2.95
$NiBr_2(py)_2$	2.85^{282}	7^{282}		6.5
$ErNiAl$	15^{283}	-1^{283}		8 at 4.2 K[283]
$TmNiAl$	12^{283}	-11^{283}		8 at 1.6 K[283]
$TbFeO_3$	3.1^{285}			1.52 at 1.15 K[285]
$DyAu_2$	31^{286}	-13^{286}		50, at 4.2 K[286]
$TbAu_2$	55^{286}	-21^{286}		100, at 4.2 K[286]
$DyAg_2$	15^{286}	-21.5^{286}		40, at 4.2 K[286]
$TbAg_2$	34.4^{286}	-31.5^{286}		100, at 4.2 K[286]
Gd_3In	213^{287}	196^{287}		5, at 4.2 K[287]
$TbOOH$	10^{288}	0^{288}		20, at 4.2 K[288]
$DyOOH$	9^{288}	-22.6^{288}		30, at 4.2 K[288]
$ErOOH$	7.2^{288}	0^{288}		15, at 4.2 K[288]
$TmZn_2$	5.2^{290}	11.5^{290}		5, at 4.2 K[290]
$DyZn_2$	35^{290}	31.5^{290}		15, at 4.2 K[290]
Er_5Ge_3	31^{291}	35^{291}		10, at 4.2 K[291]

The H_c values for the first four compounds are bracketed with: $T \approx 0$ K[282]

	$T_N(K)$	$\theta(K)$	$T_{tri}(K)$	$H_c(kG)$
ErGaGarnet	0.789^{292}			$H_c(111) = 1.8$ $H_c(011) = 2.1$ $\quad T=0.08\,K^{292}$ $H_c(001) = 2.2$
TbA_3O_4	1.48^{293}			$H_c(100) = 2.5^{293}$

Table 1

List of Critical and Tricritical Exponents

Definition	MFT[11]	Modern Theories[4,14]
Critical Line		
$C_{H_i} \sim (T - T_c)^{-\alpha}$, H_i constant, $T > T_c$	0	0.125
$C_{H_i} \sim (T_c - T)^{-\alpha'}$, H_i constant, $T < T_c$	0	**0.125**
$M_s \sim (T_c - T)^{\beta}$, H_i constant, $T < T_c$	1/2	0.313
$\chi_i \sim (T - T_c)^{-\alpha}$, H_i constant, $T > T_c$[a]	0	0.125
$\chi_i \sim (T_c - T)^{-\alpha'}$, H_i constant, $T < T_c$[a]	0	0.125
Tricritical Point		
$C_{H_i} \sim (T - T_t)^{-\alpha_t}$, $H_i = H_t$, $T > T_t$	0	1/2
$C_{H_i} \sim (T_t - T)^{-\alpha_t'}$, $H_i = H_t$, $T < T_t$	1/2	1/2
$M_s \sim (T_t - T)^{\beta_t}$, $H = H_t$, $T < T_t$	1/4	1/4
$M_s \sim (T_t - T)^{\beta_1}$, along first order line, $T < T_t$	1/2	1/2
$M_p - M_t \sim (T_t - T)^{\beta_+}$, $T < T_t$[b]	1	1
$M_a - M_t \sim (T_t - T)^{\beta_-}$, $T < T_t$[b]	1	1
$\chi_i \sim (T - T_t)^{-\gamma_u}$, $M = M_t$, $T > T_t$	1	1
$H_i - H_t \sim (M - M_t)^{\delta_+}$, $T = T_t$, $H > H_t$	1	2
$H_i - H_t \sim (M_t - M)^{\delta_-}$, $T = T_t$, $H < H_t$	2	2
$g \sim t^{\phi}$, (phase boundary)[c]	2	2

Caption: Definitions and values for various critical and tricritical exponents. T_c denotes the value of the critical temperature

corresponding to the critical line. After ref. 1.

(a) The exponents here are the same as those describing C_{H_1}. This equivalence is predicted by the theory (see, for example, ref. 29).

(b) M_a and M_p denote the value of M at the first order line in the antiferromagnetic and paramagnetic phases respectively.

(c) This is the equation for the phase boundary in the $H_1 - T$ plane. The variables t and g are defined in Eqs. (2.5) and (2.6).

TABLE 2.

Magnetic Properties of Rare Earth Aluminates

	T_N °K	μ/μ_B	Magnetic structure	W_1^a (T=4.2°K) cm^{-1}	W_2^b (T=0°K) cm^{-1}	$W_{12}(ex)^c$ cm^{-1}	$W_{14}(ex)^d$ cm^{-1}
$TbAlO_3$	4.0	9	$A_y G_x$ μ at 35° from a	3.8	4.6	1.3	0.25
$DyAlO_3$	3.5	9.3	$A_y G_x$ μ at 33.5° from b	2.0	4.1	0.85	~ 0

a. Separation between two triplet components = total magnetic interaction energy of an ion at T = 4.2°K.

b. The same as (a) but T = 0°K.

c. Exchange interaction between two ions along the c-axis.

d. Exchange interaction between two ions in the a-b plane.

Table 3 . Magnetic properties of $UP_{1-x}S_x$ solid solutions. The paramagnetic Curie temperatures θ_p, the effective magnetic moment μ_{eff}, the initial ordering temperature, and the value of σ_{00} were obtained from the magnetization experiments. The types of antiferromagnetic order and μ_{sat}, the fully ordered moment at 5°K, were obtained from neutron experiments. After ref. 242.

Nominal x	Chem. anal. x	a_0 (Å)	θ_p (±5) (K)	μ_{eff} (±0.05) (μ_B)	Initial ordering (K)		Subsequent transitions		μ_{sat} (±0.05) (μ_B)	σ_{00} (μ_B)
0	...	5.559	63.5	3.14	125	I	22°K	I	1.95	
0.02	0.022	5.586	45.1	3.22	122	I	22°K	I	2.00	
0.05	0.055	5.581	50.1	3.25	116	I	27–35°K	LA	1.9	
0.075	0.083	5.582	70.5	3.10	110	I	32–42°K	LA	1.9	
0.10	0.103	5.579	67.4	3.16	98	LA	—	LA	1.9	
0.15	0.118	5.576	57.8	2.86	95	LA	↑		1.8	
0.20	0.203	5.570	101.6	2.96	92	LA	3→3 –	↑	1.8	
0.25	0.235	5.567	113.6	2.90	98	F	5→4 –	LA	1.7	1.28
0.28	0.287	5.561	114.7	3.06	109	F	LW?	LA + F	~1.7	1.18
0.33	0.342	5.561	126.4	2.82	112	F	LW?	F	~1.7	1.35
0.50	0.486	5.543	148.2	2.79	150	F			1.7	1.50

Table 4. Magnetic data for the UAs$_{1-x}$Se$_x$ system. After ref. 248.

composition	lattice constant a (in Å)	Magnetic phases and their stability temperatures							T_N, T_C from χ or σ
		$N=1$ (type I)	$N=2$ (type IA)	$N=5$	$N=7$	$N=9$	$N=11$	ferro-magnetic	
UAs [16] [17]	5.779	66 to 127 °K 1.93 BM	4.2 to 66 °K 2.20 BM	—	—	—	—	—	128 °K [15]
UAs$_{0.96}$Se$_{0.04}$	5.778	100 to 116 °K	4.2 to 110 °K 2.16 BM	—	—	—	—	—	116 °K
UAs$_{0.78}$Se$_{0.22}$	5.777	—	4.2 to 120 °K 2.19 BM	—	—	—	—	—	130 °K
UAs$_{0.69}$Se$_{0.31}$	5.778	—	4.2 to 113 °K 2.25 BM	60 to 137 °K	traces	—	—	—	135 °K
UAs$_{0.67}$Se$_{0.33}$	5.775	—	4.2 to 90 °K	—	4.2 to 136 °K	—	—	—	134 °K
UAs$_{0.63}$Se$_{0.37}$	5.776	—	—	—	4.2 to 138 °K	4.2 to 131 °K	—	—	134 °K
UAs$_{0.59}$Se$_{0.41}$	5.776	—	—	—	—	traces	4.2 to 135 °K	—	138 °K
UAs$_{0.50}$Se$_{0.50}$	5.779	—	—	—	—	—	4.2 to 134 °K	4.2 to 146 °K	150 °K
UAs$_{0.45}$Se$_{0.55}$	5.775	—	—	—	—	—	traces	4.2 to 175 °K	165 °K
UAs$_{0.40}$Se$_{0.60}$	5.776	—	—	—	—	—	—	4.2 to 170 °K	170 °K

Table 5. Crystal and magnetic data of the $UP_{1-x}Se_x$ system. After ref. 252.

composition $x \pm 0.02$	lattice constant ± 0.001	magnetic structure	ordered magnetic moment at 4.2 K (μ_B)	T_N, T_C (K)	moment-change temperature T_e (K)
0.05	5.591	SF type I	1.93 ± 0.05 1.71 ± 0.05 at 82 K	121 ± 3	24 ± 2
0.10	5.602	AF type IA	1.51 ± 0.05	97 ± 2	62 ± 3
0.20	5.620	AF type IA	1.56 ± 0.05	92 ± 3	55 ± 5
0.25	5.622	AF type IA	1.56 ± 0.05	93 ± 3	60 ± 3
0.30	5.633	AF type IA	1.46 ± 0.05	90 ± 3	60 ± 3
0.33	5.640	AF type IA	1.34 ± 0.05	87 ± 3	60 ± 3
0.37	5.645	F	1.4 ± 0.1	113 ± 3	-
0.40	5.630	F	1.2 ± 0.1	125 ± 3	-

Table 6. Values of the tricritical exponents reported for $FeCl_2$, DAG and $CsCoCl_3 \cdot 2H_2O$. Also given for comparison are the theoretically predicted values.

	β_+	β_-	$\delta_\pm$	γ	β^*	β_1	ϕ
$FeCl_2$ (ref. 72, 254)	1	0.36 ±0.04			0.37± 0.03	0.19± 0.02	
$FeCl_2$ (ref. 255, 67)	1.03± 0.05	1.13± 0.14					
DAG (ref. 256, 257, 259)	1	1	2.1± 0.2	1.01 ±0.07			1.95± 0.11
$CsCoCl_3 2(D_2O)$ (ref. 260)	0.65± 0.2	0.65 ±0.2	3 ± 1	1.3	0.36± 0.05	0.15± 0.02	
Theory (see section II)	1	1	2	1	1/2	1/2	2
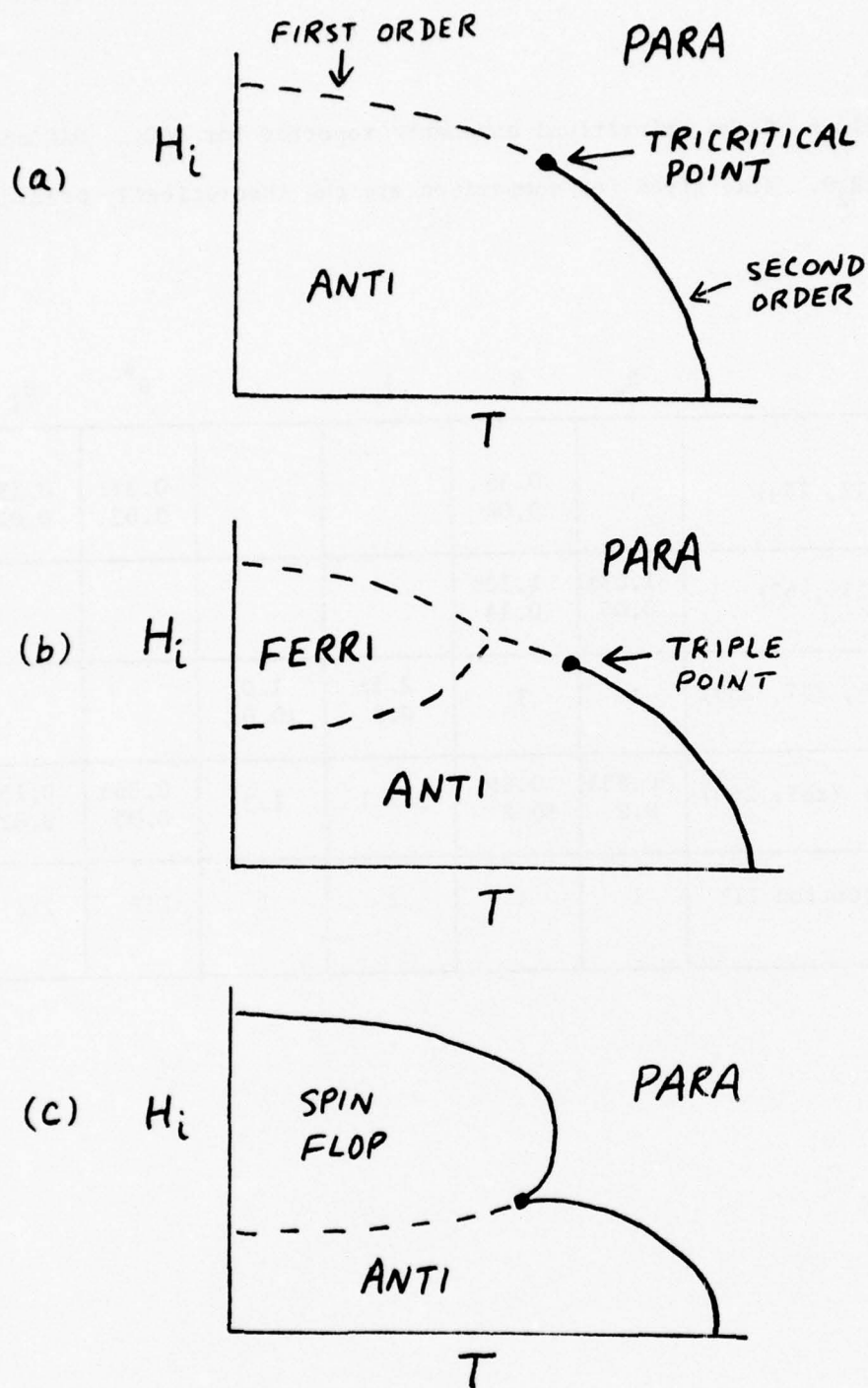
Fig. 1. a) Schematic phase diagram for $FeCl_2$ and $DyPO_4$. Anti and Para denote the antiferromagnetic and paramagnetic phases respectively. H_i is the internal field and T is the temperature. The solid (dashed) lines indicate second (first) order transitions. b) Schematic phase diagram of $CoCl_2 \cdot 2H_2O$ and $FeCl_2 \cdot 2H_2O$. Ferri denotes the ferrimagnetic phase. The order of the transition near the triple point is not known. c) Schematic phase diagram of MnF_2 and $GdAlO_3$.
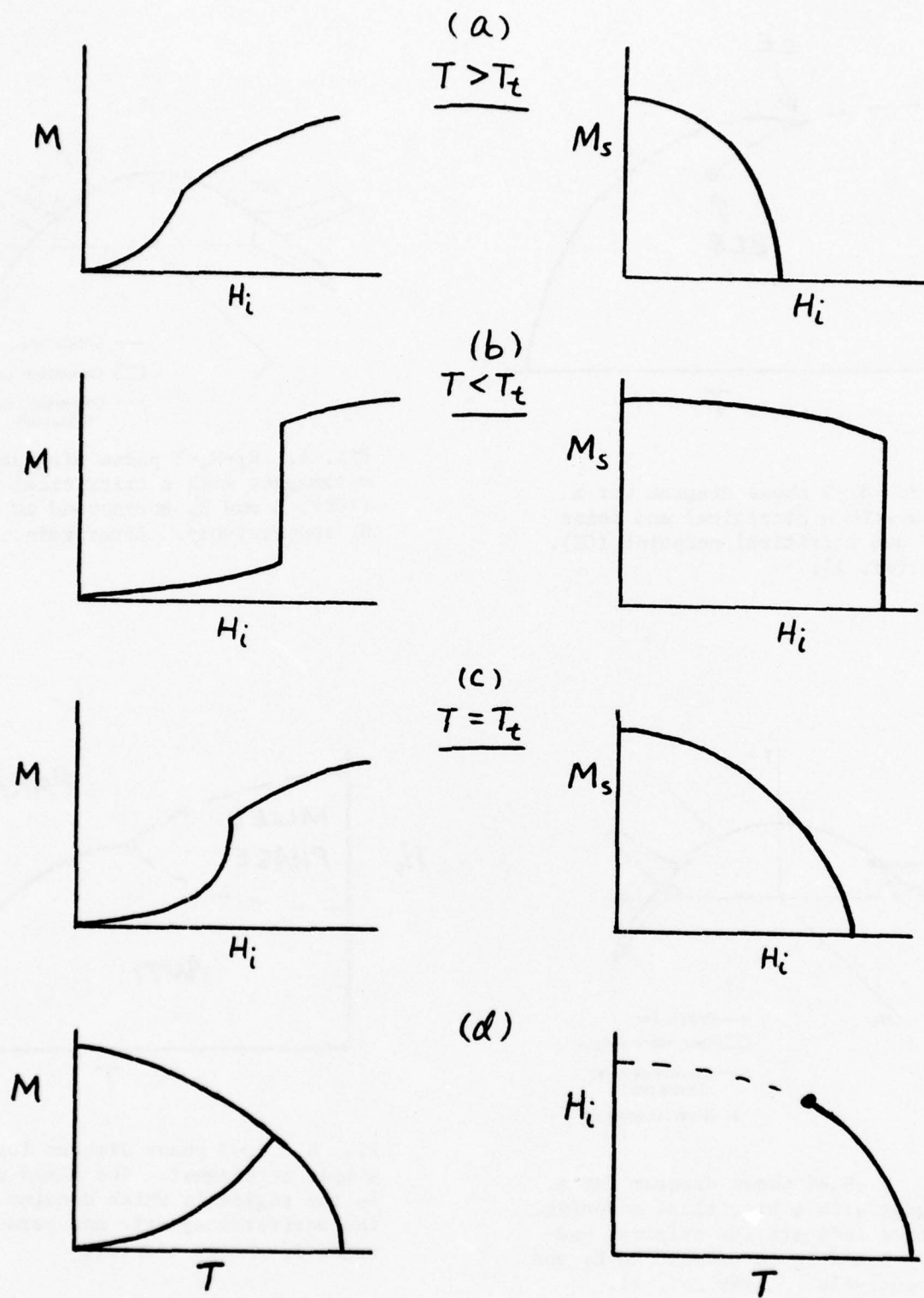
Fig. 2. Schematic behavior of M and M_S for a simple metamagnet. Also shown are the M-T and H_i-T phase diagrams.
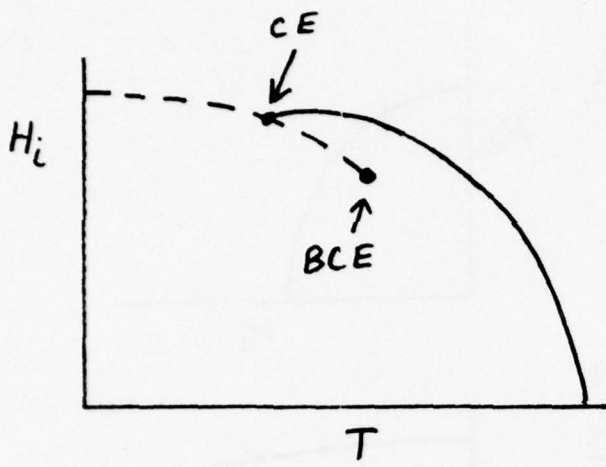
Fig. 3. H_i-T phase diagram for a
system with a bicritical end point
(BCE) and a critical endpoint (CE).
After ref. 11.
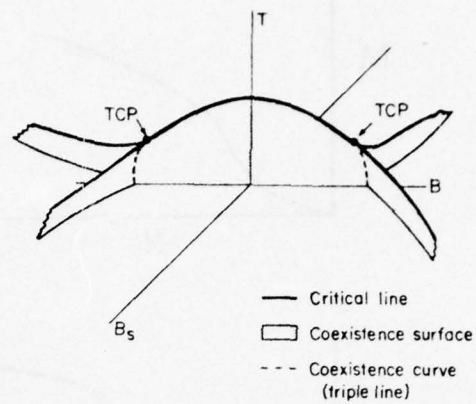
Fig. 4. H_i-H_s-T phase diagram for a
metamagnet with a tricritical point
(TCP). B and B_s correspond to H_i and
H_s respectively. After refs. 5 and 11.
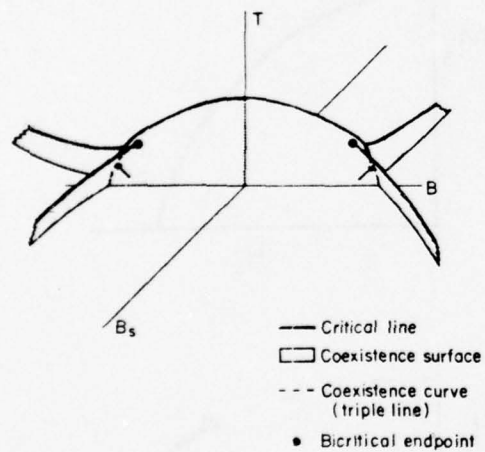
Fig. 5. H_i-H_s-T phase diagram for a
metamagnet with a bicritical endpoint.
The arrows indicate the critical end-
points. B and B_s correspond to H_i and
H_s respectively. After ref. 11.
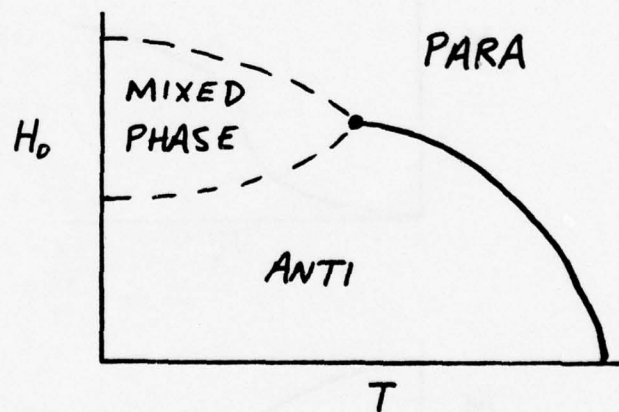
Fig. 6. H_o-T phase diagram for a
simple metamagnet. The mixed phase
is the region in which domains of
the antiferromagnetic and para-
magnetic phases coexist.
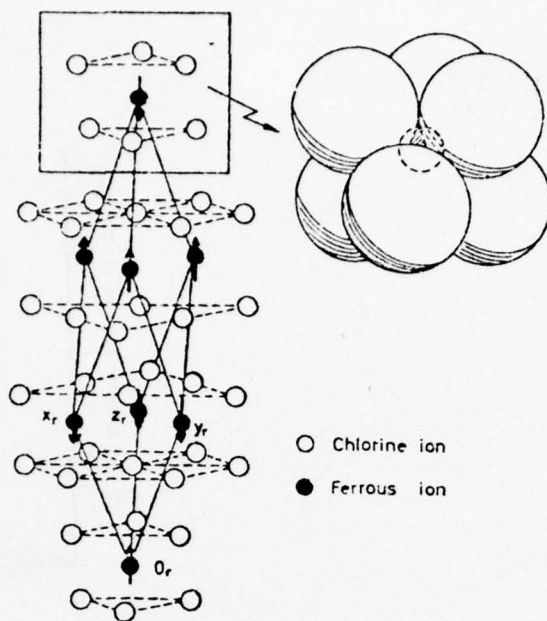
Fig. 7. Crystal and magnetic structure of $FeCl_2$. O_r, X_r, Y_r and Z_r define the rhombohedral primitive axes. After ref. 57.
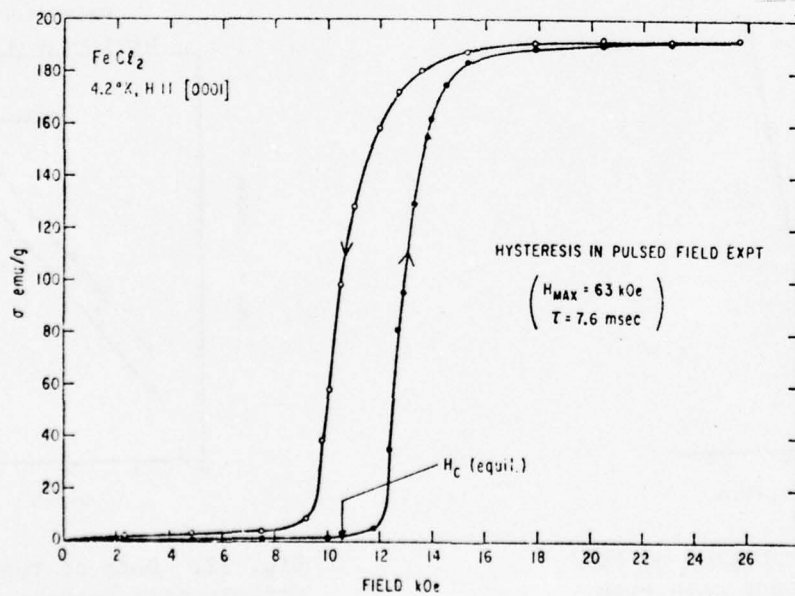
Fig. 8. Magnetization versus field at 4.2 K. Pulsed magnetic fields (H_{max} = 63 kOe, half period = 7.6 msec) and a single crystal of $FeCl_2$ ($H||[001]$) were used. After ref. 61.
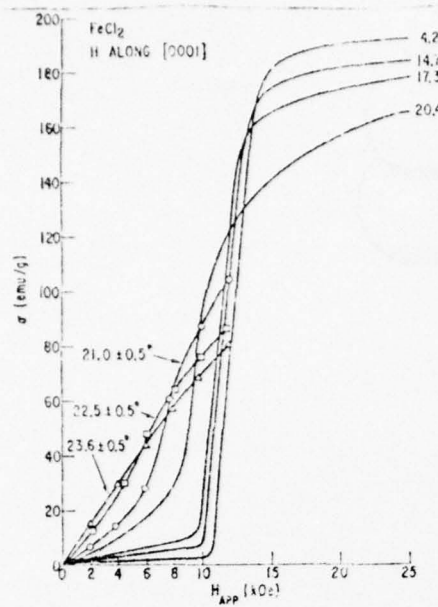
Fig. 9. Magnetization isotherms, σ versus H. A steady magnetic field ($H || [0001]$) and a single crystal of $FeCl_2$ were used. After ref. 61.
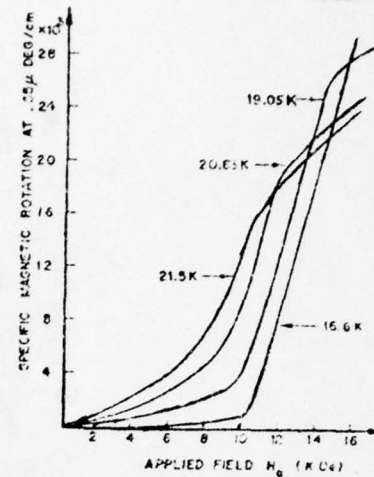
Fig. 10. Isotherms of Faraday rotation of $FeCl_2$ versus applied magnetic field. After ref. 63.
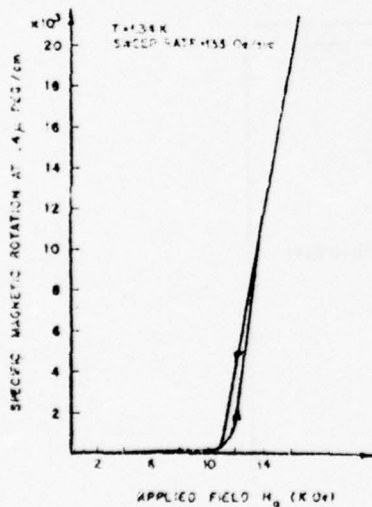
Fig. 11. Faraday rotation of $FeCl_2$ at a fixed temperature with both increasing and decreasing applied magnetic fields. T = 1.34 K. Sweep rate of applied field = 133 Oe/sec. After ref. 63.
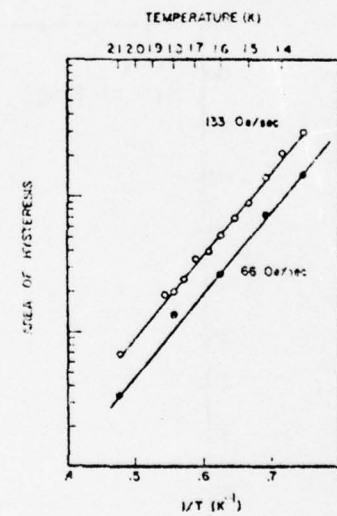
Fig. 12. Data on the area of the metamagnetic hysteresis of $FeCl_2$ at several temperatures plotted to show the logarithmic dependence on 1/T. After ref. 63.
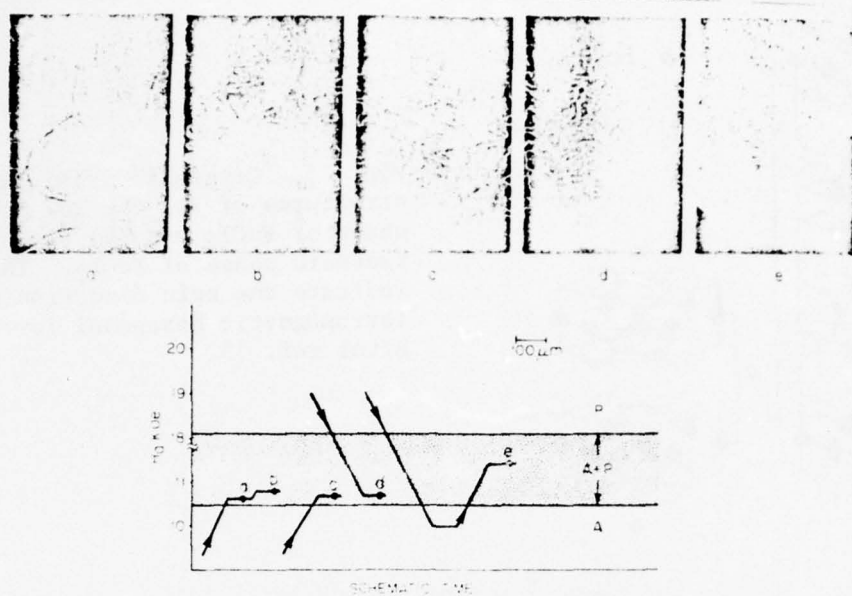
Fig. 13. Photomicrographs taken in a polarizing microscope of the mixed A-P phase of thin $FeCl_2$ sheets. Field treatments are shown schematically above. (a) Simple ribbons of paramagnetic material seen on very gentle first entry into A-P 1.3 K, 10.673 kOe. (b) A severely convoluted ribbon which developed from (a) on increase of field. 1.3 K, 10.821 kOe. (c) Extensively branched ribbon structure seen in increasing field, 2.1 K, 10.753 kOe. (d) Disconnected structure in the same sample at about the same field, but in decreasing field, 2.1 K, 10.745 kOe. (f) A portion of a "mixed phase platelet" observed after crystal had been saturated, 1.3 K, 11.408 kOe. After ref. 64.
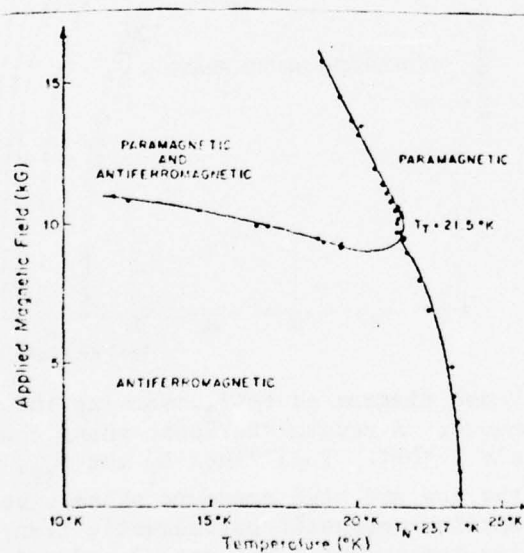
Fig. 14. Magnetic-phase diagram of $FeCl_2$, obtained from optical measurements. After ref. 66.
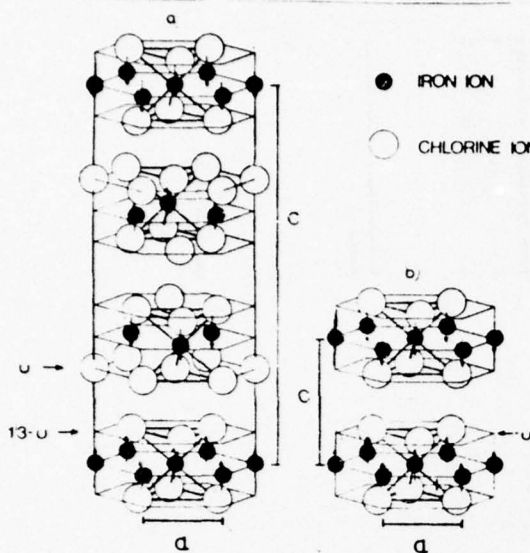
Fig. 15. Crystallographic and magnetic structures of (a) the low pressure phase of $FeCl_2$ and (b) the high pressure phase of $FeCl_2$. The arrows indicate the spin direction of the ferromagnetic hexagonal layers. After ref. 75.
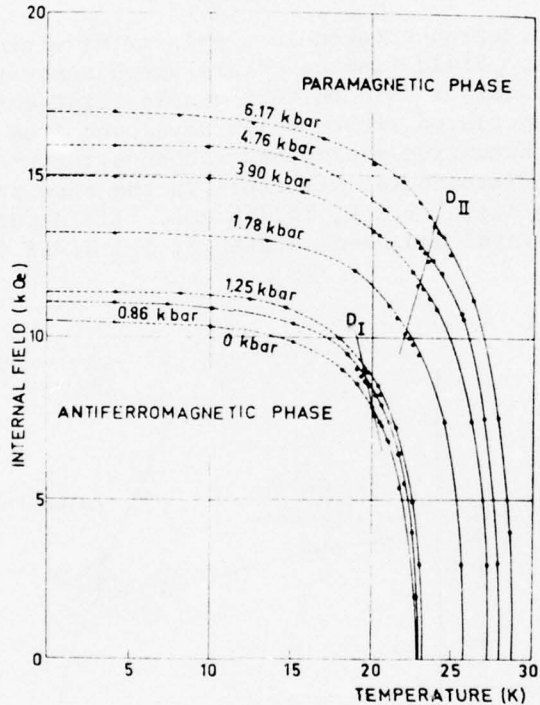
Fig. 16. Phase diagram of $FeCl_2$, showing the effect of hydrostatic pressure. A crystallographic phase change occurs at approximately 2 kbar. Full lines D_I and D_{II}, which are associated with the low and high pressure phases, separate regions where the antiferromagnetic-paramagnetic transition is of first order (at low temperature) and second order (at high temperature). After ref. 73.
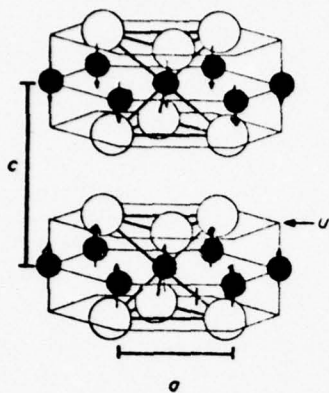
Fig. 17. The crystallographic and magnetic structures of FeBr$_2$. Layers of ferrous ions are sandwiched between layers of bromine ion with distance μ. Magnetic moments are parallel within layers and antiparallel between layers. After ref. 88.
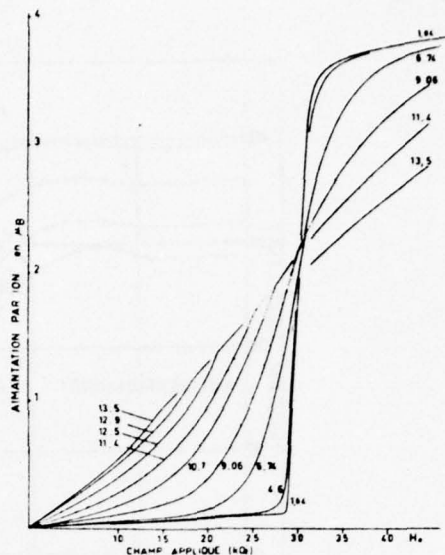
Fig. 18. Magnetization isotherms of FeBr$_2$ for $T_{tri} < T < T_N$. After ref. 82.
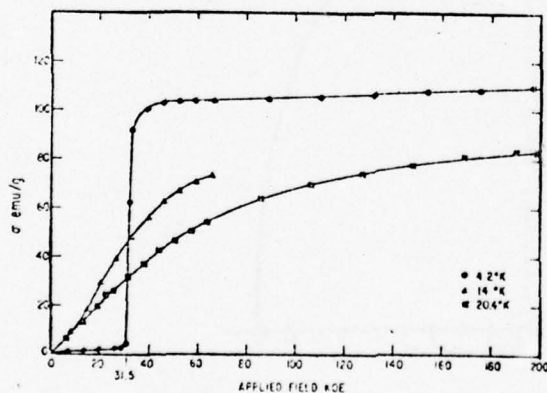
Fig. 19. High field magnetization of a single crystal of FeBr$_2$ along the c axis at three different temperatures. After ref. 85.
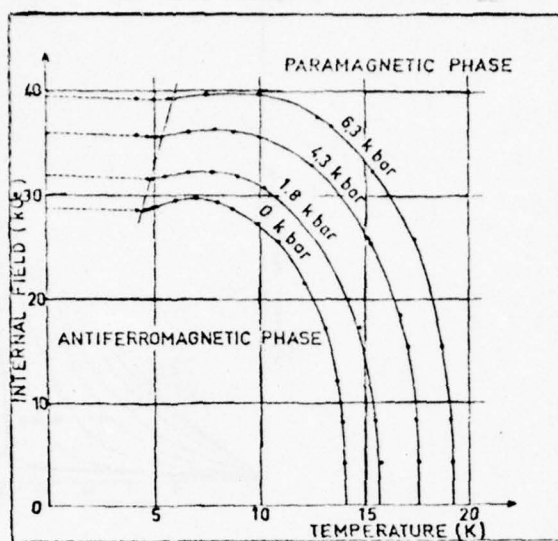
Fig. 20. Magnetic phase diagrams of FeBr$_2$, showing the dependance of the phase boundary on hydrostatic pressure. Full straight line separates regions where the metamagnetic transition is first order (at low temperature) and second order (at high temperature). After ref. 73.
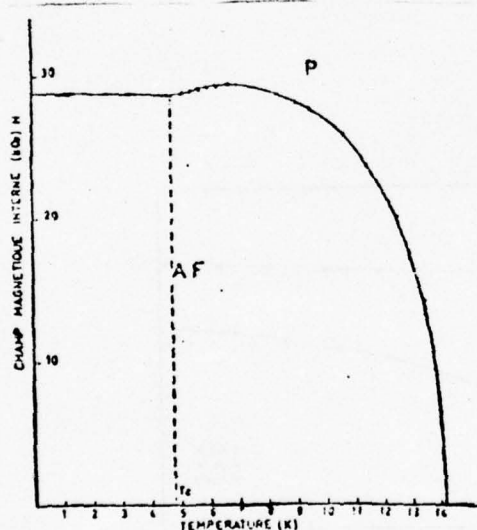
Fig. 21. Magnetic phase diagram of FeBr$_2$. The dotted line intersects the horizontal axis at the tricritical point. After ref. 82.
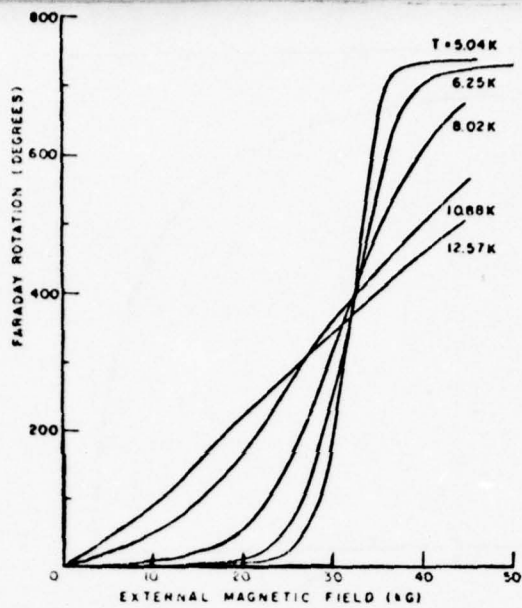
Fig. 22. Faraday rotation of FeBr$_2$ at $\lambda = 632.8$ nm versus applied magnetic field for temperatures 5 K < T < 12.6 K. After ref. 89.
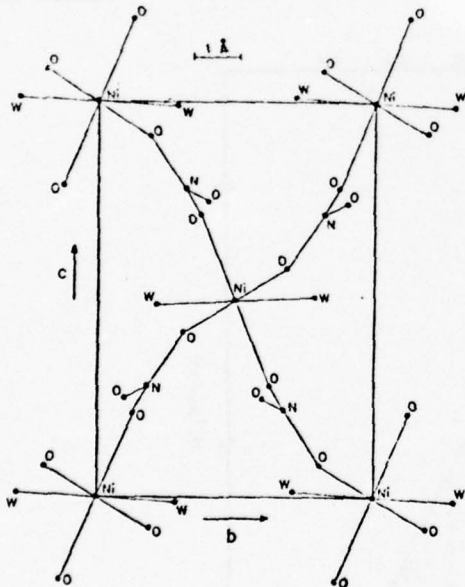
Fig. 23. Projection of the unit cell of nickel nitrate dihydrate on the bc plane. The nickel ions form a face-centered pattern. The symbol W is used to describe a water molecule. After ref. 90.
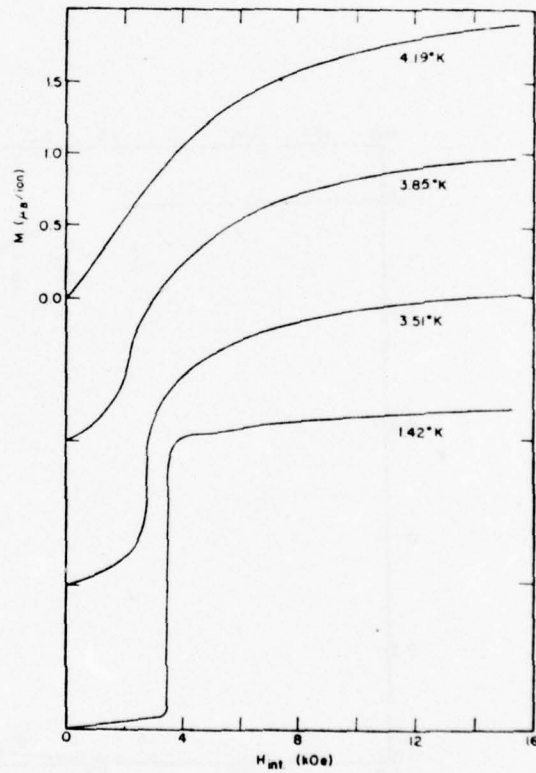
Fig. 24. Typical magnetization isotherms of Ni(NO$_3$)$_2$·2H$_2$O with the magnetic field applied along the a-axis. Note that the curves are displaced vertically and that all are drawn to the same scale. After ref. 91.
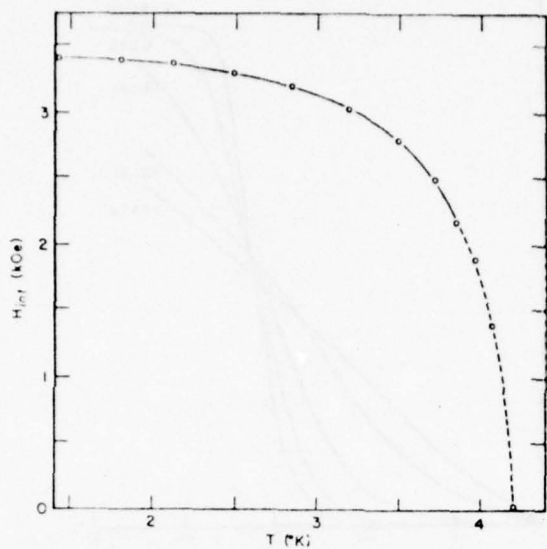
Fig. 25. Experimental (H,T) phase
diagram for $Ni(NO_3)_2 \cdot 2H_2O$ with
$H||$z-axis. After ref. 91.
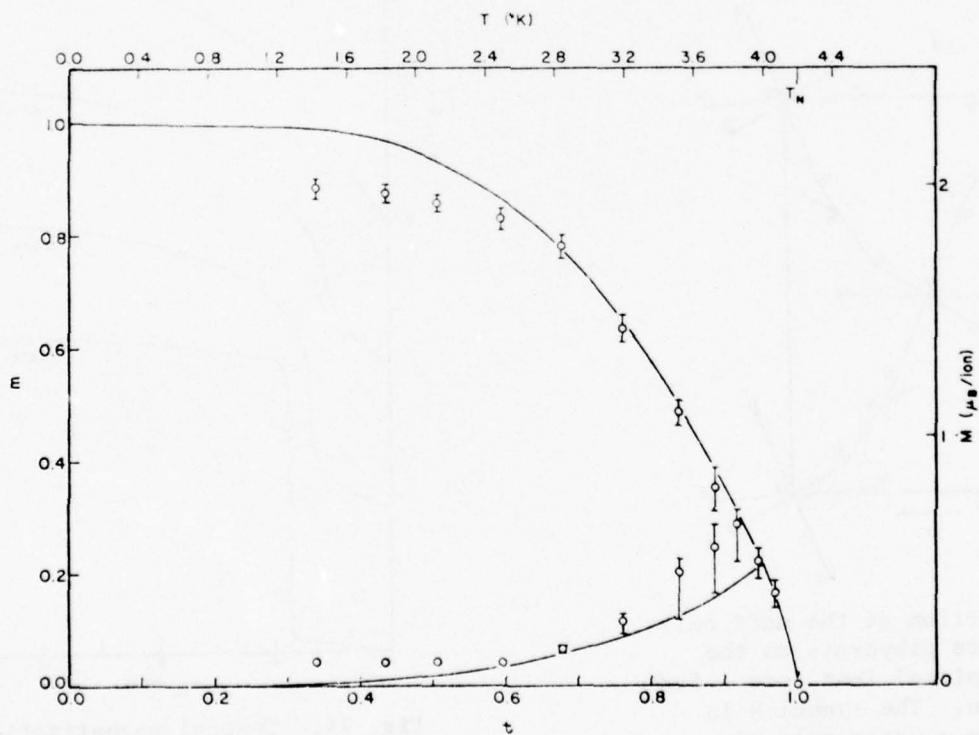
Fig. 26. M, T (m,t) phase diagram for $Ni(NO_3)_2 \cdot 2H_2O$ with $H||$ a axis. m = M/Mo and
t = T/T_N. The solid curves are calculated from a mean field model described in ref.
91. After ref. 91.
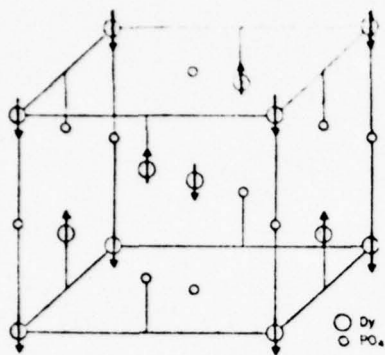
Fig. 27. Antiferromagnetic state of DyPO$_4$. After ref. 93.
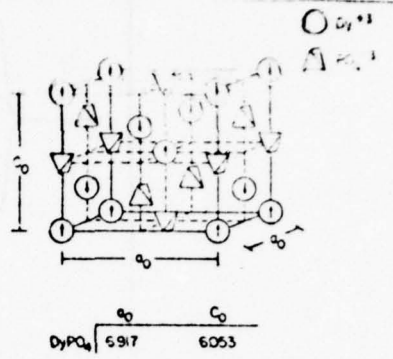
Fig. 28. Unit cell and lattice parameters of DyPO$_4$. The arrows in the circles indicate the ordered magnetic state of DyPO$_4$. The nearest neighbors of the central Dy^{3+} ion are the four Dy^{3+} ions lying on the faces of the unit cell. After ref. 100.
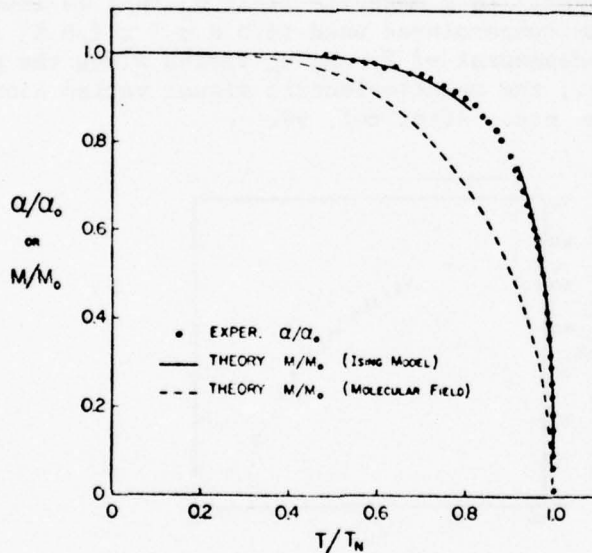
Fig. 29. Comparison of the temperature dependence of α/α_o (reduced magnetoelectric susceptibility) of DyPO$_4$ with the temperature dependences of the theoretical M/M_o (reduced magnetization) according to the mean field and Ising models. After ref. 97.
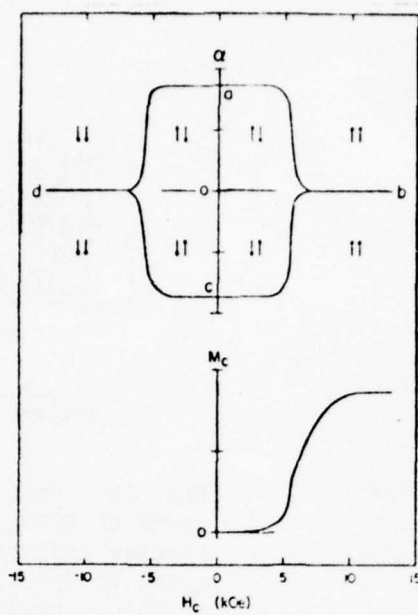
Fig. 30. Metamagnetic behavior in DyPO$_4$. Upper curve shows
the measured dependence of the magnetoelectric susceptibility
on static magnetic field H$_c$ (uncorrected for demagnetization
effects). The lower curve shows the measured magnetization
on the same crystal in a magnetic field H$_c$ applied along the
c axis. At the temperatures used (1.5 K $\leq$ T $\leq$ 1.6 K) α is
essentially independent of T. As H$_c$ varied along the path
o-b-o-d-o- etc., the magnetoelectric signal varied along the
path a-b-c-d-a- etc. After ref. 99.
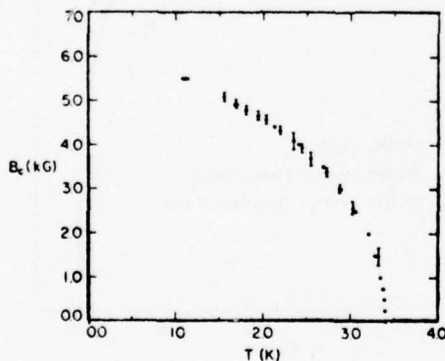
Fig. 31. Magnetic phase diagram of DyPO$_4$ at temperatures
above 1 K. The solid circles represent the data obtained by
locating the maximum in the heat capacity in a given field B.
The open circles represent the data obtained from the spectro-
scopic measurements. The vertical and horizontal lines rep-
resent the estimated error in the measurements. After ref. 100.
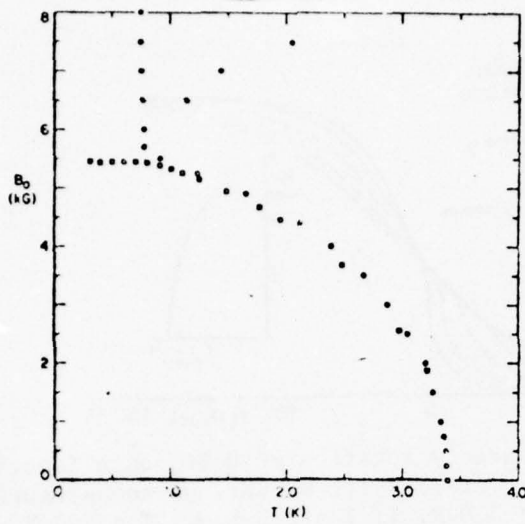
Fig. 32. Phase diagram of DyPO$_4$. The squares are obtained from
peaks in the susceptibility for a long needle, demagnetization
factor = D $\approx$ 0.02, and the circles are from maxima in the heat
capacity at constant applied field of a sample having D $\approx$ 1.
The locus of the Schottky maximum is also shown. After ref. 93.
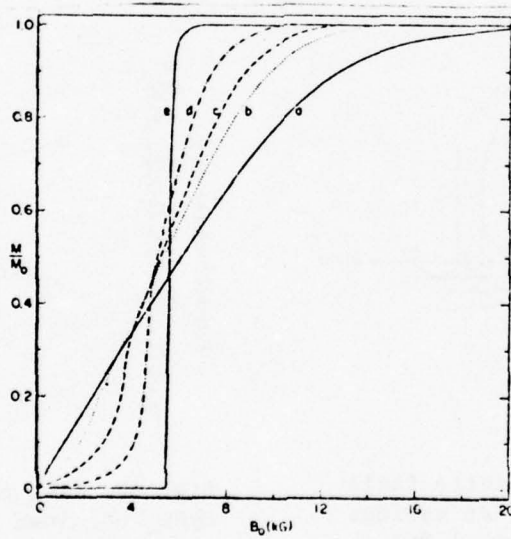
Fig. 33. Magnetization as a function of applied field at the
temperatures a, 4.20 K; b, 2.97 K; c, 2.48 K; d, 1.77 K; e,
0.498 K. After ref. 93.
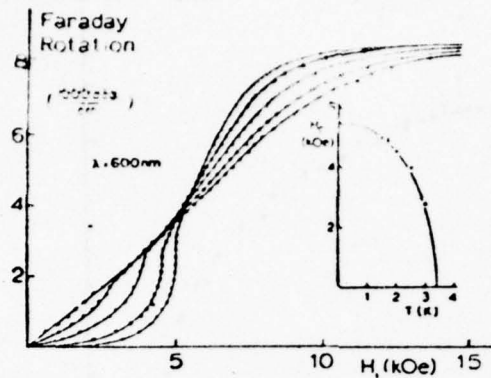
Fig. 34. Specific Faraday rotation of $DyPO_4$ as a function of
the internal magnetic field $H_i \| c$ at various temperatures:
o: T = 3.4 K, ●: T = 3.0 K, +: T = 2.5 K, ■: T = 2.0 K, x:
T = 1.5 K. The internal field was obtained by using an
approximate demagnetising factor $N_c/4\pi$ = 0.045. In the insert
the critical fields derived from these curves (dots) are
compared with the results of Koonce et al. (solid line).
After ref. 101.
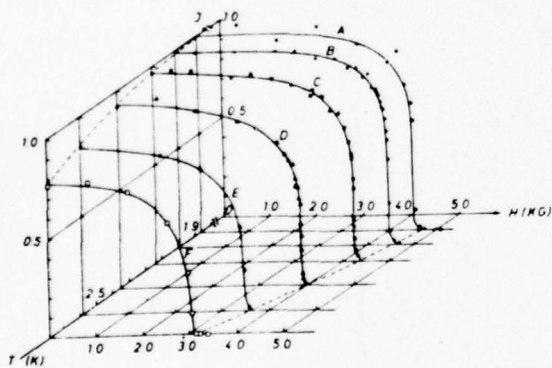
Fig. 35. Series of the magnetic field
dependent neutron intensity at various
fixed temperature points. A: 1.863 ±
0.001 K,....., F = 2.774 ± 0.005 K. After
ref. 94.   0.001
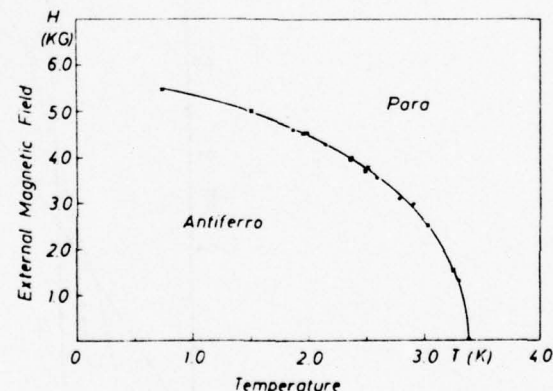
Fig. 36. The phase diagram of
$DyPO_4$ obtained from neutron diffrac-
tion. The closed circles are
obtained from the neutron results.
The crossed points are from the
magnetization measurements of Koonce
et al. The demagnetization factors
of the neutron diffraction and
magnetization samples were both ∿ 0.02.
After ref. 94.
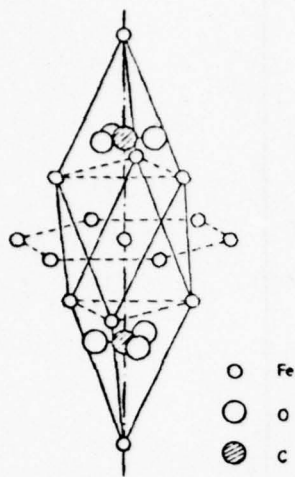
Fig. 37. Illustration of the crystal structure of $FeCO_3$. The vertical axis shown is the trigonal (C_3) axis and optic axis of the crystal. The central Fe^{2+} ion has six nearest neighbors, three in a plane above and three in a plane below as shown. The six-next-nearest neighbors lie in the plane containing the central ion. After ref. 103.

Fig. 38. Magnetization curves at 4.2 K for natural samples of $FeCO_3$. The curves a and b are calculated from a model described in ref. 107. After ref. 107.

Fig. 39. Dependence of the longitudinal magnetization of $FeCO_3$ on the intensity of a magnetic field directed along the axis of symmetry of the crystal. After ref. 108.
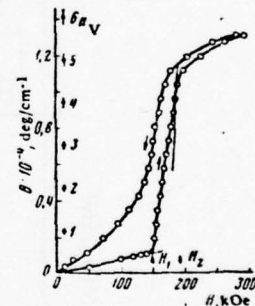
Fig. 40. Relationship between the rotation of the plane of polarization of light in siderite ($FeCO_3$) and the magnetic field applied to the sample. Sample temperature 24.5°K. After ref. 112.
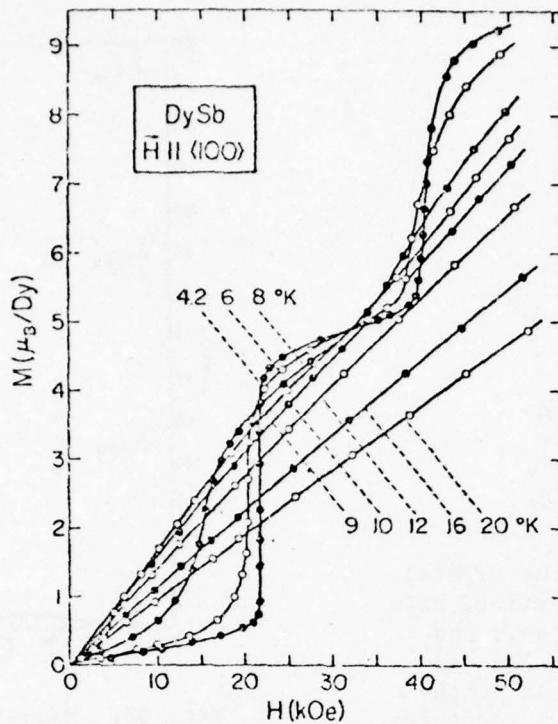
Fig. 41a. Magnetization isotherms of
DySb versus field applied along [100].
After ref. 117.
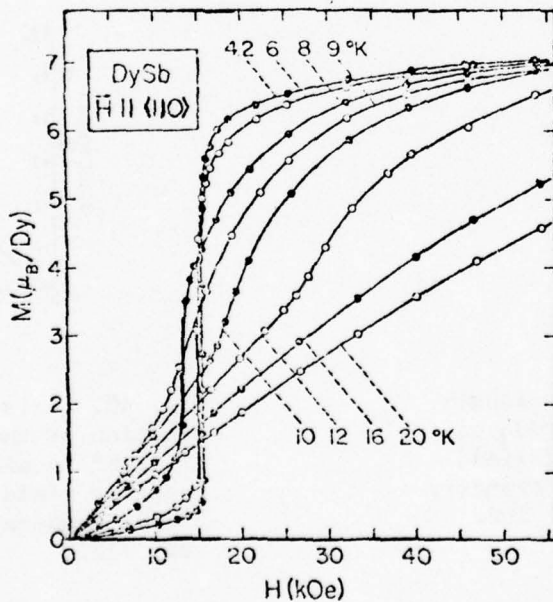
Fig. 41b. Magnetization isotherms of
DySb versus field applied along [110].
After ref. 117.
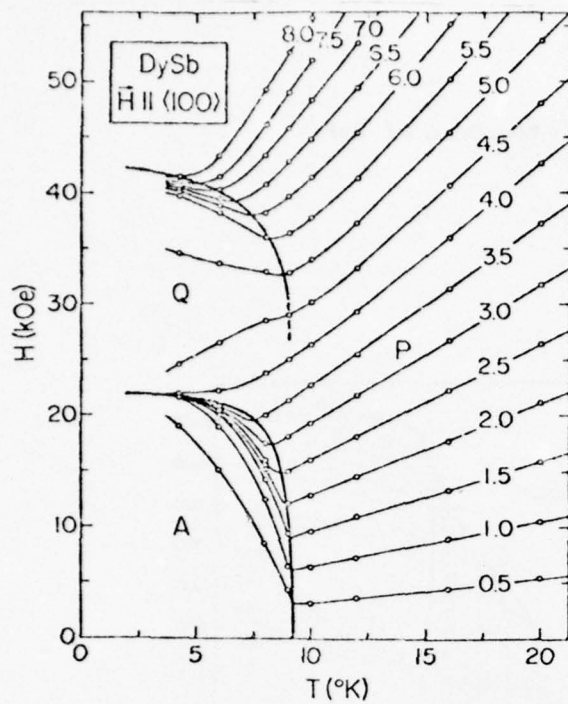
Fig. 42. Magnetic phase diagram of DySb for H‖[100]. Curves of constant magnetization (in μ_B/Dy ion) are also drawn. A denotes the antiferromagnetic state, P the paramagnetic state and Q the intermediate ferrimagnetic state. After ref. 117.
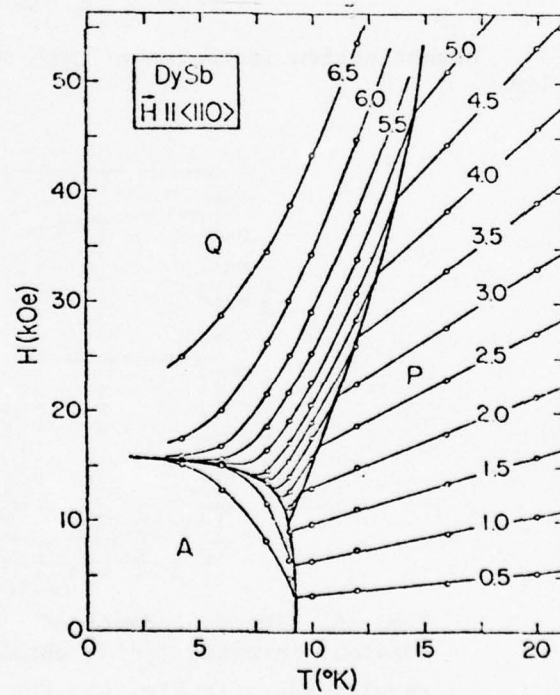
Fig. 43. Magnetic phase diagram of DySb for H‖[110]. Curves of constant magnetization (in μ_B/Dy ion) are also drawn. After ref. 117.
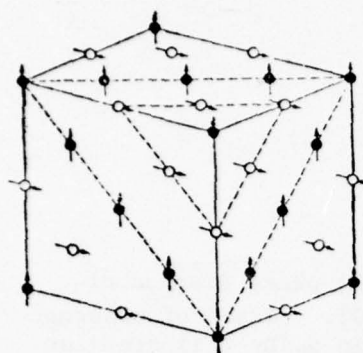
Fig. 44. Magnetic structure of HoP.
After ref. 108.
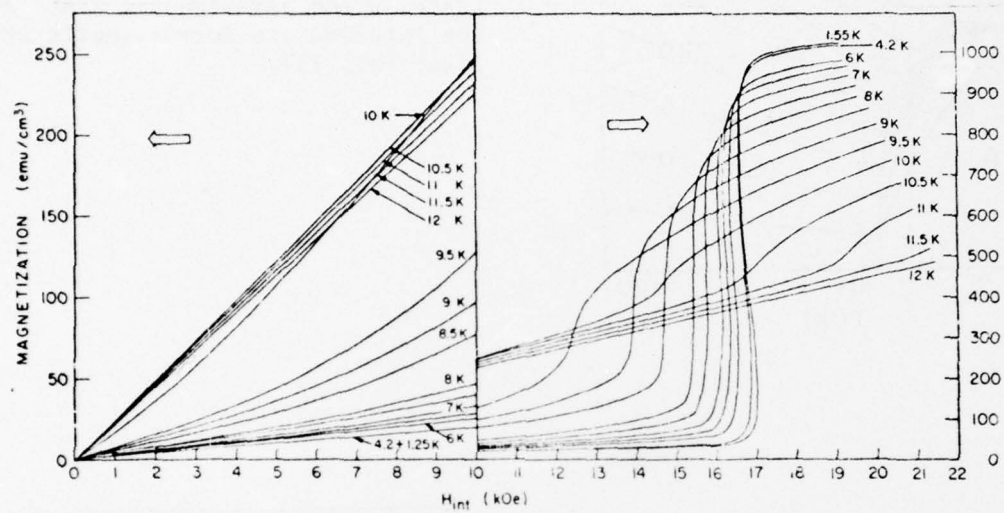
Fig. 45. Magnetization isotherms of DySb versus internal field. H||[110]. After
ref. 119.
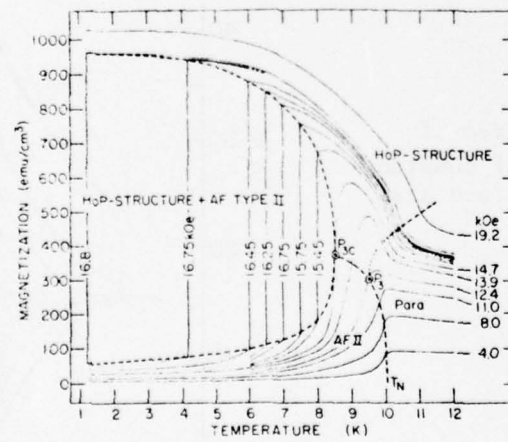
Fig. 46. The dependence of magnetization on temperature at
constant internal field, obtained by interpolation of the
results shown in Fig. 45. For temperatures less than that
of the tricritical point, P_{3c}, the dashed line represents
the coexistence region of the two phases associated with a
first order transition. After ref. 119.
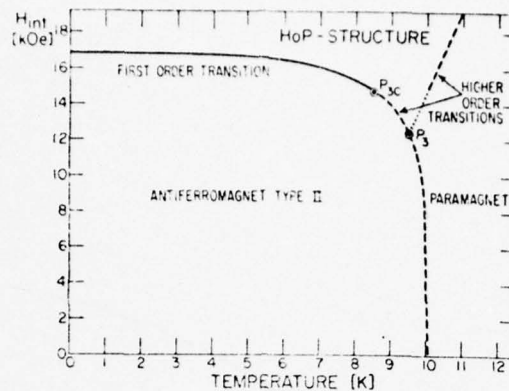
Fig. 47. The phase diagram of DySb determined for H in a (110) direction for applied fields H < 23.6 kOe. The line drawn from above T_N and ending at the triple point, P_3, has been dotted in the region where direct experimental corroboration is not presently available. After ref. 119.
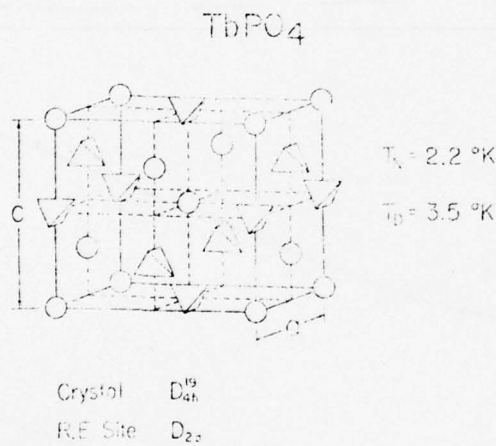
Fig. 48. High-temperature tetragonal-phase unit cell of $TbPO_4$. The tetra-hedra represent the $(PO_4)^{3.4}$ radicals; the spheres represent the Tb^{3+} ions. The Jahn-Teller distortion tempera-ture T_D and the Neel T_N are given along with the appropriate symmetry classes. After ref. 123.
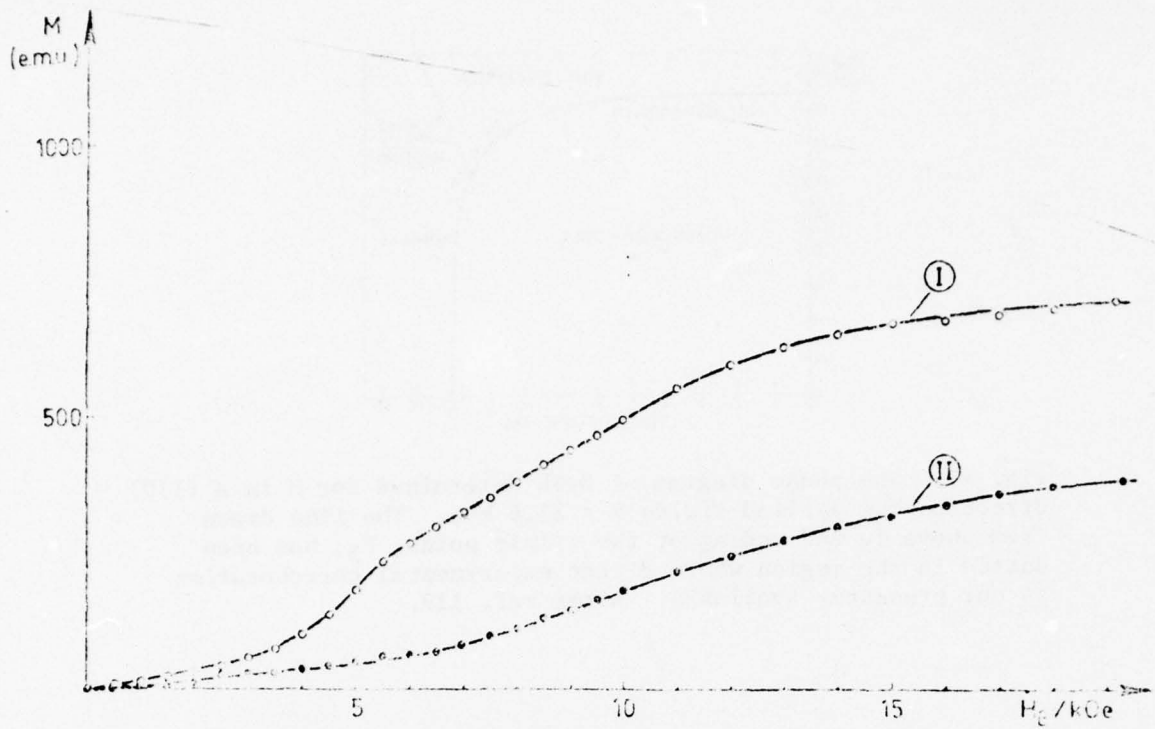
Fig. 49. Magnetization of TbPO$_4$ as a function of the external field H$_a$ at T = 1.4 K.
Curve I = Magnetization parallel to the c-axis. Curve II = Magnetization perpendicular
to the c-axis. After ref. 120.
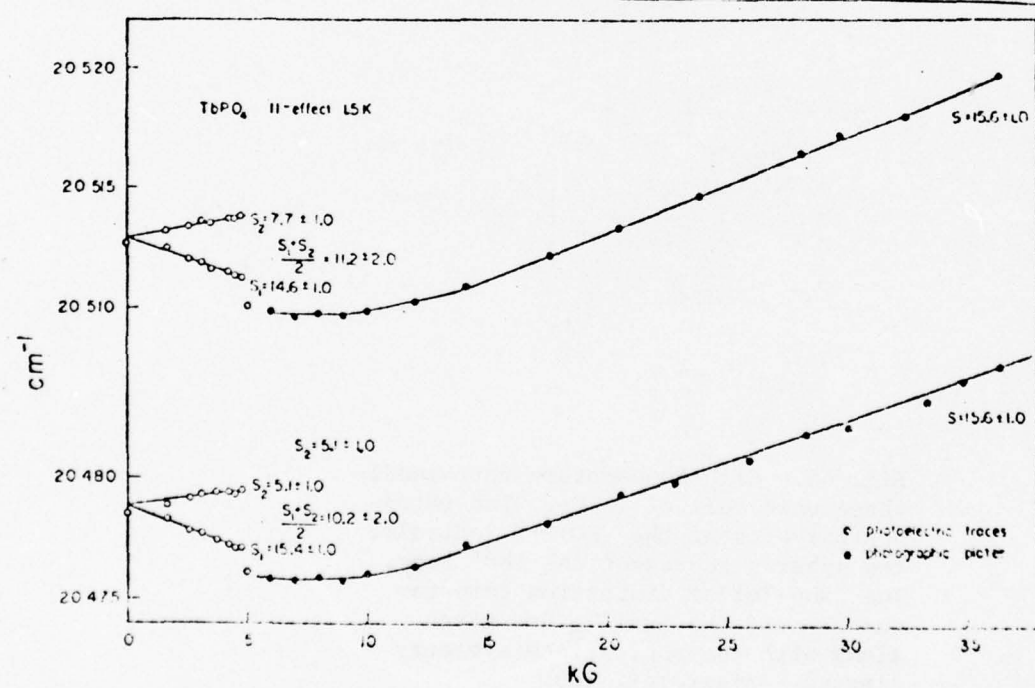
Fig. 50. Parallel Zeeman effect for optical transitions to $^5D_4$ in TbPO$_4$ at 1.5 K.
S denotes the splitting factor. After ref. 121.

(a)   (b)
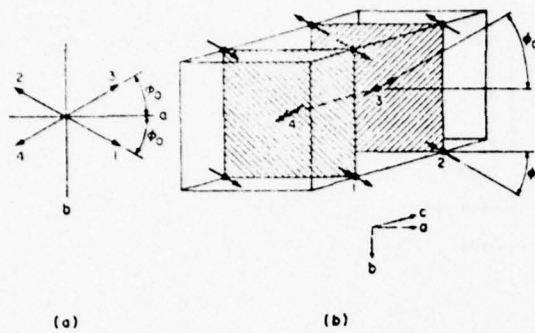
Fig. 51. Magnetic structure of anti-
ferromagnetic $TbAlO_3$; (a) four sub-
lattice model deduced from magnetiza-
tion data (ref. 131); (b) magnetic unit
cell (symmetry G_xA_y) from neutron dif-
fraction. Magnetic moments are
confined in planes at Z=1/4 and
Z=3/4. After ref. 127.

$\bigcirc$ Dy^{3-} $\bullet$ Al^{3-} $\alpha = 33.5°$
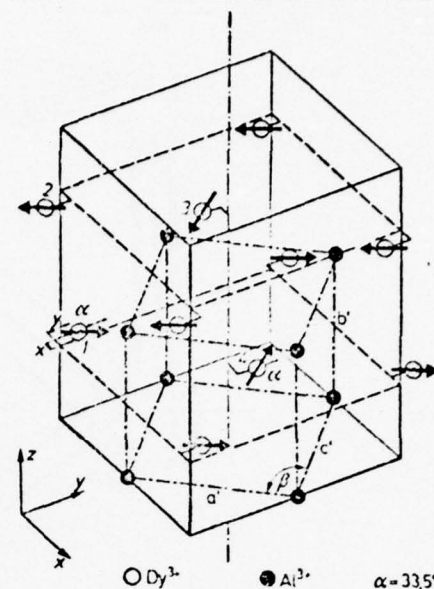
Fig. 52. Magnetic structure of $DyAlO_3$.
After ref. 128.

CRYSTAL   CRYSTAL FIELD
FIELD   +(n − n) INTERACTION
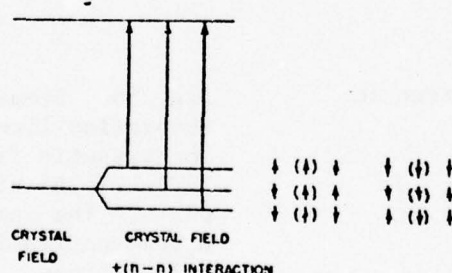
Fig. 53. Pseudo-energy-level diagram (energy-difference dia-
gram) showing the origin of the triplets. (↑) and (↓) designate
the spin of the ion under question, whereas ↑ and ↓ are the
spins of the neighboring ions along the a axis. Each level
of the ground state is still doubly degenerate [spin up (↑)
and spin down (↓)]; this degeneracy can be removed by an
external magnetic field. All excited states are singlets.
After ref. 127.
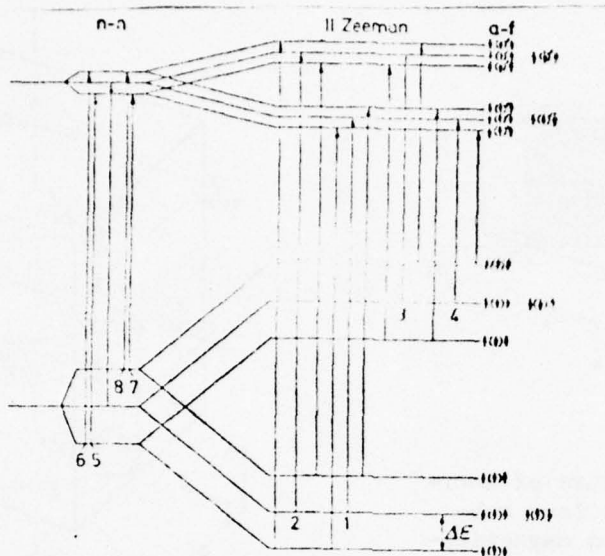
Fig. 54. Pseudo energy level diagram if a dysprosium ion (↑) or (↓) interacts with two neighbors ↑ or ↓. An antiferromagnetic coupling is assumed between the ions. After ref. 128.
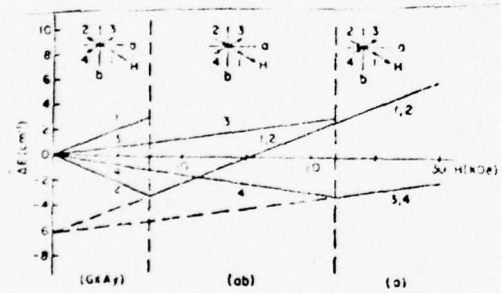
Fig. 55. Idealized Zeeman pattern in TbAlO₃. After ref. 127.
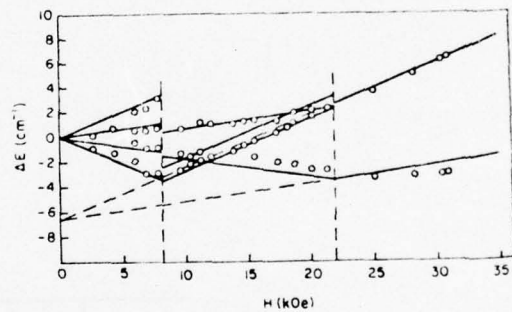
Fig. 56. Zeeman pattern of a typical absorption line of TbAlO₃ at 1.4 K. The magnetic field is directed at an angle of 35° off the a axis in the a-b plane. The sample is disk shaped with a demagnetization factor < 0.001. The solid curves are derived from mean field theory. After ref. 127.
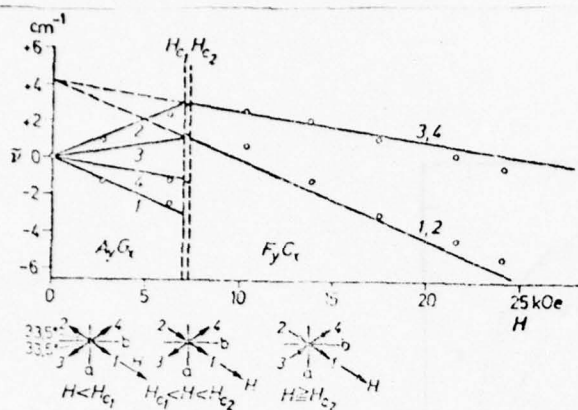
Fig. 57. Zeeman splitting of the groundstate of $DyAlO_3$ as a function of the externally applied magnetic field, $H||\mu_1$. The straight lines are calculated for $T = 0$ K as outlined for the magnetic structure G_xA_y. After ref. 128.
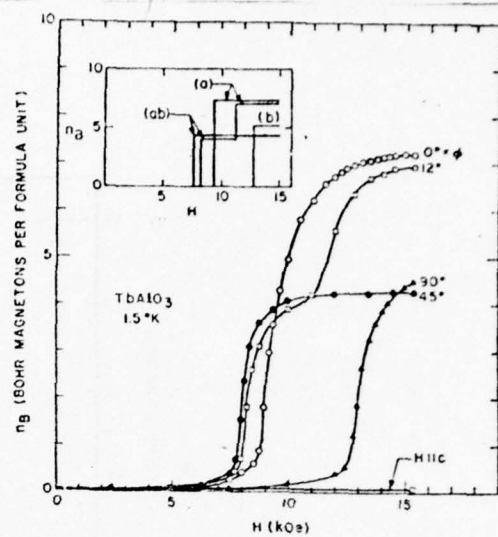
Fig. 58. Magnetization curves in a-b plane at 1.5°K for a disk-shaped sample. Inset shows idealized theory at $T = 0$ K. Labels (a), (ab) and (b) refer to magnetic configurations. ϕ is angle measured from a axis. After ref. 131.
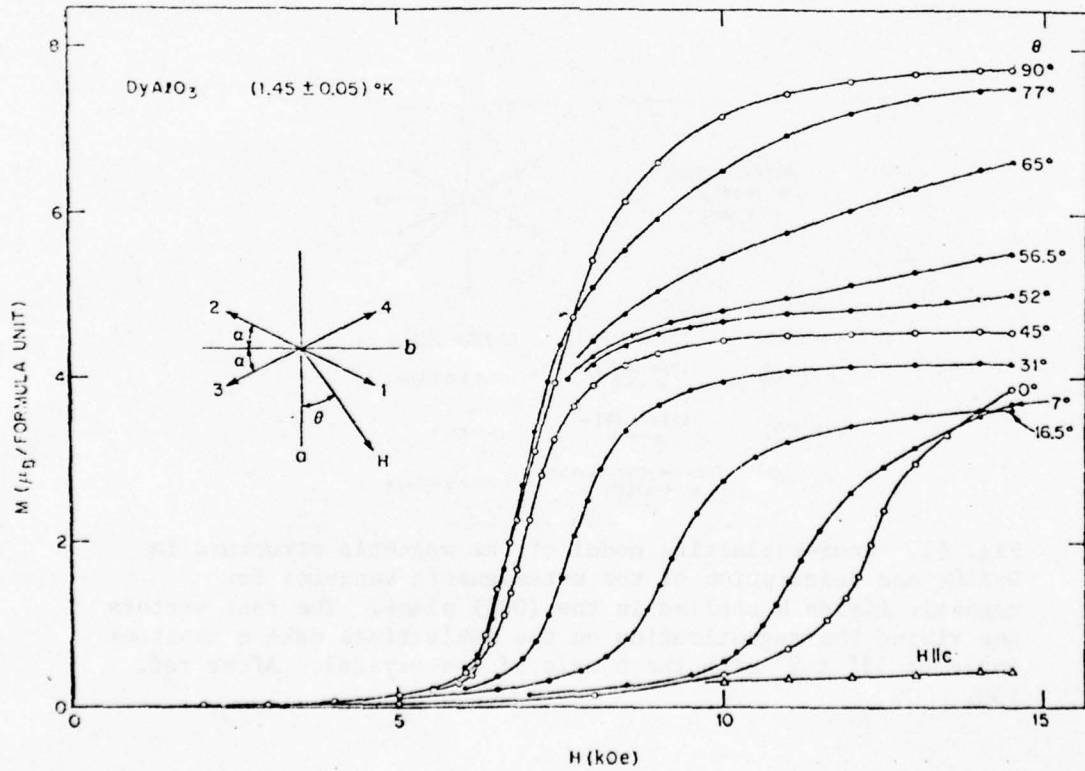
Fig. 59. Magnetization curves at (1.45 ± 0.05)°K in $DyAlO_3$. The angle θ (see insert) defines the orientation of the applied magnetic field $\vec{H}$ in the (001) plane relative to the a axis. After ref. 126.
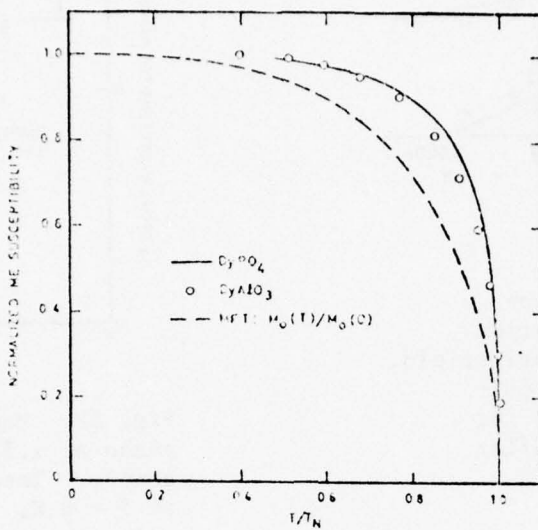
Fig. 60. Comparison of magnetoelectric data on two Ising-like materials. $DyPO_4$ (T_N = 3.39 K) smoothed data from ref. 97 and $DyAlO_3$ (T_N = 3.52 K) data from ref. 132. Dashed lines show sublattice magnetization from mean field theory, effective spin 1/2. After ref. 98.
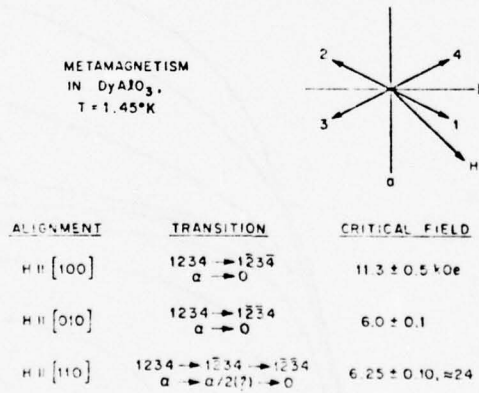
Fig. 61. Four-sublattice model of the magnetic structure in $DyAlO_3$ and description of the metamagnetic behavior for magnetic fields H applied in the (001) plane. The four vectors describing the magnetization on the sublattices make a constant angle of 33° ± 2° with the b axis of the crystal. After ref. 133.
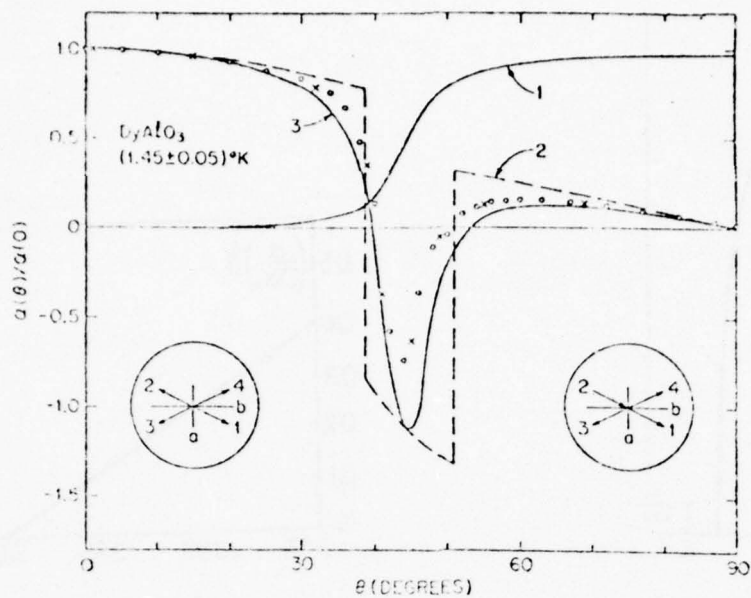
Fig. 62. ME data for rotation into the [110] direction in
DyAlO₃, with H_{dc} = 10 kOe. The circular points are for
increasing θ and the x-shaped points are for decreasing θ.
The insets show the arrangement of the four sublattices at
low θ and at high θ in H_{dc} = 10 kOe. The solid curve No. 1
is the normalized magnetization calculated from the data in
ref. 126. The theoretical curves Nos. 2 and 3 are described
in ref. 133. After ref. 133.
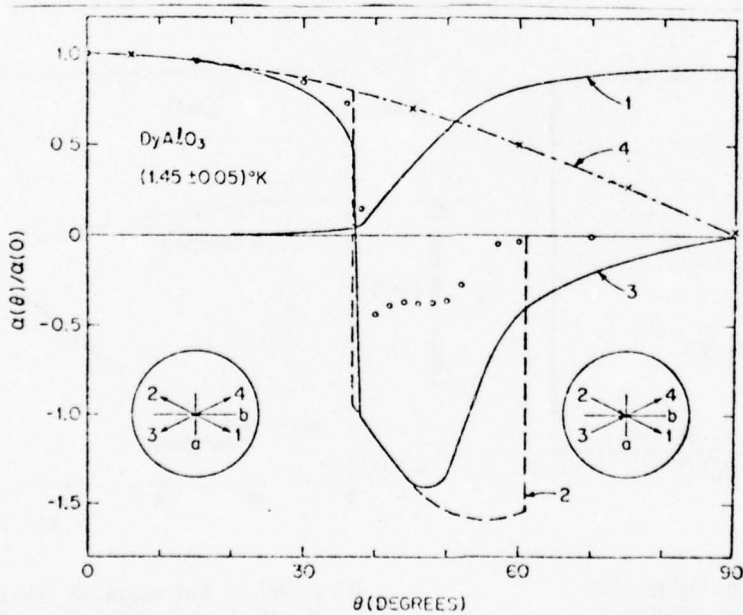
Fig. 63. ME data for rotation into the [010] direction in
DyAlO₃. The x-shaped points are for H_{dc} = 200 Oe. The
circular points are for H_{dc} = 10 kOe. The insets show the
arrangement of the four magnetic sublattices at low θ and at
high θ in H_{dc} = 10 kOe. The solid curve No. 1 is the normal-
ized magnetization calculated from the data in ref. 126.
The dot-dashed curve No. 4 is cos θ. A description of
theoretical curves Nos. 2 and 3 is given in ref. 133. After
ref. 133.
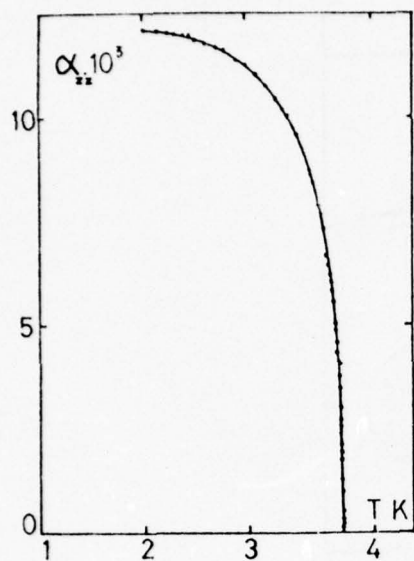
Fig. 64. Magnetoelectric suscepti-
bility of TbAlO$_3$ in an applied field
of 500 Oe. After ref. 134.
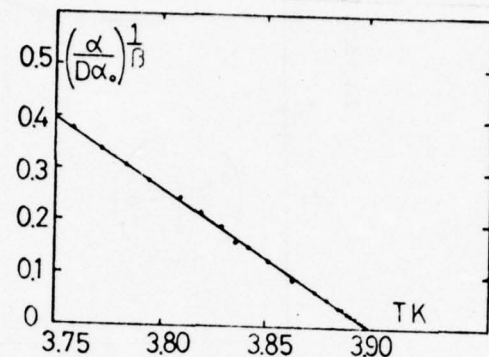
Fig. 65. Verification of the Ising
nature of TbAlO$_3$ by observation of
the temperature dependence of the
magnetoelectric susceptibility.
$\beta=0.32$. After ref. 134.
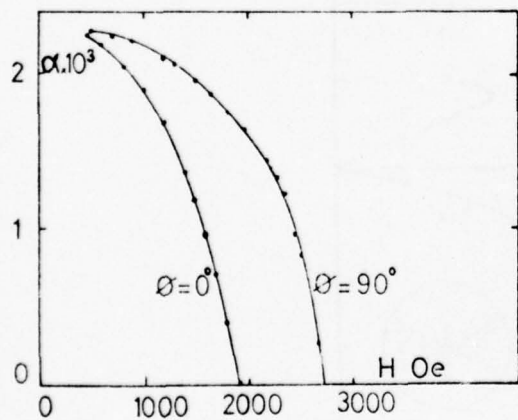
Fig. 66. Variation of the magneto-
electric susceptibility of TbAlO$_3$
with applied field with the field
applied along two different directions.
After ref. 134.
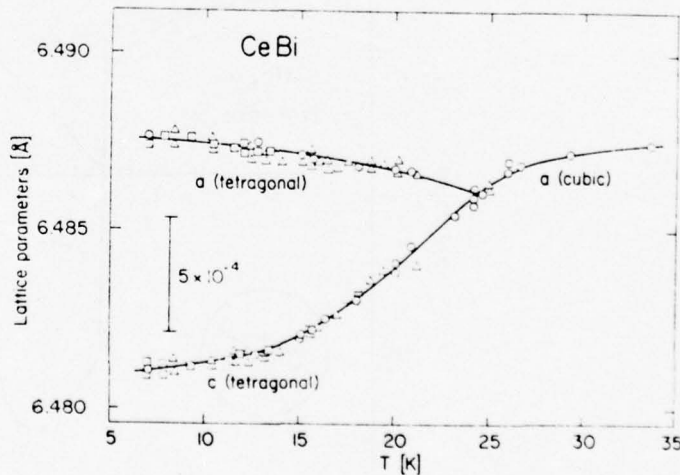
Fig. 67. Tetragonal distortion of the
rocksalt cell of CeBi below the Neel
temperature. After ref. 137.
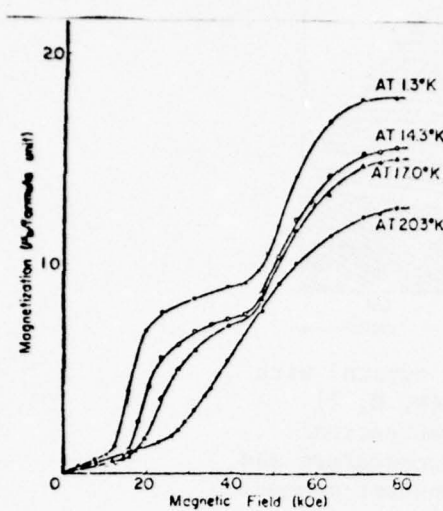
Fig. 68. Magnetization versus applied magnetic field for CeBi. After ref. 139.
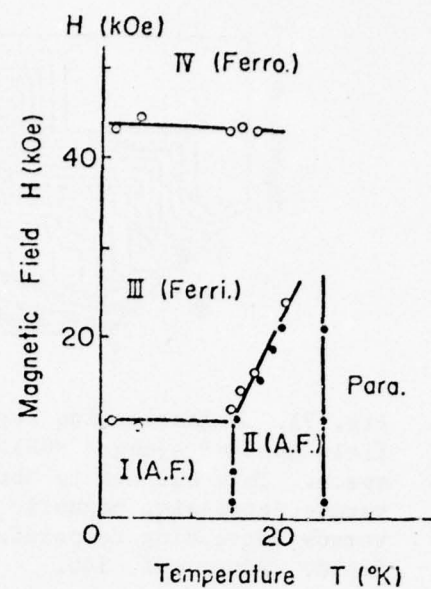
Fig. 69. Magnetic phase diagram of CeBi. ● – data from ref. 146. O – data from ref. 139. After ref. 139.
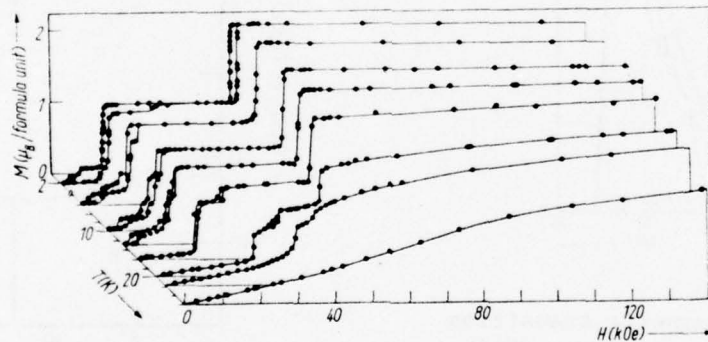
Fig. 70. Magnetization isotherms of CeBi. The magnetic field was applied along the [001] direction. The curves have been obtained in both increasing and decreasing field. After ref. 140.
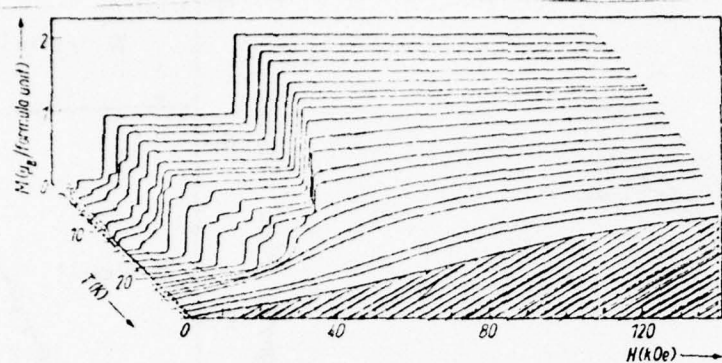
Fig. 71. Magnetization surface of CeBi single crystal with field applied along a <001> direction, in the (M, H, T) space. This surface is obtained from the magnetizations versus decreasing magnetic field at constant temperature and versus increasing temperature from 4.2 K at constant magnetic field. After ref. 140.
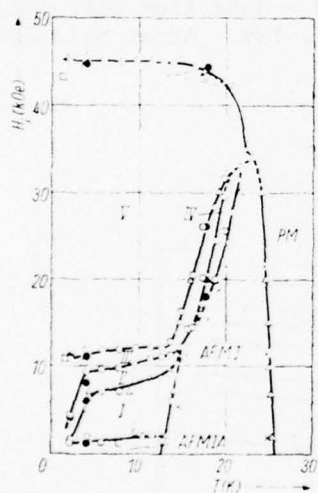
Fig. 72. Internal magnetic transition fields versus temperature for a <001> direction of CeBi. These transition fields are determined from the magnetization versus decerasing field curves at constant temperature (O sample 1; ● sample 2); from the magnetization versus increasing temperature at constant magnetic field (Δ sample 1); (X) the results of Tsuchida and Wallace (ref. 146) and (◻) the results of Tsuchida and Nakamura (ref. 139) obtained with polycrystals. After ref. 140.
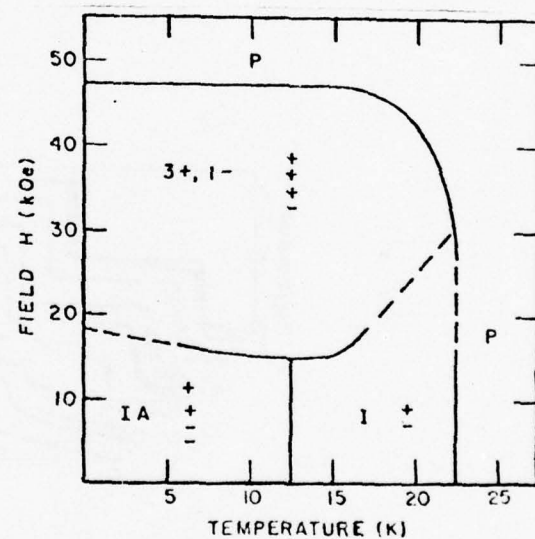
Fig. 73. Phase diagram of CeBi obtained from neutron diffraction measurements. The three magnetic phases are shown. After ref. 138.
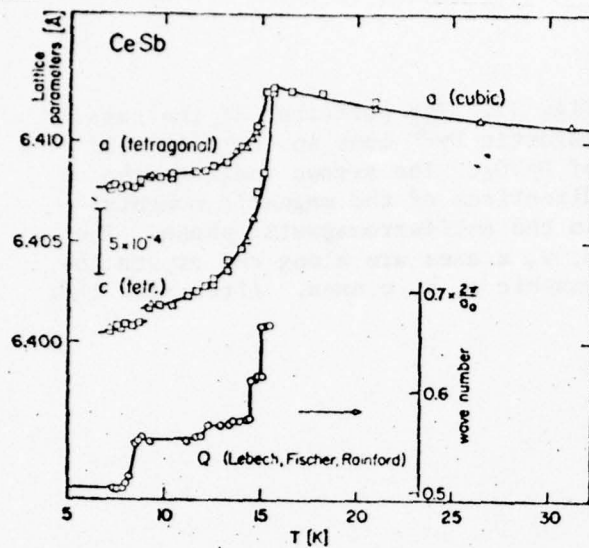
Fig. 74. Tetragonal distortion of the rocksalf cell of CeSb below the Neel temperature. The temperature dependence of the structure modulation vector Q is added to illustrate the correlation between both. After ref. 137.
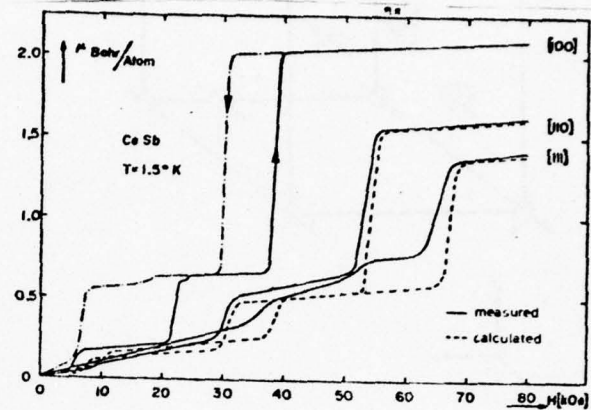
Fig. 75(a). Magnetic moments of CeSb at 1.5°K, measured in external fields along the [110] and [111] axis. After ref. 144.
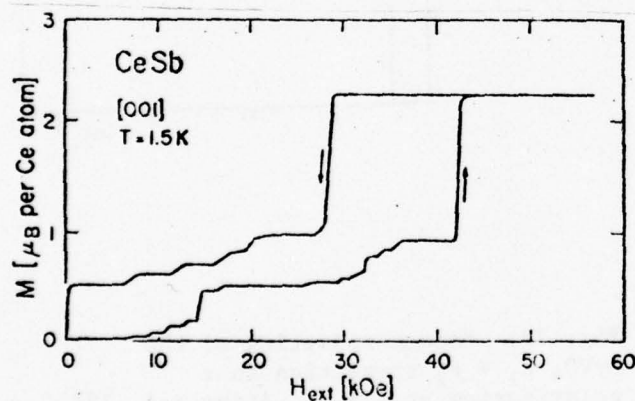
Fig. 76. Magnetization of a CeSb single crystal along [001] at 1.5 K in a pulsed magnetic field. After ref. 137.
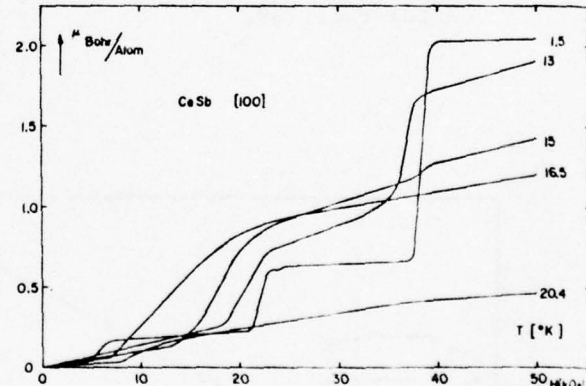
Fig. 75(b). Magnetic moments of CeSb in external fields along the [100] axis at different temperatures. After ref. 144.
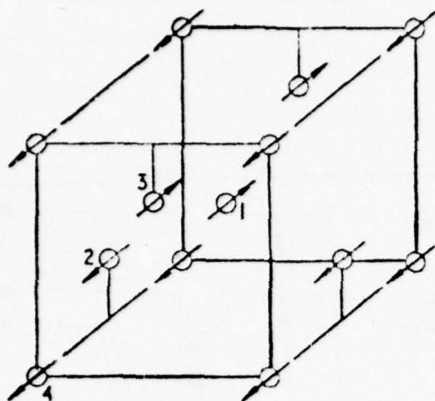
Fig. 77. The positions of the para-
magnetic Dy^{3+} ions in the unit cell
of $DyVO_4$. The arrows indicate the
directions of the magnetic moments
in the antiferromagnetic phase. The
x, y, z axes are along the crystallo-
graphic a, b, c axes. After ref. 148.

Fig. 78. The magnetisation of $DyVO_4$
as a function of the internal magnetic
field applied along the ordering
direction at a temperature of 0.5 K.
After ref. 149.
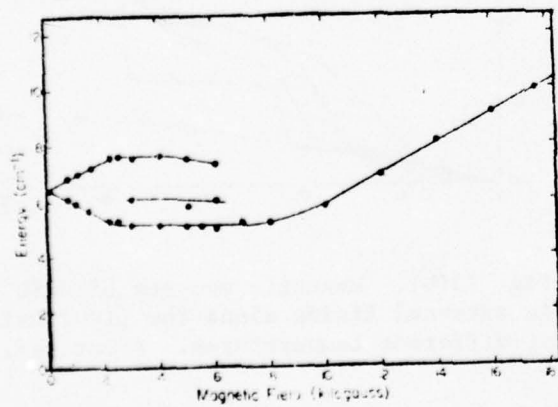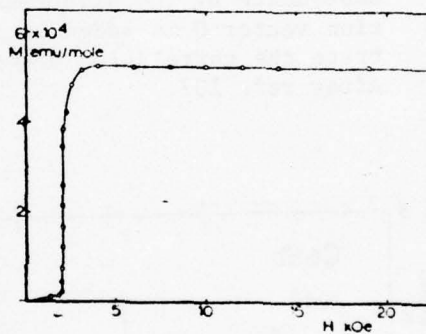
Fig. 79. Zeeman splitting of the
$DyVO_4$ $Z_1 \rightarrow F_1$ transition in π
polarization at 1.5 K. After ref. 154.
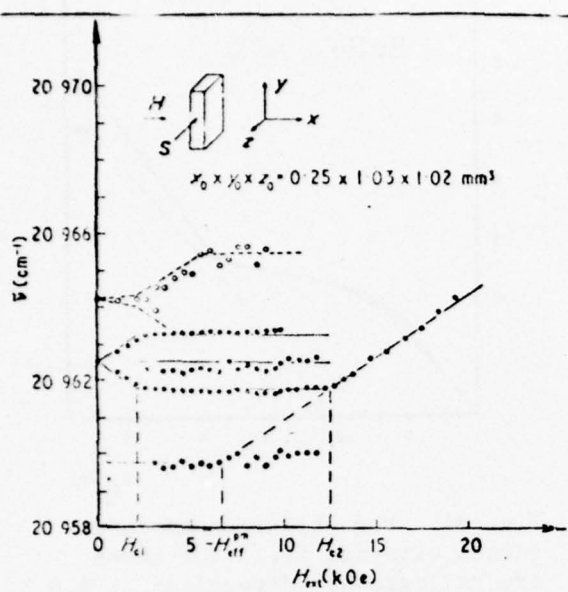
Fig. 80. Zeeman pattern of the transition $Z_1 \to F_1$ at T = 1.4 K in light polarized parallel to the applied field. The extra lines when $H_{c1} < H < H_{c2}$ are explained in ref. 148. After ref. 148.
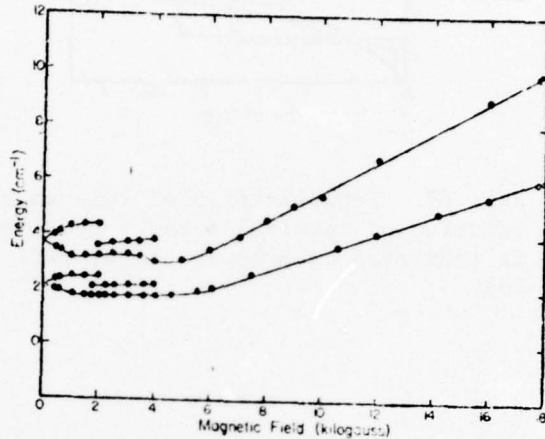
Fig. 81. Zeeman splitting of the $DyAsO_4$ $Z_1 \to F_1$ transition at 1.5 K. After ref. 147.
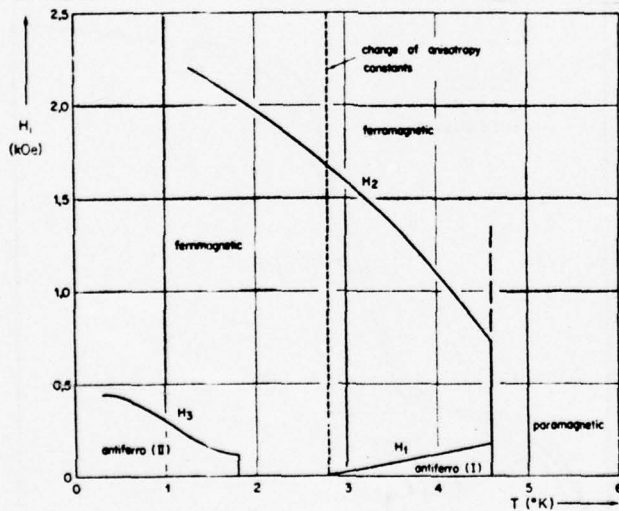
Fig. 82. Magnetic phases of EuSe as a function of temperature and internal magnetic field, as derived from magnetization and dilatometric measurements. Dilatometric and differential susceptibility measurements indicate that a change of anisotropy constants occurs at 2.8 K. After ref. 151.
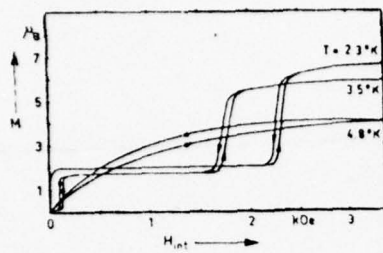
Fig. 83. Magnetization of EuSe as a
function of internal field. Hysteresis
is indicated by arrows. After ref.
157.
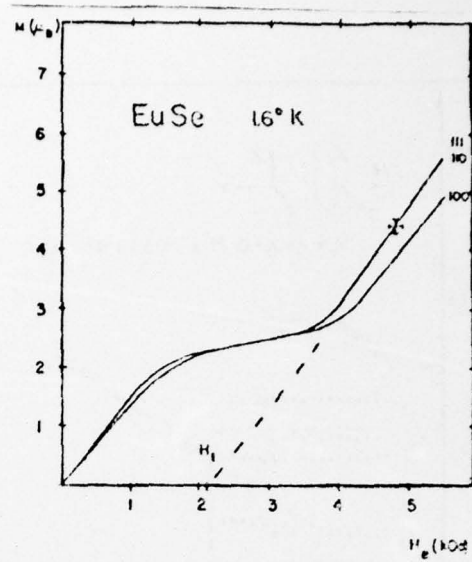
Fig. 84. Magnetization of EuSe
versus external field for three
crystallographic directions at 1.6 K.
After ref. 156.
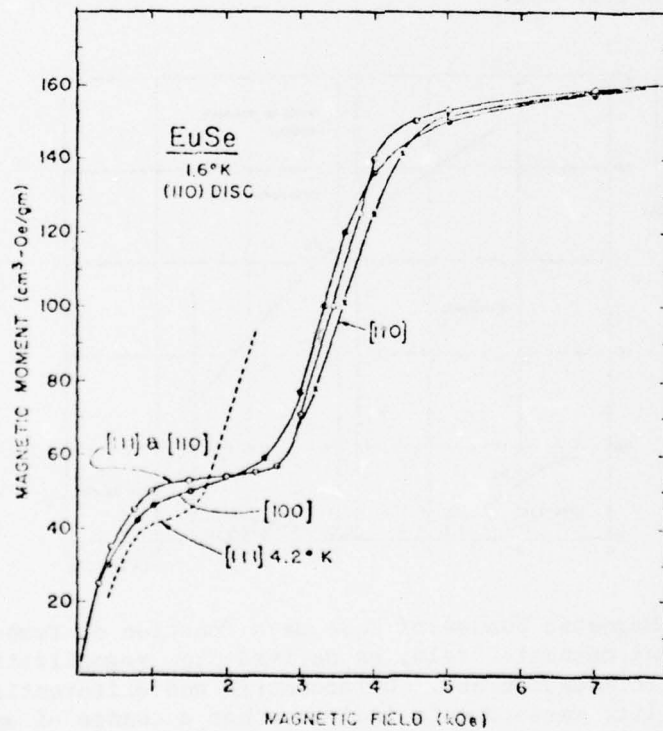
Fig. 85. Magnetic moments vs. field at 1.6°K for single
crystal EuSe: magnetic field parallel to crystallographic
axis indicated. After ref. 155.
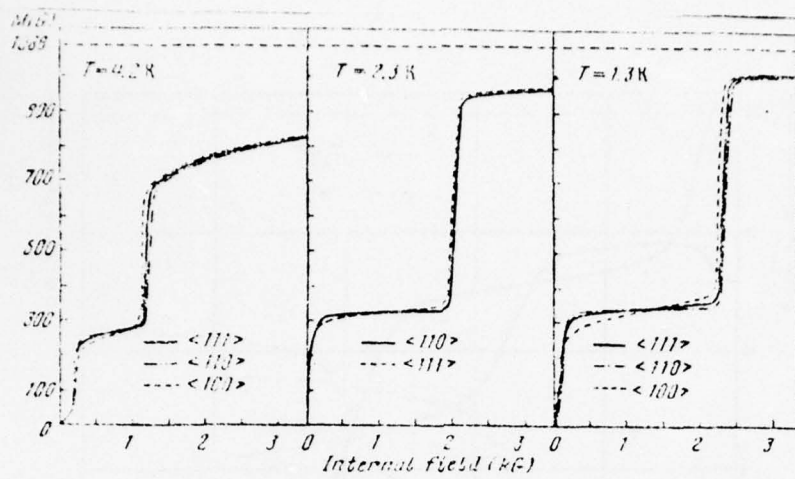
Fig. 86. The magnetization of EuSe plotted versus internal field. The temperatures represent the three known phases existing in zero field. The legend refers to the three crystallographic directions along which the field was applied. After ref. 158.
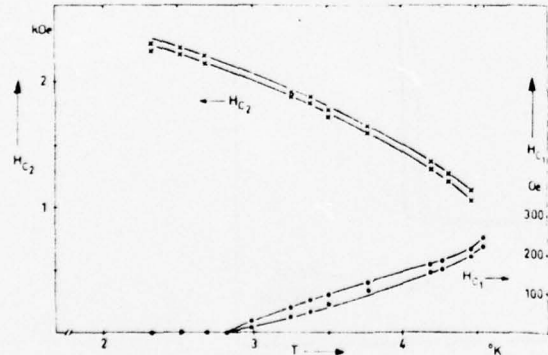
Fig. 87. Temperature dependences of the critical fields. After ref. 157.
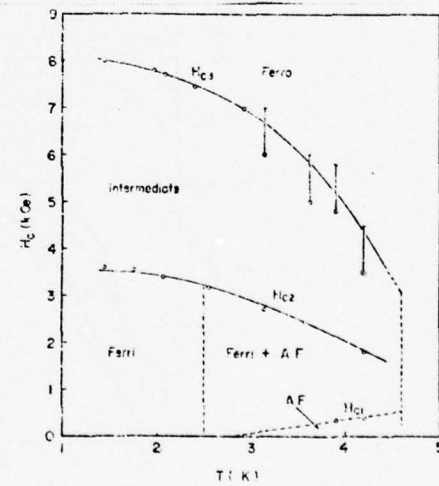
Fig. 88. Magnetic phase diagram of EuSe proposed from NMR data. After ref. 154.
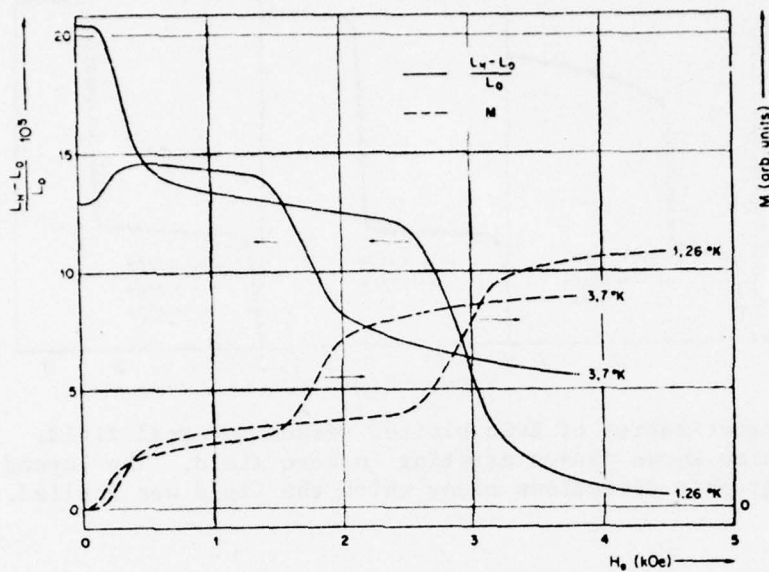
Fig. 89. Length changes and magnetization of EuSe in the [100]
direction vs. external magnetic field for two temperatures.
The curves given are taken with increasing field. After ref.
151.
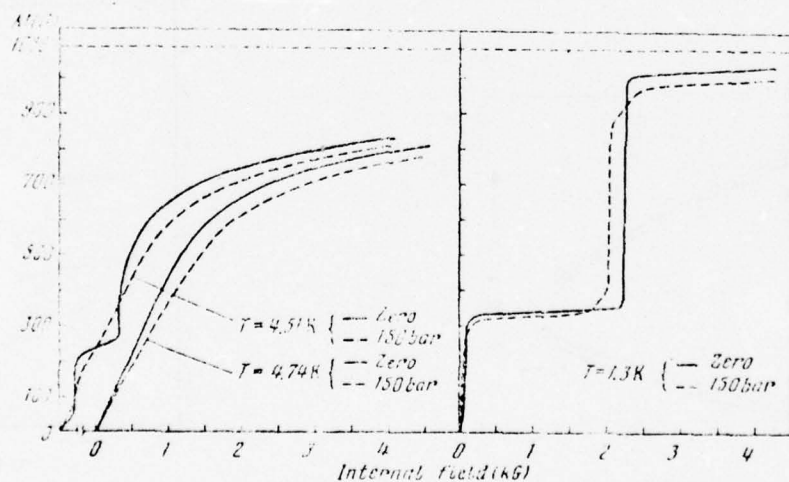
Fig. 90. The magnetization plotted versus internal field at zero and an applied
stress of 150 bar. The stress is applied along a (111) direction and the field is
in a 112 direction of the (111) plane. After ref. 158.
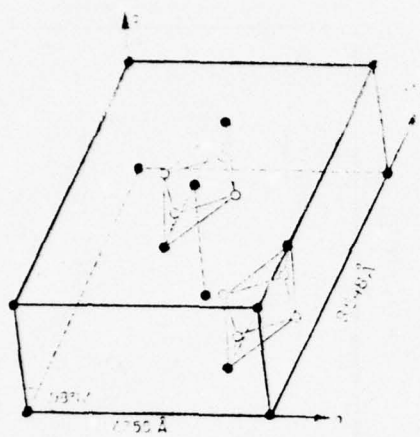
Fig. 91. Crystal structure of $FeCl_2 \cdot 2H_2O$. After ref. 176.
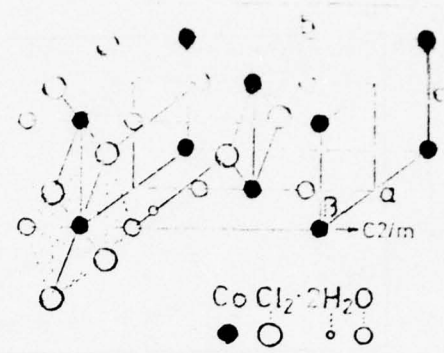
Fig. 92. Crystal structure of $CoCl_2 \cdot 2H_2O$. After ref. 178.
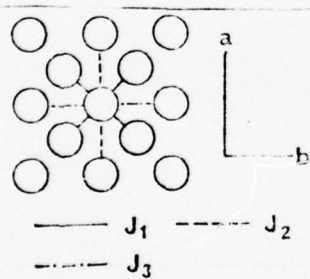
Fig. 93. A section of the $CoCl_2 \cdot 2H_2O$ type lattice parallel to the ab plane. Each circle represents a chain running along the c axis. A spin on a given chain interacts with another spin on a neighboring chain with an interaction constant J_i, where the subscript i distinguishes topologically different neighbors. After ref. 8.
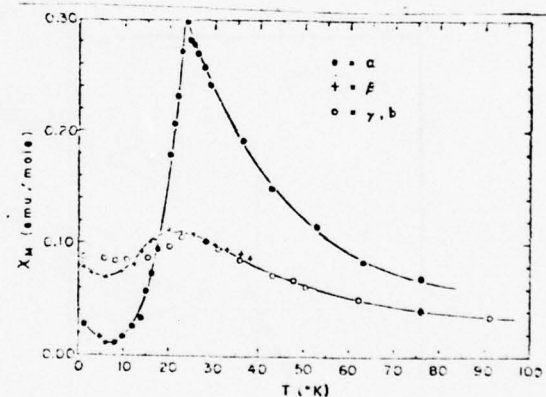
Fig. 94. Plot of the principal molar magnetic susceptibilities of $FeCl_2 \cdot 2H_2O$ as a function of temperature. After ref. 162.
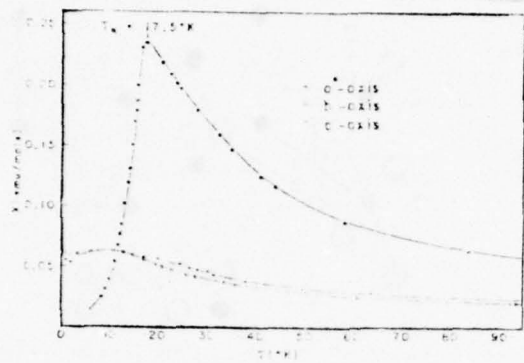
Fig. 95. Plot of the principal molar
magnetic susceptibilities of $CoCl_2 \cdot 2H_2O$
as a function of temperature. After
ref. 160.
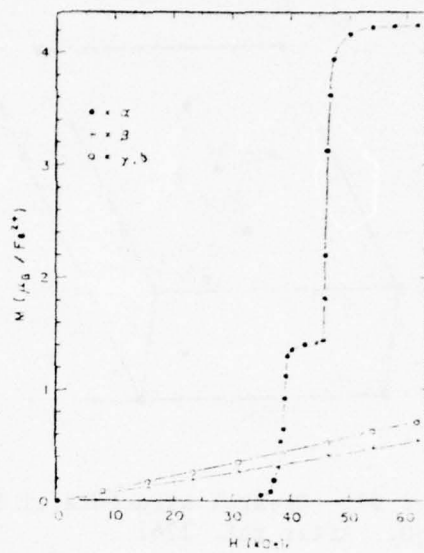
Fig. 96. Plot of the $FeCl_2 \cdot 2H_2O$ sin-
gle-crystal magnetization behavior at
$T = 40°K$. After ref. 162.
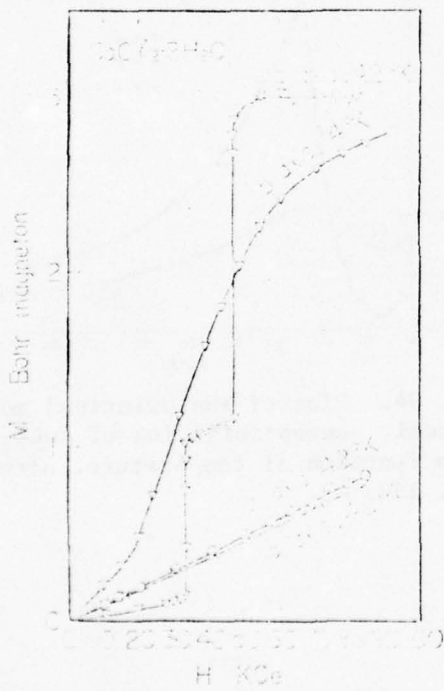
Fig. 97. The molar magnetization of
$CoCl_2 \cdot 2H_2O$ as a function of magnetic
field. After ref. 163.
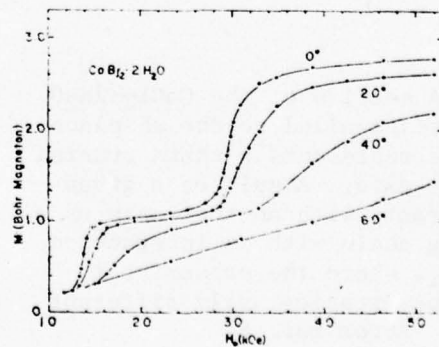
Fig. 98. Bulk magnetization behavior
of antiferromagnetic $CoBr_2 \cdot 2H_2O$ at 4.0 K
for $H \perp$ c-axis as a function of angle
between H_o and the b-axis. After
ref. 168.
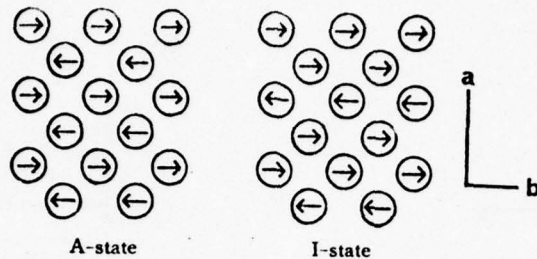
Fig. 99. The spin arrangements in
the antiferromagnetic state (labeled
as A) and the intermediate state
(labeled as I). After ref. 8.
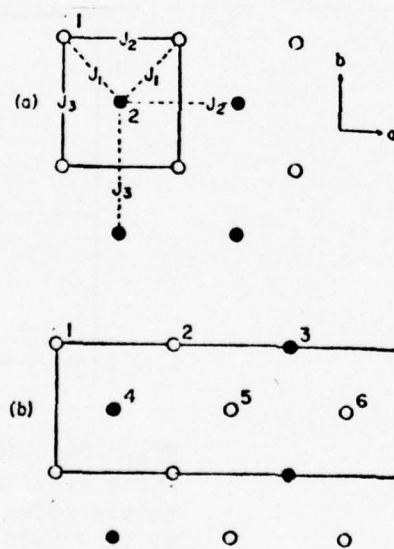
Fig. 100. Projection of $FeCl_2 \cdot 2H_2O$ spin arrangements along the
c axis on the ab plane. Open circles represent spins directed
along the + α axis. (a) Zero field, two sublattice magnetic
structure, showing the exchange paths. The numbered positions
identify the sublattices. (b) Intermediate-field, six sub-
lattice magnetic structure in a magnetic field directed along
the α axis. After ref. 162.
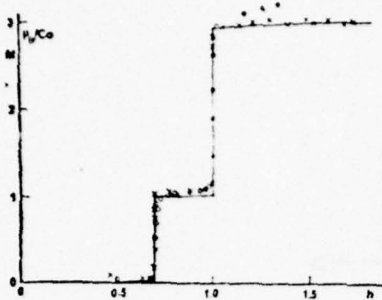
Fig. 101. Magnetization versus field relation at 4.2 K on $CoCl_2 \cdot 2H_2O$. M denotes the magnetization per Co ion in Bohr magnetons; h is the external field measured in units of H_{c1}, the first transition field. The full line represents the result of the calculation, by Yamada and Kanamori, ref. 81; the X's and O's are the experimental data taken from Kobayashi and Haseda (ref. 163) and Narath (ref. 160), respectively. After ref. 8.
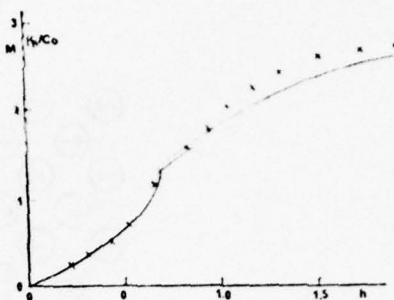
Fig. 102. Magnetization versus field relation at 14 K in $CoCl_2 \cdot 2H_2O$. The full line is the result of a calculation by Yamada and Kanamori (ref. 8). The x's are from the experimental data of Kobayashi and Haseda (ref. 163). After ref. 8.
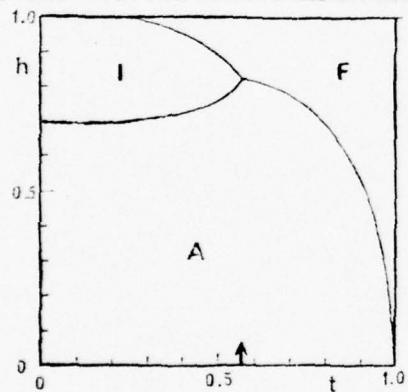
Fig. 103. The calculated magnetic phase diagram of $CoCl_2 \cdot 2H_2O$. F, A and I stand for the ferromagnetic (paramagnetic), antiferromagnetic, and intermediate phases, respectively; h is the external field measured in the unit of H_{c1} at absolute zero, and t is the reduced temperature $t = T/T_N$; the arrow indicates the triple point temperature $t_o = 0.574$. After ref. 8.
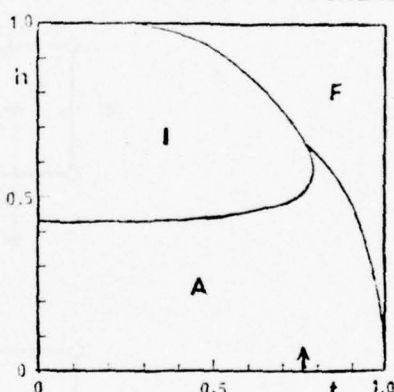
Fig. 104. The calculated magnetic phase diagram of $CoBr_2 \cdot 2H_2O$. The triple point temperature is given by $t_o = 0.763$. After ref. 8.
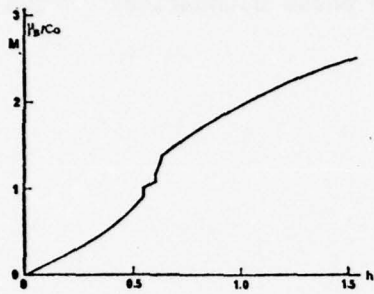
Fig. 105. The calculated magnetization vs. field curve at t = 0.785 (T = 7.46°K) in CoBr$_2$·2H$_2$O. After ref. 8.
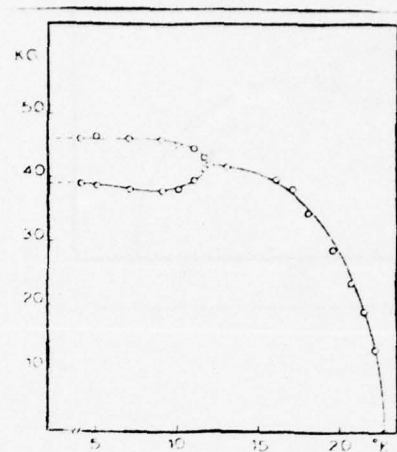
Fig. 106. Magnetic phase diagram of FeCl$_2$·2H$_2$O in applied effective fields up to 47 kG at temperatures ranging between 4.2 and 25 K. After ref. 7.
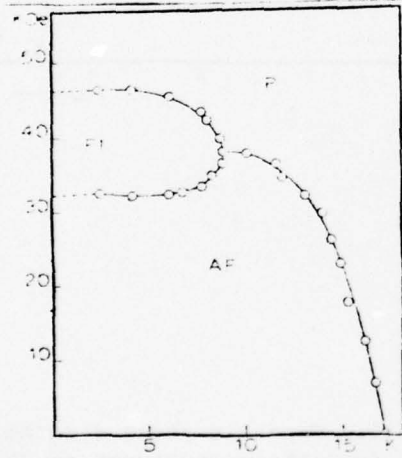
Fig. 107. Magnetic phase diagram of CoCl$_2$·2H$_2$O in applied external fields up to 50 kOe at temperatures ranging between 2.5 and 18 K. The regions of the antiferromagnetic and ferrimagnetic phases are indicated. After ref. 6.
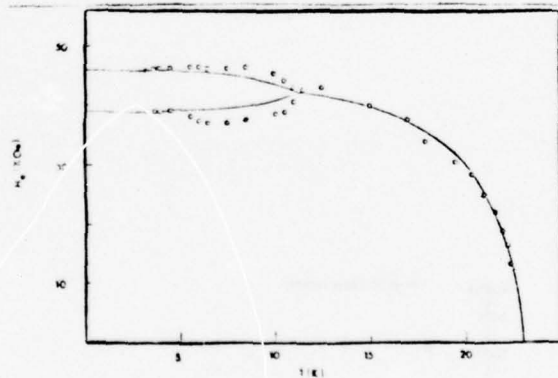
Fig. 108. Magnetic field vs. temperature phase diagram for FeCl$_2$·2H$_2$O. Circles: experimental points. Solid line: calculated phase diagram for effective spin S = 2. After ref. 170.
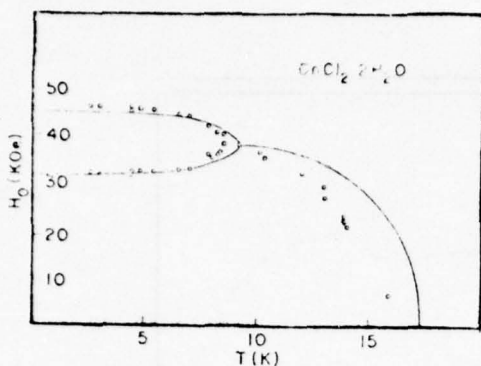
Fig. 109. Magnetic field vs. temperature phase diagram $CoCl_2 \cdot 2H_2O$. Circles: experimental points. Solid line: calculated phase boundaries. After ref. 171.

Fig. 110. Magnetic phase diagram for $CoCl_2 \cdot 2H_2O$ with $H \| b$-axis. The circles are from the strain gauge measurements of Lowe et al. (ref. 171). The points labelled with a ∇ are from the high frequency susceptibility measurements of van Duyneveldt et al. (ref. 172). After ref. 172.
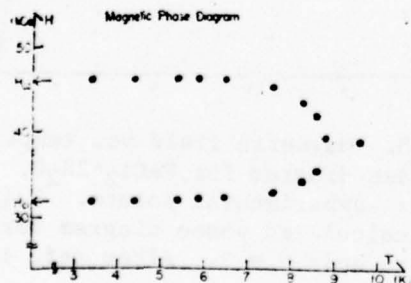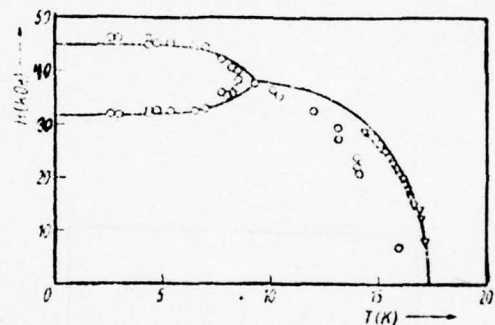
Fig. 111. Magnetic phase diagram obtained from the measurement of $\partial M/\partial H$ in the temperature region from 3.4 K up to 9.8 K. The magnetic triple point is at 8.9 K and 39.3 kOe. After ref. 173.
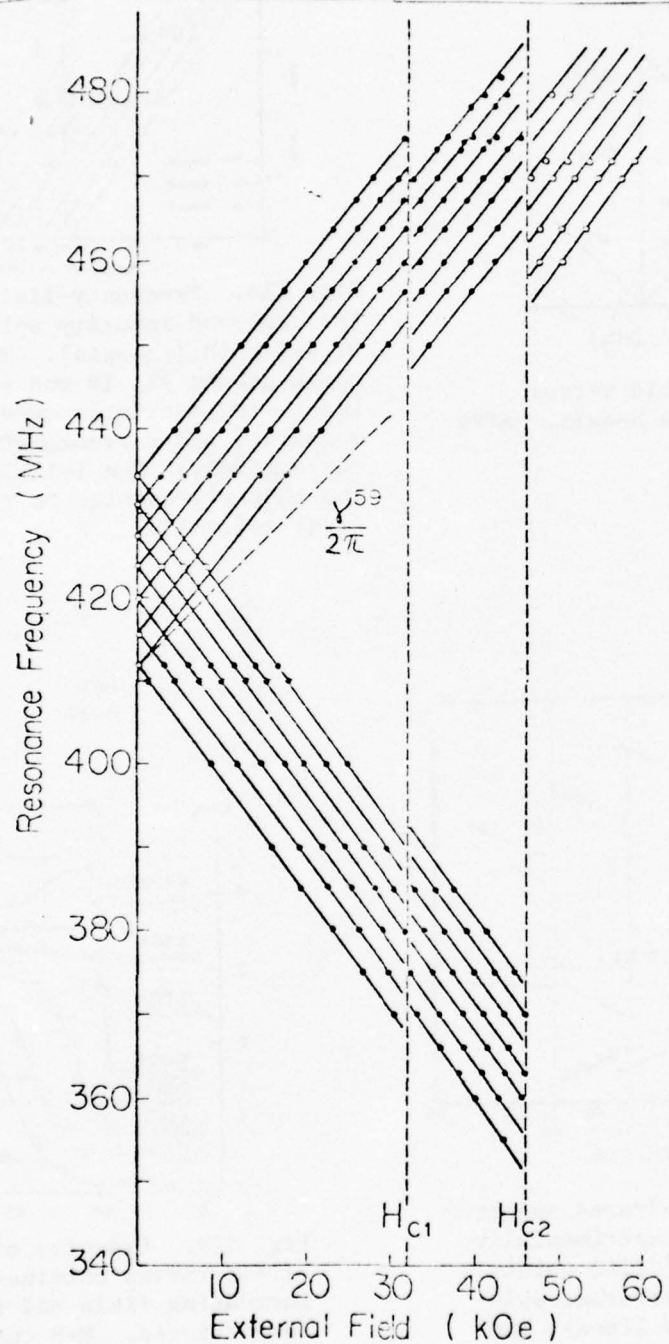
Fig. 112. NMR frequencies of $CoCl_2 \cdot 2H_2O$ versus the external field parallel to the b-axis at 2.2 K. After ref. 178.
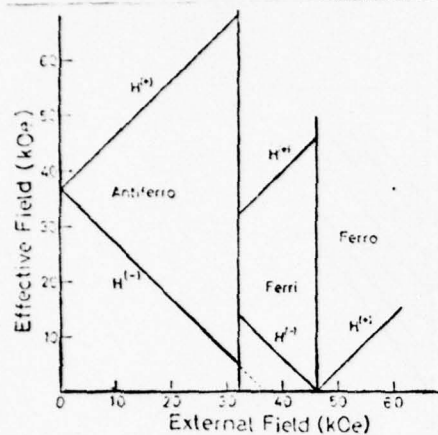
Fig. 113. Effective field versus external field along the b-axis. After ref. 180.
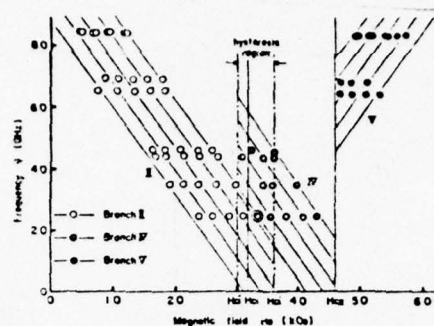
Fig. 114. Frequency-field diagram of the observed impurity spin resonance at 4.2 K ($H_o||b$-axis). There are three groups II, IV and V corresponding to the antiferromagnetic, ferrimagnetic, and ferromagnetic regions, respectively. The full lines represent the theory presented in ref. 181. After ref. 181.
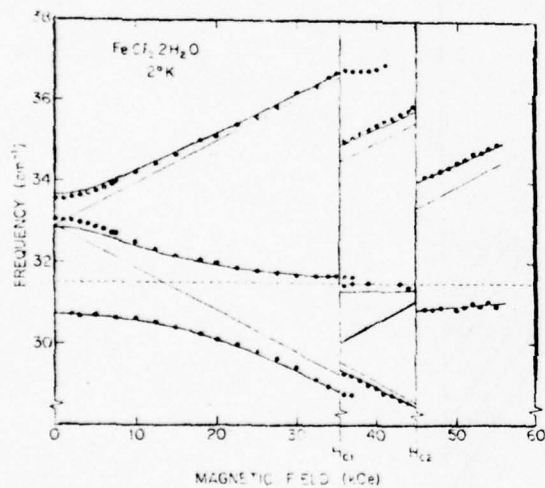
Fig. 115. The far-infrared spectrum of $FeCl_2 \cdot 2H_2O$. The experimentally observed resonances (solid points), the theoretical, unperturbed spin-wave energies (narrow lines), and the phonon (dashed line) are all plotted against the applied magnetic field. The heavy lines are the result of including a phenomenological magnon-phonon interaction. Absorption due to the phonon in the ferrimagnetic phase is weak. After ref. 174.
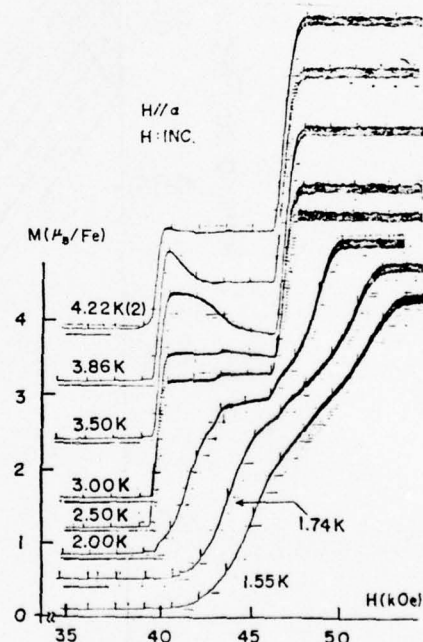
Fig. 116. Examples of recorder traces of M-H curves obtained in a slowly increasing field and at various temperatures. M-H curves are displayed vertically for clarity and the base lines are shown in the figure. After ref. 182.
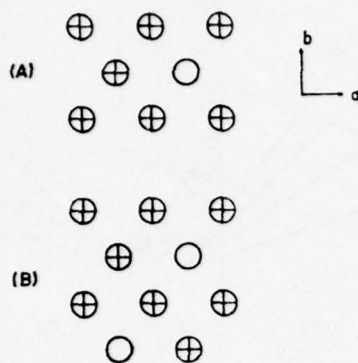
Fig. 117. Examples of the arrangements of magnetic moments in the $M_S/2$ state which are constructed by a simple reversal of down chains in the A.F. state. This figure shows the projection of the magnetic moments on the ab-plane. After ref. 182.
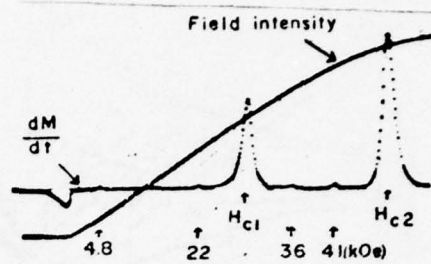
Fig. 118. Magnetization change dM/dt observed on $CoCl_2 2H_2O$ under a decreasing pulsed magnetic field from right to left as a function of time (200 µsec/div.). The field intensity change is also shown. There are four small peaks at 4.8, 22.36 and 41 kOe in addition to H_{c1} and H_{c2}. After ref. 186.
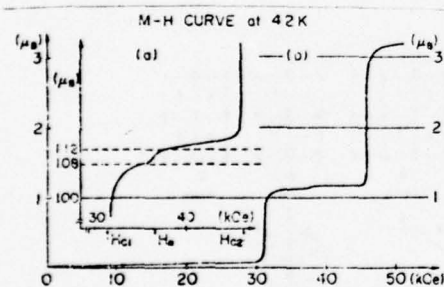
Fig. 119(a), (b). M-H curve in H parallel to the b-axis at 4.2 K. (a) is a magnified curve between the field H_{c1} and H_{c2}. (b) shows a whole curve. After ref. 186.
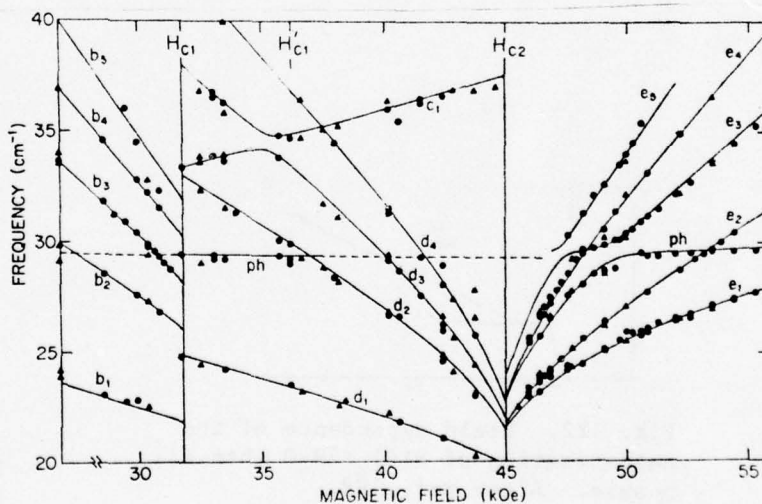
Fig. 120. A detailed comparison between theory (solid lines) and experiment for $CoCl_2 \cdot 2H_2O$ between 20 and 40 cm^{-1}. After ref. 33.
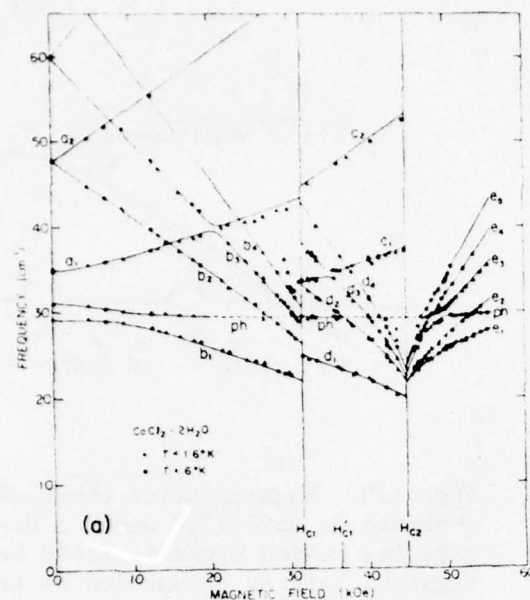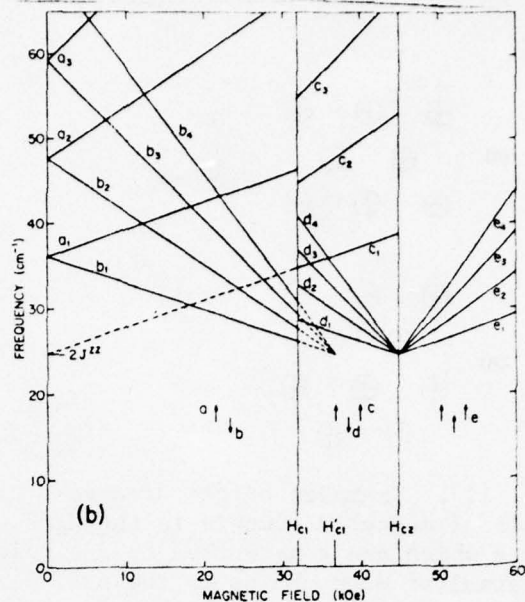
Fig. 121. (a) The observed resonance frequencies are plotted against the magnetic field H_o which is applied along the b-axis. Measurements were taken at $T \leq 1.6$ K (triangles) and $T = 6$ K (circles). The lines are the results of detailed theoretical calculations. (b) The simple Ising-model excitation spectra for spin clusters in the chains of $CoCl_2 \cdot 2H_2O$. After ref. 33.
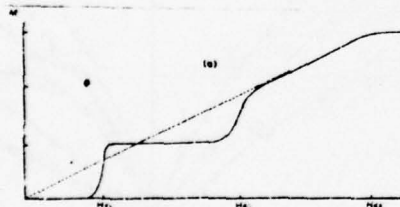
Fig. 122. Field dependence of the magnetization of $NiCl_2 \cdot 2H_2O$ when $H\|$ b-axis. After ref. 198.
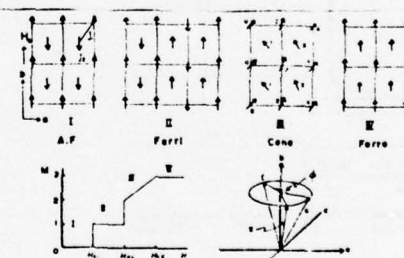
Fig. 123. Schematic view of the proposed spin arrangements of $NiCl_2 \cdot 2H_2O$ and definitions of J_1, J_2 and $\emptyset$. After ref. 198.
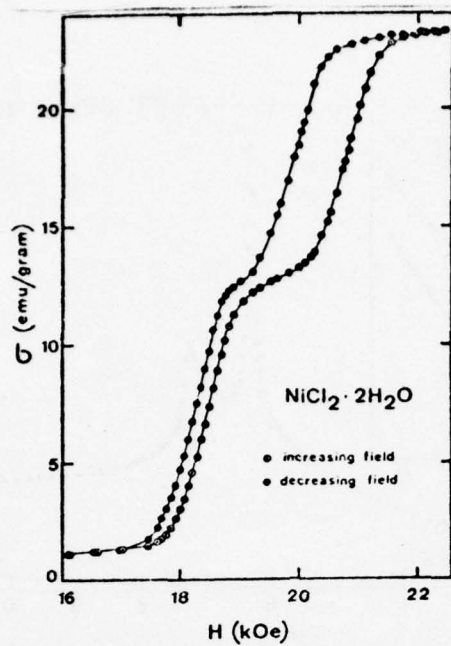
Fig. 124. Field dependence of the magnetization in the vicinity of the first critical field at 4.4 K. The magnetic field is along the easy axis. After ref. 195.
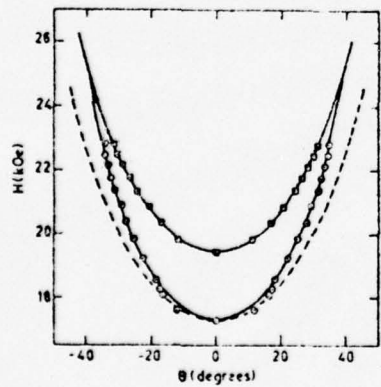
Fig. 125. Critical angles versus field in the bc-plane at 4.353 K; c-axis at zero; $\theta - \theta_{cr1}$; $\boxdot - \theta_{cr2}$. After ref. 196.
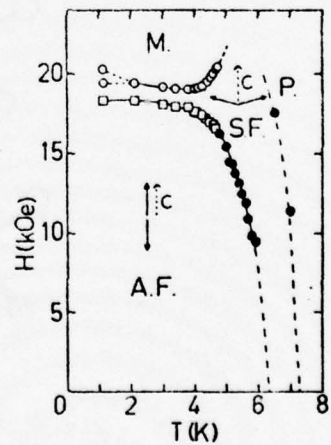
Fig. 126. Phase diagram of $NiCl_2 \cdot 2H_2O$. Open and solid symbols come from magnetization and susceptibility measurements, respectively. After ref. 196.
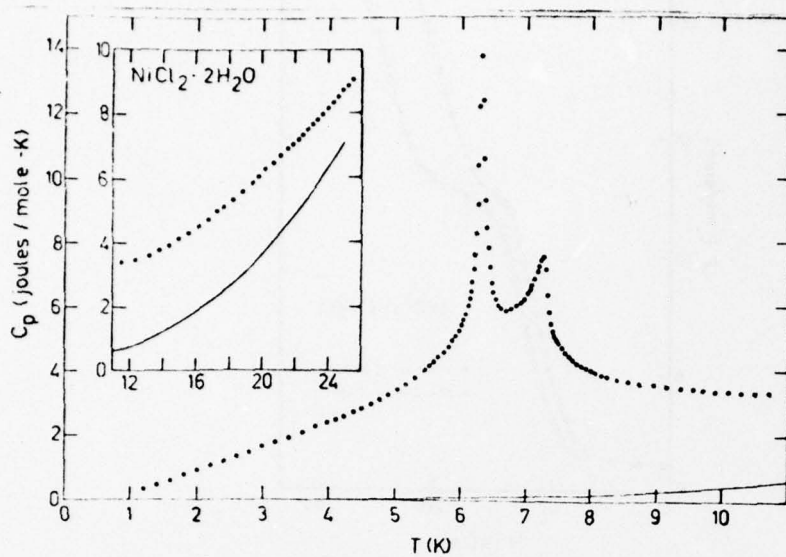
Fig. 127. Specific heat of $NiCl_2 \cdot 2H_2O$. The solid line denotes
the estimate of the lattice specific heat. After ref. 199.
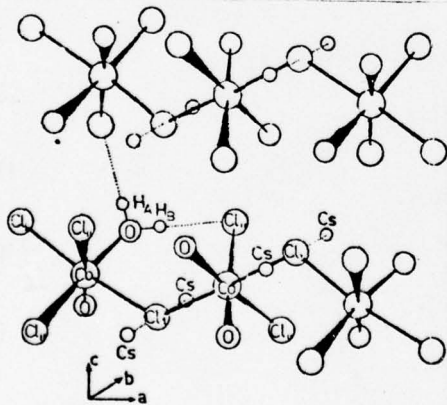
Fig. 128. Structure of $CsCoCl_3 \cdot$
$2H_2O$. Only one set of hydrogen atoms
and hydrogen bonds are shown. After
ref. 200.
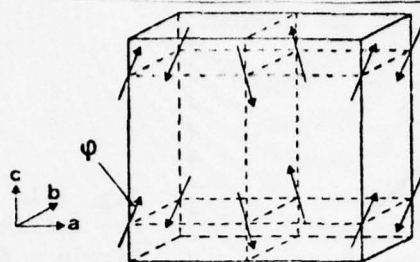
Fig. 129. Arrangement of the magnetic moments accoding to the magnetic space group $P_{2b}cca'$. All spins are in the ac-plane. After ref. 200.
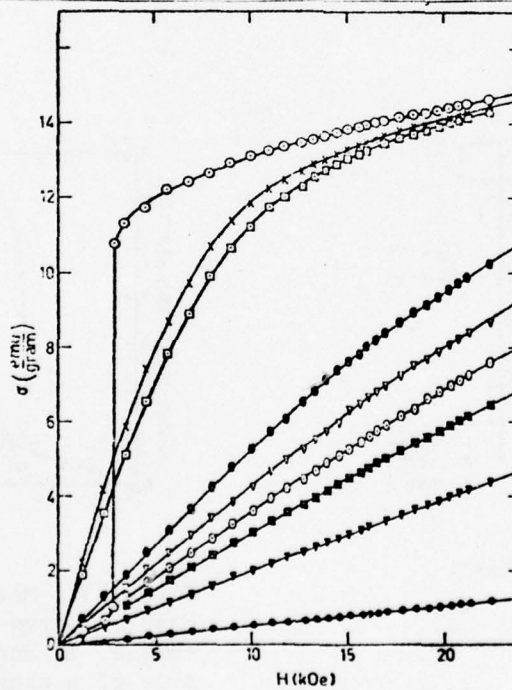
Fig. 130. Magnetization of $CsCoCl_3 \cdot 2H_2O$ as a function of the magnetic field $\vec{H}$ parallel to the $\vec{a}$ direction at various temperatures; open circle - 1.1 K, x - 4.2 K, open square - 4.3 K, solid oval - 10 K, open triangle - 11.10 K, open oval - 13.1 K, solid square 14.8 K, solid triangle - 20.3 K, solid circle - 77.3 K. After ref. 200.
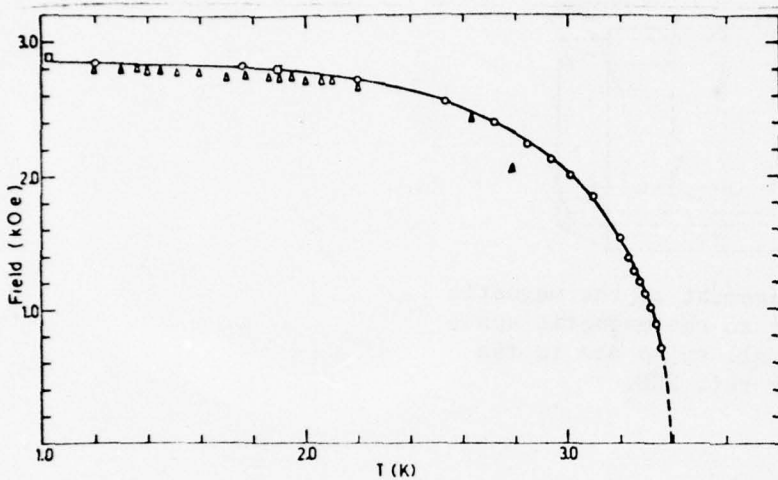
Fig. 131. Temperature dependence of the critical field of $CsCoCl_3 \cdot 2H_2O$. Circle - NMR, triangle - AFMR, square - magnetization. After ref. 200.

(a)

$a = 10.035 \, \text{Å}$
$b = 12.054 \, \text{Å}$
$c = 3.502 \, \text{Å}$

Eu_3O_4

O $Z = 1/4$
$Z = 3/4$

5.6 Å

C AXIS

3.5 Å

(b)
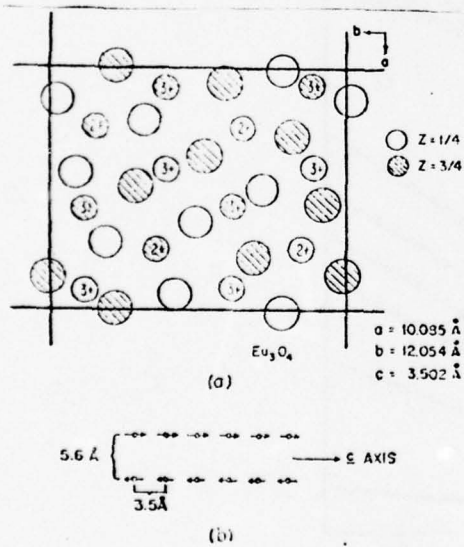
Fig. 132. (a) Unit cell of Eu_3O_4. Large circles, oxygen; small circles, divalent and trivalent europium. (b) Neighboring chains of Eu^{3+}. Arrows show proposed structure. After ref. 203.

$M_c (2.2 °K)$
$M_p (2.3 °K)$
$M_b (2.2 °K)$
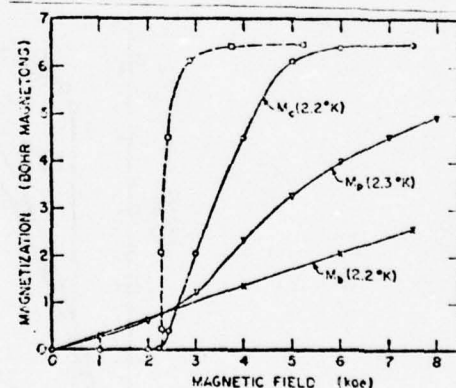
Fig. 133. Magnetization curves for Eu_3O_4. Curve M_p is for a powder sample, M_b and M_c are for the b and c axes of a single crystal fragment. Dashed curve shows M_c corrected for assumed demagnetizing field ($1.27 \, \pi M_c$). After ref. 203.
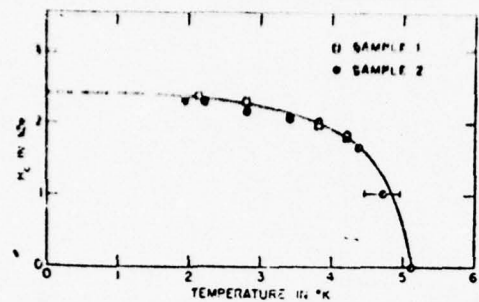
Fig. 134. Critical field H_c of Eu_3O_4 versus temperature. After ref. 202.
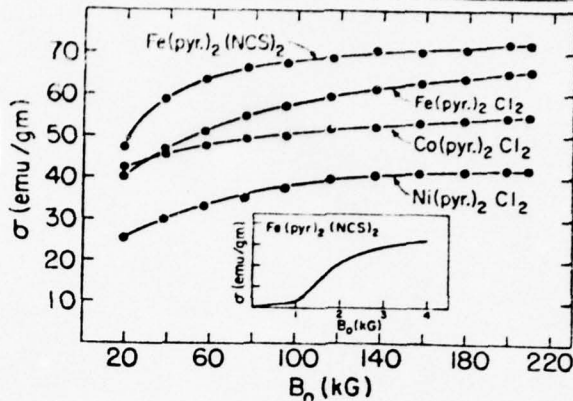
Fig. 135. Magnetic moment, σ, versus applied field, B_0, for several pyridine compounds. The insert shows an example of a low field transition for $Fe(pyr)_2Cl_2$. After ref. 206.
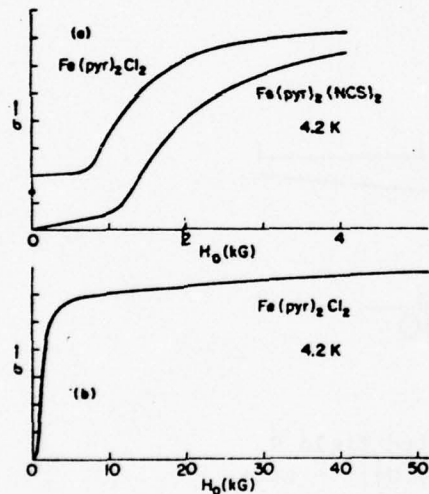
Fig. 136. Relative magnetic moment, σ, vs applied field, H_0, at 4.2 K. (a) Low field data. Note the break in ordinate axis and that the relative moment scale differs fro the two sets of data. For the $Fe(pyr)_2Cl_2$ data, $\sigma = 27$ e.m.u./g (1.4 μ_B/Fe atom) at 3.9 kG; for the $Fe(pyr)_2(NCS)_2$ data, $\sigma = 34$ e.m.u./g (2.0 μ_B/Fe atom) at 4.2 kG. (b) High field data showing that saturation is not achieved in the powder material. For the $Fe(pyr)_2Cl_2$, $\sigma = 51$ e.m.u./g (2.6 μ_B/Fe atom) at 55 kG. After ref. 205.
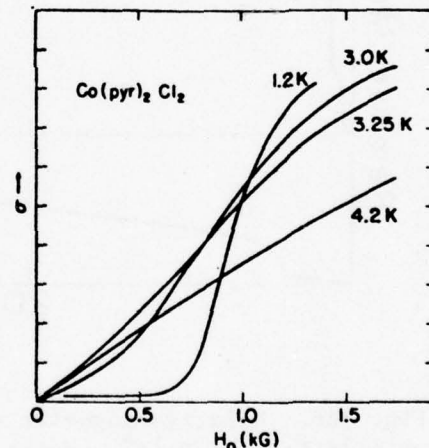
Fig. 137. (a) Relative magnetic moment, σ, vs applied magnetic field, H_0, for $Co(pyr)_2Cl_2$ for several temperatures. At 1.2 K and 1.5 kG, $\sigma = 31$ e.m.u./g (1.6 μ_B/Co atom). At 4.2 K and 48 kG, $\sigma = 47$ e.m.u./g (2.4 μ_B/Co atom). After ref. 205.
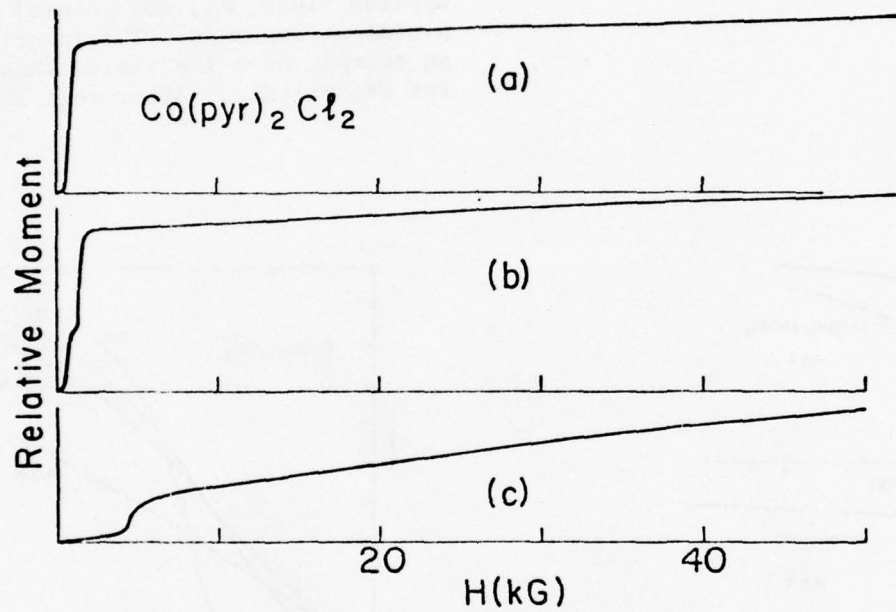
Fig. 138. Relative magnetic moment σ versus applied field H
at 1.25 K: (a) $H||a^*$ - axis; (b) $H||b$ - axis; (c) $H||c$ - axis.
The moments at H - 52 kG are $\sim$ 1.6 μ_B/Co atom for (a) and (b),
and $\sim$ 0.8 μ_B/Co atom for (c). After ref. 204.
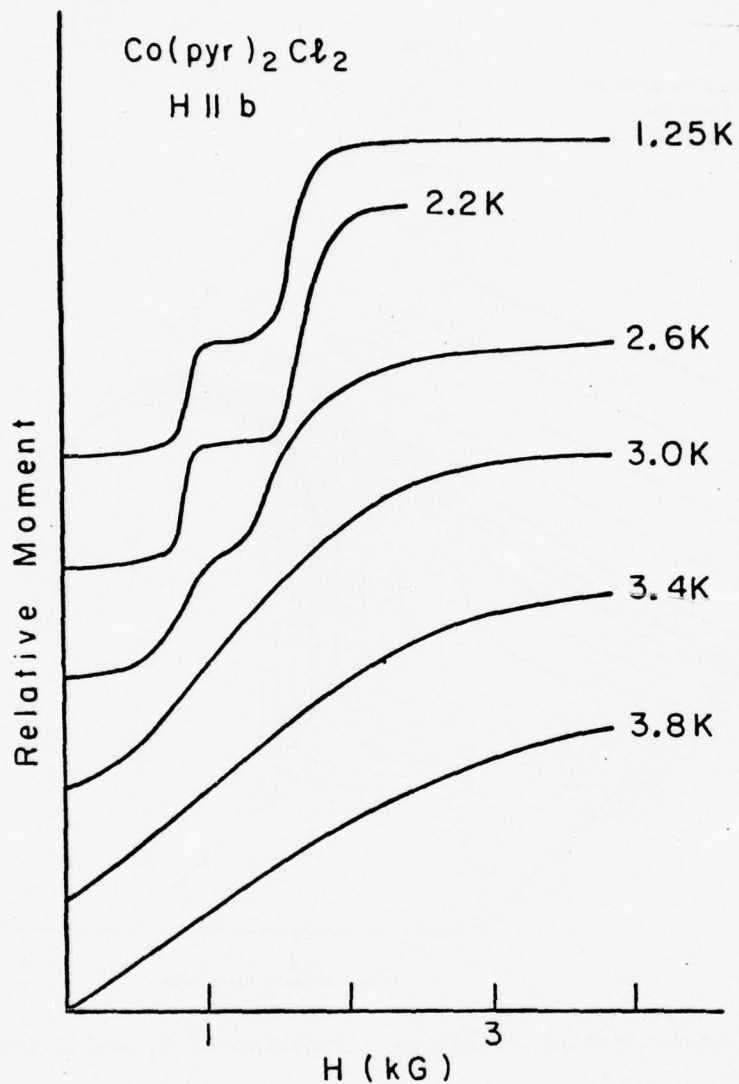
Fig. 139. Relative moment σ versus applied field H for 1.25 $\leq$ T $\leq$ 3.8 K. The curves are idsplaced along the ordinate for clarity. After ref. 204.

Magnetization of DAG as a Function of
Internal Magnetic Field for
Different Temperatures

800
700
600
500
400

4.230
3.790
3.593
2.996
2.647
2.497
2.419
2.276
2.106
1.882
1.715
1.600
1.506
1.464
1.395
1.254
1.138

Temperature (°K)

Magnetization (emu/cm³).

800
700
600
500
400
300
200
100
0

M

T

H_{int}

0   1   2   3   4   5

Internal Magnetic Field (kOe)
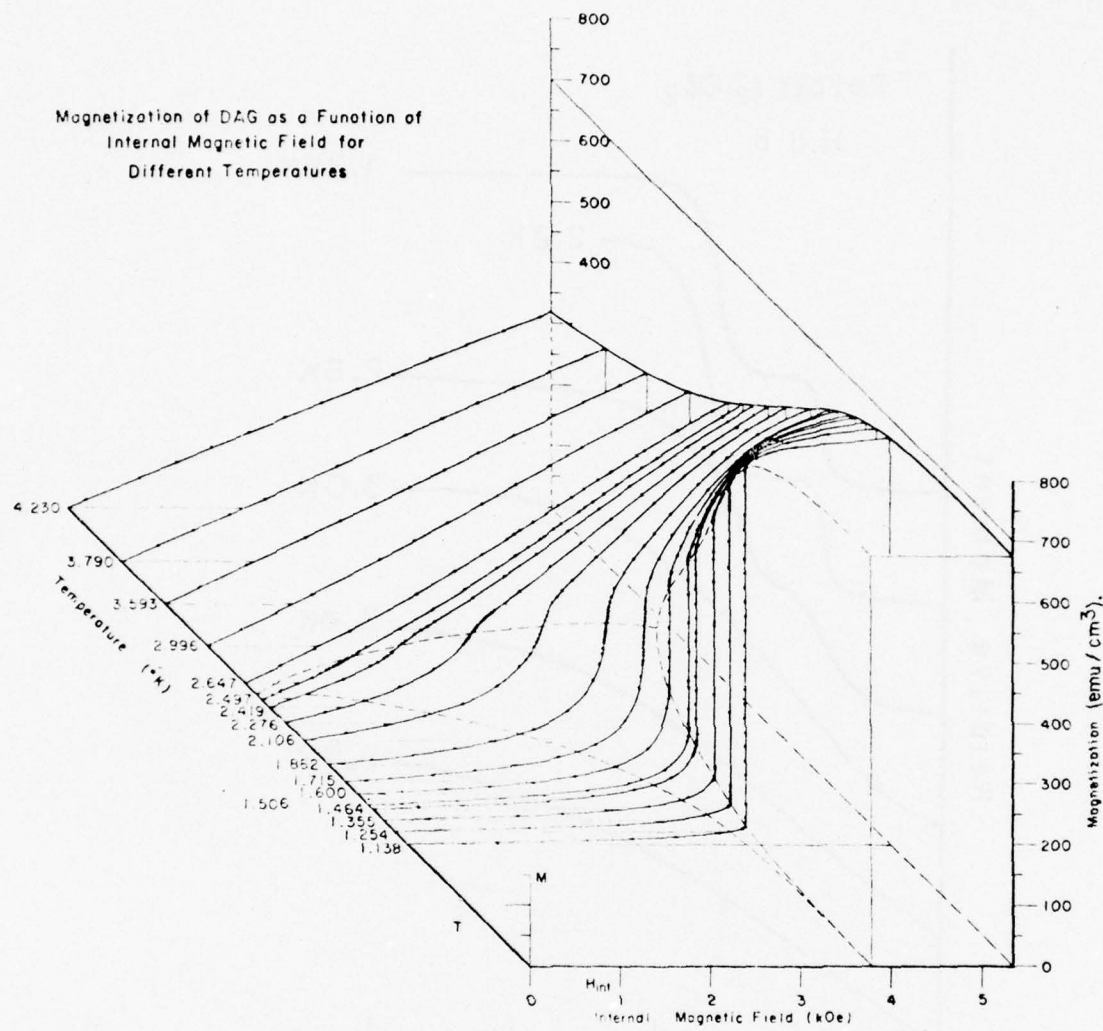
Fig. 140. Isothermal magnetization of DAG as a function of H_i and T for fields along
{111}. After ref. 207.
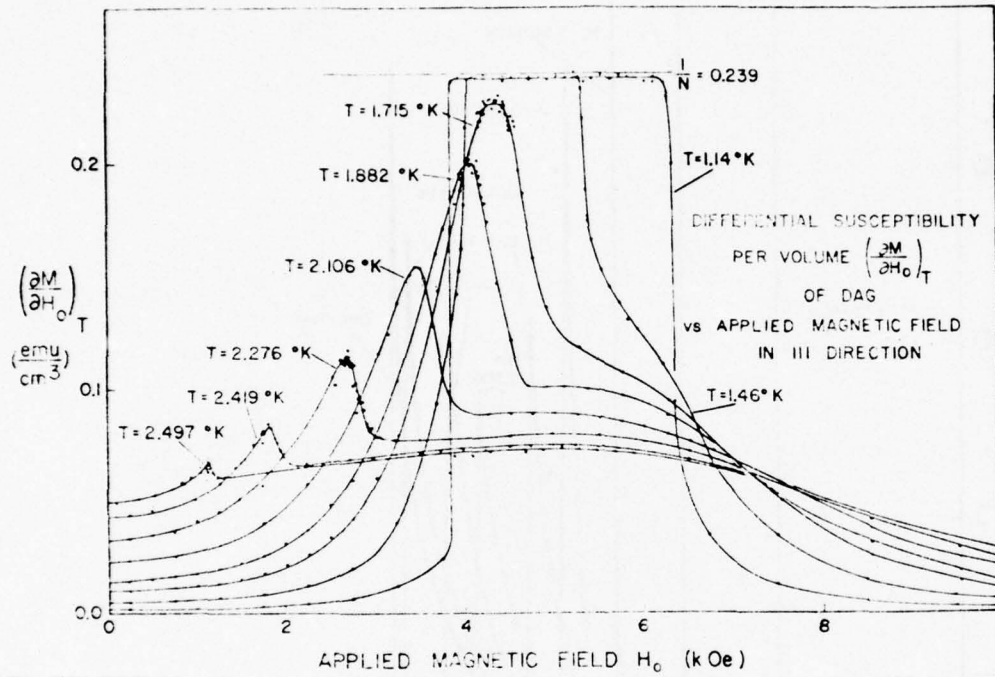
Fig. 141. Differential susceptibility $\chi_0 = (\partial M / \partial H_0)_T$, of a DAG sphere as a function of H_0 for T for fields along {111}. The horizontal line at $\chi_0 = 1/N$ is the limit corresponding to $\chi_i = (\partial M / \partial H_i)_T$ diverging to infinity. After ref. 207.

Specific Heat of DAG in Constant Internal Fields vs Temperature
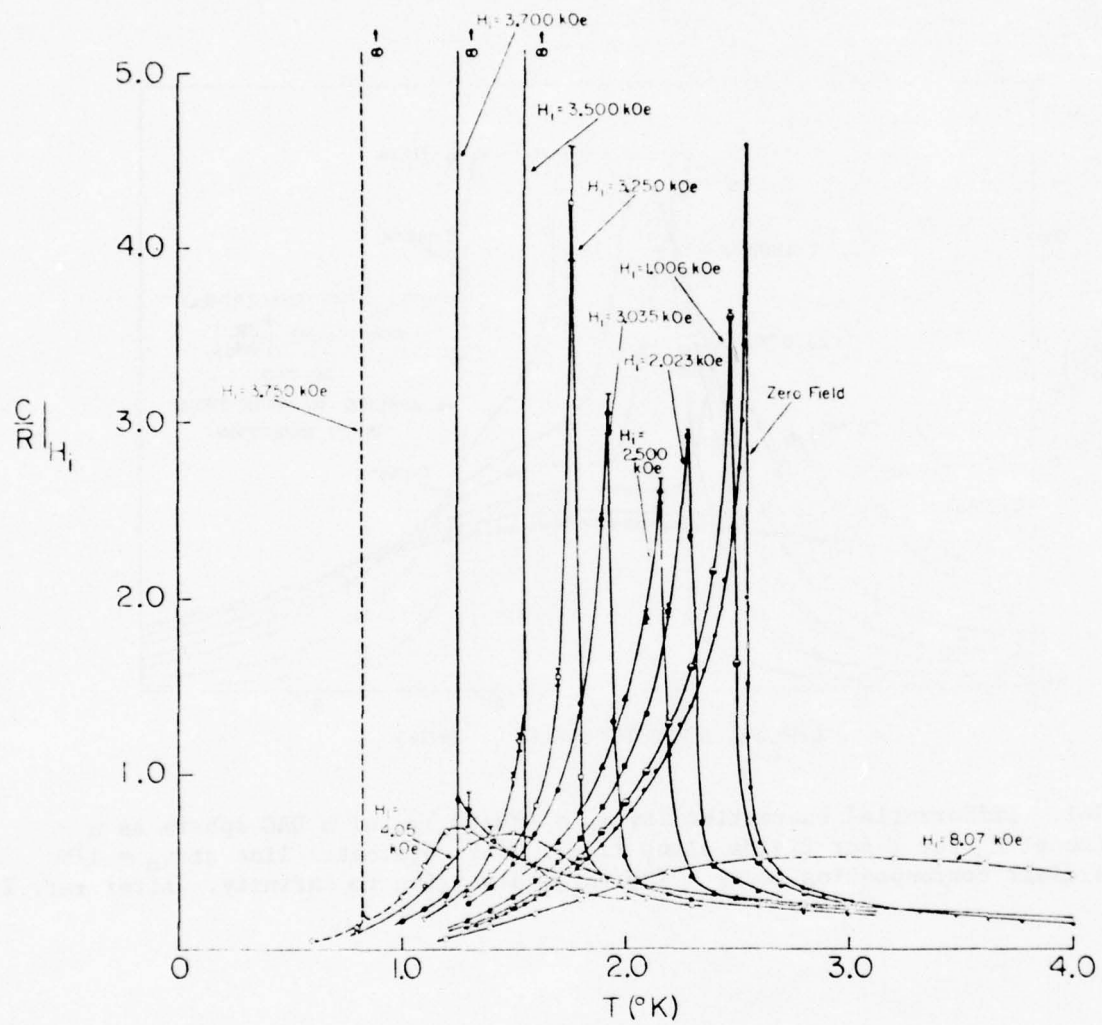
Fig. 142. Specific heat of DAG at constant H_i as a function of H_i and T. The δ-function peaks appearing below 1.66 K correspond to the latent heat at the first order transition. After ref. 207.
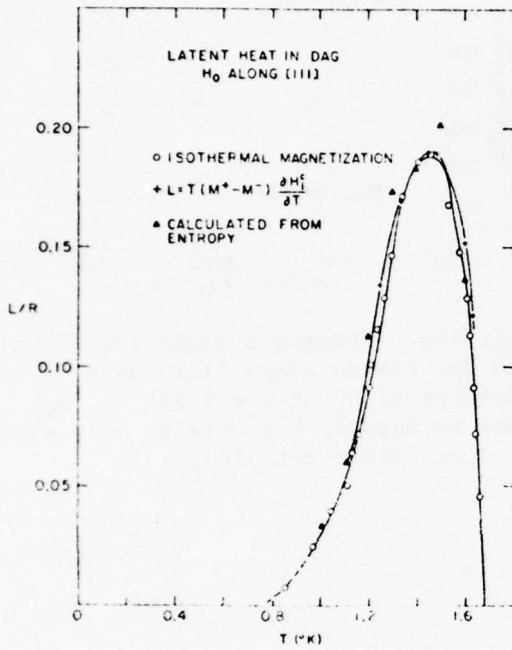
Fig. 143. Latent heat of DAG for the first order antiferromagnetic-paramagnetic transition for fields along [111]. After ref. 207.
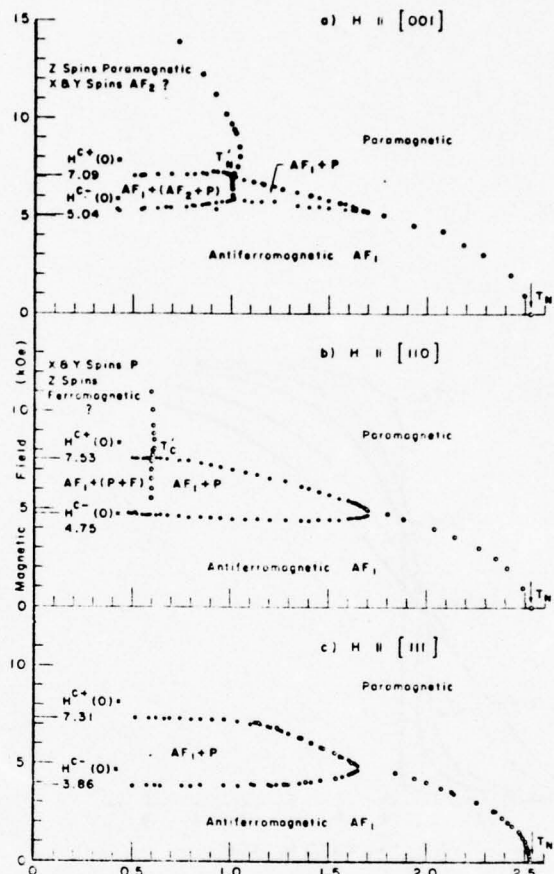
Fig. 144. H_o - T phase diagrams for DAG for fields along (a) [111]; (b) [110]; (c) [100]. The sample is an ellipsoid with N = 5.35 for all three directions. After ref. 214.

Fig. 146. Staggered magnetization of DAG for fields along [111] as a function of H_i at $T = 1.855$ K. M_s goes to zero in high fields only when $H_i \rightarrow \infty$. After ref. 223.

Fig. 145. Faraday rotation of DAG for fields along [111] as a function of H_i and T. For $T \leq 1.80$ K the curves are double valued in small fields corresponding to the hysteresis described in the text. After ref. 220.
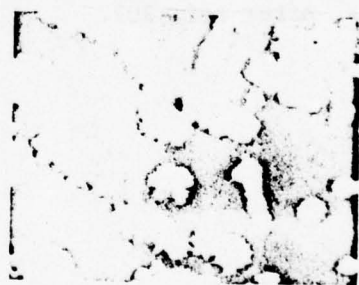
Fig. 147. Micrograph of DAG at 1.32 K at a field just inside the mixed phase region. After ref. 222.
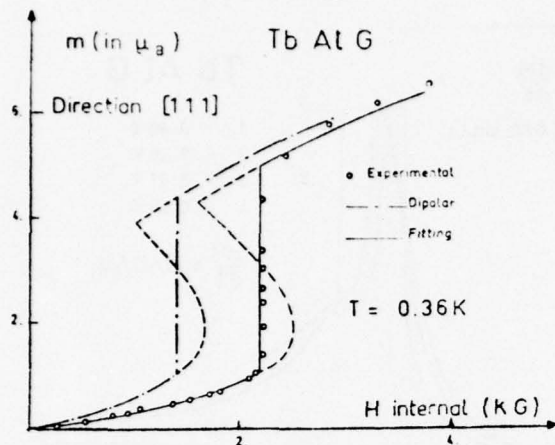
Fig. 148. Magnetization versus internal field in the direction [111], at 0.36 K. For the experimental curve, m is taken as the magnetic moment per Tb^{3+} ion measured in the [111] direction multiplied by $\sqrt{3}$. The other two curves are from the theory described in ref. 228. After ref. 228.
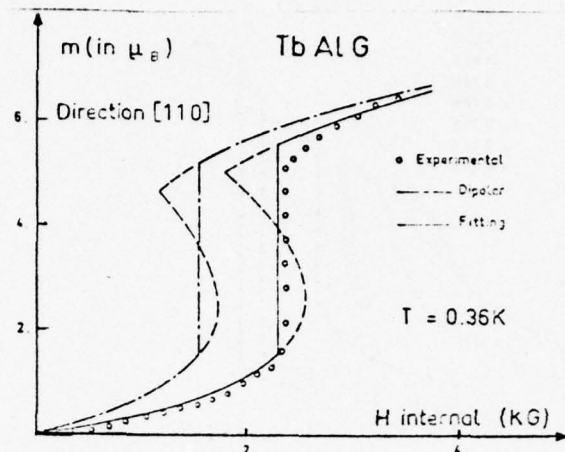
Fig. 149. Magnetization versus internal field in the direction [110] at 0.36 K. For the experimental curve, m is taken as the magnetic moment per Tb^{3+} ion measured in the [110] direction multiplied by $\sqrt{2}$. The other two curves are from the theory described in ref. 228. After ref. 228.
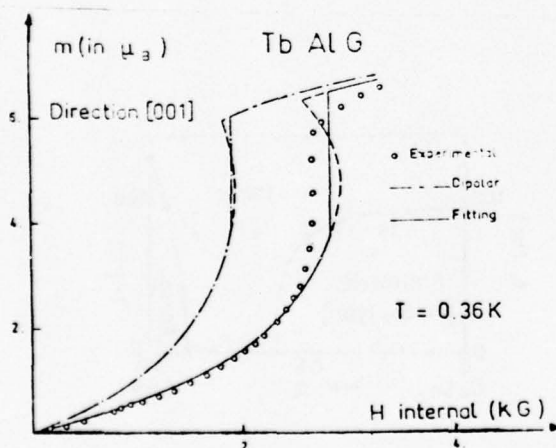
Fig. 150. Magnetization versus internal field in the direction [001] at 0.36 K. For the experimental curve m is the magnetic moment per Tb^{3+} ion measured in direction [001]. The other two curves are from the theory described in ref. 228. AFter ref. 228.
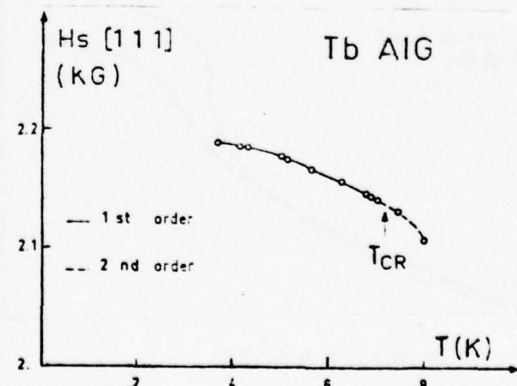
Fig. 151. Magnetic phase diagram of TbAlG in direction [111] as a function of temperature. The threshold field is plotted against temperature. After ref. 228.

$T_{CR} = 0.71\ °K$
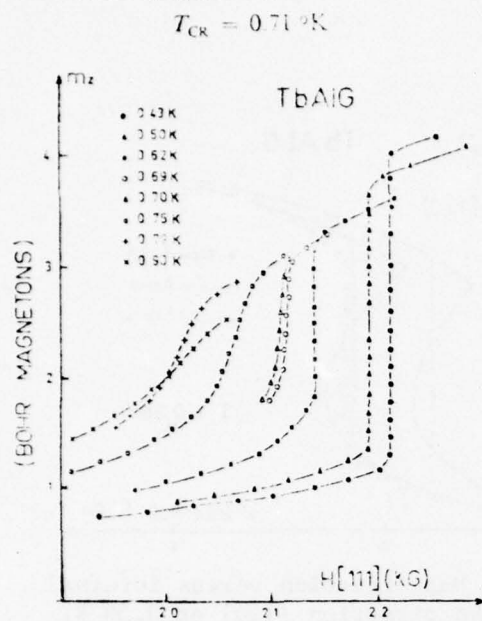
Fig. 152. Magnetization versus internal field in direction [111] for different temperatures. After ref. 228.
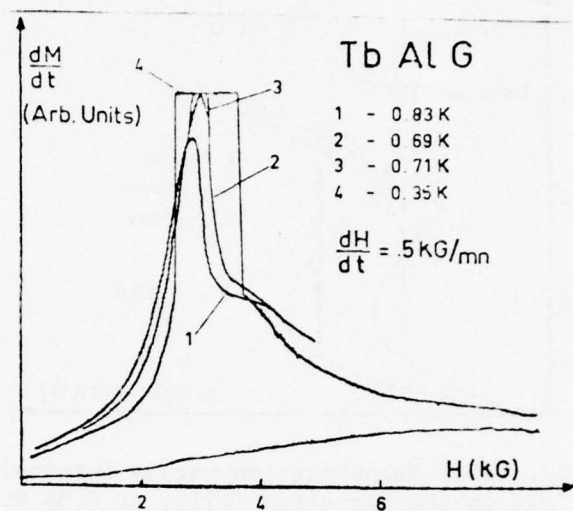
Fig. 153. dM/dt versus internal magnetic field at different temperatures. dM/dt is proportional to the differential susceptibility, dH/dt being constant. After ref. 228.
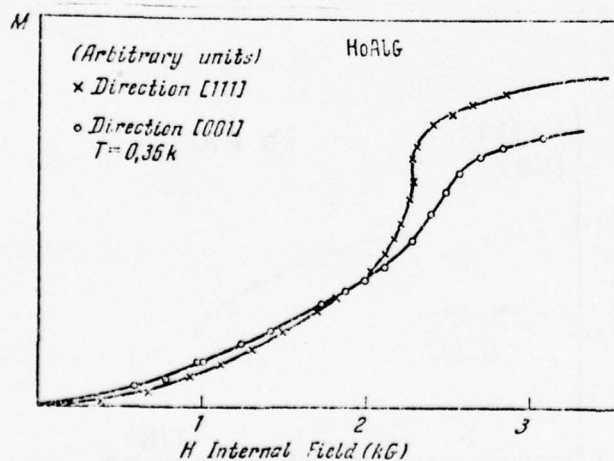
Fig. 154. Magnetization isotherms at 0.36 K in directions [111] and [001].
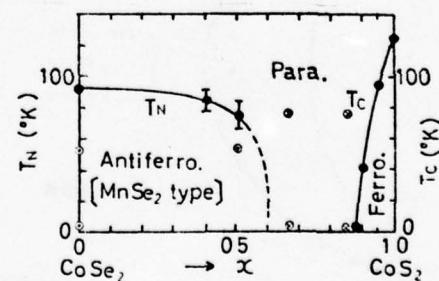
Fig. 155. The magnetic phase diagram of $Co(S_xSe_{1-x})_2$ without magnetic field. The neutron diffraction was done at the points denoted by ⊙ and ⊗. After ref. 233.
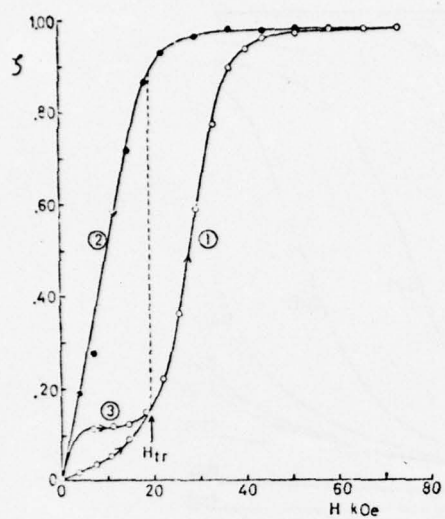
Fig. 156. The magnetization curve of $Co(S_{0.86}Se_{0.14})_2$ at 4.2 K. ζ is the magnetization relative to the saturation moment of CoS_2. The curve labeled, 1, corresponds to an initial increasing field. The curve, 2, corresponds to a decreasing field, while the curve, 3, corresponds to the second increasing field. The transition field, H_{tr}, is defined as the broken vertical line, which divides the hysteresis loop, formed by curves 1 and 2, into equal areas. After ref. 233.
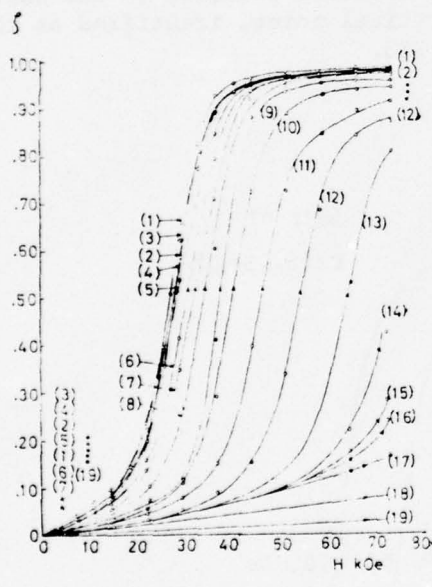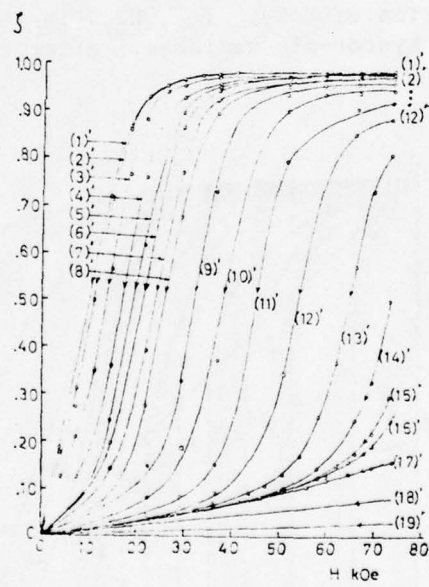
|(a)|(b)|

Fig. 157 (a). The magnetization curves of $Co(S_{0.86}Se_{0.14})_2$ for increasing field at various temperatures in K;
(1) 4.2, (2) 5.8, (3) 9.1, (4) 13.0, (5) 16.5, (6) 19.5,
(7) 22.3, (8) 24.8, (9) 29.5, (10) 33.8, (11) 41.6,
(12) 49.0, (13) 54.5, (14) 60.6, (15) 64.3, (17) 78.0,
(18) 150, (19) 450.
(b). The magnetization curves of $Co(S_{0.86}Se_{0.14})_2$ for decreasing field at various temperatures in K. (1)', (2)'
...(19)' are the same temperature with those given in Fig. (a). The curves (11)' to (19)' are reversible. After ref. 233.
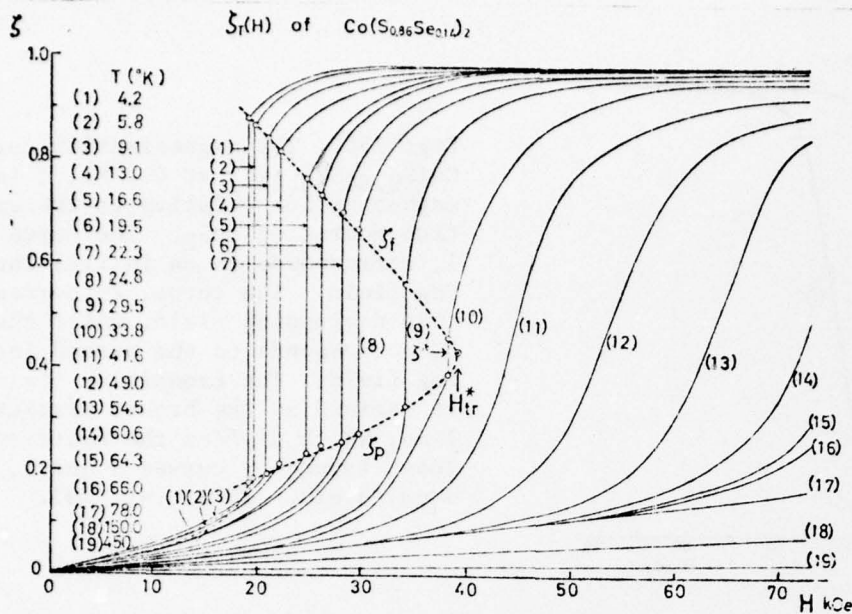
Fig. 158. Magnetization curves defined as the stable state at various temperatures for $Co(S_xSe_{1-x})_2$. The transition fields were connected by the broken curve. The ferromagnetic and the paramagnetic relative magnetization are defined as ζ_f and ζ_p for above and below ζ^*, where ζ is the magnetization relative to the saturation magnetization of CoS_2. (ζ^*, H_{tr}^*) is the critical point, identified as the point where the hysteresis vanishes. After ref. 233.
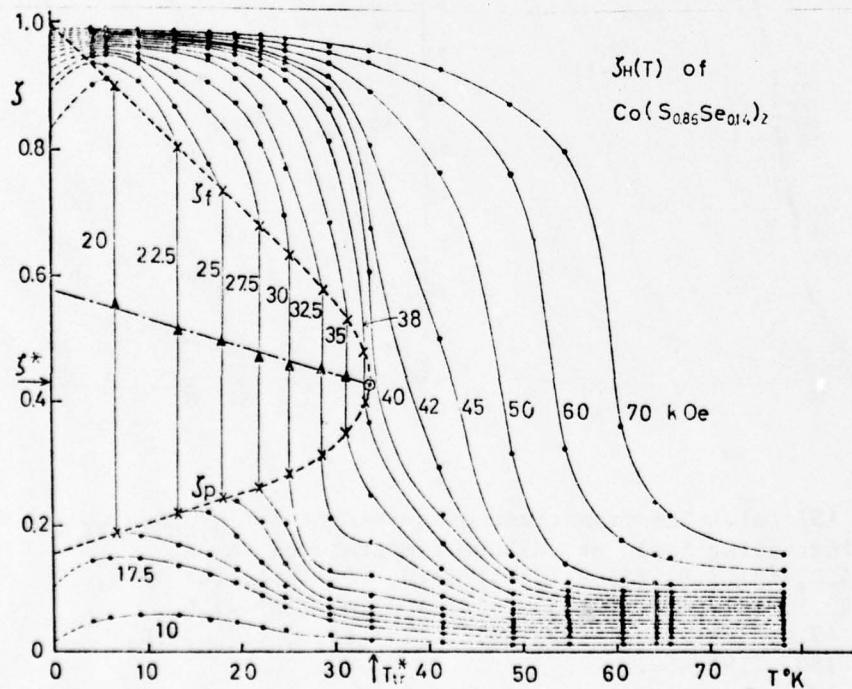
Fig. 159. The thermomagnetic curves in various magnetic field strengths, which is denoted in kOe. The transition temperatures are denoted by χ, the broken curve is the coexistence of ζ_f and ζ_p, and the middle point between ζ_f and ζ_p is denoted by Δ below T_{tr}^*. After ref. 233.
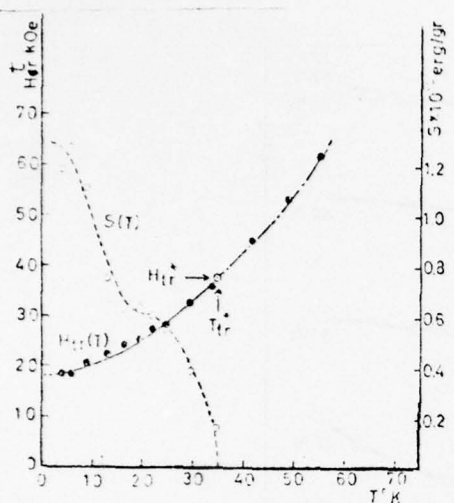
Fig. 160. The temperature dependence
of the area of the hysteresis loop
S(T) erg/gr. (broken curve), which
is obtained from Figs. 157a & 157b.
The transition field versus tempera-
ture $H_{tr}(T)$; the solid curve
corresponds to discontinuous transi-
tions below the critical point T_{tr}^*,
marked by Ⓒ. The chained curve
was obtained from inflection points
on the reversible magnetization curve.
After ref. 233.
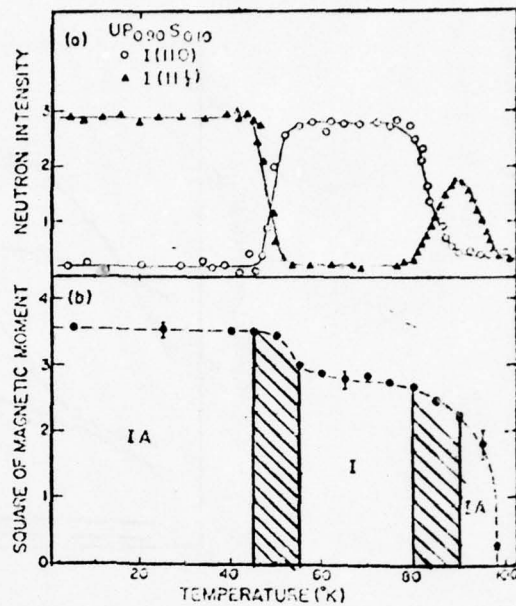
Fig. 161. (a) Intensity of the (110)
and (11 1/2) diffraction peaks of
$UP_{0.90}S_{0.10}$ as a function of tempera-
ture. (b) Magnetic phase diagram
derived from the intensities in (a).
I and IA refer to the antiferro-
magnetic structures, described in
the text. The shaded areas indicate
mixed-phase regions. After ref. 242.
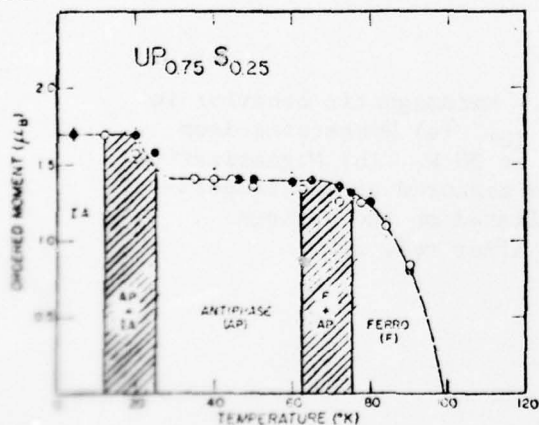
Fig. 162. Ordered moment per
uranium atom in $UP_{0.75}S_{0.25}$ as a
function of temperature. IA rep-
resents the type - IA antiferromagnetic
structure, AP the antiphase configura-
tion and F ferromagnetism. These
structures are described in the text.
The shaded areas indicate mixed
phases. Values taken during cool-
ing are represented by open circles
and those taken on heating by filled
circles. After ref. 246.
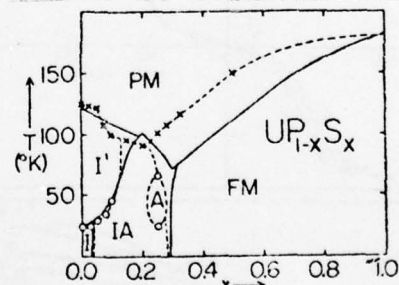
Fig. 163. Magnetic-phase diagram of
$UP_{1-x}S_x$ as a function of tempera-
ture T and composition x. The circles
and crosses are from data in ref. 89.
The solid curves are from the theory
of ref. 243. I, IA are types of
antiferromagnetic ordering. I' is
the "low moment" phase of type I;
FM is ferromagnetism; PM is paramag-
netism; A is antiphase magnetic
structure. After ref. 243.
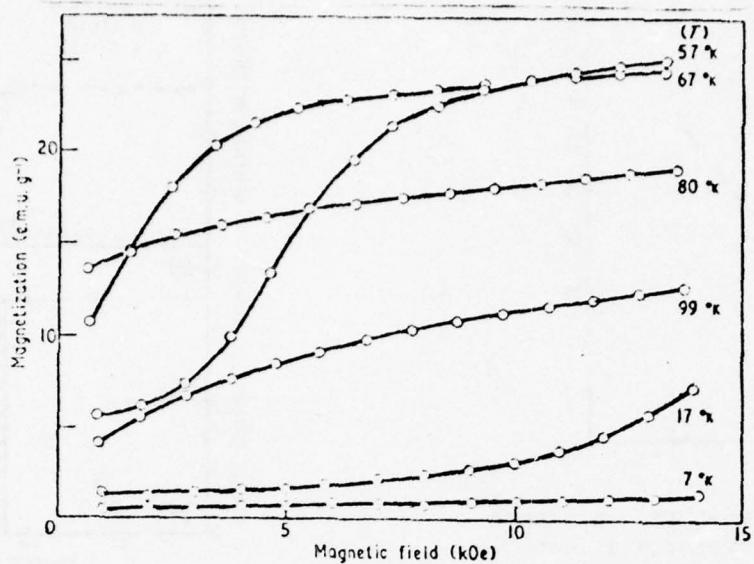
Fig. 164. Variation of magnetization of UP$_{0.75}$S$_{0.25}$ with field (corrected for demagnetization) at various fixed temperatures. After ref. 247.
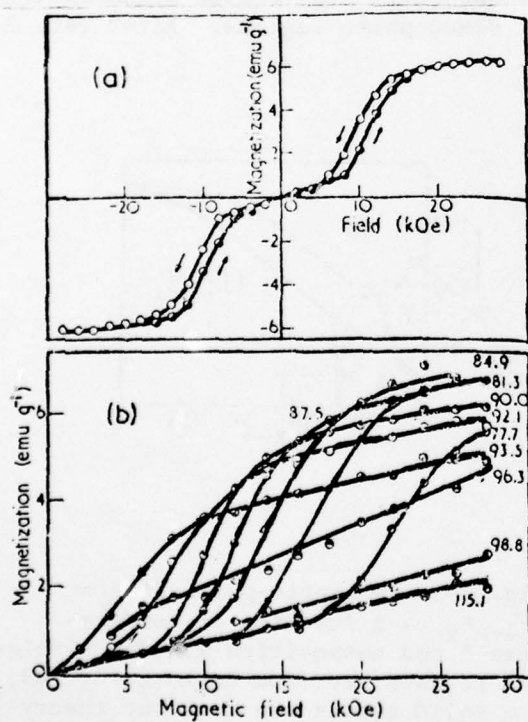
Fig. 165. Metamagnetic behavior in UP$_{0.90}$S$_{0.10}$. (a) Hysteresis loop measured at 90 K. (b) Magnetization isotherms measured at the temperature indicated on the various curves. After ref. 242.

```
N = 5    + + − − + + · · ·
N = 7    + + − − − − + · + · · ·
N = 9    + + + − − − − + + · · · ·
N = 11   + + + − − − − − + + · + + · + · · ·
```

Fig. 166. Possible stacking arrangements of the ferromagnetic layers of the $UAs_{1-x}Se_x$ system. After ref. 248.
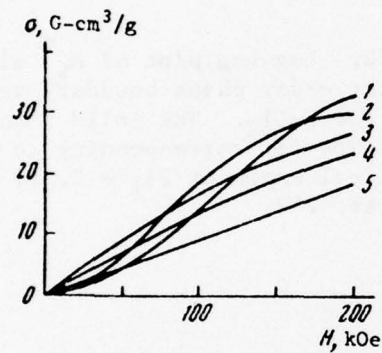
Fig. 167. Magnetization isotherms of $UAs_{0.75}Se_{0.25}$: 1. 80 K, 2. 100 K, 3. 120 K, 4. 130 K, 5. 140 K. After ref. 250.
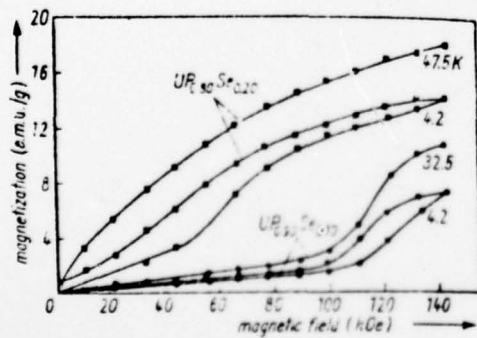
Fig. 168. Magnetization isotherms of $UP_{0.80}Se_{0.20}$ and $UP_{0.90}Se_{0.10}$. After ref. 251.
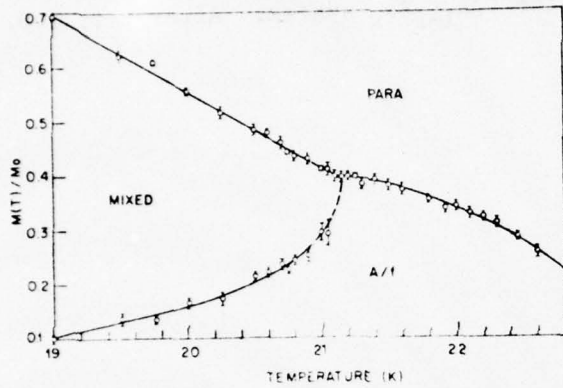
Fig. 169. M-T phase diagram for
$FeCl_2$. After ref. 253.
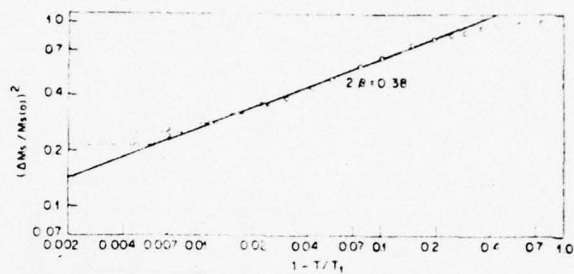
Fig. 170. Log-Log plot of M_s^2 along
the first order phase boundary versus
(T_t-T) for $FeCl_2$. The solid line is
a power law fit corresponding to the
tricritical exponent $2\beta_1 = 0.38$.
After ref. 253.
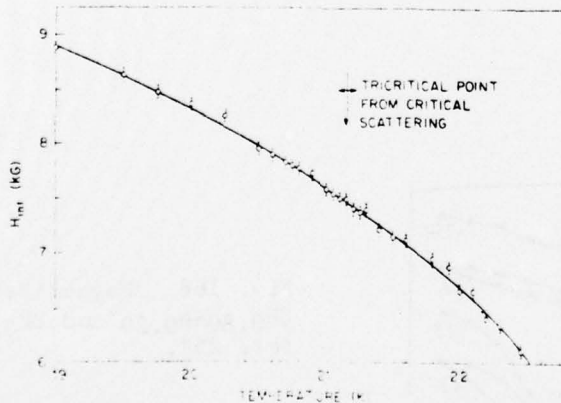
Fig. 171. H_1-T phase diagram for
$FeCl_2$. After ref. 253.
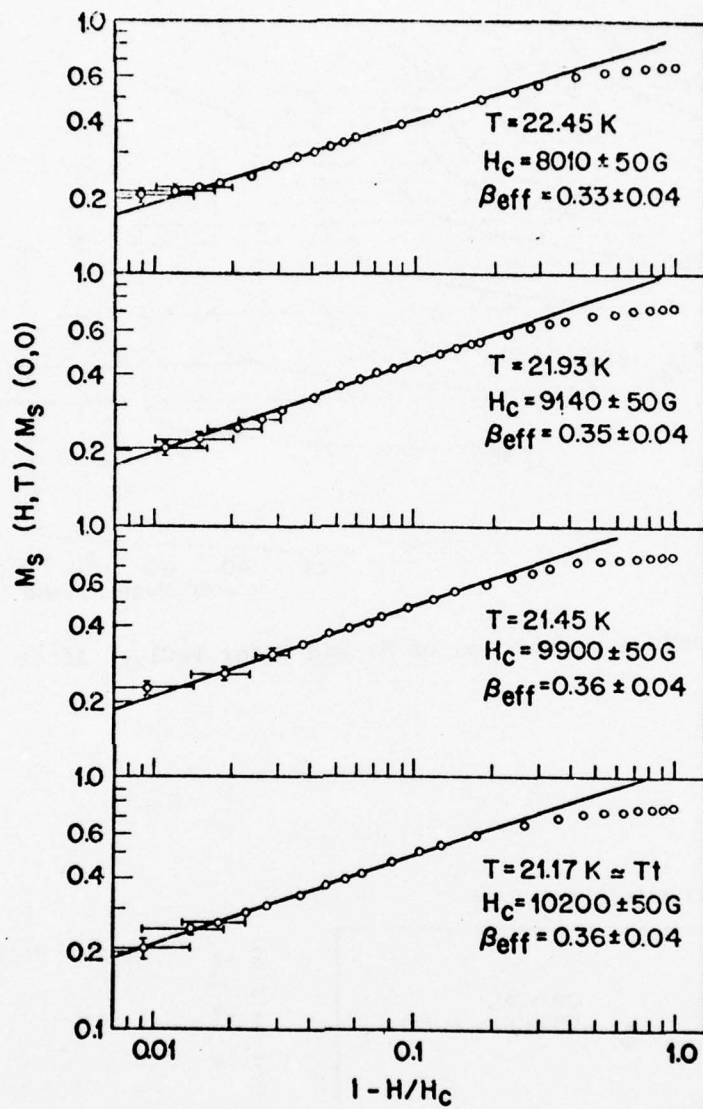
Fig. 172. Log-Log plot of M_S versus field for $FeCl_2$ for temperatures corresponding to (a–c) the critical line and (d) the tricritical point. After ref. 253.
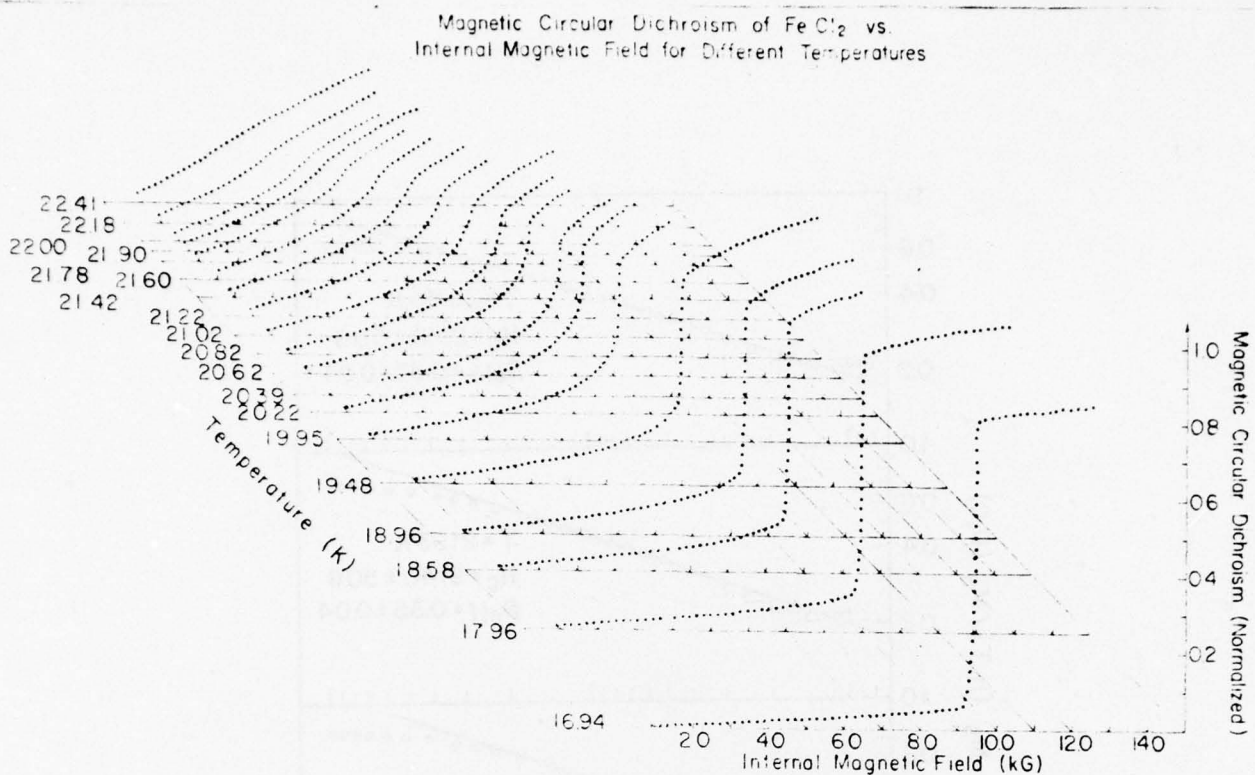
Fig. 173. MCD as a function of H_i and T for $FeCl_2$. After ref. 67.
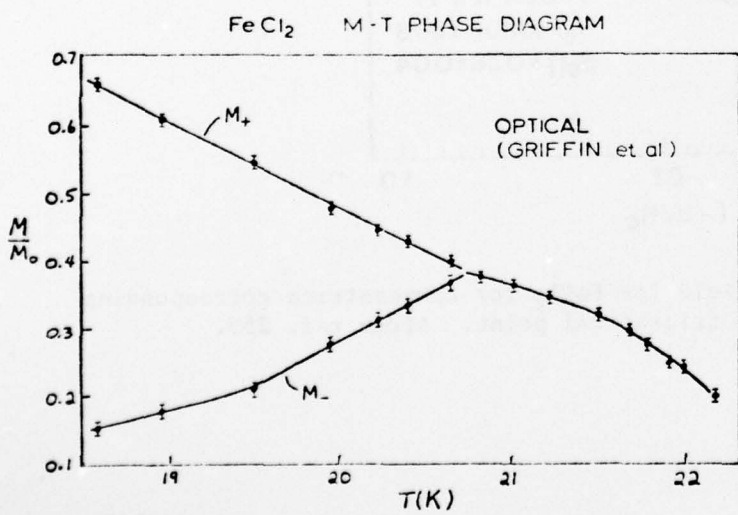
Fig. 174. M-T phase diagram for $FeCl_2$ derived from the MCD data of fig. 173. After ref. 255.
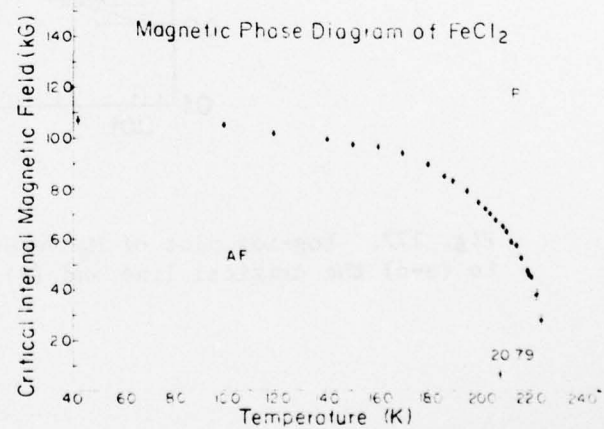
Fig. 175. H_i-T phase diagram for $FeCl_2$ derived from the MCD data of fig. 173. After ref. 67.
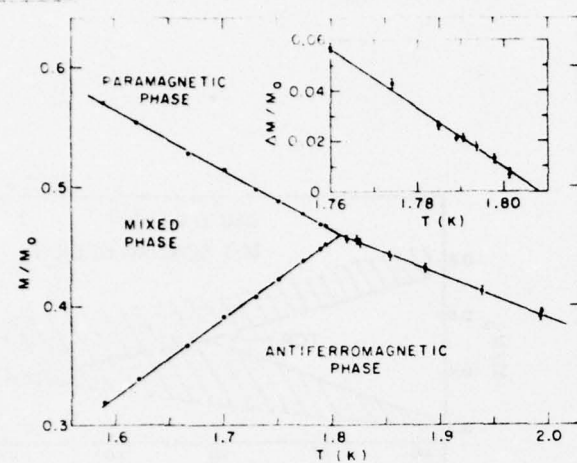
Fig. 176. M-T phase diagram for DAG
for fields along [110] after ref. 256.
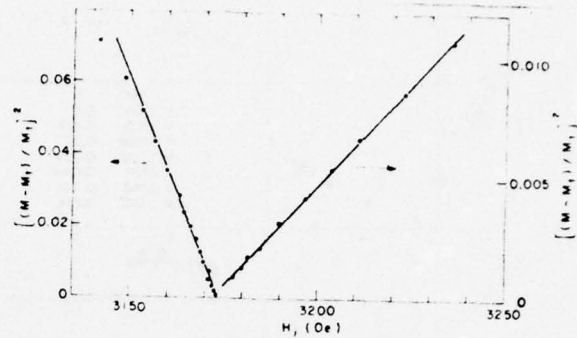
Fig. 177. $((M-M_t)/M_t)^2$ versus H_i for
$T = T_t$ for DAG for fields parallel to
[110]. After ref. 256.
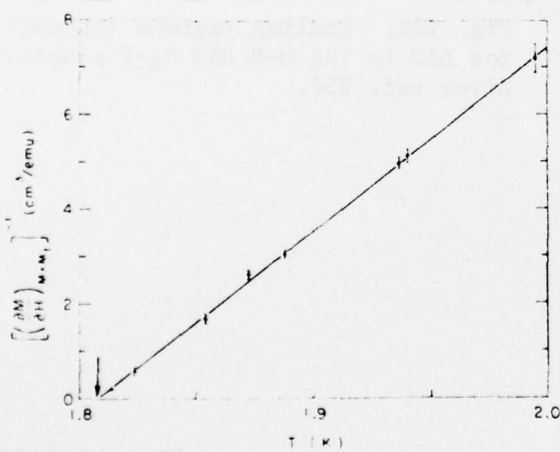
Fig. 178. $((\partial M/\partial H_i)_T)^{-1}$ for $M = M_t$
versus T for DAG for fields along [110].
After ref. 256.
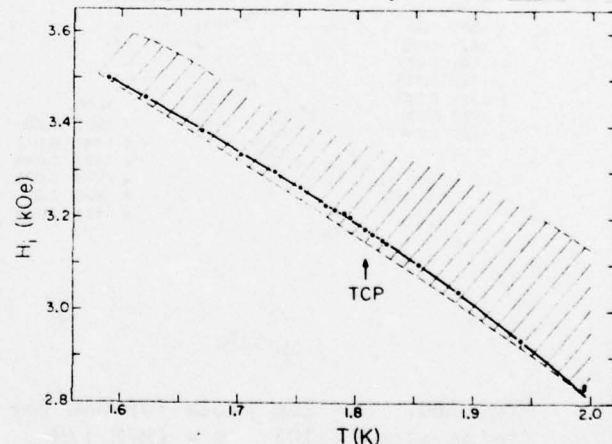
Fig. 179. H_i-T phase diagram for DAG
for fields along [110]. After ref.
257. The shaded region is the scal-
ing region.
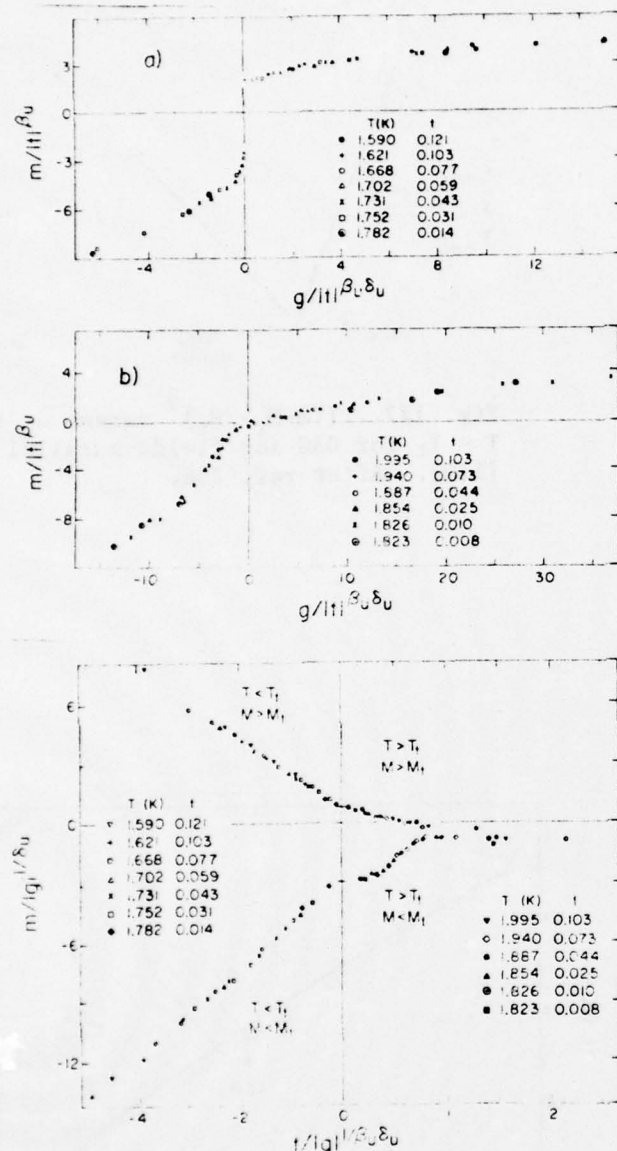
Fig. 180. Scaling plots for DAG for fields along [110]. $m = (M-M_t)/M_t$. See section II for definitions of the various symbols. After ref. 257.
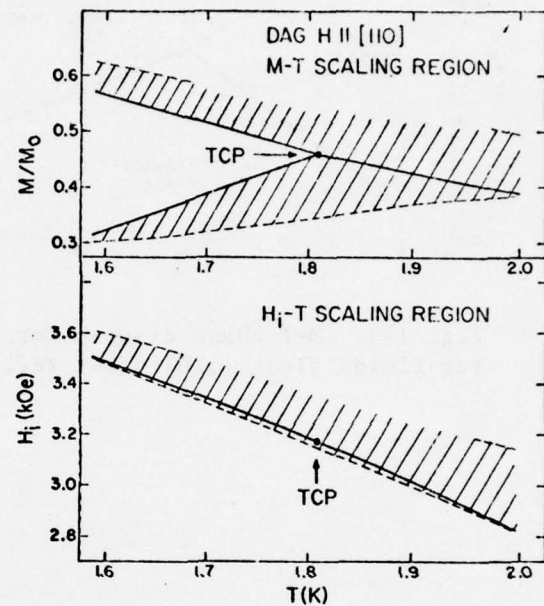
Fig. 181. Scaling regions (shaded) for DAG in the M-T and H_i-T planes. After ref. 257.
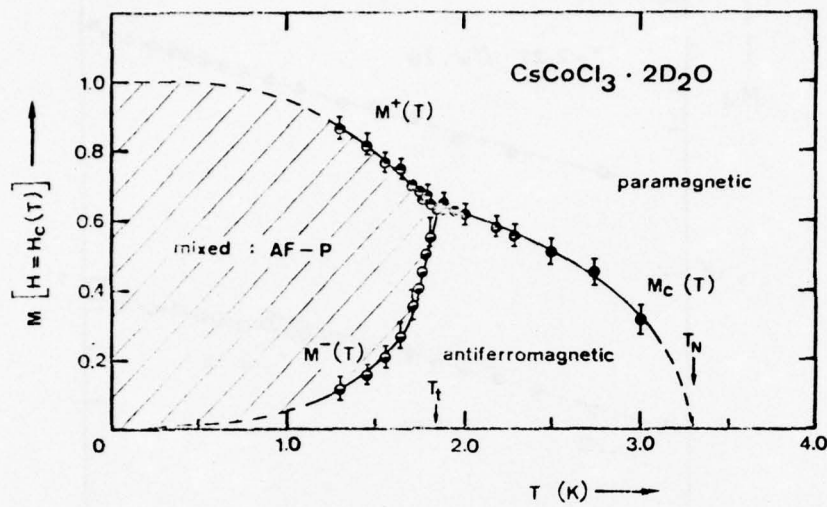
Fig. 182. M-T phase diagram for $CsCoCl_3 \cdot 2D_2O$. After ref. 260.
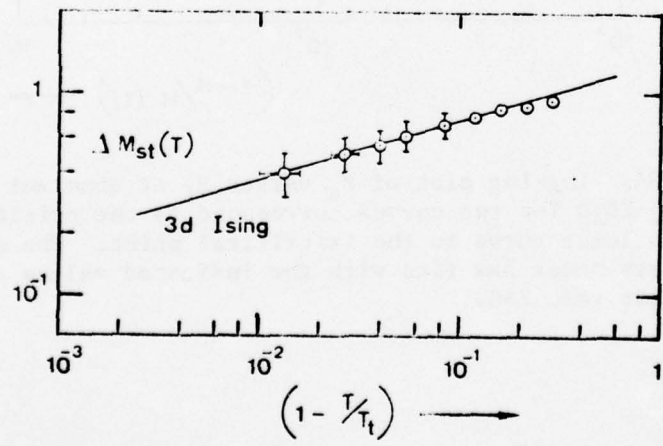
Fig. 183. Log-Log plot of M_s along the first order phase boundary versus $(T_t - T)$. The solid line is a fit to a power law corresponding to $\beta_1 \simeq 0.31$. After ref. 260.
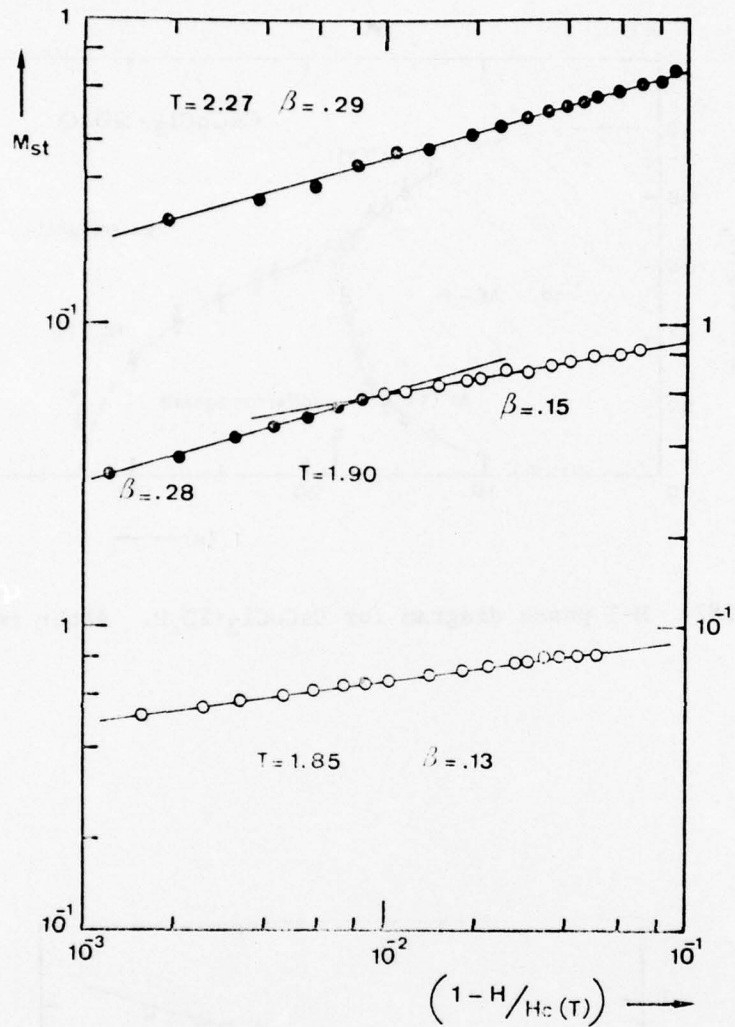
Fig. 184. Log-Log plot of M_s versus H_i at constant T for $CsCoCl_2 \cdot 2D_2O$ Top two curves correspond to the critical line, and the lower curve to the tricritical point. The solid lines are power law fits with the indicated values of exponent β. After ref. 260.

M_st / |x_3|^{β_tr}

CsCoCl_3 · 2D_2O

2.5

T < T_t

2.0

T > T_t

1.5

T_t = 1.85 K
β_t = 0.15
β_tr = 0.30
φ = 2.0

1.0

0.5

x_2 / |x_3|^φ

0   − 25   − 50   − 75   − 100

M_st / |x_2|^{β_t}

CsCoCl_3 · 2D_2O

1.5

1.0

○ T = 1.63
● T = 1.71
○ T = 1.75
● T = 1.775
¢ T = 1.80
⊟ T = 1.905
⊠ T = 1.945
▫ T = 2.00
■ T = 2.19
◪ T = 2.27

0.5

T_t = 1.85 K
β_t = 0.15
β_tr = 0.30
φ = 2.0

x_3 / |x_2|^{1/φ}

− 1.5   − 1.0   − 0.5   0.5   1.0   1.5   2.0   2.5
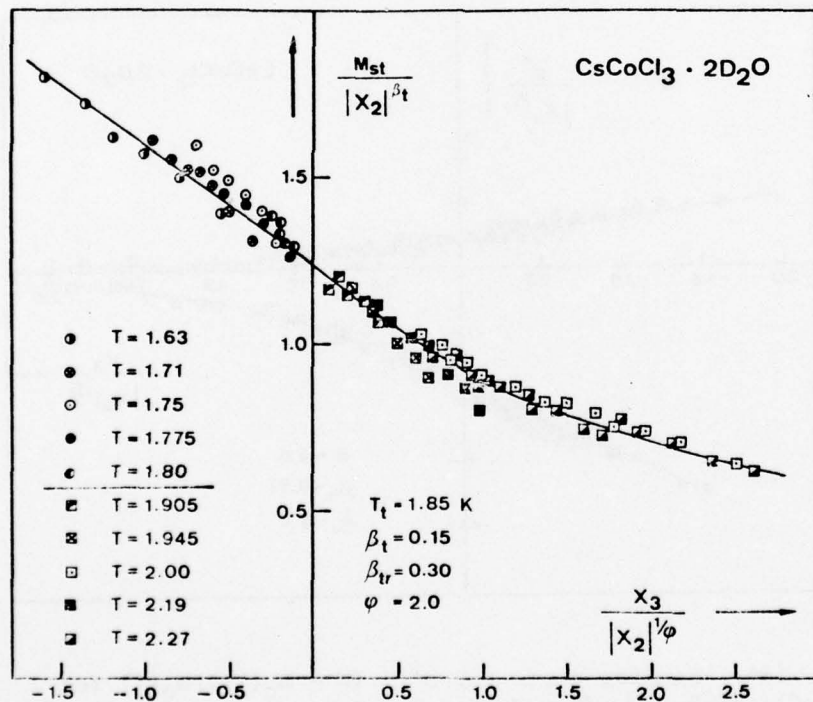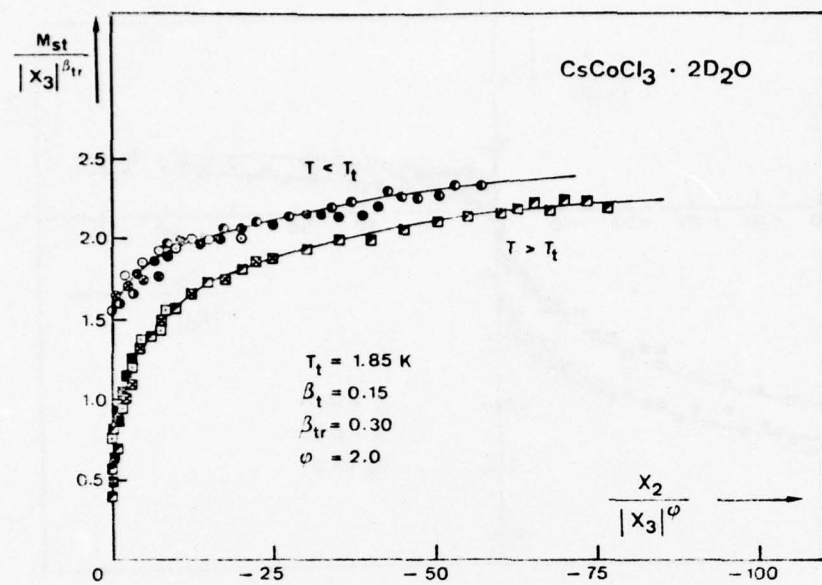
Fig. 185.   Scaling plots for the staggered magnetization, M_{st}, for $CsCoCl_3 \cdot 2D_2O$. x_2 and x_3 correspond to the variables g' and t in section II, and $β_{tr}$ is equal to $β_t/φ$. After ref. 260.
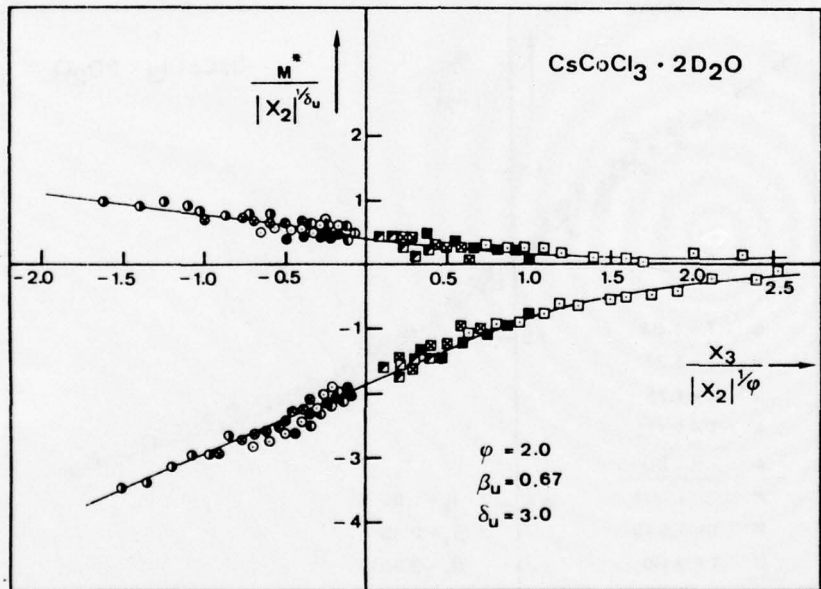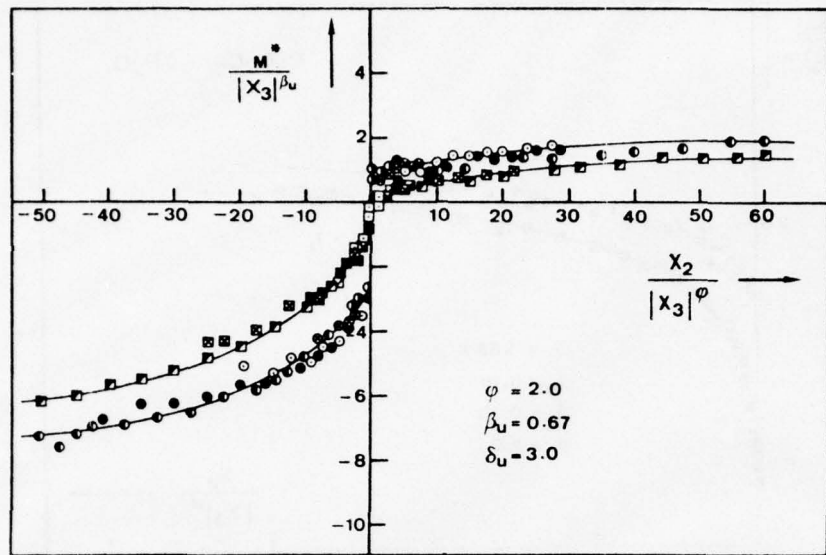
Fig. 186. Scaling plots for $M^* = (M - M_c(T))/M_c(T)$ for $CsCoCl_3 \cdot 2D_2O$. $M_c(T) = M_t$ for $T < T_t$, and corresponds to the critical line for $T > T_t$. x_2 and x_3 correspond to the variables g' and t in section II. After ref. 260.
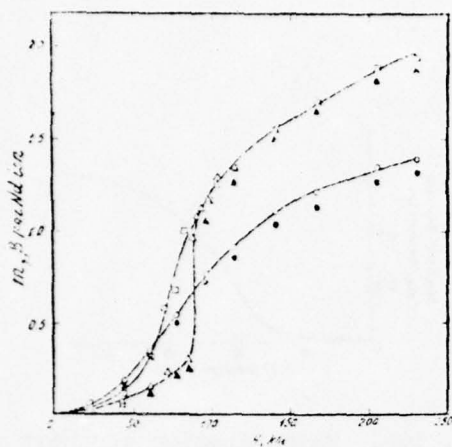
Fig. 187. Magnetic moment versus field for powder samples of Ndx. X = S-0, 0 Se- ; Te-Δ, Δ at 1.6 and 4.2 K, respectively. After ref. 262.
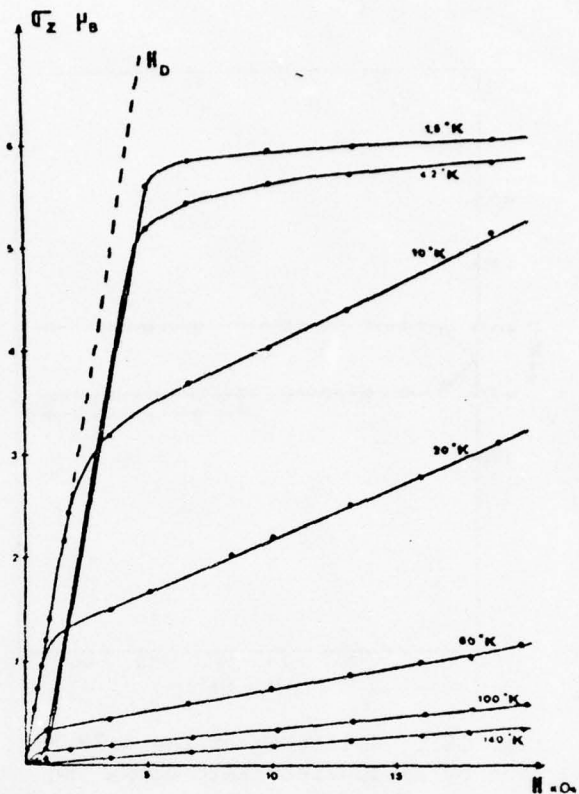

Fig. 188. Magnetization isotherms of $ErCrO_3$ as a function of external field H_z. After ref. 263.

OMn ○C ∘H_2O(above)
○O ⊕H_2O(2) ⊕H_2O(below)
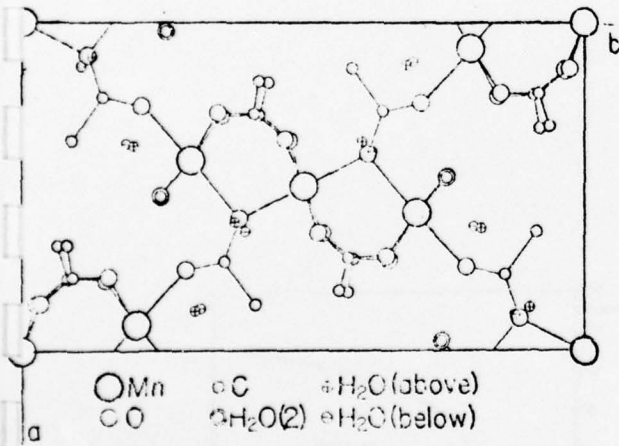
Fig. 189. The structure of $Mn(COOCH_3)_2 \cdot 4H_2O$. The projection is along the perpendicular c^* direction. Two water molecules in the Mn_2 coordination octahedron which are shown superimposed are actually one above and one below the Mn plane. After ref. 264.
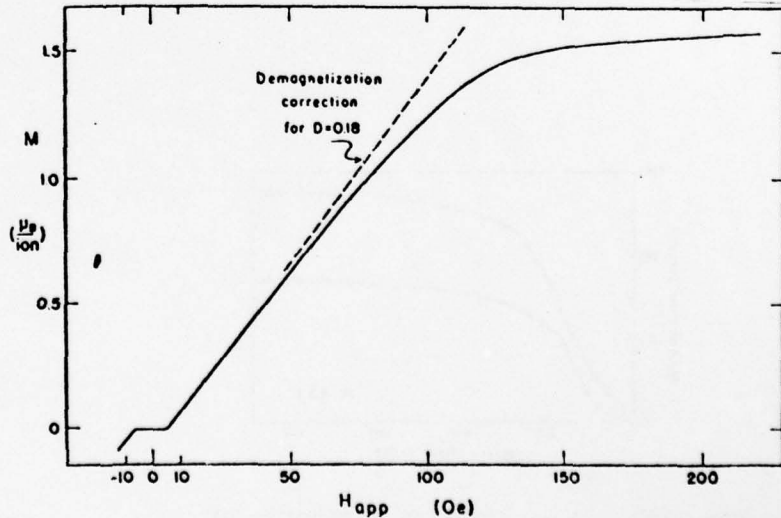
Fig. 190. Magnetization isotherm of $Mn(CH_3COO)_2 \cdot 2H_2O$ at 1.41 K with H || a axis. After ref. 265.
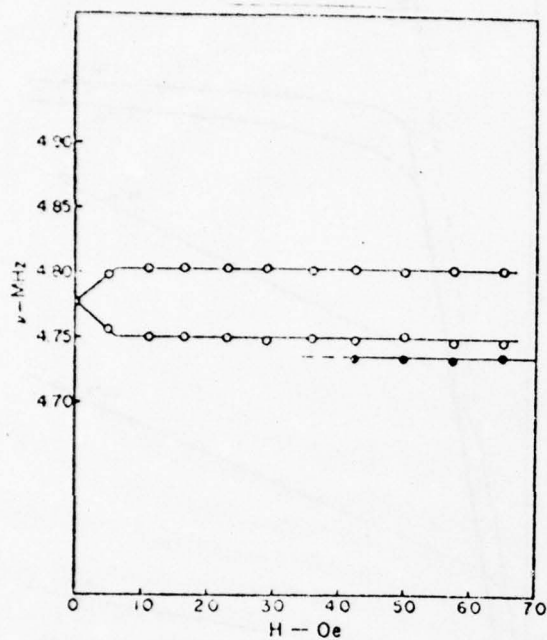
Fig. 191. Splitting of the 4.78 MHz
line by an applied field along the
a axis. The metamagnetic transition
occurs at ≃ 6 Oe. The resonances
from antiferromagnetic material are
indicated with open circles. Resonances
from saturated paramagnetic material
are indicated with solid circles.
After ref. 265.
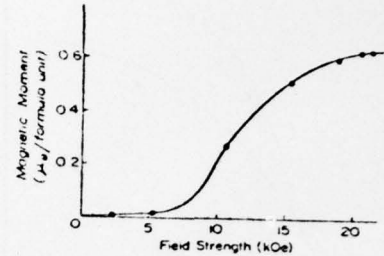
Fig. 192. Magnetization isotherm of
a powder sample of CeAl at 4.2 K.
After ref. 266.
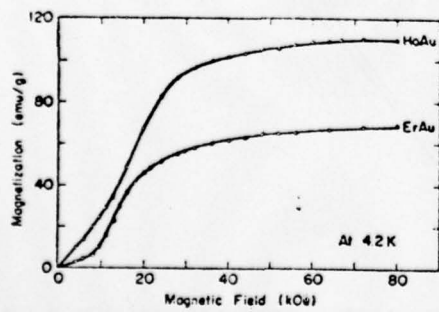
Fig. 193. Magnetization isotherms of
powder samples of HoAu and ErAu at
4.2 K. After ref. 267.
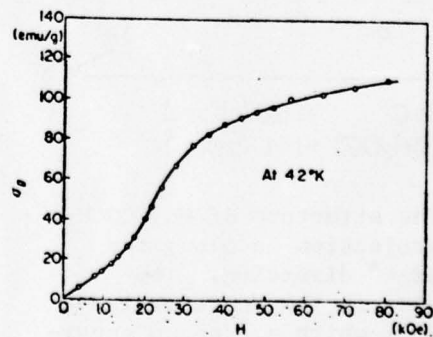
Fig. 194. Magnetization isotherm of
powder sample of DyAu at 4.2 K. After
ref. 268.
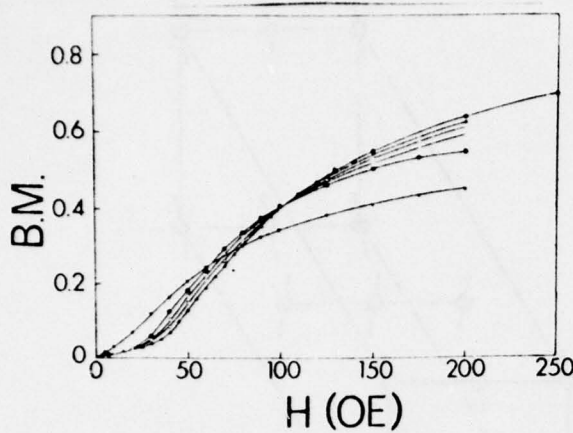
Fig. 195. Polycrystalline magnetization data at 4.2 K (●), 4.52 K (▲), 5.52 K (□), 6.86 K (○), 7.34 K (*), and 8.65 (▼). Solid lines have been drawn through the data as a visual aid. After ref. 269.
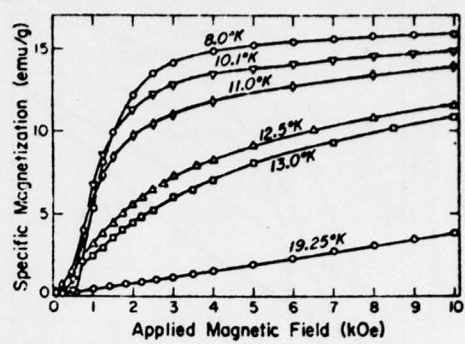
Fig. 196. Magnetization isotherms of a powdered sample of neptunium (V) oxalate. Note the S-shaped character of the isotherms for 8.0, 10.1 and 11.0°K, indicating metamagnetic behavior. After ref. 270.
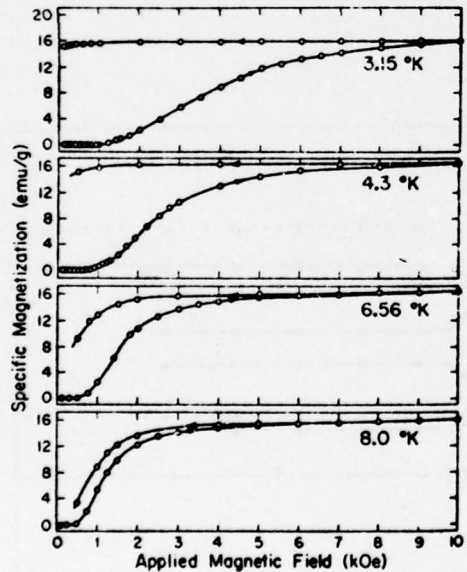

Fig. 197. Magnetization isotherms of neptunium (V) oxalate below $T^* \sim 9°K$, showing magnetic hysteresis in steady-field measurements. After ref. 270.
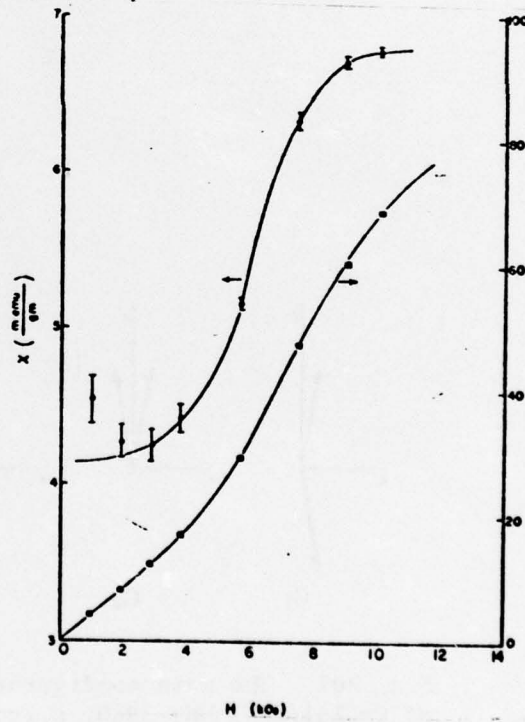

Fig. 198. Susceptibility (left scale) and magnetization (right scale) of ortho-$HoMnO_3$ at 4.2 K as a function of applied magnetic field. After ref. 271.
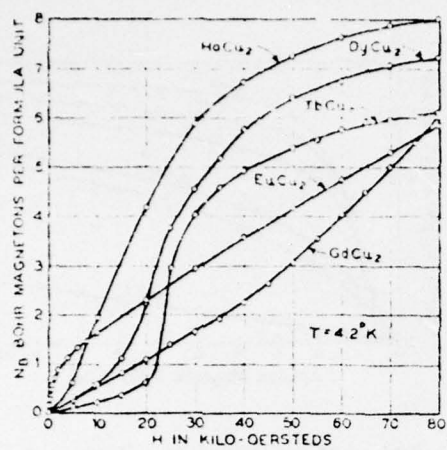
Fig. 199. Magnetization curves measured at 4.2°K for some of the RCu_2 compounds. After ref. 272.
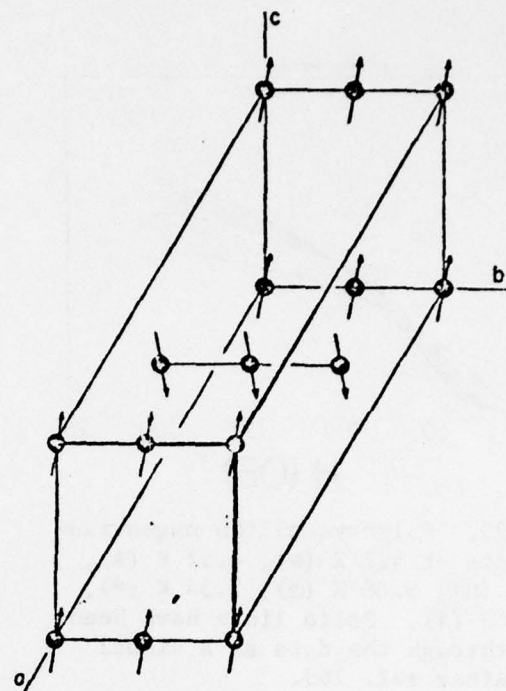
Fig. 200. The spin arrangement in the ordered state of $CoCl_3[(CH_3)_3NH]\cdot 2H_2O$. After ref. 274.
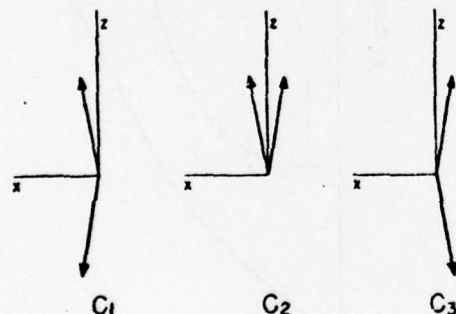
Fig. 201. The spin configurations of $CoCl_3[(CH_3)_3NH]\cdot 2H_2O$, c_1, c_2 and C_3. C_1 and C_3 are equally present in the zero field antiferromagnetic state. C_2 is the field induced state. After ref. 274.
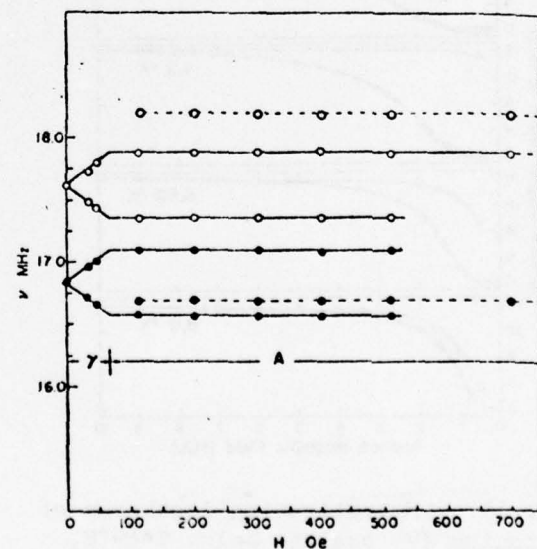
Fig. 202. Resonance frequencies of the water protons with H parallel to the c axis. Solid lines are resonances from material with a C_1+C_3 spin configuration. Dashed lines are resonances from material with a C_2 spin configuration. $T = 2.25°K$. After ref. 275.
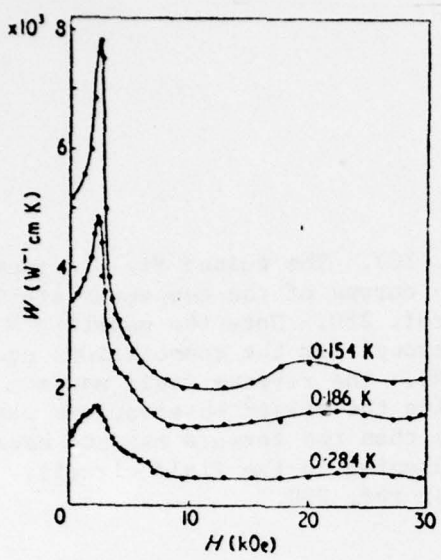
Fig. 203. The thermal resistivity, W, of $ErVO_4$ versus applied field. H is parallel to the c-axis and to the heat flow. After ref. 276.
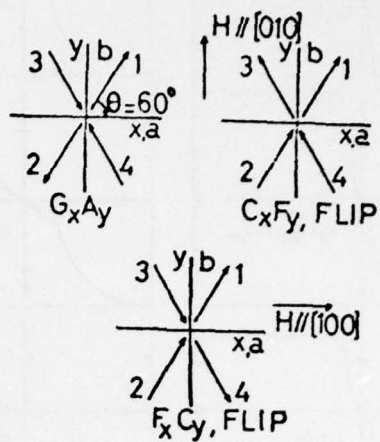
Fig. 204. Magnetic structure of $DyCoO_3(G_xA_y)$ and possible effect of a magnetic field. After ref. 279.
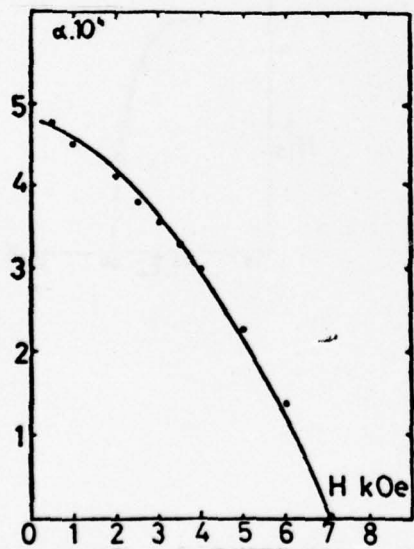
Fig. 205. Metamagnetic behavior demonstrated by the magnetoelectric effect on a powder sample of $DyCoO_3$ at a temperature slightly below $T_N=3.6$ K. After ref. 277.
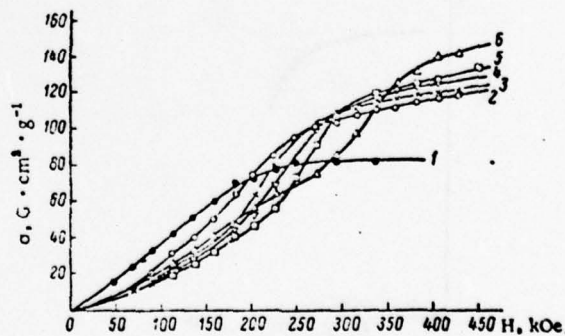
Fig. 206. Mn_3B_4 magnetization isotherms: T, °K: 1) 294; 2) 180; 3) 153; 4) 139; 5) 122; 6) 83. After ref. 279.
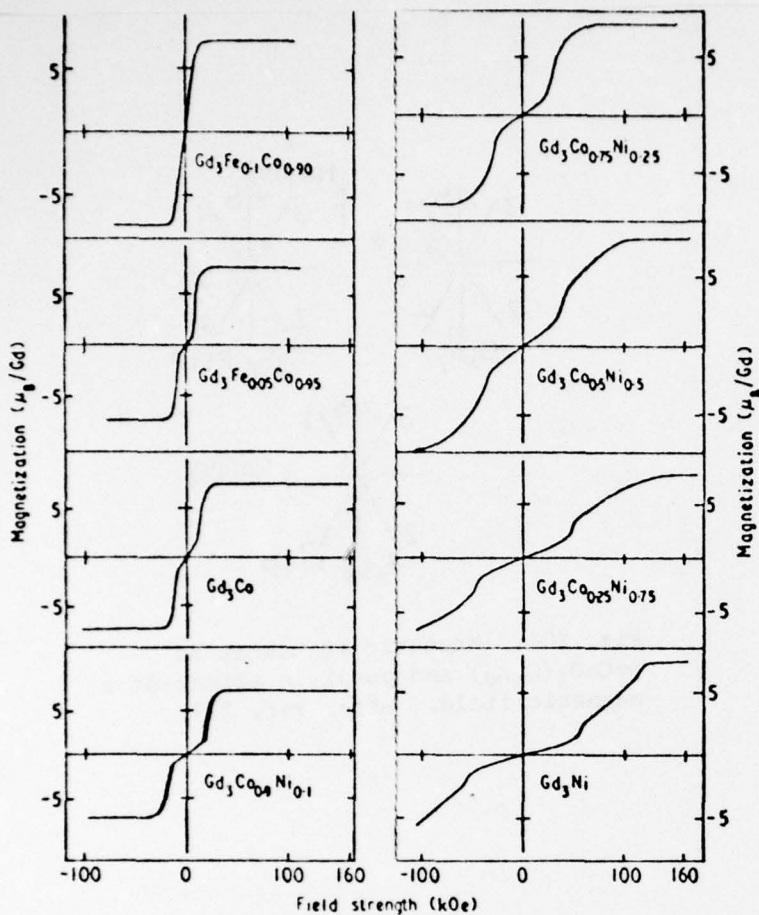
Fig. 207. The pulsed field magnetization curves of the compounds studied in ref. 280. Note the negative M intercept for the compositions near Gd₃Ni. The reverse field maximum during the pulsed observations was less than the forward maximum because of damping in the field circuit. After ref. 280.
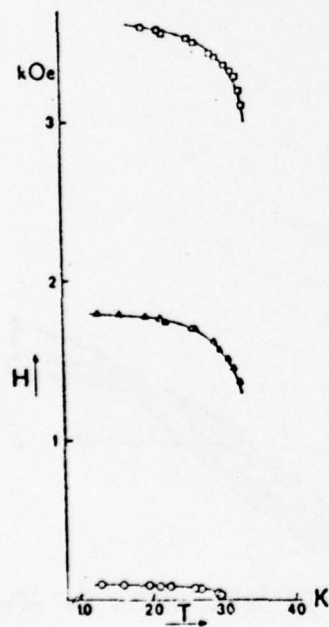
Fig. 208. Transition fields versus temperature for H ‖ c axis of RbCoCl₃·2H₂O. After ref. 281.
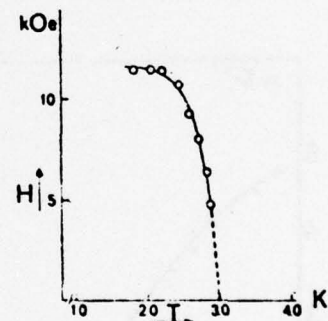
Fig. 209. Transition fields versus temperature for H ‖ b-axis of RbCoCl₃·2H₂O. After ref. 281.
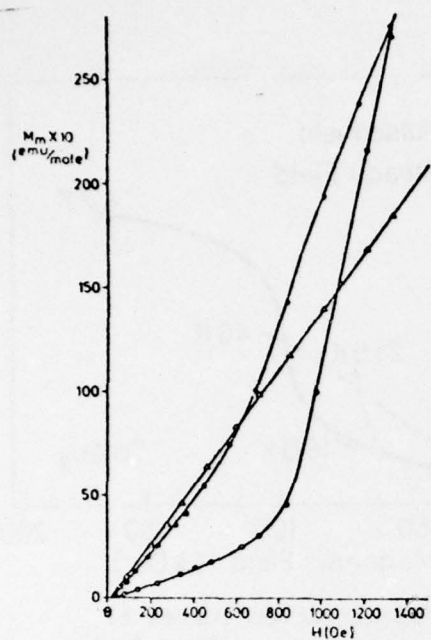
Fig. 210. Magnetization isotherms of $NiBr_2(pz)_2$. O: T = 2.2 K, O: T = 2.9 K, Δ = T = 4.2 K. After ref. 282.
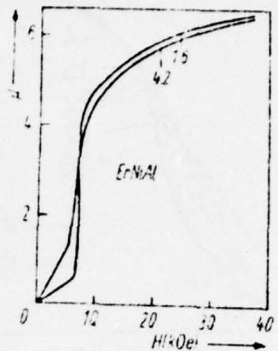
Fig. 211. Magnetic moment versus internal field for a powder sample of ErNiAl. After ref. 284.
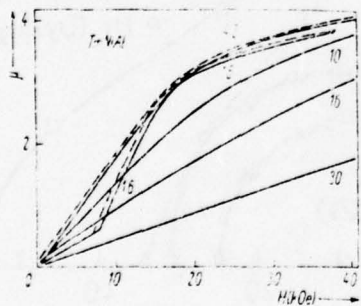
Fig. 212. Magnetic moment versus internal field for a powder sample of TmNiAl. The dashed curves represent measurements with decreasing fields. After ref. 284.
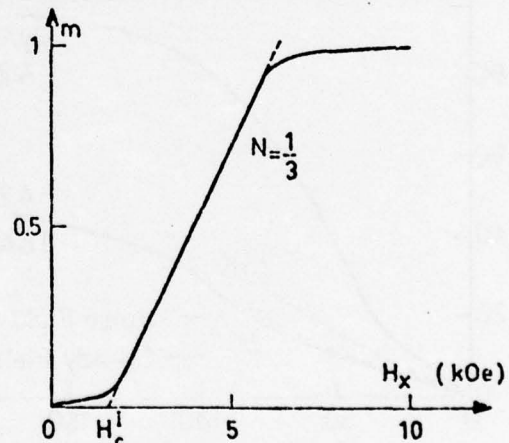
Fig. 213. Magnetization isotherm of spherical single crystal of $TbFeO_3$ at 1.15 K. After ref. 285.
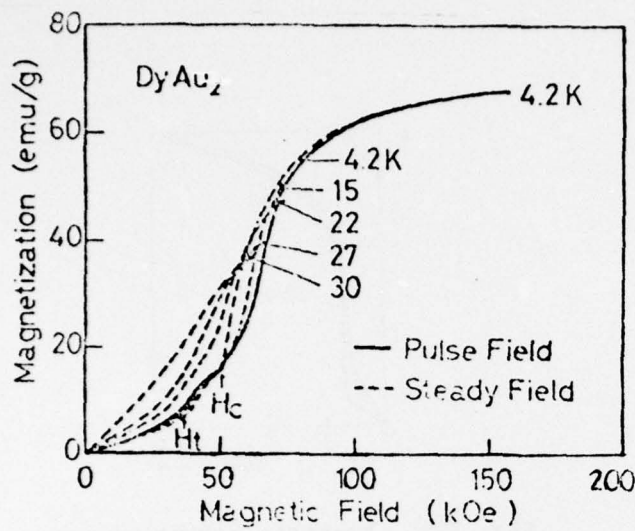
Fig. 214. Magnetization curves of DyAu$_2$, ———: under the pulsed field, ...: under the steady field. After ref. 286.
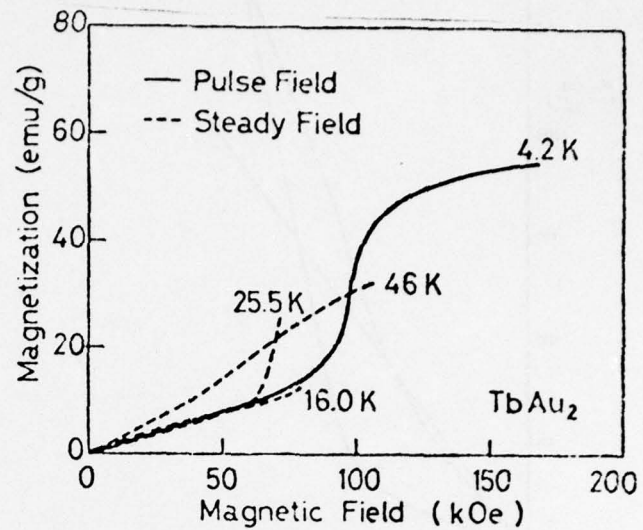
Fig. 215. Magnetization curves of TbAu$_2$, ———: under the pulsed field, ...: under the steady field. After ref. 286.
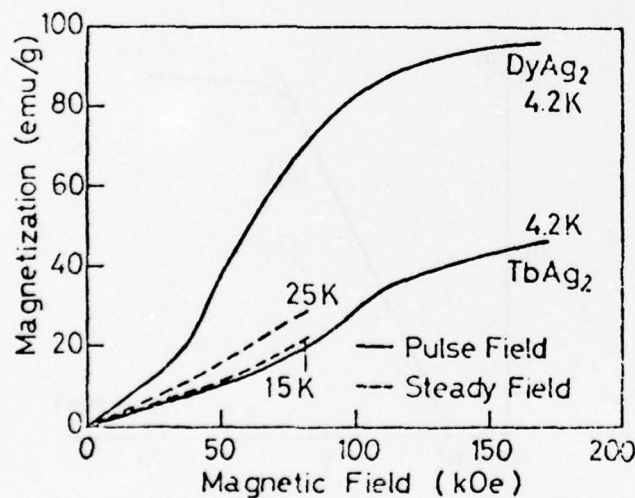
Fig. 216. Magnetization curves of DyAg$_2$ and TbAg$_2$, ———: under the pulsed field, ...: under the steady field. After ref. 286.
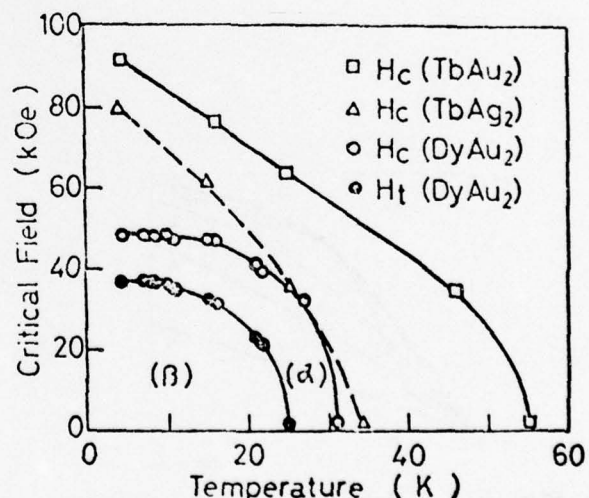
Fig. 217. Magnetic phase diagrams of DyAu$_2$, TbAu$_2$ and TbAg$_2$. H$_t$ is the field for transition from the β-state to the α-state of DyAu$_2$. After ref. 286.
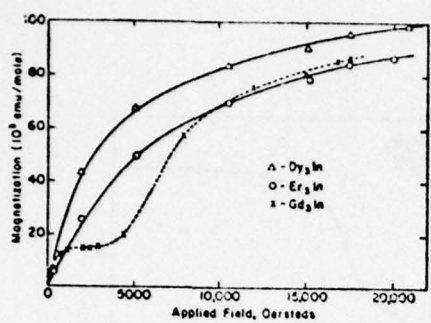
Fig. 218. Magnetization isotherms for Gd$_3$In(x). The isotherms for Dy$_3$In (Δ) and Er$_3$In (O) are also shown. After ref. 287.
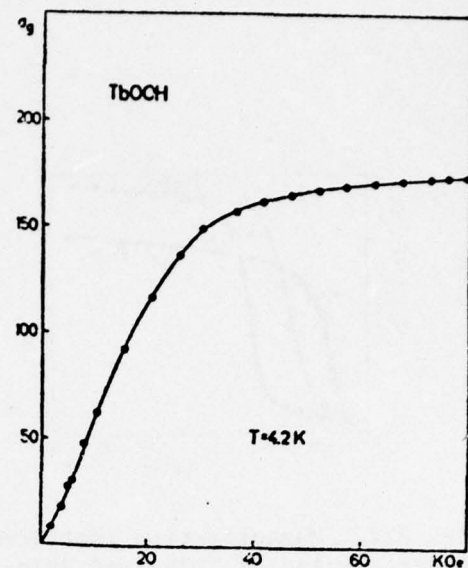
Fig. 219. Magnetization isotherm of powder sample of TbOOH at 4.2 K. After ref. 288.
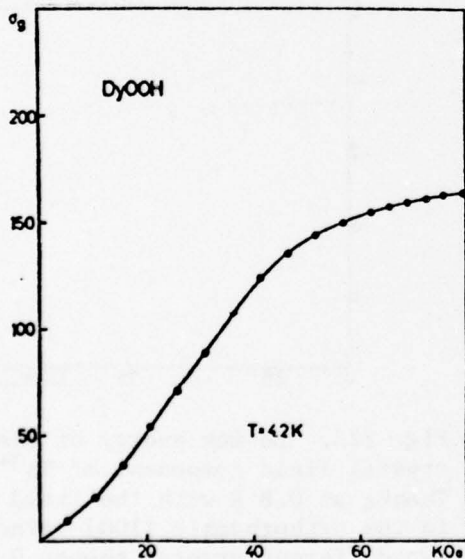
Fig. 220. Magnetization isotherm of powder sample of DyOOH at 4.2 K. After ref. 288.
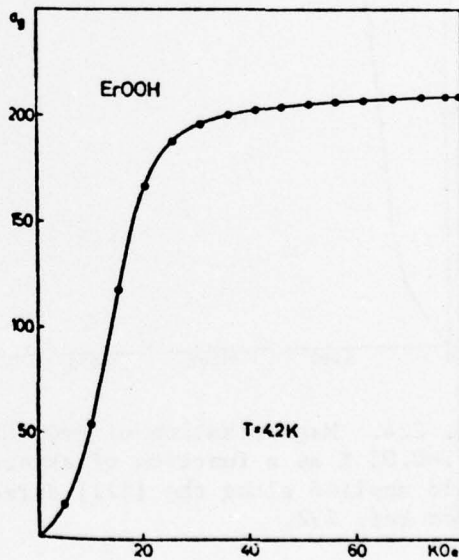
Fig. 221. Magnetization isotherm of powder sample of ErOOH at 4.2 K. After ref. 288.
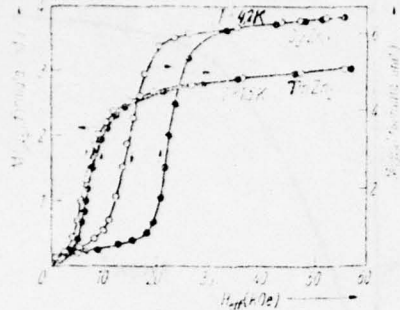
Fig. 222. Magnetization isotherms of powder samples of $TmZn_2$ and $DyZn_2$. After ref. 290.
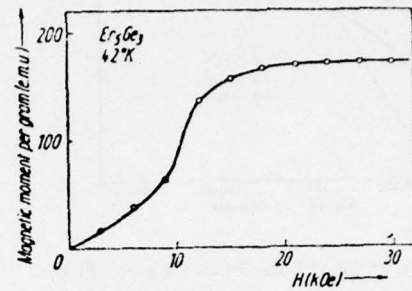
Fig. 223. Magnetization isotherm of powder sample of Er_5Ge_3. After ref. 291.
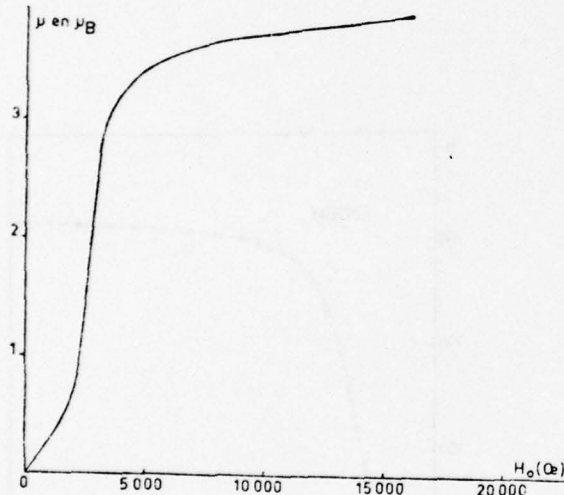
Fig. 224. Magnetization of ErGa Garnet at T=0.08 K as a function of external field applied along the [111] direction. After ref. 292.
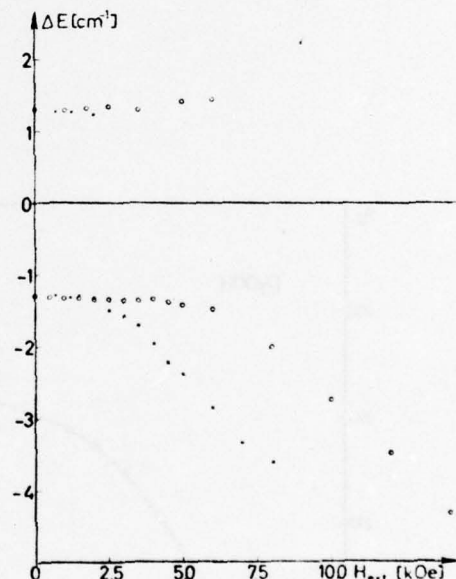
Fig. 225. Zeeman energy of the lowest crystal field component of Tb^{3+} in $TbAsO_4$ at 0.8 K with the field applied in the orthorhombic [100] direction for two different crystal shapes 0 and X.

List of References

1. H.A. Kramers, unpublished (see ref. 2).

2. I.S. Jacobs and P.E. Lawrence, Phys. Rev. $\underline{164}$, 866 (1967).

3. C.S. Koonce, B.W. Mangum and D.D. Thornton, Phys. Rev. B$\underline{4}$, 4075 (1971).

4. H.E. Stanley, Introduction to Phase Transitions and Critical Phenomena, (Oxford University Press 1971).

5. R.B. Griffiths, Phys. Rev. Lett. $\underline{24}$, 715 (1970).

6. H. Weitzel and W. Schneider, Solid State Commun. $\underline{14}$, 1025 (1974).

7. W. Schneider and H. Weitzel, Solid State Commun. $\underline{13}$, 303 (1973).

8. K. Yamada and J. Kanamori, Prog. Theor. Phys. $\underline{38}$, 541 (1967).

9. Y. Shapira and S. Foner, Phys. Rev. B$\underline{1}$, 3083 (1970).

10. K.W. Blazey, H. Rohrer and R. Webster, Phys. Rev. B$\underline{4}$, 2287 (1971).

11. J.M. Kincaid and E.D.G. Cohen, Phys. Rep. C$\underline{22}$, 57 (1975).

12. J.M. Kincaid and E.D.G. Cohen, Phys. Lett. A$\underline{50}$, 317 (1974).

13. See for example, M.E. Fisher, Rev. Mod. Phys. $\underline{46}$, 597 (1974).

14. E.K. Riedel and F.J. Wegner, Phys. Rev. Lett. $\underline{29}$, 349 (1972); F.J. Wegner and E.K. Riedel, Phys. Rev. B$\underline{7}$, 248 (1973).

15. D.R. Nelson and M.E. Fisher, Phys. Rev. B$\underline{11}$, 1030 (1975).

16. M.E. Fisher and D.R. Nelson, Phys. Rev. B$\underline{12}$, 263 (1975).

17. R. Bausch, Z. Phys. $\underline{254}$, 81 (1972).

18. F. Harbus and H.E. Stanley, Phys. Rev. B$\underline{8}$, 1141 (1973); ibid B$\underline{8}$, 1156 (1973); see also ref. 19.

19. M. Wortis, F. Harbus and H.E. Stanley, Phys. Rev. B$\underline{11}$, 2689 (1975).

20. D.M. Saul, M. Wortis and D. Stauffer, Phys. Rev. B$\underline{9}$, 4964 (1974).

21. J.C. Bonner and J.F. Nagle, Annu. Rev. Phys. Chem. (to be published). This is a review article and contains extensive references to earlier work.

22. R.B. Griffiths, Phys. Rev. B7, 545 (1973).

23. See for example, L.P. Kadanoff in Proceedings of the International
    School of Physics Enrico Fermi, M.S. Green, ed. (Academic Press 1971).

24. See for example, R.B. Griffiths, Phys. Rev. Lett. 24, 1479 (1970).

25. D.R. Nelson and J. Rudnick, Phys. Rev. Lett. 35, 178 (1975).

26. V.J. Emery, Phys. Rev. B11, 3397 (1975).

27. M.J. Stephen, E. Abrahams and J.P. Straley, Phys. Rev. B12, 256 (1975).

28. M.E. Fisher, Rep. Progr. Phys. 30, 615 (1967).

29. E.K. Riedel, Phys. Rev. Lett. 28, 675 (1972).

30. A. Hankey, H.E. Stanley and T.S. Chang, Phys. Rev. Lett. 29, 278 (1972).

31. R.B. Griffiths, private communication.

32. J.B. Torrance and M. Tinkham, Phys. Rev. 187, 587 (1969).

33. J.B. Torrance and M. Tinkham, Phys. Rev. 187, 595 (1969).

34. A.I. Mitsek, Phys. Status Solidi B59, 309 (1973).

35. A.I. Mitsek and P.F. Gaidanskii, Sov. Phys.-JETP 35, 1178 (1972).

36. M. Tinkham, Phys. Rev. 188, 967 (1969).

37. M. Motokawa, J. Phys. Soc. Jap. 35, 1315 (1973).

38. R.M. Bozorth, Ferromagnetism (Van Nostrand, Princeton, NJ., 1951).

39. A.F.G. Wyatt, J. Phys. C1, 684 (1968).

40. P.M. Levy and D.P. Landau, J. Appl. Phys. 39, 1128 (1968).

41. M.E. Fisher, Phys. Rev. 176, 257 (1968).

42. L. Landau, Phys. Z. Sowjetunion 11, 26 (1937); Phys. Z. Sowjetunion 11,
    545 (1937).

43. L. Landau, Phys. Z. Sowjetunion 4, 675 (1933).

44. C.J. Gorter and T. van Peski-Tinbergen, Physica (Utr.) 22, 273 (1956).

45. O.P. van Wier, T. van Peski-Tinbergen and C.J. Gorter, Physica (Utr.) 25, 116 (1959).

46. J.W. Leech and A.J. Manuel, Proc. Phys. Soc. Lond. B69, 210 (1956).

47. J.W. Leech and A.J. Manuel, Proc. Phys. Soc. Lond. B69, 220 (1956).

48. H. Bizette, C. Terrier and B. Tsai, Comptes rendus 243, 895 (1956).

49. A. Ito and O. Kazuo, J. Phys. Soc. Jap. 20, 784 (1965).

50. R.H. Schultz, Physica (Utr.) 7, 413 (1940).

51. J. Kanamori, Prog. Theor. Phys. 20, 890 (1958).

52. S. Yomosa, J. Phys. Soc. Jap. 15, 1068 (1960).

53. C. Starr, F. Bitter and A.R. Kaufman, Phys. Rev. 58, 977 (1940).

54. C. Starr, Phys. Rev. 58, 984 (1940).

55. C.G.B. Garrett, J. Chem. Phys. 19, 1154 (1951).

56. B.R. Heap, Proc. Phys. Soc. Lond. 80, 248 (1962).

57. I.S. Jacobs and P.E. Lawrence, Phys. Rev. 164, 866 (1967).

58. R.J. Birgeneau, W.B. Yelon, E. Cohen and J. Makowsky, Phys. Rev. B5, 2607 (1972); W.B. Yelon and R.J. Birgeneau, Phys. Rev. B5, 2615 (1972).

59. K. Ono, A. Ito and T. Fujita, J. Phys. Soc. Jap. 19, 2119 (1964).

60. M.K. Wilkinson, J.W. Cable, E.O. Wollan and W.C. Koehler, Phys. Rev. 113, 497 (1959).

61. H. Bizette, C. Terrier and B. Tsai, C.R. Acad. Sc. (Paris) 261, 653 (1965).

62. R. Alben, J. Phys. Soc. Jap. 26, 261 (1969).

63. E.Y. Chen, J.F. Dillon and H.J. Guggenheim, AIP Conf. Proc. 18, 329 (1973).

64. J.F. Dillon, E.Y. Chen and H.J. Guggenheim, Solid State Commun. 16, 371 (1975).

65. J.F. Dillon, E.Y. Chen and H.J. Guggenheim, AIP Conf. Proc. 24, 200 (1974).

66. J.A. Griffin, S.E. Schnatterly, Y. Farge, M. Regis and M.P. Fontana, Phys. Rev. B10, 1960 (1974).

67. J.A. Griffin and S.E. Schnatterly, AIP Conf. Proc. 24, 195 (1974).

68. D.J. Robbins and P. Day. Chem. Phys. Lett. 19, 529 (1973).

69. J.A. Griffin and S.E. Schnatterly, Phys. Rev. Lett. 33, 1576 (1974).

70. V.A. Trunov, A.Z. Yagud, A.I. Egerov, R.P. Dmitriev, V.A. Ul'yanov and A.F. Ioffe, Sov. Phys.-JETP Lett. 14, 146 (1971).

71. V.A. Trunov, G.M. Drabkin, A.I. Yegorov, R.P. Dmitriev, V.A. Ul'yanov and M.Y. Krautsova, 18th All-Union Conf. on Low Temp. Physics, Kiev, 149 (1974).

72. R.J. Birgeneau, G. Shirane, M. Blume and W.C. Koehler, Phys. Rev. Lett. 33, 1098 (1974).

73. C. Vettier, H.L. Alberts and D. Bloch, Phys. Rev. Lett. 31, 1414 (1973).

74. C. Vettier and W.B. Yelon, J. Phys. Chem. Solids 36, 401 (1975).

75. C. Vettier and W.B. Yelon, Phys. Rev. B11, 4700 (1975).

76. A. Narath, J. Appl. Phys. 37, 1124 (1966).

77. C. Tsallis, J. Phys. (Paris) 32, 903 (1971).

78. J.A. Nasser, J. Phys. (Paris) 34, 891 (1973).

79. J.A. Nasser, J. Phys. (Paris) 35, 83 (1974).

80. M. Motokawa and M. Date, J. Phys. Soc. Jap. 23, 1216 (1967).

81. M. Date and M. Motokawa, Phys. Rev. Lett. 15, 854 (1965).

82. A.R. Fert, P. Carrara, M.C. Lanusse, G. Mischler and J.P. Redoules, J. Phys. Chem. Solids 34, 223 (1973).

83. H. Bizette, C. Terrier and B. Tsai, Comptes rendus 245, 507 (1957).

84. W.B. Yelon and C. Vettier, J. Phys. C8, 2760 (1975).

85. I.S. Jacobs and P.E. Lawerence, J. Appl. Phys. 35, 996 (1964).

86. C. Vettier, H.L. Alberts, J. Beille and D. Bloch, C.R. Acad. Sc. (Paris) 275B, 915 (1972).

87. A.R. Fert, J. Gelard and D. Carrara, J. Phys. Chem. Solids 35, 261 (1974).

88. W.B. Yelon and C. Vettier, J. Phys. C8, 2769 (1975).

89. J.A. Griffin and J.D. Litser, AIP Conf. Proc. 29, 652 (1975).

90. L. Berger and S.A. Friedberg, Phys. Rev. A136, 158 (1964).

91. V.A. Schmidt and S.A. Friedberg, Phys. Rev. B1, 2250 (1970).

92. L.G. Polgar and S.A. Friedberg, Phys. Rev. B4, 3110 (1971).

93. C.S. Koonce, B.W. Mangum and D.D. Thornton, Phys. Rev. B4, 4054 (1971).

94. N. Schibuya, K. Knorr, H. Dachs, M. Steiner and B.M. Wanklyn, Solid State Commun. 17, 1305 (1975).

95. J.C. Wright and H.W. Moos, Phys. Lett. A29, 495 (1969).

96. J.C. Wright and H.W. Moos, J. Appl. Phys. 41, 1244 (1970).

97. T. Rado, Solid State Commun. 8, 1349 (1970).

98. L.M. Holmes, Int. J. Magn. 6, 111 (1974).

99. G.T. Rado, Phys. Rev. Lett. 23, 644 (1969).

100. J.C. Wright, H.W. Moos, J.H. Colwell, B.W. Mangum and D.D. Thornton, Phys. Rev. B3, 843 (1971).

101. J.E. Battison, A. Kasten, M.J.M. Leask and J.B. Lowry, Solid State Commun. 17, 1363 (1975).

102. R.A. Alikhanov, Sov. Phys.-JETP 36, 1690 (1959).

103. G.A. Prinz, D.W. Forester and J.L. Lewis, Phys. Rev. B8, 2155 (1973).

104. R.F. Altman, S. Spooner, D.P. Landau, AIP Conf. Proc. 10, 1163 (1972).

105. D.E. Wrege, S. Spooner and H.A. Gersch, AIP Conf. Proc. 5, 1334 (1971).

106. Y.A. Popkov, V.V. Eremenko, V.I. Fomin and A.P. Mokhir, Sov. Phys. Solid State 14, 1985 (1973).

107. I.S. Jacobs, J. Appl. Phys. 34, 1106 (1963).

108. K.L. Dudko, V.V. Eremenko and V.M. Fridman, Sov. Phys. JETP, 41, 326 (1975).

109. V.I. Ozhogin, Sov. Phys.-JETP 45, 1687 (1963).

110. V.M. Naumenko, N.F. Kharchenko, V.V. Eremenko, K.L. Dudko and Y.G. Litvinenko, Low Temp. Phys., LT 13, Vol. 12, ed. Timmerhaus, O'Sullivan and Hammel.

111. Y.G. Litvenko, V.V. Eremenko and V.I. Myatlik. Sov. Phys. Solid State 15, 871 (1973).

112. N.F. Kharchenko, L.I. Belyi and V.V. Eremenko, Bull. Acad. Sci. U.S.S.R. Phys. Ser. 36, 1099 (1972).

113. V.V. Eremenko, K.L. Dudko, Y.G. Litvenko and N.F. Kharchenko, IEEE Trans. Magn. 8, 645 (1972).

114. K.B. Lyons, H.L. Carter and P.A. Fleury, Proc. of the 3rd Int. Conf. on Light Scattering in Solids, Campinas, Brazil, p. 244, July 1975.

115. E. Bucher, R.J. Birgeneau, J.P. Maita and G.P. Felcher and T.O. Brun, Phys. Rev. Lett. 28, 746 (1972).

116. T.J. Moran, R.L. Thomas, P.M. Levy and H.H. Chen, Phys. Rev. B $\underline{7}$, 3238 (1973).

117. T.O. Brun, G.H. Lander, F.W. Korty, J.S. Kouvel, AIP Conf. Proc. $\underline{24}$, 244 (1974).

118. H.R. Child, M.K. Wilkinson, J.W. Cable, W.C. Koehler and E.O. Wollan, Phys. Rev. $\underline{131}$, 922 (1963).

119. P. Streit, G.E. Everett and A.W. Lawson, Phys. Lett. A$\underline{50}$ 199 (1974).

120. H.C. Schopper, Int. J. Magn. $\underline{3}$, 23 (1972).

121. J.N. Lee and H.W. Moos, Phys. Rev. B $\underline{5}$, 3645 (1972).

122. J.N. Lee, H.W. Moos and B.W. Mangum, Solid State Commun. $\underline{9}$, 1139 (1971).

123. J.F.L. Lewis and G.A. Prinz, Phys. Rev. B $\underline{10}$, 2892 (1974).

124. H.C. Schopper, P.J. Beekerm W. Böhm, G. Dummer, H.G. Kahle, L. Klein and G. Muller-Vogt, Phys. Status Solidi B$\underline{46}$, K115 (1971).

125. J.D. Cashion, A.H. Cooke, T.L. Thorp and M.R. Wells, Phys. C. $\underline{1}$, 539 (1968).

126. L.M. Holmes, L.G. van Uitert, R.R. Hecker and G.W. Hull, Phys. Rev. B $\underline{5}$, 138 (1972).

127. S. Hüfner, L. Holmes, F. Varsanyi and L.G. van Uitert, Phys. Rev. $\underline{171}$, 507 (1968).

128. H. Schuchert, S. Hüfner, R. Faulhaber, Z. Phys. $\underline{222}$, 105 (1969).

129. S. Hüfner, L. Holmes, F. Varsanyi and L.G. van Uitert, Phys. Lett., 301 (1967).

130. H. Schuchert, S. Hüfner and R. Faulhaber, J. Appl. Phys. $\underline{39}$, 1137 (1968).

131. L. Holmes, R. Sherwood and L.G. van Uitert, J. Appl. Phys. $\underline{39}$, 1373 (1968).

132. L.M. Holmes, L.G. van Uitert and G.W. Hull, Solid State Commun. $\underline{9}$, 1373 (1971).

133. L.M. Holmes and L.G. van Uitert, Phys. Rev. B $\underline{5}$, 147 (1972).

134. G. Velleaud and M. Mercier, J. Phys. (Paris), L251 (1975).

135. J.W. Cable and W.C. Koehler, AIP Conf. Proc. $\underline{5}$ 1381 (1971).

136. N. Nereson and G. Arnold, J. Appl. Phys. $\underline{42}$, 1625 (1971).

137. F. Hulliger, M. Landolt, H.R. Ott and R. Schmelczer, J. Low Temp. Phys. $\underline{20}$, 269 (1975).

138. G.H. Lander, M.H. Mueller and O. Vogt, AIP Conf. Proc. $\underline{24}$, 430 (1974).

139. T. Tsuchida and Y. Nakamura, J. Phys. Soc. Jap. $\underline{22}$, 942 (1967).

140. H. Bartholin, D. Florence, Tcheng-si Wang and O. Vogt, Phys. Status Solidi $\underline{24}$, 631 (1974).

141. H. Többe, Z. Physik $\underline{237}$, 403 (1970).

142. T. Tsuchida and Y. Nakamura, J. Phys. Soc. Jap. $\underline{25}$, 284 (1968).

143. G. Busch and O. Vogt, Phys. Lett. $\underline{20}$, 152 (1966).

144. G. Busch and O. Vogt, Phys. Lett. A$\underline{25}$, 449 (1967).

145. H. Bartholin, D. Florence, W. Tcheng-si and O. Vogt, Phys. Status Solidi $\underline{29}$, 275 (1975).

146. T. Tsuchida and W.E. Wallace, J. Chem. Phys. $\underline{43}$, 2885 (1965).

147. J.C. Wright and H.W. Moos, Phys. Rev. B $\underline{4}$, 163 (1971).

148. A. Kasten and P.J. Becker, J. Phys. C $\underline{7}$, 3120 (1974).

149. A.H. Cooke, C.J. Ellis, K.A. Gehring, M.J.M. Leask, D.M. Martin, B.M. Wanklyn, M.R. Wells and R.L. White, Solid State Commun. $\underline{8}$, 689 (1970).

150. D. Wappler, Phys. Kondens. Mater. 17, 113 (1974).

151. R. Griessen, M. Landolt and H.R. Ott, Solid State Commun. 9, 2219 (1971).

152. T. Janssen, Phys. Kondens. Mater 15, 142 (1972).

153. P. Fisher, W. Haelg, W. Von Wartenburg, P. Schwob and O. Vogt, Phys. Kondens. Mater. 9, 249 (1969).

154. T. Komaru, T. Hihara, Y. Koi, J. Phys. Soc. Jap. 31, 1391 (1971).

155. T.R. McGuire, F. Holtzberg and R.J. Joenk, J. Phys. Chem. Solids 29, 410 (1967).

156. P. Schwob and O. Vogt, Phys. Lett. 22, 374 (1966).

157. C. Kuznia and G. Kneer, Phys. Lett. A 27, 664 (1968).

158. T.M. Kwon, and G.E. Everett, Proc. Int. Conf. of Mag., Moscow, 3, 520 (1973).

159. G.E. Everett and R.C. Jones, Phys. Rev. B 4, 1561 (1971).

160. A. Narath, Phys. Rev. A136, 766 (1964).

161. A. Narath, Phys. Rev. A140, 552 (1965).

162. A. Narath, Phys. Rev. A139, 1221 (1965).

163. H. Kobayashi and T. Haseda, J. Phys. Soc. Jap. 19, 765 (1964).

164. T. Oguchi and F. Takano, J. Phys. Soc. Jap. 19, 1265 (1964).

165. T. Oguchi, J. Phys. Soc. Jap. 20, 2236 (1965).

166. A. Narath, Phys. Lett. 13, 12 (1964).

167. D.E. Cox, G. Shirane, B.C. Frazer and H. Narath, J. Appl. Phys. 37, 1126 (1966).

168. A. Narath, J. Phys. Soc. Jap. 19, 2244 (1964).

169. J. Kanamori, Prog. Theor. Phys. 35, 16 (1966).

170. M. Lowe, C.R. Abeldo and A.A. Misetich, AIP Conf. Proc., 5, 307 (1971).

171. M.A. Lowe, C.R. Abeldo and A.A. Misetich, Phys. Lett. A37, 274 (1971).

172. A.J. van Duyneveldt and J. Soeteman, Phys. Status Solidi 16, K17 (1973).

173. Y. Kuramitsu, J. Watanabe and T. Haseda, J. Phys. Soc. Jap. 38, 61 (1975).

174. K.A. Kay and J.B. Torrance, Phys. Rev. B 2, 746 (1970).

175. C.E. Johnson, Proc. Phys. Soc. 88, 943 (1966).

176. K. Inomata and T. Oguchi, J. Phys. Soc. Jap. 23, 765 (1967).

177. K. Inomata and T. Oguchi, J. Phys. Soc. Jap. 28, 905 (1970).

178. H. Nishihara, H. Yasuoka and A. Hirai, J. Phys. Soc. Jap. 32, 1135 (1972).

179. T. Goto, J. Phys. Soc. Jap. 31, 1842 (1971).

180. T. Goto, A. Hirai and T. Haseda, J. Phys. Soc. Jap. 34, 353 (1973).

181. N. Fijii, M. Motokawa and M. Date, J. Phys. Soc. Jap. 25, 700 (1968).

182. K. Katsumata, J. Phys. Soc. Jap. 39, 42 (1975).

183. M. Date and M. Motokawa, Phys. Rev. Lett. 16, 1111 (1966).

184. M. Motokawa and M. Date, J. Phys. Soc. Jap. 20, 465 (1965).

185. T. Oguchi, Prog. Theor. Phys. 52, 363 (1974).

186. Y. Kuramitsu, K. Amaya and T. Haseda, J. Phys. Soc. Jap. 33, 83 (1972).

187. I. Ono and T. Oguchi, Phys. Lett. A38, 39 (1972).

188. I. Ono, Phys. Lett. A46, 483 (1974).

189. J.B. Torrance, Jr. and M. Tinkham, J. Appl. Phys. 39, 822 (1968).

190. M. Date and M. Motokawa, J. Phys. Soc. Jap. 24, 41 (1968).

191. D.F. Nicoli and M. Tinkham, Phys. Rev. B 9, 3126 (1974).

192. J.B. Torrance and K.A. Hay, AIP Conf. Proc. 10, 1694 (1972).

193. K.L. Ngai and J. Ruvalds, Phys. Rev. Lett. 31, 166 (1973).

194. J.B. Torrance and K.A. Hay, Phys. Rev. Lett. 31, 163 (1973).

195. A.L.M. Bongaarts, B. Van Laar, A.C. Botterman and W.J.M. de Jonge, Phys. Lett. A41, 411 (1972).

196. A.C. Botterman, W.J.M. de Jonge, and K. Kopinga, Proc. Int. Conf. Mag., Moscow, 3, 325 (1973).

197. T. de Neef and W.J.M. de Jonge, Phys. Rev. B 10, 1059 (1974).

198. M. Motokawa, Proc. 12th Int. Conf. on Low Temp. Phys., Kyoto, 703
     (1970).

199. L.G. Polgar, A. Herweijer and W.J.M. de Jonge, Phys. Rev. B 5, 1957 (1972).

200. A. Herweijer, W.J.M. de Jonge, A.C. Botterman, A.L.M. Bongaarts and
     J.A. Cowen, Phys. Rev. B 5, 4618 (1972).

201. A.L.M. Bongaarts and B. van Laar, Phys. Rev. B 6, 2669 (1972).

202. L. Holmes and M. Schieber, J. Appl. Phys. 37, 968 (1966).

203. L. Holmes and M. Schieber, Phys. Rev. 167, 449 (1968).

204. S. Foner, R.B. Frankel, W.M. Reiff, H. Wong and G.J. Long, 21st Magnetism
     Conf., Philadelphia (1975).

205. S. Foner and R.B. Frankel, Solid State Commun. 16, 159 (1975).

206. S. Foner, R.B. Frankel and E.J. McNiff, Jr., W.M. Reiff, B.F. Little and
     G.J. Long, 20th Magnetism Conf., San Fransisco, 363 (1974).

207. D.P. Landau, B.E. Keen, B. Schneider and W.P. Wolf, Phys. Rev. B 3,
     2310 (1971).

208. W.P. Wolf, AIP Conf. Proc. 24, 255 (1974).

209. W.P. Wolf, D.P. Landau, B.E. Keen and B. Schneider, Phys. Rev. B 5,
     4472 (1972).

210. B. Schneider, D.P. Landau, B.E. Keen and W.P. Wolf, Phys. Lett. 23, 210 (1966).

211. R. Bidaux, P. Carrara and B. Vivet, J. Phys. Chem. Solids 28, 2453 (1967).

212. A.F.G. Wyatt, thesis, Oxford University, 1963 (unpublished).

213. M. Ball, W.P. Wolf and A.F.G. Wyatt, J. Appl. Phys. 35, 937 (1964);
     Phys. Lett. 10, 7 (1964).

214. B.E. Keen, D. Landau, B. Schneider and W.P. Wolf, J. Appl. Phys. 37, 1120 (1966).

215. D.P. Landau, thesis, Yale University, 1967 (unpublished); D.P. Landau and B.E. Keen (to be published).

216. R. Bidaux, P. Carrara and B. Vivet, J. Phys. (Paris) 28, 187 (1967); R. Bidaux and B. Vivet, J. Phys. (Paris) 29, 57 (1968).

217. R. Bidaux, P. Carrara and B. Vivet, J. Phys. (Paris) 29, 357 (1968).

218. G.F. Tuthill, F. Harbus and H.E. Stanley, Phys. Rev. Lett. 31, 527 (1973).

219. A.T. Skjeltorp, R. Alben and W.P. Wolf, AIP Conf. Proc. 18, 770 (1974).

220. J.F. Dillon, Jr., E. Yi Chen and W.P. Wolf, Proc. of the Int. Conf. on Mag., Moscow, 6, 38 (1973).

221. J.F. Dillon, E. Yi Chen and W.P. Wolf, AIP Conf. Proc. 18, 334 (1973).

222. J.F. Dillon, Jr., E. Yi Chen, N. Giordano and W.P. Wolf, Phys. Rev. Lett. 33, 98 (1974).

223. M. Blume, L.M. Corliss, J.M. Hastings and E. Schuller, Phys. Rev. Lett. 32, 544 (1974).

224. N. Giordano and W.P. Wolf (to be published).

225. J.F. Dillon, Jr., E. Yi Chen and H. Guggenheim, AIP Conf. Proc. 24, 200 (1974).

226. R. Alben, M. Blume, L.M. Corliss and J.M. Hastings, Phys. Rev. B 11, 295 (1975).

227. A. Gavignet-Tillard, J. Hammann and L. de Seze, J. Phys. (Paris) 34, 27 (1973).

228. R. Bidaux, A. Gavignet-Tillard and J. Hammann, J. Phys. (Paris) 34, 19 (1973).

229. A.M. Cooke, T.L. Thorp and M.R. Welles, Proc. Phys. Soc. Lond. 92, 400 (1967).

230. A. Gavignet-Tillard, J. Hammann and L. de Seze, Proc. Int. Conf. Mag., Moscow, 1, 374 (1973).

231. K. Adachi, K. Sato and M. Takeda, J. Phys. Soc. Jap. 26, 631 (1969).

232. K. Sato, K. Adachi, T. Okamoto and E. Tatsumoto, J. Phys. Soc. Jap. 26, 639 (1969).

233. K. Adachi, K. Sato, M. Matsuura and O. Masayoshi, J. Phys. Soc. Jap. 29, 323 (1970).

234. M. Hattori, K. Adachi and H. Nakano, J. Phys. Soc. Jap. 26, 642 (1969).

235. M. Hattori, K. Adachi and H. Nakano, J. Phys. Soc. Jap. 35, 1025 (1973).

236. Y. Kasai, S. Miyazima and I. Syozi, Prog. Theor. Phys. 42, 1 (1969).

237. Y. Kasai and I. Syozi, Prog. Theor. Phys. 50, 1182 (1973).

238. M. Hattori and H. Nakano, Prog. Theor. Phys. 40, 958 (1968).

239. S. Katsura and F. Matsubara, Can. J. Phys. 52, 120 (1974).

240. N.F. Mott and Z. Zinamon, Rep. Prog. Phys. 33, 881 (1971).

241. M. Kuznietz, IBM J. Res. Dev. 14, 224 (1970).

242. R.C. Maglic, Phys. Rev. B 10, 1943 (1974).

243. J.M. Robinson and P. Erdös, Phys. Rev. B 9, 2187 (1974).

244. M. Kuznietz, G.H. Lander and Y. Baskin, J. Appl. Phys. 40, 1130 (1969).

245. G.H. Lander, M. Kuznietz, J. Crangle and Y. Baskin, Bull. Am. Phys. Soc., 14 387 (1969).

246. G.H. Lander, M. Kuznietz and D.E. Cox, Phys. Rev. 188, 963 (1969).

247. J. Crangle, M. Kuznietz and G.H. Lander, Proc. Phys. Soc. Lond. (Solid State) J. Phys. C2, 925 (1969).

248. J. Leciejewicz, R. Troc, A. Murasik and T. Palewski, Phys. Status Solidi 48, 445 (1971).

249. A. Ligenza, A. Murasik, A. Zygmunt and J. Leciejewicz, Phys. Status Solidi 16, K171 (1973).

250. K.P. Belov, A.S. Dmitrievskii, R.Z. Levitin, T. Palewski, Yu. F. Popov and W. Suski, Sov. Phys.-JETP Lett. $\underline{17}$, 56 (1973).

251. W. Suski, A. Wojakowski and T. Palewski, Phys. Status Solidi $\underline{27}$, K113 (1975).

252. J. Leciejewicz, R. Troc and T. Palewski, Phys. Status Solidi B$\underline{65}$, K57 (1974).

253. R.J. Birgeneau, private communication.

254. R.J. Birgeneau, AIP Conf. Proc. $\underline{24}$, 258 (1974).

255. J.A. Griffin and S.E. Schnatterly, Phys. Rev. Lett. $\underline{33}$, 1576 (1974).

256. N. Giordano and W.P. Wolf, Phys. Rev. Lett. $\underline{35}$, 799 (1975).

257. N. Giordano and W.P. Wolf, AIP Conf. Proc. $\underline{29}$, 459 (1975).

258. E.K. Riedel, H. Meyer and R.P. Behringer, J. Low Temp. Phys. $\underline{22}$, 369 (1976).

259. N. Giordano (to be published).

260. A.L.M. Bongaarts, thesis, Technische Hogeschool, Eindhoven 1975.

261. A.L.M. Bongaarts, Phys. Lett. A$\underline{49}$, 211 (1974).

262. A.T. Starovoitov, V.I. Ozhogin and G.M. Loginov, Phys. Lett. A$\underline{29}$, 617 (1969).

263. C. Veyret, J.B. Ayasse, J. Chaussey, J. Mareschal and J. Sivardiere, J. Phys. (Paris) $\underline{31}$, 607 (1970).

264. R.D. Spence, J. Chem. Phys. $\underline{62}$, 3659 (1975).

265. V.A. Schmidt and S.A. Friedberg, Phys. Rev. $\underline{188}$, 809 (1969).

266. F. Kissell and W. Wallace, J. Less Common Met. $\underline{11}$, 417 (1966).

267. T. Kaneko, S. Miura and M. Ohashi, J. Phys. Soc. Jap. $\underline{34}$, 1100 (1973).

268. T. Kaneko, J. Phys. Soc. Jap. $\underline{25}$, 905 (1968).

269. D.B. Losee, W.E. Hatfield and I. Bernal, Phys. Rev. Lett. $\underline{35}$, 1665 (1975).

270. E.R. Jones and J.A. Stone, J. Chem. Phys. 56, 1343 (1972).

271. V.E. Wood, A.E. Austin, E.W. Collings and K.C. Brog, J. Phys. Chem. Solids 34, 859 (1973).

272. R.C. Sherwood, H.J. Williams and J.H. Wernick, J. Appl. Phys. 35, 1049 (1964).

273. T.O. Brun, G.P. Felcher and J.S. Kouvel, AIP Conf. Proc. 5, 1376 (1971).

274. R.D. Spence and J.L. Knirk, Proc. Int. Conf. Mag., Moscow, 3, 297 (1973).

275. R.D. Spence and A.C. Botterman, Phys. Rev. B 9, 2993 (1974).

276. M.J. Metcalfe and H.M. Rosenberg, J. Phys. C 5, 474 (1972).

277. G. Velleaud and M. Mercier, Solid State Commun. 17, 237 (1975).

278. H. Hirota and A. Yanase, J. Phys. Soc. Jap. 20, 1596 (1965).

279. V.I. Timoshchuk and I.G. Fakidov, Sov. Phys. Solid State 13, 85 (1971).

280. C.A. Poldy and K.N.R. Taylor, J. Phys. F. 3, 145 (1973).

281. J. Flokstra, G.J. Gerritsma and B. van den Brandt, Phys. Lett. A53, 159 (1975).

282. H.T. Witteven, W.L.C. Rutten and J. Reedijk, J. Inorg. Nucl. Chem. 37, 913 (1975).

283. H. Oesterreicher, J. Less-Common Met. 30, 225 (1973).

284. H. Oesterreicher, Phys. Status Solidi A12, K109 (1972).

285. R. Bidaux, J.E. Bouree and J. Hammann, AIP Conf. Proc. 24, 67 (1974).

286. T. Kaneko, M. Ohashi, S. Miura, K. Kamigaki, A. Hoshi and H. Yoshida, AIP Conf. Proc. 24, 423 (1974).

287. R.D. Hutchens and W.E. Wallace, J. Solid State Chem. 9, 152 (1974).

288. A.N. Christensen, J. Solid State Chem. $\underline{4}$, 46 (1972).

289. A.N. Christensen, R.M. Hornreich and B. Sharon, Solid State Commun. $\underline{13}$, 963 (1973).

290. D. Debray, B.F. Wortmann and S. Methfessel, Phys. Status Solidi $\underline{30}$, 713 (1975).

291. K.H.J. Buschow and J.F. Fast, Phys. Status Solidi $\underline{21}$, 593 (1967).

292. J.P. Redoules, P. Carrara, A.R. Fert, M.C. Lanusse and G. Mischler, J. Phys. (Paris) $\underline{33}$, 281 (1972).

293. W. Wüchner and J. Laugsch, Int. J. Magn. $\underline{5}$, 181 (1973).